

# Sheffield Hallam University

*Crain-based nanoscale multilayer coatings dedicated to wear and oxidation protection.*

REINHARD, Christina.

Available from the Sheffield Hallam University Research Archive (SHURA) at:

<http://shura.shu.ac.uk/20272/>

## A Sheffield Hallam University thesis

This thesis is protected by copyright which belongs to the author.

The content must not be changed in any way or sold commercially in any format or medium without the formal permission of the author.

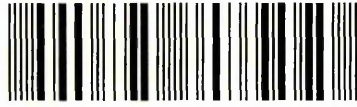
When referring to this work, full bibliographic details including the author, title, awarding institution and date of the thesis must be given.

Please visit <http://shura.shu.ac.uk/20272/> and <http://shura.shu.ac.uk/information.html> for further details about copyright and re-use permissions.

Sheffield S1 1WB

25655

101 895 511 9



Sheffield Hallam University  
Learning and IT Services  
Adsetts Centre City Campus  
Sheffield S1 1WB

**REFERENCE**

Return to Learning C...

ProQuest Number: 10700917

All rights reserved

INFORMATION TO ALL USERS

The quality of this reproduction is dependent upon the quality of the copy submitted.

In the unlikely event that the author did not send a complete manuscript and there are missing pages, these will be noted. Also, if material had to be removed, a note will indicate the deletion.



ProQuest 10700917

Published by ProQuest LLC (2017). Copyright of the Dissertation is held by the Author.

All rights reserved.

This work is protected against unauthorized copying under Title 17, United States Code  
Microform Edition © ProQuest LLC.

ProQuest LLC.  
789 East Eisenhower Parkway  
P.O. Box 1346  
Ann Arbor, MI 48106 – 1346

# CrAlN-based Nanoscale Multilayer Coatings Dedicated to Wear and Oxidation Protection

Christina Reinhard

A thesis submitted in partial fulfilment of the requirements of  
Sheffield Hallam University for the degree Doctor of Philosophy

November 2007



---

---

# Abstract

---

---

This study explores the wear and oxidation resistance of novel CrAlYN/CrN nanoscale multilayer coatings grown by a combined high power impulse magnetron sputtering (HIPIMS) / unbalanced magnetron (UBM) sputtering process.

Firstly, it is found that a HIPIMS substrate etching pre-treatment prior to the coating deposition effectively removes contaminants from the substrate surface and provides the base for epitaxial growth. Subsequently, an improvement in the adhesion and the tribological performance of CrAlYN/CrN is observed compared to coatings pre-treated with a conventional cathodic arc pre-treatment.

Secondly, the effect of the deposition conditions on the microstructure and the subsequently arising coating properties is investigated. A variation in the energy of ions impinging at the substrate during the coating growth permits a change in the microstructure from polycrystalline columnar to partially single crystalline. Depending on the microstructure, CrAlYN/CrN reveals a maximum high hardness of 51 GPa and extremely low wear rate of  $10^{-17} \text{ m}^3\text{N}^{-1}\text{m}^{-1}$ . Modifications of the microstructure from nano-layered columnar to "near-monolithic" columnar are discovered with a change in the chemical composition. These structural changes only have a mild effect on the mechanical and tribological performance.

Finally, the oxidation performance of CrAlYN/CrN is extensively investigated. Annealing in air leads to simultaneously occurring processes with (i) the thermal degradation of the nanolayered CrAlYN/CrN into  $\text{Cr}_2\text{N}$  and  $\text{AlN}$  and (ii) the surface oxidation with the formation of corundum-type oxides and at long exposure times (iii) diffusion of substrate elements through the coating. The observed phase transformation into  $\text{Cr}_2\text{N}$  and  $\text{AlN}$  may be promoted by the diffusion of the substrate element Cr into the coating. The results suggest that the oxidation performance of CrAlYN/CrN can be improved if the coating is grown under high energetic bombardment. The coating is prevented from cracking and therefore protects the substrate material more effectively from oxidative attack. Furthermore, it is found that the oxidation resistance can also be improved when changing the chemical composition. Highly Al-containing coatings form  $\text{Cr}_2\text{O}_3\text{-Al}_2\text{O}_3$  oxides which protect the underlying more effectively than  $(\text{Cr,Al})_2\text{O}_3$  oxides grown on low Al-containing CrAlYN/CrN.

---

---

# Acknowledgements

---

---

This study would not have been possible without the help of numerous people.

K. Tinkam (Corus, Swinden Technology Centre) very kindly performed the SNMS analysis presented in this thesis.

Dr. R. Braun and M. Froehlich (both Institute of Materials Research, German Aerospace Centre) conducted the TG analysis shown in this study.

Dr. Q. Luo (Sheffield Hallam University), Dr. H. Bagshaw (University of Sheffield) and Prof. P.B. Barna (Research Institute of Technical Physics and Materials Science, Hungarian Academy of Science) introduced me to the fascinating world of the TEM. Dr. Luo and Dr. Bagshaw took the time to intensively train me on the various TEM instruments at the Materials & Research Centre of Sheffield Hallam University as well as at the Sorby Centre of University of Sheffield. Furthermore, I had the opportunity to visit Prof. Barna at the Hungarian Academy of Science and to use the TEM facilities at the Research Institute for Technical Physics and Materials Science. During this stay, extensive TEM analysis was performed on a variety of specimens.

G. Robinson, S. Creasey and L. Bowen and all technical staff in the Materials & Engineering Research Institute assisted me with many little things. C. Schimpf, U. Ratayski and K. Bernert, all placement students in the group, also supported my work and helped in various places.

Dr. Z. Zhou (University of Sheffield) discussed various results and showed me a lot of little tricks to make the life as a scientist easier.

A very special thanks to Dr. I.M. Ross (University of Sheffield) for being an excellent adviser, a partner in discussion and a good friend. Every meeting was an inspiration.

Thanks to all the people what contributed to this work in a more social way, especially my colleagues and fellow students I shared my office with. D. Horsfield nicely supported me in improving my "Yorkshire". S. Pilli was a good incentive in the writing up period. N. Mitromara shared all the good and bad experiences about doing a PhD. A. Gunay, K. Charlesworth, W. Jablonska, M. Yakutovich and A. Fouillet, A. Hecimovic and A. Vetushka were always up for a tea break.

Finally, thanks to my family without whom this work would have been impossible. Roswitha and Melanie always supported me with their love and never gave up believing in me. David patiently read my thesis and also kindly cleaned up the dishes after dinner.

---

---

# Advanced Studies

---

---

## i Conferences/Meetings

During this PhD study, it was possible to attend several conferences and meetings.

1. Technological Plasmas Workshop 2004: 19. Dec 2005, University of Sheffield, Sheffield, UK
2. 2nd HIPIMS-ABS Days, Advances in Industrial PVD Technologies: 12.-13. Jul 2005, Sheffield Hallam University, Sheffield, UK
3. Materials and Engineering Research Institute Open Day: 18. Jan 2006, Sheffield Hallam Univeristy, Sheffield, UK  
Award: Winner in Poster Competition
4. 3rd HIPIMS Days, Advances in Industrial PVD Technologies: 11.-12. Jul 2006, Sheffield Hallam University, Sheffield, UK
5. PSE Plasma Surface Engineering: 10.-15. Sept 2006, Garmish-Partenkirchen, Germany
6. Royal Microscopy Society Meeting: Microstructure of High Temperature Oxidation: 6. Feb 2007, Loughborough University, Loughborough, UK

## ii Publications

Various papers were published during this PhD study. These papers are summarised in the following:

Oxidation performance of nano-scale multilayer coatings on  $\gamma$ -TiAl,  
*I.M. Ross, W.M. Rainforth, Z. Zhou, J.C. Walker, C. Reinhard, A.P. Ehiasarian,  
P.Eh. Hovsepian and R. Braun,*  
accepted for publication in: Proceedings of the Electron Microscopy and Analysis

Group Conference 2007 (EMAG 2007), 3.-7. Sept 2007, Glasgow, UK

Oxidation Behaviour of Nanoscale Multilayer CrAlYN/CrN Coatings Deposited by the Combined High Power Impulse Magnetron Sputtering/ Unbalanced Magnetron Sputtering (HIPIMS/UBM) Technique,

*C. Reinhard, A.P. Ehiasarian, P.Eh. Housepian,*  
Plasma Processes and Polymers 4 (2007) S910-S915

CrN/NbN Superlattice Structured Coatings with Enhanced Corrosion Resistance Achieved by HIPIMS Interface Pre-treatment,

*C. Reinhard, A.P. Ehiasarian, P.Eh. Housepian,*  
Thin Solid Films 515 (2007) 3685-3892

Industrial-Scale Production of Corrosion-Resistant CrN/NbN Coatings Deposited by the Combined High Power Impulse Magnetron Sputtering Etching/ Unbalanced Magnetron Sputtering Deposition (HIPIMS/UBM) Process,

*A.P. Ehiasarian, C. Reinhard, P.Eh. Housepian, J.M. Colton,*  
49th Annual Technical Conference Proceedings Society of Vacuum Coaters (2006)  
349-353

CrAlYN/CrN Superlattice Coatings Deposited by the Combined High Power Impulse Magnetron Sputtering/Unbalanced Magnetron Sputtering Technique

*P.Eh. Housepian, C. Reinhard, A.P. Ehiasarian,*  
Surface & Coatings Technology 204 (2006) 4105-4110

---

---

# Table of Contents

---

---

<b>Acknowledgements</b>	<b>i</b>
<b>Advanced Studies</b>	<b>iii</b>
i    Conferences/Meetings . . . . .	iii
ii   Publications . . . . .	iii
<b>1 Introduction</b>	<b>1</b>
1.1 Aims & Objectives . . . . .	3
1.2 Outline of this Thesis . . . . .	4
<b>2 Literature Review</b>	<b>6</b>
2.1 Oxidation . . . . .	6
2.1.1 Oxidation of Metallic Materials . . . . .	6
2.1.2 Oxidation of PVD Coatings . . . . .	9
2.2 Physical Vapour Deposition . . . . .	11
2.2.1 Basics of Sputter Deposition . . . . .	11
2.2.1.1 Plasma Generation . . . . .	11
2.2.1.2 Ion-Solid Interactions at the Cathode . . . . .	12
2.2.2 Unbalanced Magnetron Sputtering . . . . .	14
2.2.3 High Power Impulse Magnetron Sputtering . . . . .	16
2.2.4 Steered Cathodic Arc Evaporation . . . . .	19
2.2.5 Comparison of the PVD Techniques . . . . .	20
2.3 Thin Film Growth . . . . .	22
2.4 Development of a Coating for Oxidation and Wear Protection . . . . .	26
2.4.1 Techniques to Achieve Good Substrate/Coating Adhesion . . . . .	26
2.4.1.1 Effect of a Substrate Surface Plasma Ion Etching Pre-Treatment . . . . .	26
2.4.1.2 Effect of a Deposition of an Intermediate Base Layer	28
2.4.2 Effect of a Nanoscale Multilayer Structure . . . . .	28
2.4.2.1 Mechanical Performance . . . . .	29
2.4.2.2 Oxidation Performance . . . . .	31

2.4.3	Effect of the Chemical Composition . . . . .	31
2.4.3.1	CrN Coatings . . . . .	32
2.4.3.2	CrAlN Coatings . . . . .	33
2.4.3.3	Y Containing Coatings . . . . .	37
2.5	Why Design CrAlYN/CrN Nanoscale Multilayer Coatings?? . . .	39
<b>3</b>	<b>Experimental Methods</b>	<b>40</b>
3.1	Fabrication of CrAlYN/CrN Coatings . . . . .	40
3.1.1	Deposition Equipment . . . . .	40
3.1.2	Substrate Preparation . . . . .	42
3.1.3	Substrate Etching Pre-Treatment . . . . .	43
3.1.4	Coating Deposition . . . . .	44
3.2	Microstructure and Phase Analysis . . . . .	49
3.2.1	Secondary Neutral Mass Spectrometry . . . . .	49
3.2.2	X-Ray Diffraction Techniques . . . . .	49
3.2.2.1	Functioning Principle of X-Ray Diffraction . . . . .	50
3.2.2.2	Phase Analysis . . . . .	51
3.2.2.3	Texture Determination . . . . .	52
3.2.2.4	Nanoscale Bi-Layer Periodicity Determination . . . . .	53
3.2.2.5	Stress Analysis . . . . .	53
3.2.3	Scanning Electron Microscopy and Energy Dispersive X-ray Analysis . . . . .	54
3.2.4	Transmission Electron Microscopy . . . . .	55
3.2.5	Electron Energy Loss Spectroscopy . . . . .	57
3.3	Mechanical and Tribological Testing . . . . .	58
3.3.1	Ball-Cratering Thickness Measurement . . . . .	58
3.3.2	Surface Roughness Measurement . . . . .	58
3.3.3	Adhesion Measurement . . . . .	58
3.3.3.1	Scratch Adhesion . . . . .	59
3.3.3.2	Rockwell C ( $HR_C$ ) Indentation . . . . .	59
3.3.4	Friction and Dry Sliding Wear Measurement . . . . .	60
3.3.5	Micro- and Nano-Hardness, Young's Modulus . . . . .	61
3.3.5.1	Knoop Indentation . . . . .	61
3.3.5.2	Nano-Indentation . . . . .	61
3.3.6	Dry High Speed Milling . . . . .	63
3.4	Oxidation Texting . . . . .	63
3.4.1	Thermogravimetric Analysis . . . . .	63
3.4.2	Isothermal Oxidation Analysis . . . . .	63

<b>4</b>	<b>Influence of the Substrate Etching Pre-Treatment on the Coating Microstructure and Performance</b>	<b>65</b>
4.1	Microstructural Characterisation . . . . .	66
4.1.1	SEM Analysis . . . . .	66
4.1.2	TEM Analysis . . . . .	68
4.2	Influence of the Interface Structure on the Mechanical Properties .	74
4.2.1	Adhesion . . . . .	74
4.2.2	Tribological Analysis . . . . .	76
4.3	Chapter Summary . . . . .	79
<b>5</b>	<b>Development of a Novel CrAlYN/CrN Coating</b>	<b>80</b>
5.1	Influence of Energetic Particle Bombardment on the Microstructure and Mechanical Properties . . . . .	80
5.1.1	SNMS Analysis . . . . .	81
5.1.2	XRD Analysis . . . . .	84
5.1.3	Texture Analysis . . . . .	88
5.1.4	SEM Analysis . . . . .	88
5.1.5	TEM Analysis . . . . .	92
5.1.6	Nanoscale Bi-Layer Periodicity . . . . .	105
5.1.7	Residual Stress . . . . .	105
5.1.8	Hardness and Young's Modulus . . . . .	109
5.1.9	Adhesion . . . . .	109
5.1.10	Friction and Dry Sliding Wear . . . . .	114
5.1.11	Dry High Speed Milling . . . . .	123
5.2	Influence of the Stabilisation of Bias Voltage on the Microstructure and Mechanical Properties . . . . .	127
5.3	Influence of the Chemical Composition on the Microstructure and Mechanical Properties . . . . .	128
5.3.1	Nanoscale Bi-Layer Periodicity . . . . .	128
5.3.2	SNMS Analysis . . . . .	131
5.3.3	XRD Analysis . . . . .	135
5.3.4	TEM Analysis . . . . .	138
5.3.5	Texture Analysis . . . . .	145
5.3.6	Residual Stress . . . . .	145
5.3.7	Hardness and Young's Modulus . . . . .	148
5.3.8	Adhesion . . . . .	151
5.3.9	Friction and Dry Sliding Wear . . . . .	152
5.4	Chapter Summary . . . . .	157

<b>6</b>	<b>Oxidation Behaviour of CrAlYN/CrN</b>	<b>159</b>
6.1	Thermogravimetric Analysis . . . . .	159
6.2	Short Term Oxidation for 1 h up to 1000°C . . . . .	162
6.2.1	Reactions after 1 h at 850°C . . . . .	162
6.2.2	Reactions after 1 h at 900°C . . . . .	170
6.2.3	Reactions after 1 h at 950°C . . . . .	172
6.2.4	Reactions after 1 h at 1000°C . . . . .	178
6.2.5	Thermogravimetric Analysis vs. Isothermal Heat-Treatment	186
6.3	Long term oxidation up to 100 h at 850°C . . . . .	187
6.3.1	Reactions after 1 h . . . . .	187
6.3.2	Reactions after 5 h . . . . .	187
6.3.3	Reactions after 20 h . . . . .	200
6.3.4	Reactions after 50 h . . . . .	203
6.3.5	Reactions after 100 h . . . . .	207
6.3.6	Determination of the Scale Growth Rate . . . . .	213
6.4	Influence of the Energetic Particle Bombardment on the Oxidation Performance . . . . .	216
6.4.1	Thermogravimetric Analysis . . . . .	216
6.4.2	Isothermal Heat-Treatment for 100 h at 850°C . . . . .	217
6.4.2.1	SEM Analysis . . . . .	217
6.4.2.2	XRD Analysis . . . . .	219
6.4.2.3	TEM Analysis . . . . .	219
6.4.3	Thermogravimetric Analysis vs. Isothermal Heat-Treatment	226
6.5	Influence of the Chemical Composition on the Oxidation Perfor- mance of CrAlYN/CrN Coatings . . . . .	228
6.5.1	Thermogravimetric Analysis . . . . .	228
6.5.2	Isothermal Oxidation . . . . .	229
6.5.2.1	SEM Analysis . . . . .	229
6.5.2.2	XRD Analysis . . . . .	232
6.5.2.3	TEM Analysis . . . . .	233
6.5.3	Thermogravimetric Analysis vs. Isothermal Heat-Treatment	238
6.6	Chapter Summary . . . . .	240
<b>7</b>	<b>Conclusion and Further Work</b>	<b>244</b>
7.1	Summary of the results . . . . .	244
7.1.1	Implementation of High Power Impulse Magnetron Sputter- ing as Etching Pre-Treatment Technique . . . . .	244

7.1.2	Design and Development of the Novel Nanoscale Multilayered CrAlYN/CrN Coatings . . . . .	245
7.1.3	Oxidation Performance . . . . .	246
7.2	Conclusion . . . . .	248
7.3	Future Work . . . . .	249
	Bibliography . . . . .	251

# CHAPTER 1

---

---

## Introduction

---

---

Within the last decades the demand for the protection of materials against oxidation and wear has been ever growing. This led to a new field of surface engineering - the design of a composite system (coating plus substrate) that produces a performance which cannot be achieved by either of the components on its own [1].

A very successful way of protecting various substrate materials is given with the deposition of coatings by physical vapour deposition (PVD). These often nitride based thin films combine high wear resistance with excellent oxidation resistance to serve high temperature applications such as dry high speed machining [2,3] and protection of special grades aerospace [4-6] and automotive alloys [7,8].

Various PVD methods can be exploited to generate thin films with a great diversity of properties. Unbalanced magnetron (UBM) sputtering is a well established PVD method to produce hard coatings. This technique permits the generation of complex coating systems like monolithically grown multicomponent coatings [9] or films with a nanoscale multilayer structure [10] and grants good control of the film structure and the resultant properties as the correlation between these factors and the process parameters are well understood. The use of the UBM technique is furthermore of advantage as the technique does not generate coatings afflicted with macro-particle induced growth defects which are known to compromise the film performance.

The deposition of a protective hard coating alone, however, is not sufficient to ensure enhanced functionality of the coating/substrate system. Additionally, strong adhesive forces between the coating and the substrate are required to guarantee stability of the compound. Well adherent coatings can be established when the substrate surface is subjected to energetic particle bombardment. A novel method with great potential for this task is found in the high power impulse magnetron sputtering (HIPIMS) process. For the last few years, many studies, mainly dealing with the plasma conditions and film deposition, have been performed on this matter [11–13]. However, knowledge about the impact of the ion bombardment by HIPIMS on the interface structure and the successively emerging coating properties is limited.

In view of the mechanical performance, the demand for coatings combining high hardness and excellent wear performance is steadily increasing. Monolithically grown multicomponent nitrides only provide a limited solution to this problem. A new attempt to generate high performance coatings can be made by the fabrication of nanolayered structures. These films can achieve a hardness largely exceeding the the hardness of the constituent layers [14]. If the hardness exceeds a value of 40 GPa, these coatings are referred to as superhard. The wear mechanism of these nanoscale modulated structures is also more favourable as the removal of wear debris is strongly reduced [15]. The nanolayer structure additionally suppresses the columnar growth and increases the coating density. It is therefore desirable to generate coatings with a nanoscale multilayer structure as these provide improved hardness and enhanced wear resistance in comparison to monolithically grown films [16–18].

Regarding the oxidation behaviour, the chemical coating composition is of crucial importance. Many coatings for oxidation protection applications are based on TiN, such as TiAlN [19], TiAlCrYN or TiAlCrN/CrN [20]. In these coatings, Ti turns out as the high temperature limiting element as it forms porous  $\text{TiO}_2$  oxides which cannot slow down further oxidation of the underlying material and therefore provide only poor oxidation protection.

The partial replacement of Ti with Al into TiAlN demonstrates that the high temperature performance can be significantly improved by utilising the alloying effects and benefiting from oxide scales with higher density [19]. Further improvement can be achieved by allowing other more oxidation resistant elements, such as Cr and Y [21]. Following this strategy, the complete removal of Ti as an element forming a porous non-protective oxide scales  $\text{TiO}_2$  appears as a following logical step. Coatings based on Cr and Al appear to be successful candidates for excellent oxidation resistance as they are expected to form dense and well adherent  $\text{Cr}_2\text{O}_3$  and  $\text{Al}_2\text{O}_3$  scales. Such oxides are known to effectively protect the underlying material against oxidation [22]. Additionally, engineering of the coating structure can be used as a the metallurgical approach improve the coating performance. The nanoscale multilayer films which were initially introduced to provide high hardness or favourable wear properties also effectively amplify the time needed for oxidising gases to reach the substrate surface thus reducing the oxidation rates [23].

Based on these facts, the development of a new type of coating seems possible that combines the advantages of a nanolayer modulation and a chemical modification to successfully protect the substrate material from environmental attack such as oxidation, corrosion and wear.

## 1.1 Aims & Objectives

The work presented in this PhD project addresses the development of an oxidation and wear resistant CrAlYN/CrN coating system deposited by PVD techniques. The aims of this study were initially defined as follows:

- to engineer the coating substrate interface by ion bombardment using the novel HIPIMS technology as substrate surface etching pre-treatment
- to develop a new generation of Ti-free nanoscale multilayer structured PVD coatings involving the elements Cr, Al and Y and correlate the deposition conditions to the coating microstructure and the performance properties

- to understand the mechanism of oxidation processes in these coating materials on various substrate materials and find a correlation between the microstructure and the resistance to environmental attack

## 1.2 Outline of this Thesis

Aside from this introduction, this thesis is organised as follows.

In chapter 2, a comprehensive literature review on the state-of-the-art techniques in the field of PVD is given, specifically, unbalanced magnetron sputtering as basis deposition technique as well its further development into high power impulse magnetron sputtering as substrate surface etching pre-treatment technique are addressed. Details on the effects governing the thin film growth mechanism as well as the mechanical and tribological performance are given. Additionally, the basics of oxidation are summarised and the oxidation capability of selected Cr-based nitride thin films is compared. Finally, this chapter provides a description of the theoretical considerations leading to the development of CrAlYN/CrN nanoscale multilayer films.

Chapter 3 considers the experimental equipment used during this PhD project. It also gives an inside in the measurement and analysis methods used to obtain and interpret information.

The chapters 4 to 6 comprises the knowledge obtained during this study.

Chapter 4 investigates the effect of the HIPIMS process to chemically and physically modify the substrate/coating interface. A comparison between the novel HIPIMS technique and the commonly used cathodic arc evaporation as pre-treatment method is provided.

Chapter 5 presents the influence of the deposition conditions during the coating growth on the microstructure and the mechanical performance of CrAlYN/CrN. Firstly, the effect of energy of energetic particle bombardment is investigated. Then, a modification of the chemical composition of the coating is analysed.

In chapter 6, the oxidation performance of CrAlYN/CrN in a medium and high

temperature regime is considered. Additionally, a comparison between the individual coatings is provided in order to assess the effect of the deposition conditions on the oxidation resistance.

Finally, chapter 7 brings together the main results and conclusions of this thesis and suggestions for future areas of work are listed.

# CHAPTER 2

---

---

## Literature Review

---

---

### 2.1 Oxidation

All materials react with their environment when exposed to oxygen containing atmospheres at elevated temperatures. These oxidation processes can be a serious threat for the integrity of components exposed to such harsh environments as oxidation leads to the degradation of the components which, in turn, lose the ability to fulfill their initial function. To successfully prevent or at least reduce oxidation, a basic knowledge of oxidation is desirable. The following section therefore will introduce the basic principles of oxidation of metallic materials.

#### 2.1.1 Oxidation of Metallic Materials

Most metals  $M$  form thin oxide scales  $M_xO_y$  when in contact with oxygen. This basic reaction can be described by the following equation:



The formation of an oxide layer can be divided into four major steps (see Fig. 2.1) [24]. Firstly,  $O_2$  is adsorbed at the metal surface and reacts with the metal (see Fig. 2.1(a)). This initial reaction forms the base for further oxidation,

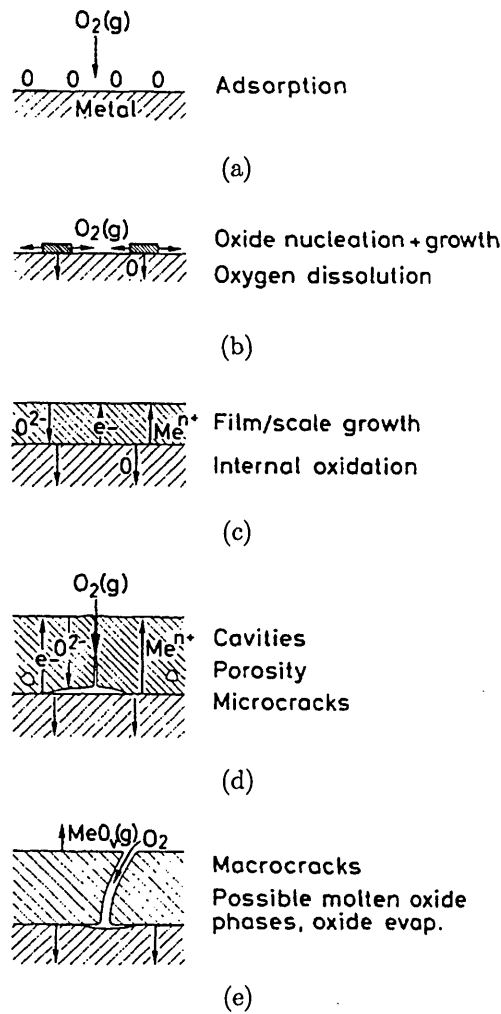


Fig. 2.1: (a)-(c) Growth reaction mechanism occurring during oxidation, (d),(e) Pathways for O diffusion through the coating

nucleation and the lateral growth of the oxide scale (see Fig. 2.1(b)). Once the surface is completely covered with a thin oxide film, a compact oxide layer grows (see Fig. 2.1(c)). Depending on the oxide structure, different transport mechanisms contribute to the growth [25]. These comprise gas transport through cavities and pores, diffusion along grain boundaries, lattice diffusion (see Fig. 2.1(d)) and through cracks (see Fig. 2.1(e)). For temperatures below  $2/3$  of the melting temperature  $T_M$  of the material, the transport is controlled by diffusion along the grain boundaries, whereas volume diffusion is dominant at higher temperatures [26].

The oxidation reaction can be described by means of thermodynamic and ki-

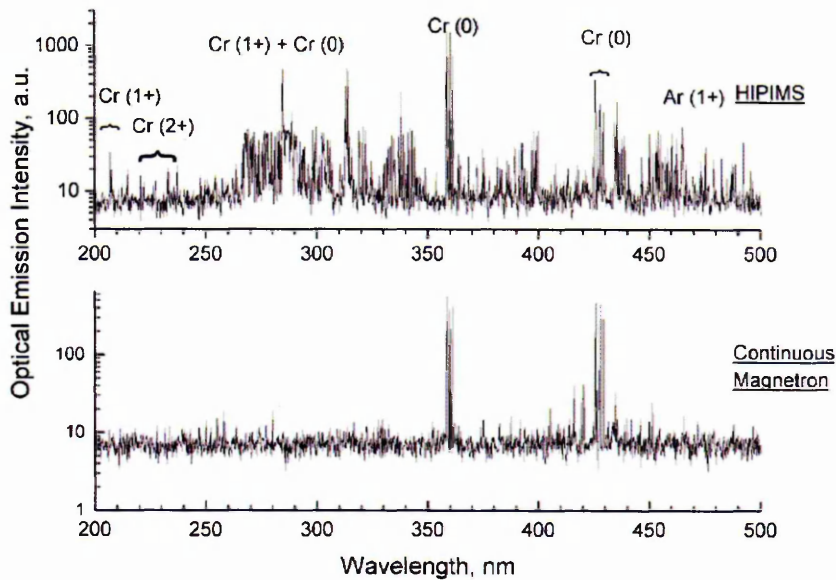


Fig. 2.7: Optical emission spectra (OES), comparing the plasma composition of a Cr/Ar plasma in a HIPIMS and a conventional d.c. UBM discharge at the same average power: Ions with higher ionisation states are detected in the HIPIMS plasma [51]

either of a very low amplitude or completely absent (see Fig. 2.7) [51]. In a HIPIMS discharge, which is run at the same average power, in contrast, numerous spectral lines of  $\text{Cr}^+$  are detected. This direct comparison of HIPIMS and UBM clearly shows that the HIPIMS discharge with its high energy input over a short period of time is able to generate highly charged metal ions in the plasma whereas the generation of such states is rather limited in a UBM discharge.

It was stated previously that the maximum ionisation degrees in a UBM plasma are well below 5% (see Sec. 2.2.2). In a HIPIMS discharge, in contrast, high degrees of ionisation at the cathode can be achieved. This degree of ionisation can be as high as 90% for Ti [52] and 70% for Cu [11] whereas the ionisation degree of Al is comparatively low with 9.5% [50]. From this, it can be concluded that HIPIMS provides higher degrees of ionisation compared to UBM.

In a d.c. magnetron discharge, the excitation of the inert gas and the metal species occurs simultaneously. During the on-time of a HIPIMS discharge, how-

netic contributions. The enthalpy of formation allows a prediction of the stability of a formed compound (see Tab. 2.1). The more negative this value is, the higher is the compound stability. While the direction and stability of reaction products are affected by thermodynamics, the time dependent behaviour of the oxidation is controlled by kinetics.

Tab. 2.1: Enthalpy of formation  $\Delta H_f^O$  of various nitrides and oxides under standard conditions

Compound	$\Delta H_f^O$ [kJ.mol <sup>-1</sup> ]
CrN [27]	-118
Cr <sub>2</sub> N [28]	-126
AlN [28]	-318
Cr <sub>2</sub> O <sub>3</sub> [28]	-1135
Al <sub>2</sub> O <sub>3</sub> [28]	-1621
TiO <sub>2</sub> [29]	-945

The growth kinetics of the oxide layer can be described by means of time laws. The most commonly observed rate laws are linear, logarithmic and parabolic, although they represent only limited and ideal cases. A linear law is mostly found for surface or phase boundary reactions. It is also valid when a protective scale cracks or spalls and allows direct access of gas to the metal. A logarithmic law refers to the formation of very thin oxide layers at low temperatures. A parabolic relationship was first formulated by Wagner [25] and can be expressed by the following equation:

$$x^2 = k_p \cdot t \quad (2.2)$$

Here,  $k_p$  represents the parabolic rate constant and  $t$  the reaction time. The variable  $x$  corresponds to either a weight gain or a thickness of the growing oxide layer. This parabolic law is often observed when the further growth of the dense scale involves the transport of either metal ions or oxygen ions. Here, metal ions migrate from the substrate/oxide interface to the oxide/gas interface while the latter move from the gas/oxide interface into the material. Assuming, the scale

is compact and well adherent, and a thermodynamic equilibrium is established at the substrate/scale and the scale/gas interface, the transport of these ions is controlled by the diffusion as rate determining mechanism.

One way to slow down the oxidation reactions of a metal is to provide a thin protective layer between the exposed material and the oxidising atmosphere. Cr and Al, for example, naturally form such protective layers in form of dense and well adherent, corundum-type  $\text{Cr}_2\text{O}_3$  and  $\text{Al}_2\text{O}_3$ . Especially  $\text{Al}_2\text{O}_3$  significantly reduces the inward diffusion of O and therefore effectively protects the underlying material [22]. If such protective layers cannot be provided naturally from the metal component, it may be desirable to apply a coating to protect the metal from oxidative attack. A variety of coating systems have been developed to fulfill these requirements. One group of coatings which is well established for the oxidation protection are hard nitride based coatings grown by physical vapour deposition (PVD). Although these coatings oxidise at significantly higher temperatures and lower rates compared to the unprotected metal, oxidation, however, cannot be completely prevented.

The following section shortly states possible reactions taking place in a substrate/coating system exposed to air at elevated temperatures.

### **2.1.2 Oxidation of PVD Coatings**

The oxidation of hard PVD coatings is mainly determined by degradation of the coating through a reaction with the environment and diffusion interaction between coating and substrate [25]. PVD coatings often exhibit a polycrystalline columnar structure. The degradation of coatings by reaction with the environment is strongly influenced by this structure as porosity at the column boundaries permits the penetration of gas into the coating and, hence, allows oxidation with or underneath the coating. In addition, the coating composition changes gradually with time. In nitride coatings, the replacement of N by O plays a major role [30]. Reactions between coating and substrate involve the diffusion of oxide forming elements out of the coating, slowly degrading the coating's ability to form

protective scales [31].

Oxidation of binary nitrides (TiN, CrN, ZrN), ternary nitrides (TiAlN [19], CrAlN [27], TiZrN, TiCrN [23]) and multilayer coatings (TiN/CrN [23]) often follows a parabolic growth law and implies diffusion-controlled oxidation processes. In multicomponent materials, in contrast, selective oxidation can be often detected where the separate components form oxides with different stability. TiAlN [19,32] and TiAlSiN [32], for example, form a double oxide with an outer Al-rich and an inner Ti-rich layer upon heating.

## 2.2 Physical Vapour Deposition

It was previously shown (see Sec. 2.1) that PVD coatings are promising candidates for the high temperature oxidation protection of metals. Here, the basic principle of PVD will be introduced.

Coating deposition via PVD involves the generation of a metal vapour of coating material and its subsequent condensation onto a substrate to form a thin film [33]. Two of the most important PVD techniques for the plasma generation are sputtering and evaporation. In sputtering, atoms are ejected from a solid surface by impact of gaseous ions, whereas in evaporation, atoms are removed from the surface by thermal heating [34]. The subsequent condensation at the substrate position to form a coating is independent of the plasma formation mechanism (see Sec. 2.3).

Sputtering (see Sec. 2.2.1) and evaporation (see Sec. 2.2.4) will be covered in the following in more detail. Additionally, two specific sputtering techniques, namely unbalanced magnetron (UBM) sputtering (see Sec. 2.2.2) and high power impulse magnetron sputtering (HIPIMS) (see Sec. 2.2.3) as well as the evaporation technique cathodic arc evaporation (see Sec. 2.2.4) will be characterised.

### 2.2.1 Basics of Sputter Deposition

#### 2.2.1.1 Plasma Generation

Sputter deposition is based on the generation of an electrically driven discharge. A simple arrangement for a discharge is shown schematically in Fig. 2.2(a) with a diode sputtering system.

It consists of a cathode (or target)/anode combination and a voltage source. By applying a voltage through a low-pressure gas (usually Ar), the gas "breaks down" into a collection of positively charged ions and free electrons which are not bound to an atom or molecule (see Fig. 2.2(b)) [35]. These usually weakly ionized plasmas are electrically conductive so that they respond strongly to electromagnetic fields.

### 2.2.1.2 Ion-Solid Interactions at the Cathode

As the cathode in a sputtering system is negatively charged to generate the discharge, it attracts positive ions from the plasma. When these ions are accelerated towards the cathode, they impact at the surface activating several mechanisms [36]. The ions transverse the solid and undergo collisions with target atoms. These target atoms are displaced from their lattice sites during these processes. According to the linear collision theory, knock-on of atoms generates collision cascades transferring momentum between the target atoms [37]. During this process, atoms close to the surface (max. depth~5 nm [38]) can be ejected from the solid and then migrate into the vapour phase. This process is generally referred to as sputtering.

Particle bombardment causes numerous further effects at the target, such as generation of interstitials and vacancies, ion implantation and intermixing, irradiation damage in form of amorphisation and large-amplitude vibrations (thermal spike) resulting in local heating and thermally activated diffusion [36]. Furthermore, secondary electrons are ejected and X-ray photons are generated (see Fig. 2.3) [39].

Sputtering can be quantified in terms of sputtering yield  $S$  which is defined as the number of target atoms ejected per incident particle.

$$\text{Sputter yield } S = \frac{\text{Ejected atoms}}{\text{Incident atom}} \quad (2.3)$$

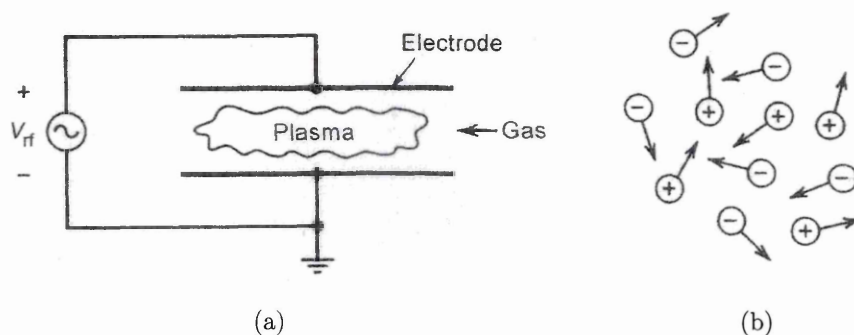


Fig. 2.2: Schematic view of (a) discharge in a diode sputtering system, (b) charged particles in a plasma [35]

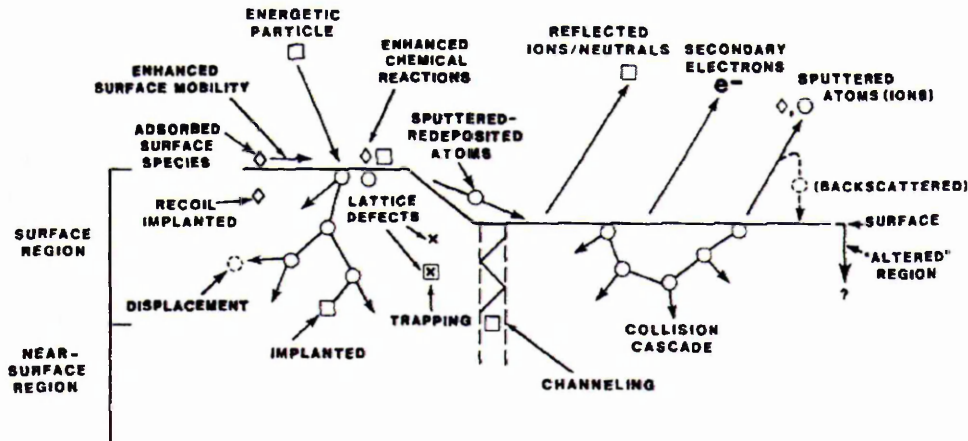


Fig. 2.3: Possible interactions between the target material and the impinging ions from the plasma [34]

The yield depends on the target material as well as the energy and angle of the bombarding species [40]. The bombarding ion needs to exceed a threshold energy of 20-40 eV before sputtering occurs. Above this threshold, the yield increases nearly linearly up to several 100 eV with typically 5 to 20 lattice atoms ejected per incident atom. The highest sputter yields are achieved when the bombarding particle has a comparable or larger mass than the target atom. However, strongly reduced sputter yields can be observed when sputtering takes place with reactive gases such as  $N_2$  and  $O_2$ . This reduced sputter yield is then attributed to a coverage of the target surface with reaction products between the reactive gas and the target material [41]. This process is called target poisoning.

Sputtered atoms have an energy distribution which has a maximum around a few eV and tails of towards higher energies [42]. The average energy of these sputtered neutral atoms arriving at the substrate position is 10-40 eV and therefore much higher than that of thermally evaporated atoms in a vacuum (0.2-0.4 eV) (see Sec. 2.2.4) [43].

When the ejected ions enter the plasma bulk, they become partially excited or ionised. However, the ionisation of the sputtered metal species is only very low with less than 1% in this basic sputtering process [44]. High ionisation degrees, however, are important to condense coatings with high density (see Sec. 2.3). It is

therefore desirable to enhance the ionisation degree of the plasma. An important step to overcome this drawback of the basic sputtering process was made with the development of unbalanced magnetron (UBM) sputtering. The principle of this technique will be introduced in the following.

### 2.2.2 Unbalanced Magnetron Sputtering

Magnetron discharges are cold cathode discharges within a magnetic field. They are commonly operated at pressures  $p < 7.5 \times 10^{-6}$  Pa with current densities  $I_{d,dens}$  of 0.01-0.1 A.cm<sup>-2</sup> for the cathode and negative discharge voltages  $U_d$  of 700-1000 V [45].

A typical magnetron plasma discharge is generated inside a crossed electric and magnetic field  $\vec{E} \times \vec{B}$  to confine the electron path to the near cathode region. The electric field is applied by the voltage to the cathode while the magnetic field is provided by an arrangement of permanent magnets behind the cathode (see Fig. 2.4). Electrons in the plasma travel on helical trajectories along the magnetic field lines and are confined near the target surface. This confinement acts as trap for the plasma. This confinement provides a high density plasma with a high collision probability between electrons and sputtered metal atoms. The metal ionisation is then initiated by electron impact which is the main ionization and excitation mechanism in magnetron discharges [46]. The ionisation degrees for metal species in the basic magnetron operation are typically less than 1% and therefore in a similar range to the basic sputtering process described earlier [44].

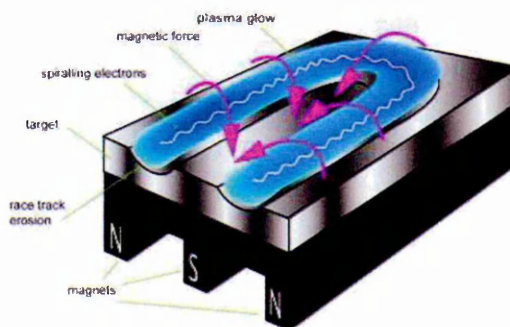


Fig. 2.4: Magnetron with superimposed  $\vec{E} \times \vec{B}$  field

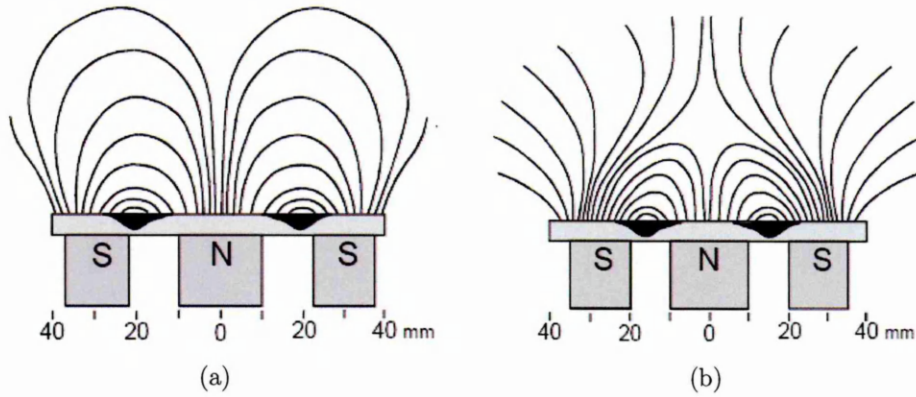


Fig. 2.5: Magnetic field lines in (a) a conventional, balanced magnetron and (b) an unbalanced magnetron [47]

A method to enhance ionisation and ion flux to the substrate was introduced by unbalancing the magnetron magnetic field [47, 48]. Here, the magnetic field lines are changed by strengthening the outer poles of the magnets, resulting in some magnetic lines proceeding perpendicular to the cathode surface, while the lines close to the target surface are still arched (see Fig. 2.5). Unbalancing the magnetron significantly improves degree of ionisation with maximum metal ionisation degrees of 5% [44]. The ion flux to the substrate increases strongly at the same time. Some electrons are no longer confined to the near-target region, but are able to follow the magnetic field lines towards the substrates. The ions are forced to follow the electron movement due to the ambipolarity of the plasma medium and, as a consequence, the ion bombardment at the substrate is increased. This ion bombardment during coating growth, in turn, enhances the density of deposited coatings.

A further increase in ionisation levels can be achieved by using multiple-magnetron systems in a closed field assembly, also referred to as closed field-UBM (CF-UBM, see Fig. 2.6) [49]. Magnets, installed close to each other, are of opposite polarity, forming a trap for the electrons in the plasma. This closed loop arrangement decreases the loss of electrons to the chamber walls, maintains a dense plasma in the middle of the chamber and ensures the coating deposition at reasonable growth rates.

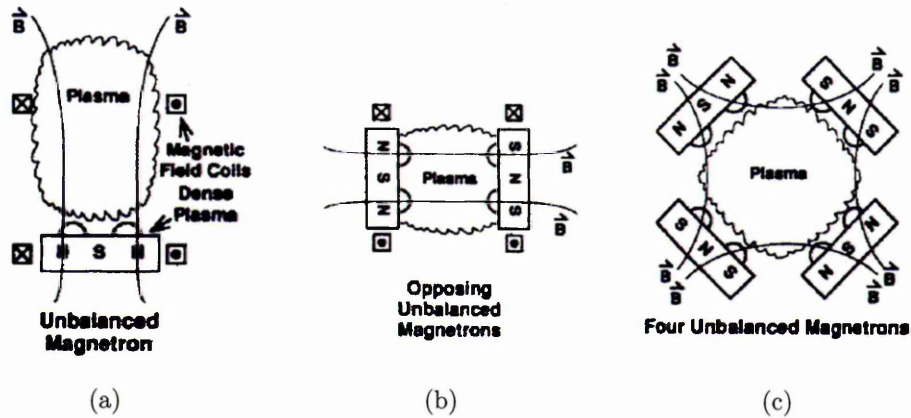


Fig. 2.6: Possible magnet configurations magnetron systems [34]: (a) unbalanced magnetron, (b) opposing unbalanced magnetrons and (c) four unbalanced magnetrons in a closed field assembly

### 2.2.3 High Power Impulse Magnetron Sputtering

As mentioned earlier, a high degree of ionisation in the plasma can be beneficial to produce coatings with high density. It is therefore of interest to further increase the degree of ionisation of the UBM sputtered material.

One way to achieve this is by increasing the power applied to the cathode. This technique, however, is limited by the heat bearing capability of the target as most of the applied power is transformed into heat. Target over-heating can be avoided by applying extremely high powers in short pulses with duty cycles (ratio of the time with pulse switched on to the time with pulse switched off) of less than 1% [11]. This method is referred to as high power impulse magnetron sputtering (HIPIMS).

Conventional d.c. magnetron sputtering is typically operated at cathode current densities  $I_{d,dens} < 0.1 \text{ A.cm}^{-2}$  and power densities  $P_{d,dens}$  up to  $50 \text{ W.cm}^{-2}$  [49]. HIPIMS discharges, in contrast, are operated with cathode voltages  $U_d$  ranging from 500-2000 V resulting in current densities  $I_{d,dens}$  of 3-4  $\text{A.cm}^{-2}$  and extremely high peak power densities  $P_{d,peak}$  up to  $3000 \text{ W.cm}^{-2}$  [50]. These rather different operation conditions strongly influence the properties of the respectively generated plasma. Optical emission spectroscopy (OES) of a Cr/Ar UBM discharge reveals that spectral lines of charged metal species, such as  $\text{Cr}^+$  ion, are

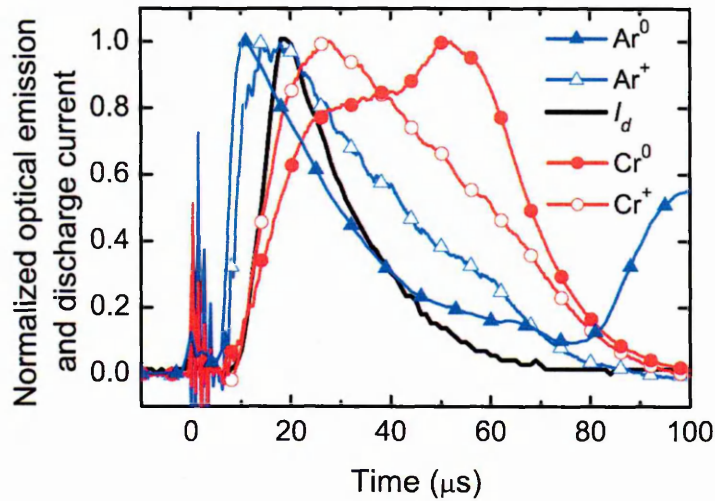


Fig. 2.8: Time-evolution of the plasma chemistry during the HIPIMS discharge: Directly after the pulse ignition,  $\text{Ar}^0$  is predominantly present whereas with time,  $\text{Cr}^+$  becomes more dominant [13]

ever, the excitation of the different species takes place at different times after pulse initiation. The chemical composition of a Ar/Cr plasma, measured by time-resolved OES, reveals the simultaneous development of  $\text{Ar}^0$ ,  $\text{Cr}^0$ ,  $\text{Cr}^{1+}$  and  $\text{Cr}^{2+}$  at low powers. At high powers, however, the plasma composition changes from Ar to Cr dominated during the pulse (see Fig. 2.8). Higher ionisation states evolve later on during the pulse as these states require a higher energy input in form of multiple electron impact for ionisation. Similar behaviour was found for Ar/Ti discharges [53].

A drawback of HIPIMS as deposition technique is its rather low deposition rate compared to UBM deposition. These rates are in a range of 20% to 80% of those rates obtained from a d.c. UBM discharge at equal average powers [54].

After this brief overview of the sputtering techniques UBM and HIPIMS, the following section covers the evaporation technique steered cathodic arc (CA) evaporation.

## 2.2.4 Steered Cathodic Arc Evaporation

Steered cathodic arc (CA) evaporation is a PVD technique that allows the formation of a metal plasma due to thermal evaporation from the target [55].

Such cathodic arcs discharges are usually run at high discharge currents  $I_d > 10$  A and relatively small voltages  $U_d < 100$  V. A magnetic field is normally applied to steer the motion of the arcs across the target and to ensure controlled surface erosion.

The plasma generation via evaporation starts when an arc strikes the cathode and initiates an arc spot at micro-protrusions on the surface. The applied voltage generates an electric field with current densities  $I_{d,dens}$  up to  $>10^{12}$   $A.m^{-2}$  in a volume of less than  $1 \mu m^3$  causing extreme Ohmic heating with temperatures up to  $6000^\circ C$  [56]. If a critical amount of energy is exceeded, an explosion-like sublimation takes place and a high density plasma is emitted. Formation, rearrangement and self-extinction of a spot takes place in less than  $20 ns$  until a new spot ignites at a different location. This process generates a metal plasma at micron-size, non-stationary cathode spots [56]. The emitted plasma flux reveals a high degree of ionisation up to 90% with high degrees of multiply charged ions [56].

CA evaporation allows the fast deposition of coatings as it provides high deposition rates which are significantly higher compared with the rates of the previously described sputtering techniques [55,59]. A major drawback of CA evaporation for coating deposition, however, is the ejection of macro-particles, or droplets, from the target [55]. As mentioned above, temperatures sufficiently high for sublimation of material are reached within cathode spots. Material adjacent to the spot, however, can only reach a molten state. During the explosive evaporation, this material is also ejected into the plasma. The size and quantity of these macro-particles emitted mainly depend on the melting point of the target material. Droplets of high melting point materials, such as Cr, often reach dimensions of several  $\mu m$  when deposited onto the substrate [60]. Here, they cause abnormal film growth due to atomic shadowing during coating deposition and result in large-scale growth defects (see Fig. 2.9(a)) [57]. The detrimental effects of macro-

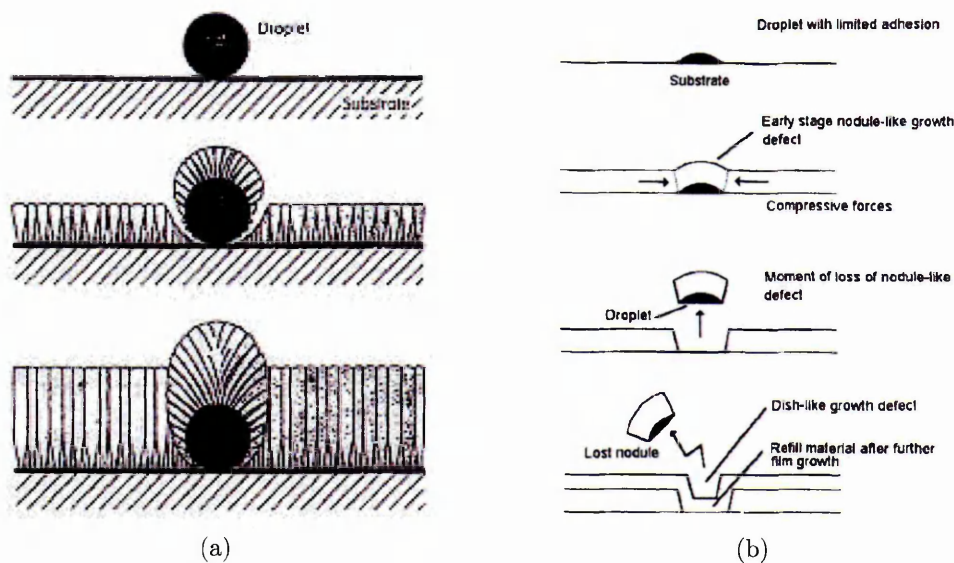


Fig. 2.9: Failure mechanism occurring during coating growth: (a) deposition of macro-particles leading to large scale growth-defects [57], (b) self-expulsion mechanism of loosely bonded growth defects with subsequent material refill [58]

particles and growth-defects on thin film performance are local loss of coating adhesion, surface roughening as well as porosity due to self-expulsion mechanism (see Fig. 2.9(b)) [58]. Macro-particle containing coatings therefore reveal decreased wear performance as both macro-particles and growth-defects detach from the coating and act as third body abrasive particle [61]. Furthermore, the corrosion protection is significantly reduced as under-dense areas surrounding the droplets and growth-defects allow easy access of corrosive media to the substrate [62]. The oxidation performance is also compromised by the same mechanism, allowing fast oxygen diffusion into the coating and towards the substrate [31].

### 2.2.5 Comparison of the PVD Techniques

This section shortly summarises the plasma conditions, the rate of deposition as well as the macro-particle generation of the PVD techniques UBM, HIPIMS and CA (see Tab. 2.2).

UBM plasmas have low quantities of charged metal particles, but growth defect free coatings can be deposited at medium deposition rates with this technique.

Both HIPIMS and CA have high quantities of charged metal particles at high ionisation states. For the deposition of coatings, HIPIMS is limited due to its low deposition rate whereas the application of CA is problematic due to the generation of macro-particle incorporation into the growing coating.

Tab. 2.2: Comparison of the PVD techniques UBM, HIPIMS and CA regarding their plasma properties, deposition rate and macro-particle generation

	PVD Technique		
	UBM	HIPIMS	CA
Multiple ionisation	low	high	high
Degree of ionisation	low	high	high
Deposition rate	medium	low	high
Macro-particle generation	no	no	yes

## 2.3 Thin Film Growth

A coating grows when the plasma comes in contact with a comparatively cold surface, such as the substrate, and subsequently condenses there. Sec. 2.2 explicitly covers techniques for the plasma generation. Here, the coating growth will be shortly examined.

The coating growth can be divided into three general steps [63]: (i) the transport of the coating atoms to the substrate, (ii) the adsorption of these atoms onto the substrate, their diffusion and incorporation into the coating and (iii) their movement to their final position due to diffusion processes.

It is well established that the coating microstructure and properties are highly influenced by the plasma characteristics in the substrate region [64].

A first attempt to describe the relationship between the plasma parameters and the coating microstructure was given by a structure zone model (SZM) from Movchan and Demchishin [65]. This phase diagram represents the microstructure of evaporated thin films as a function of homologous temperature  $T/T_M$  ( $T$  - substrate temperature,  $T_M$  - melting point of the depositing thin film) and classifies three different growth morphologies, referred to as the zones 1-3. Zone 1 ( $T/T_M < 0.3$ ) structures show an open columnar arrangement caused by low ion bombardment and atomic shadowing during transport to the substrate. In zone 2 ( $0.3 < T/T_M < 0.5$ ), increasing temperature results in the growth of dense columnar structures with larger grain size formed under conditions of surface diffusion. The high temperature zone 3 ( $T/T_M > 0.5$ ) structure consists of near-spherical, so-called equiaxed grains.

Thornton [63] extended the SZM to magnetron sputtered metal films by taking into account the effect of Ar working gas pressure (see Fig. 2.10). The increase in pressure causes a rise in collisional scattering between the particles in the plasma and, hence, reduces the average particle energies. This reduction in particle bombardment at the substrate shifts the transition between the constituent zones to higher homologous temperatures. Additionally, a fourth zone T consisting of a dense array of fibrous grains in the region between zone 1 and zone 2 was identified.

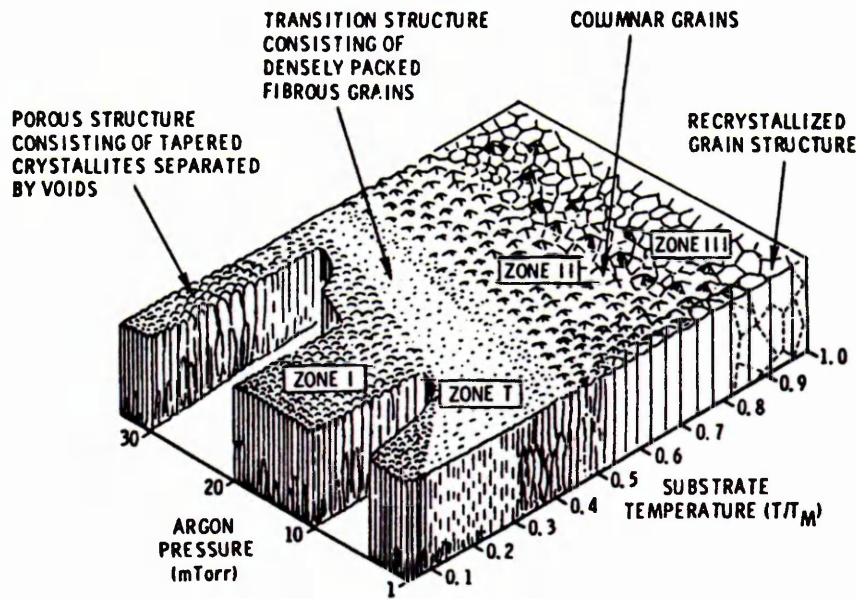


Fig. 2.10: Structure zone model by Thornton, showing the phase structure of magnetron sputtered metal coatings depending on the homologous temperature  $T/T_M$  and the Ar working pressure  $p$  [63]

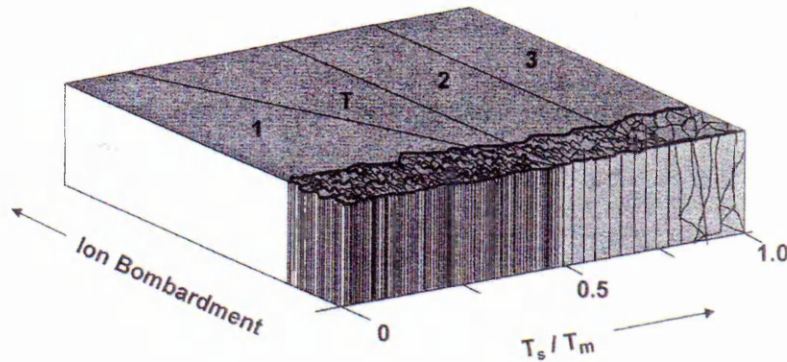


Fig. 2.11: Structure zone model by Messier et al. [66], showing the phase structure of sputtered coatings as function of homologous temperature  $T/T_M$  (here  $T_s/T_m$ ) and energy of the bombarding ions

During coating deposition, often a negative bias voltage  $U_b$  is applied to the substrates to attract the positively charged ions in the plasma to bombard the growing coating. Messier et al. [66] varied  $U_b$  to influence the energy of the impinging ions during growth and found that the zone 1/zone T structures in the

SZM vary with  $U_b$  whereas the phase boundaries of zone 2 and zone 3 are nearly independent of  $U_b$  (see Fig. 2.11). Increased  $U_b$  during deposition leads to an increased mobility of the condensed atoms (ad-atoms) and high energetic particle bombardment on the substrate and, hence, denser coatings. Although applying a bias voltage  $U_b$  favours the formation of dense structures, it evokes the generation of lattice defects of the growing film at the same time [67] leading to high intrinsic (compressive) stresses [68].

Kelly and Arnell [69] developed a SZM related to the closed field-UBM (CF-UBM) (see Fig. 2.6). This model describes the growth structures in terms of ion energy and ion flux which are identified as independent deposition parameters (see Fig. 2.12).

The ion energy is here represented by the homologous temperature  $T/T_M$  and the bias voltage  $U_b$ . While the previous models did not take into account the ion flux, this parameter is characterised by the ion-to-neutral ratio  $J_i/J_a$  in

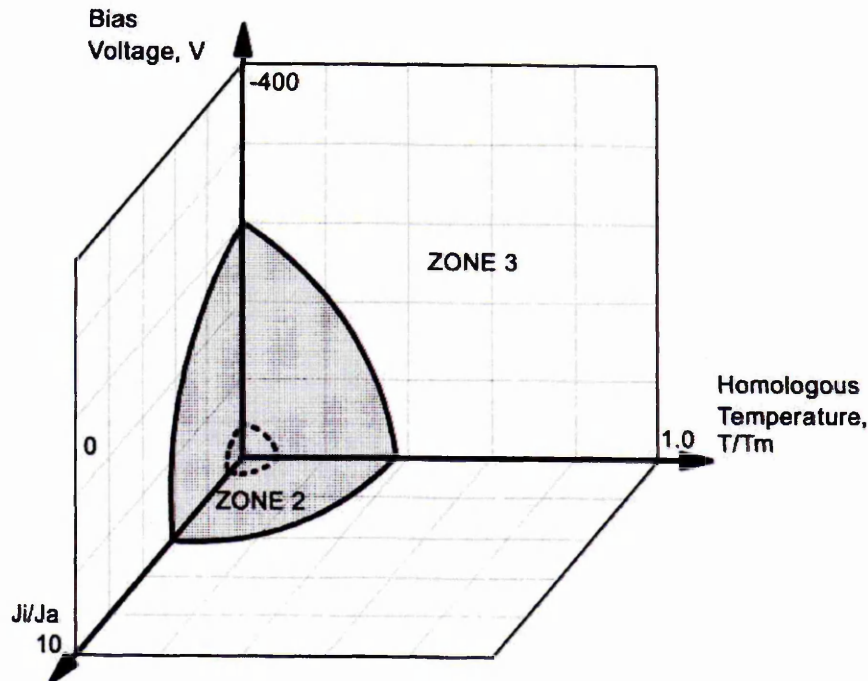


Fig. 2.12: Structure zone model for CF-UBM by Kelly and Arnell [69] representing the coating structure by means of homologous temperature  $T/T_M$ , the substrate bias voltage  $U_b$  (here V) and the ion-to-neutral ratio  $J_i/J_a$

this model. It can be shown that the coating deposition by CF-UBM promotes the formation of the high temperature structures of other magnetron techniques already at relatively low temperatures, while the formation of the low temperature zones 1 and T are suppressed. The model furthermore predicts a threshold in this  $J_i/J_a$  ratio, at a constant  $T/T_M$  and  $U_b$ , which has to be exceeded in order to obtain zone 2 or zone 3 structures.

## 2.4 Development of a Coating for Oxidation and Wear Protection

So far, the tools for growing protective coatings have been introduced. This following section suggests aspects which may be important to consider for the development of a well adherent coating with a dense microstructure and a chemical composition that limits wear and oxidation.

### 2.4.1 Techniques to Achieve Good Substrate/Coating Adhesion

A major point for good wear and oxidation protection by coatings is excellent substrate/ coating adhesion. Two different techniques can be used to produce such well adherent coatings: (i) a substrate surface etching pre-treatment and (ii) the deposition of an intermediate base layer. These processes will be introduced in the following.

#### 2.4.1.1 Effect of a Substrate Surface Plasma Ion Etching Pre-Treatment

The aim of an etching pre-treatment is to generate clean substrate surfaces to allow the formation of strong adhesive forces between the substrate and the coating [70]. The bombardment of the substrate with energetic ions from the plasma is well established as an effective pre-treatment technique as it removes contamination from the substrate surface and, hence, is beneficial for the adhesion [57]. Simultaneously, ion implantation into the top surface of the substrate can change the lattice spacing of the substrate and match more closely with the lattice of the subsequently grown coating. This, in turn, can decrease the residual stresses in the coating and furthermore enhances the adhesion. Conventionally used techniques for substrate pre-treatment are  $\text{Ar}^+$  etching [71] (in a magnetron glow discharge) and CA metal ion etching [72].

On substrates pre-treated by with  $\text{Ar}^+$  ions, contaminating oxides layers are often insufficiently removed [73]. Subsequently grown coatings reveal interface regions accumulating high quantities of Ar in the form of voids [72, 73]. These coatings, additionally, grow in the form of voids, low density structures [72, 74]. Such interface structures are brittle and highly stressed which can cause spallation of the coating from the substrate [75].

CA evaporation (see Sec. 2.2.4) was previously shown as a technique which generates plasmas with highly charged ions and high ionisation degrees. This technique is commonly used for the etching pre-treatment prior to PVD deposition. The energy of the impinging ions can be determined by the substrate bias voltage  $U_b$ . The bombardment with low energetic ions ( $U_b = 600$  V) can generate thin metal interlayers between the substrate and the coating or sharp and brittle interfaces which provide only limited adhesion [72, 74]. High energetic metal ions ( $U_b = 1200$  V), in contrast, bombard the substrate surface, are implanted into the material and intermix with substrate atoms down to depths of  $\sim 15$  nm [76]. This implantation causes a closer match between the lattice structure of the substrate and the coating and, additionally, effectively removes all contaminations from the substrate. Coatings deposited on such surfaces grow in local epitaxy to the substrate crystal, are less stressed and, hence, have a higher adhesion [57]. A drawback of the CA technique was previously identified with the generation of macro-particles from the target (see Sec. 2.2.4) as these particles induce the growth of defects in the coating. These defects are detrimental for the coating performance in applications such as corrosive [62] and oxidative environments [31] and it is therefore desirable to limit these growth defects in the coating. These macro-particles therefore limit the usability of CA as technique for the etching pre-treatment.

Recently, HIPIMS (see Sec. 2.2.3) was reported to be successfully implemented for substrate pre-treatment [77, 78]. The bombardment of the surface in a HIPIMS plasma promotes the removal of contaminants and additionally causes ion implantation with intermixing depths of up to 10 nm for Cr [77]. These implantation

depths are in a similar range as after a CA pre-treatment [72]. HIPIMS is furthermore a droplet-free technique. Subsequently grown coatings are therefore expected to be free of macro-particle induced growth defects. Hence, HIPIMS seems to be a promising candidate as a substrate surface pre-treatment technique prior to coating deposition. However, the knowledge of the effect this new pre-treatment technique on the mechanical performance of subsequently grown coatings is so far quite limited.

To conclude, a substrate pre-treatment with  $\text{Ar}^+$  is not desirable as the use of this technique promotes the growth of coatings with comparatively weak adhesion. The pre-treatment with CA, in contrast, is well established as an efficient method to improve the adhesion. The novel HIPIMS technique is expected to provide a similarly high coating/adhesion as the CA pre-treatment and to additionally eliminate the detrimental macro-particle induced growth defects.

#### **2.4.1.2 Effect of a Deposition of an Intermediate Base Layer**

PVD coatings often exhibit high compressive residual stresses  $\sigma$  in a range of several GPa. These stresses can limit the substrate/coating adhesion. It is possible to reduce these stresses by the introduction of an interlayer between the substrate and the actual coating. Ti interlayers between steel substrates and TiN coatings, for example, can reduce the residual stresses up to 50% [79]. These base layers provide a gradual stress gradient and reduce the stress concentration in the interface region. The effectiveness of these interlayers depends on a number of factors, such as the layer thickness [80,81] and the chemical and phase composition [82]. In combination with nanoscale multilayer coating, nitride based interlayers, such as CrN [82] and TiAlN [83] are successfully applied as base layer materials.

#### **2.4.2 Effect of a Nanoscale Multilayer Structure**

Previously, structure zone models (SZM) for the coating structures were described (see Sec. 2.3). However, these structures covered only single layer (monolithically grown) coatings. Coatings can alternatively be deposited in a very thin layers

forming nanoscale multilayers. These structures are characterised by the distance between each successive pair of layers, the bilayer thickness  $\Lambda$ . These multilayer films grow depending on the deposition parameters in structures [84] according to the previously described SZMs (see Sec. 2.3). These SZMs are therefore also valid for multilayer coatings.

The deposition of a nanoscale multilayer structure enables the combination of materials with different lattice structures within a shared lattice type as long as the bi-layer thickness  $\Lambda$  stays small enough. Fcc-CrN and hcp-AlN, for example, can be combined in a shared single-phase fcc lattice [85,86]. Similar findings were reported for TiN/NbN (normally fcc-TiN and hcp-NbN) and CrN/NbN (normally fcc-CrN and hcp-NbN) [83].

#### 2.4.2.1 Mechanical Performance

Coatings grown in a nanolayer structure reveal significantly higher hardness than the individual components, usually with a hardness well above those estimated by the rule-of-mixtures [14]. CrN/AlN thin films with a bilayer period of 3.8 nm, for example, reach a maximum hardness of 40 GPa which is increased by 86 % in comparison with that of the individual components CrN and AlN [86]. The hardness is provided by (i) hindering of dislocation movements by the multiple interfaces and (ii) coherency strains arising from different lattice parameters of the individual layers. These strains arise due to local variations in the lattice parameter of the individual layers. Hardening due to coherency strains, however, is limited to small values of  $\Lambda$  because strains relax when  $\Lambda$  is large (see Fig. 2.13). Nanolayers created from materials with immiscible lattice types tend to further increase the hardness as the coherency strains in these materials are higher when one component is forced into a foreign lattice type [87].

The wear resistance of nanoscale multilayers can also be improved compared to monolithically grown coatings [15]. In sliding wear, the main force is applied in the form of shear stresses. When exposed to such forces, monolithically grown coatings suffer from severe plastic deformation which can induce mechanical failure

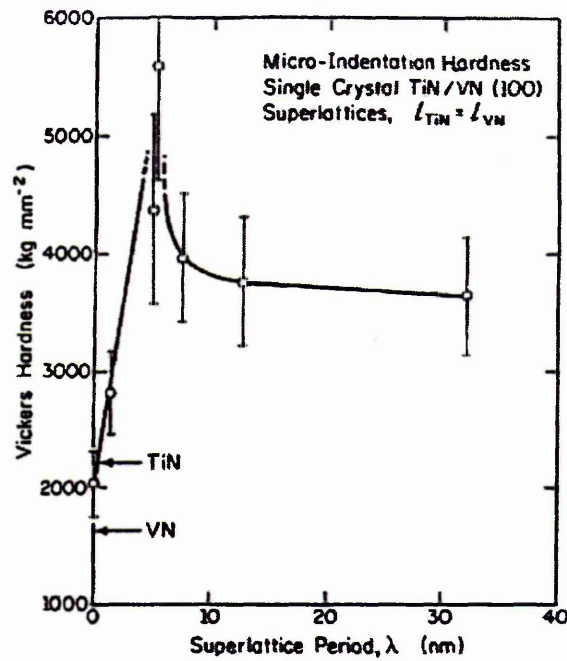


Fig. 2.13: Hardness of TiN/VN nanoscale multilayer coatings as function of bilayer thickness  $\Lambda$  (here  $\lambda$ ) [14]

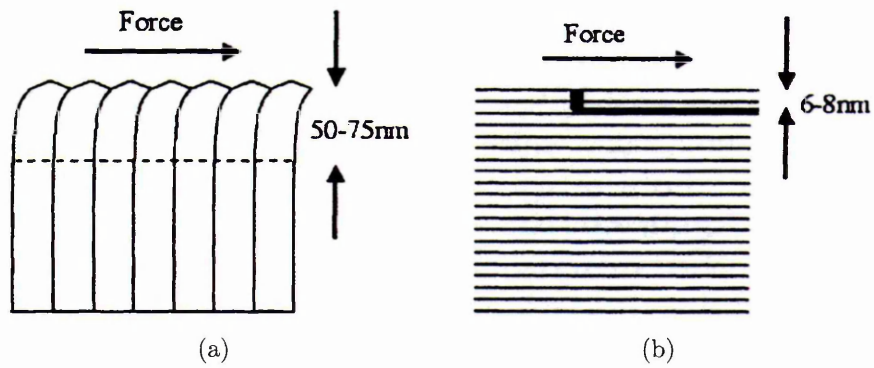


Fig. 2.14: Wear mechanism of (a) a monolithically grown coating with cracking of the column tops and (b) a nanoscale multilayer coating with nanolayer delamination [88]

with the removal of the column tops. A nanoscale multilayer, in contrast, wears by chipping or micro-delamination of individual layers [15, 89] (see Fig. 2.14). The layer structure also inhibits deep crack penetration perpendicular to the surface [15] and therefore improves the resistance to sliding wear.

### 2.4.2.2 Oxidation Performance

The deposition of a nanolayered coating can significantly improve the oxidation protection properties of this material.

TiN and CrN coatings, for example, begin to oxidise at 550°C and 650°C, respectively, whereas nanolayered TiN/CrN oxidises at higher temperatures of 700°C [23]. TiAlN similarly outperforms TiAlN and CrN [90]. CrN and AlN have an oxide layer thickness of ~400 nm and ~640 nm after 1 h exposure to air [91]. The oxide scale on a multilayered CrN/AlN with the bi-layer period  $\Lambda$  of 4 nm, in contrast, is only ~140 nm and therefore reveals superior oxidation performance.

As previously stated, oxidation processes are predominantly governed by diffusion processes (see Sec. 2.1.2). It is well established that different elements diffuse at different rates in various nitrides [92]. It is suggested that the changed diffusion processes in the materials composing the multilayer structure lead to a more complex oxidation mechanism and therefore enhance the oxidation resistance of such nanolayer coatings [23,90].

### 2.4.3 Effect of the Chemical Composition

TiN thin films were one of the first coatings in mass-production for tool coatings exhibiting low friction and wear coefficients as well as good oxidation resistance. The addition of high Al contents into the coating, formulating TiAlN, proved to be beneficial for mechanical properties as well as oxidation behaviour [93,94]. Further improvements were achieved by alloying Cr and Y [21,95–97], resulting in the development of TiAlCrYN coatings [16,20]. The high-temperature oxidation performance of Ti-containing thin films, however, is limited by the extreme low oxidation resistance of Ti leading to early failure due to the formation of porous TiO<sub>2</sub> which cannot protect the underlying material against further oxidation [98]. It is therefore desirable to remove Ti completely from the coating leading to the development of Cr-based thin films starting with CrN.

From this, it is obvious that the chemical composition of a coating is of crucial importance for the coating performance. This includes a variety of properties, such

as the microstructure, the mechanical and tribological properties as well as the oxidation resistance. In the following, the properties of various Cr-based coatings will be reviewed in more detail. Y containing coatings will also be covered.

### 2.4.3.1 CrN Coatings

#### Microstructure

Magnetron sputtered Cr nitride show a wide range of properties depending on the N content within the film [99]. The phase composition can here range from Cr, Cr+N to hcp-Cr<sub>2</sub>N. A further increase in the N atomic fraction generates a Cr<sub>2</sub>N+CrN phase mixture and stoichiometric CrN, respectively.

Near-stoichiometric CrN exhibit a NaCl-B1-phase structure with (111) preferred orientation when deposited at low energies of ion bombardment (bias voltage  $U_b < -50$  V) [100]. Above  $U_b = -50$  V, a (220) preferred orientation is commonly observed.

#### Thermal Stability

The theoretical Cr-N phase diagram based on thermodynamic considerations predicts CrN to be stable low temperature phase below 1050°C whereas the Cr<sub>2</sub>N phase is expected at higher temperatures [101].

In experiment, in contrast, the Cr<sub>2</sub>N phase is often already present at significantly lower temperatures. Magnetron sputtered CrN, for example, undergoes a phase transformation from CrN into Cr<sub>2</sub>N after annealing for 2 h in inert atmosphere at temperatures between 400°C to 750°C [102–104]. This phase transformation is attributed to a non-thermodynamic factor, most probably the relaxation high stresses in the coating.

From this, it becomes obvious that the thermal stability of CrN is not solely governed by the chemical composition but also by other factors.

## Oxidation Performance

The oxidation resistance in the Cr-N coating system increases from N-containing Cr via  $\text{Cr}_2\text{N}$  to CrN [105]. This improved oxidation resistance is caused by the higher atomic fractions of N in the coating. The oxidation of these coatings is based on a progressive exchange mechanism of N by O from the oxidising medium [106] and results in the formation of  $\text{Cr}_2\text{O}_3$  as oxidation product [27, 107–109]. Additionally,  $\text{N}_2$  is released during this process. Further growth of  $\text{Cr}_2\text{O}_3$  is governed by the outward Cr diffusion through the oxide scale [30].  $\text{N}_2$  has only a low diffusion rate in  $\text{Cr}_2\text{O}_3$  and the scale acts therefore as a diffusion barrier for the released  $\text{N}_2$ . This, in turn, can cause the accumulation of the gas in the form of voids in the coating [30].

In coating systems, also possible reactions of the substrate may be of importance for the oxidation behaviour. In Cr nitrides grown on steel substrates, substrate elements, especially Fe, are commonly found within coatings and oxide after heat-treatment. This indicates the simultaneous oxidation of substrate elements through defects in the thin film [106] as well as outward diffusion of substrate elements [110, 111].

### 2.4.3.2 CrAlN Coatings

Although Cr nitride coatings find a wide range of industrial applications, they are limited by their low oxidation temperatures at  $\sim 650^\circ\text{C}$  [23].

Experience shows that the wear performance [112, 113] and the oxidation properties [27, 113] of CrN can be improved by alloying a third element to form a ternary coating system. Al as the alloying element is one of the most promising candidates as it has the ability to form dense corundum  $\text{Al}_2\text{O}_3$  scales. Such scales, in turn, are known to effectively protect the underlying material from further oxidation (see Sec. 2.1).

## Microstructure

The incorporation of Al into CrN generates a ternary CrAlN coating with two different lattice structures depending on the Al atomic fraction. A NaCl-fcc-type (B1) structure, as observed in CrN [100] is reported for low Al contents [114]. Experimentally, a phase transformation from a fcc-type (B1) to wurzite-hcp-type (B4) structure was reported for Al atomic fractions of  $\sim 65$ -75 at% [114–116] which agrees with the theoretical maximum solubility of fcc-AlN in fcc-CrN predicted at 77 at% [117].

It is well established that Cr nitrides often form sub-stoichiometric coatings with an excess in the metal component [118]. The incorporation of Al into the lattice is reported to be beneficial for the improvement of stoichiometric coating compositions [119].

The texture of magnetron sputtered B1-fcc lattice type CrAlN changes from a (110) preferred orientation to (111) texture with increasing Al concentration [119]. A (111) preferred orientation was also reported for cathodic arc ion plated CrAlN thin films [120].

## Mechanical Performance

Coatings with higher hardness and higher Young's modulus can be produced when Al is incorporated into the coating. The hardness of CrN, for example, is increased from 18 GPa to 30 GPa for an Al/Cr ratio of 0.4 [119]. The Young's modulus similarly increases from 200 GPa to 270 GPa. The hardness and the residual stresses of arc evaporated CrAlN rise, as a further example, monotonically as function of Al atomic fraction up to an Al concentration of  $\sim 45$ -60 at% [114, 121]. This effect is due to the dissolution of Al atoms in the fcc-CrN lattice which induce lattice distortion and strains. These strains, in turn, hinder dislocation movements and, hence, increase the hardness. After the phase transition to hcp-CrAlN, the residual stress and hardness drop as only small quantities of Cr can be dissolved in the hcp-AlN lattice [114].

CrAlN exhibits low friction values which declines from 0.6 in CrN to 0.4 in CrAlN with similar hardness [119, 122]. This reduced friction is caused by re-

duced adhesive wear between coating and counterpart as Al is incorporated into the coating [122]. The dry sliding wear coefficient  $k_S$  of CrAlN is in the order of  $10^{-17} \text{ mm}^3\text{N}^{-1}\text{m}^{-1}$  and is with this more than six times better than that of CrN [119].

It can therefore be shown that the hardness and the tribological properties of CrN can be improved with the introduction of Al to form CrAlN.

### Thermal Stability

The thermal stability of arc-evaporated CrAlN can be characterised as a function of Al content [114]. Here, three different reactions take place:

- transformation of fcc-CrAlN to hcp-CrAlN
- segregation of  $\text{Cr}_2\text{N}$
- segregation of pure Cr

The phase stability diagram (see Fig. 2.15), obtained from CrAlN after annealing for 1 h in inert atmosphere shows that CrAlN coatings with an Al atomic

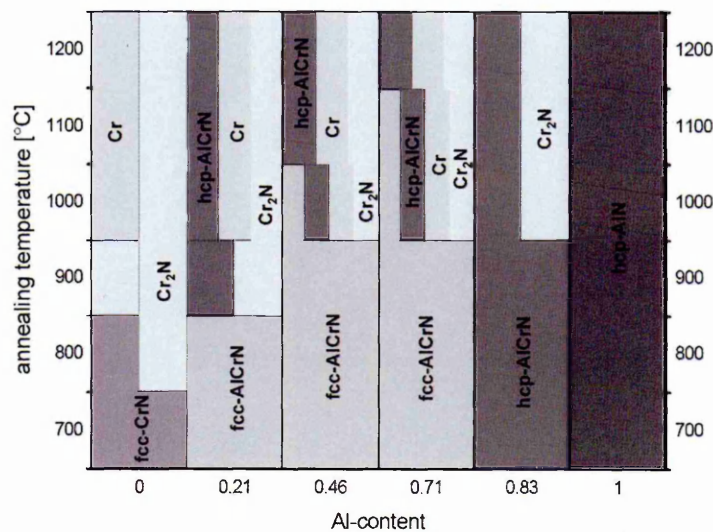


Fig. 2.15: Phase diagram of the thermal stability of CrAlN, obtained after 1 h heat-treatment in inert atmosphere [114]

fraction of  $\sim 70\text{at}\%$  Al content decomposes into hcp-AlCrN, Cr and  $\text{Cr}_2\text{N}$  with residual fcc-CrAlN at temperatures above  $950^\circ\text{C}$ .

### Corrosion and Oxidation Performance

As previously mentioned, CrN becomes more oxidation resistant with the incorporation of Al. Arc-evaporated CrN, for example, starts oxidizing at  $\sim 800^\circ\text{C}$  whereas accelerated oxidation of CrAlN with  $64\text{at}\%$  Al content occurs at  $950^\circ\text{C}$  [114]. This implies that the oxidation resistance of the fcc-CrAlN is shifted to higher temperatures as the coating becomes higher Al-containing. A further increase in the Al atomic fraction to  $79\text{at}\%$ , however, decreases this onset temperature of rapid oxidation to  $900^\circ\text{C}$  [114]. This is due to a change in the lattice structure from B1-fcc to B4-hcp which is suggested to be less oxidation resistant.

The reported oxide structures in literature differ strongly from one another and comprise amorphous [123], aluminium-rich oxides [123], Al-incorporated  $\text{Cr}_2\text{O}_3$  (Eskolaite) for low Al containing thin films to Cr-incorporated  $\text{Al}_2\text{O}_3$  (Corundum) for high Al containing films [114]. CrN/AlN multilayer thin films exhibit a fully oxidized surface layer with  $\text{Cr}_2\text{O}_3$  and either O-deficient  $\text{Al}_2\text{O}_3$  or a complex Al-Cr-O [124]. Duplex oxide layers form on top of  $\text{Cr}_{0.5}\text{Al}_{0.25}\text{N}_{0.25}$  with (i) an outermost Cr-enriched oxide layer, (ii) a mixed  $\text{Cr}_2\text{O}_3$  and  $\text{Al}_2\text{O}_3$  and (iii) an underlying oxynitride layer with wide O diffusion zone into the coating [125]. CrAlNO films, in contrast, which already contain  $25\text{at}\%$  form corundum-type  $\text{Cr}_2\text{O}_3$  and  $\text{Al}_2\text{O}_3$  [126].

The presented data shows that the formed oxides can take a variety of different structures. It is therefore difficult to predict the structure of the occurring oxide scales in a particular set-up.

### 2.4.3.3 Y Containing Coatings

The introduction of active elements, such as Y, into the coating is supposed to have a pronounced effect on the microstructure, the mechanical properties and oxidation performance of coatings.

#### Coating Structure and Mechanical Properties

Magnetron sputtered TiAlCrN is deposited with a polycrystalline columnar structure [127]. This coating has a (111) texture and exhibits medium residual stresses of -3.8 GPa. When incorporating 2at% Y to form TiAlCrYN, the coating morphology reveals strongly reduced grain sizes, a (100) texture and higher residual stresses of -6.5 GPa due to pronounced re-nucleation [127].

The polycrystalline columnar morphology of CrAlN [114] changes into an amorphous structure when 5at% Y are incorporated into the coating [128].

These examples clearly show that the coating microstructure can be influenced by Y additions.

#### Corrosion and Oxidation Performance

Y as alloying element in nitride coatings can also be used to influence the corrosion and oxidation behaviour. TiN coatings for corrosion protection applications exhibited enhanced protective properties when containing Y [129] as the diffusion of corrosive media towards the substrate is suppressed by microstructural changes. The oxidation resistance of TiAlCrN with temperature limit of 900°C can be increased up to 950°C with the addition of Y [130, 131]. In this TiAlCrYN, Y segregates at the column boundaries and suppresses the inward O diffusion and the outward diffusion of substrate atoms [130, 131]. The internal oxidation of this material is therefore decreased. Similar findings were made in CoCrAl coatings [132]. The outward diffusion of Al is here identified as main oxidation mechanism which creates a constant supply of oxidising material at the surface. In CoCrYAl, in contrast, this outward Al diffusion is strongly reduced. The addition of Y also suppresses the formation of interfacial cavities between the CoCrYAl coating and the oxide scale [133]. A comparison of ZrN and ZrYN

coatings shows that ZrYN reveals a lower weight gain and lower oxidation rates when oxidised in air [134]. This is due to the stabilisation of the low temperature tetragonal  $ZrO_2$  phase by the Y additions and the prevention of the growth of a high temperature monoclinic  $ZrO_2$ . This tetragonal  $ZrO_2$  phase induces lower growth stresses and, hence, limits the cracking of the oxide scale which, in turn, protects the underlying material more effectively from oxidation. Furthermore, the growth behaviour of  $Cr_2O_3$  scales was found to be decisively improved by the introduction of Y [135] as Y-containing  $Cr_2O_3$  show a reduced growth rate and an impeded grain growth. Additionally, the scale is better adherent to the underlying material. Y forms precipitates of  $Y_2O_3$  or  $YCr_2O_3$  in the scales or at the oxide grain boundaries and, hence, changes the transport mechanism through the scale from predominant outward Cr diffusion to inward O diffusion in the presence of Y. The oxide growth then takes place at the metal-oxide interface and the formation of voids and porosity due to outward Cr diffusion is suppressed.

From these data, it is clearly shown that the corrosion and oxidation performance of coatings can be significantly improved by the addition of Y as alloying element. Y additions clearly alter corrosion and oxidation performance of thin films.

## 2.5 Why Design CrAlYN/CrN Nanoscale Multilayer Coatings??

This literature review so far provides information which may be beneficial for the successful development of a hard coating combining excellent wear resistance and good oxidation resistance.

Cr-based nitride coatings are shown to be suitable materials for wear and oxidation protection (see Sec. 2.4.3.1). Alloying of CrN with Al (see Sec. 2.4.3.2) is well established as technique to improve the oxidation performance. A similar improvement is expected from the introduction of small amounts of Y (see Sec. 2.4.3.3). From a chemical point of view, it is therefore suggested that the combination of Cr, Al and Y in a nitride coating may be suitable to provide good oxidation protection.

The coating deposition in a nanoscale multilayer structure is beneficial for the mechanical performance and the wear resistance (see Sec. 2.4.2.1) and can also improve the oxidation performance (see Sec. 2.4.2.1). It is therefore proposed to deposit a nanoscale multilayered coating. A possible configuration for such a coating with the elements Cr, Al, Y and N is CrAlYN/CrN.

To engineer a coating with excellent properties, it is important to produce a coating which is well adherent to the substrate and furthermore free of growth defects. A substrate etching pre-treatment is therefore performed with the novel, macro-particle free HIPIMS technique (see Sec. 2.4.1.1). Additionally, a CrN base layer is deposited prior to the CrAlYN/CrN nanolayer deposition (see Sec. 2.4.1.2).

It is also advisable to produce dense coatings. Both HIPIMS (see Sec. 2.2.3) and UBM (see Sec. 2.2.2) as macro-particle free techniques can provide such dense growth as they are growth-defect free. The use of UBM during the deposition step additionally allows to grow the coatings at a reasonable time scale. The coating production is therefore carried out by a combined HIPIMS/UBM process.

These considerations lead then to the development of the novel CrAlYN/CrN nanoscale multilayer coatings produced by the HIPIMS/UBM technique.

# CHAPTER 3

---

---

## Experimental Methods

---

---

This chapter gives an insight into the experimental techniques and the set-up accomplished during these studies. In many cases, not only the measuring device is explained but also a short introduction to the working principle and theory is provided. Additionally, the potentials and limitations of the specific techniques are pointed out and solutions for the interpretation of results are given.

### 3.1 Fabrication of CrAlYN/CrN Coatings

#### 3.1.1 Deposition Equipment

The preparation of the CrAlYN/CrN films was conducted in a A HTC 1000-4 PVD coating system (Hauzer) [136]. This industrial sized vacuum coater has four rectangular plasma sources (target dimensions 600x190 mm) (see Fig. 3.1). The cathodes are operable in either steered cathodic arc (CA) or in unbalanced magnetron (UBM) sputtering mode by rearrangement of permanent magnets behind the target. The magnetic field necessary for magnetron operation is derived from SmCo-magnets behind the target. Additionally, the cathodes are concentrically surrounded by electromagnetic coils to permit unbalancing the field. The system is operated in closed field configuration (CF-UBM) to ensure a high degree

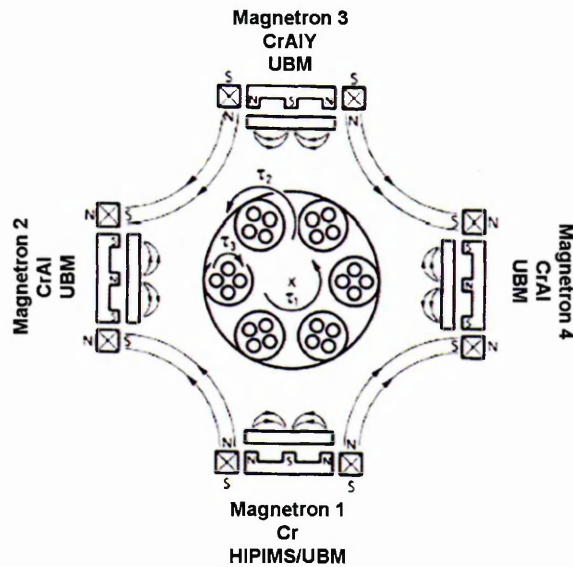


Fig. 3.1: Schematic cross-section of the HAUZER HTC 1000-4 coating machine with target materials and target configuration used in this study

of ionisation during UBM deposition. The vacuum system is equipped with two Balzers THP 2200 turbomolecular pumps, a Root pump and a rotary vane pump. The pressure measurement takes place with a Leybold VISCOVAC system. The quality of the pumping system permits a pressure independent pumping speed. The equipment is furnished with a threefold planetary rotating substrate holder (average target-to-substrate distance  $\sim 25$  cm) to allow uniform coating deposition.

In this study, the arc power supply of one of the source (target 1) is replaced with an external high power impulse magnetron sputtering (HIPIMS) power supply HMP6/11 (Huettinger, former AC Spzo.o.) which allows sequential operation in HIPIMS and UBM mode. The power supply is capable of delivering peak currents  $I_{d,peak} = 3000$  A and discharge voltages  $U_{d,peak} = 2000$  V. Pulses with duration in the range 0-200  $\mu$ s at a frequency of 0-100 Hz, equivalent to a duty cycle of 2%, can be provided.

The connection of a row of capacitors to the bias power supply during HIPIMS mode is necessary to prevent a drop-down in the substrate bias current  $I_b$  during

the on-time of the pulse. The operation without connected capacitors is referred to as unstabilised, whereas the connected state is addressed as stabilised.

The substrates are exposed to three-fold rotation (rotation speed 3.6 rpm) during thin film deposition. To produce CrAlYN/CrN, two pairs of opposing CrAl targets (Cr: 40at%, Al: 60at%), one Cr target and one CrAlY target (Cr: 48at%, Al: 48at%, Y: 4at%), all with 99.9% purity, are used (see Fig. 3.1).

The production of CrAlYN/CrN nanoscale multilayer films was conducted in three separate steps. After the substrate preparation, a Cr metal ion etching pre-treatment was carried out followed by the deposition of a complex coating architecture with CrAlN base layer and a CrAlYN/CrN nanoscale multilayer.

### 3.1.2 Substrate Preparation

Three different substrate materials were used in this study: AISI type 304 austenitic stainless steel (SS), AISI type M2 high speed steel (HSS) and PN90-grade cemented carbide ball nosed endmills (see Tab. 3.1).

All samples were polished with 1  $\mu\text{m}$  diamond paste in the final stage, resulting in a surface roughness  $R_a \leq 0.01 \mu\text{m}$ . The substrates were first cleaned in an automatic industrial cleaning line containing a range of heated ultrasonic baths including aqueous based alkali detergents and de-ionized water for cleaning. The samples were then dried in vacuum by radiation heating shortly before being loaded into the vacuum chamber to minimise the effect of water vapour condensation on the substrate surface.

Tab. 3.1: Chemical composition of substrate materials

Substrate	Elements						
304 SS	Fe	C	Cr	Ni	Mn	Si	P
	66.3-74	<0.08	18-20	8-10.5	<2	<1	<0.045
M2 HSS	Fe	C	W	Mo	Cr	V	Al
		0.85	6.3	5.1	4.2	2	1.6
PN90 CC	Co matrix with 9% WC particles						

SS substrates were used for structural analysis by transmission electron microscopy (see Sec. 3.2.4), phase analysis, texture determination and stress analysis (see Sec. 3.2.2) as well as for oxidation testing (see Sec. 3.4). HSS substrates were taken for mechanical and tribological measurements (see Sec. 3.3). Stainless steel and high speed steel samples have a cylindrical shape with a height of 6 mm and a diameter of 30 mm. The TEM samples have a rectangular geometry with 15x15x0.8 mm. Cemented carbide 8 mm ball-nosed endmills were tested in dry high speed milling applications (see Sec. 3.3.6).

### 3.1.3 Substrate Etching Pre-Treatment

Prior to the plasma processes, the vacuum chamber was evacuated to a base pressure  $p > 7.7 \times 10^{-3}$  Pa by molecular pumping and heated to 400°C by irradiation heating. Target cleaning was performed with closed shutters to avoid contamination of the substrates.

The metal ion etching pre-treatment was performed in a  $\text{Cr}^+/\text{Ar}^+$  plasma from the Cr target (see Fig. 3.1, magnetron 1).

For most specimen, the etching step was carried out in HIPIMS mode for 40 min. Preliminary tests showed that this etching time was optimal to provide good adhesion. The discharge was maintained in Ar atmosphere at pressures of 0.11 Pa with a peak discharge current  $I_{d,peak} = 1600 \text{ A.cm}^{-2}$  and an average discharge voltage  $U_d = 1000 \text{ V}$  (see Fig. 3.2). The bombarding flux under these conditions consists of equal amounts of  $\text{Cr}^+$  and  $\text{Ar}^+$  ions with a peak plasma density of  $n_{pl} = 1013 \text{ ions.cm}^{-2}$  [137]. The substrate bias voltage  $U_b$  was fixed at -500 V. Other parameters are given in Tab. 3.2.

One specimen was prepared with CA metal ion etching as benchmark coating to investigate the effect of substrate pre-treatment technique on the film performance. The CA metal ion etching pre-treatment was performed at a discharge current  $I_d = 100 \text{ A}$  for 20 min in Ar atmosphere ( $p = 0.08 \text{ Pa}$ ). The substrate bias voltage  $U_b$  was adjusted to -1200 V. These parameters are shown to provide sputter cleaning and ion implantation at the substrate and therefore generate highly

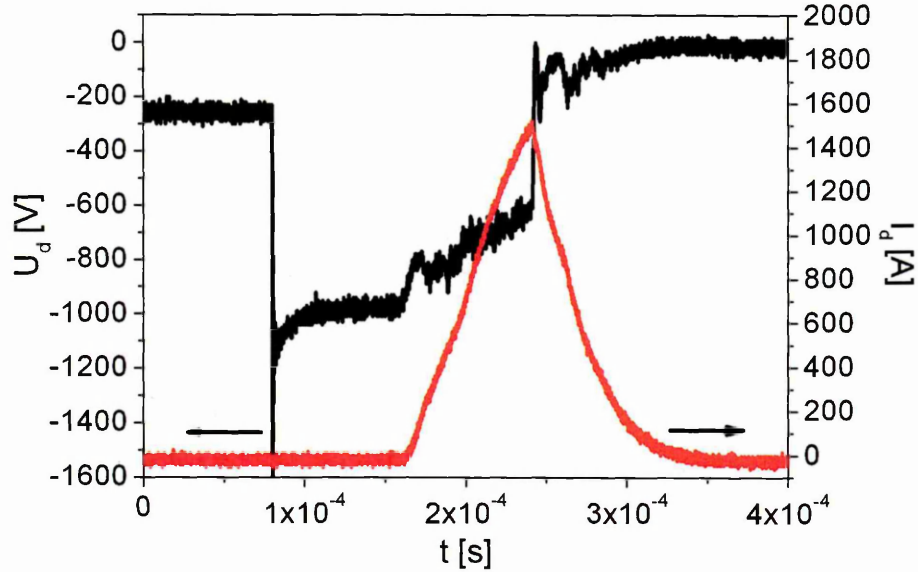


Fig. 3.2: Discharge current  $I_d$  and voltage  $U_d$  during the on-time of the pulse in HIPIMS mode as a function of time  $t$

adherent coatings [74].

During the ion etching, the substrate temperature climbed from 400°C to 450°C due to heating effects of the highly energetic plasma. This behaviour was observed in both HIPIMS and CA mode and is therefore independent of the pre-treatment technique.

### 3.1.4 Coating Deposition

Deposition of the CrAlN base layer as well as the CrAlYN/CrN nanoscale multilayer was performed in direct current (d.c.) UBM sputtering mode in a reactive mixed Ar/N<sub>2</sub> atmosphere (Ar/N<sub>2</sub> ratio 1:1,  $p = 0.36$  Pa) at a temperature of 450°C. CrAlN was condensed for 30 min from the CrAl targets (see Fig. 3.1, magnetron 2 and 4). The power  $P_{CrAl}$  on the CrAl targets during the base layer deposition step was kept at 8 kW. The nanoscale multilayer structure was produced during a 2.5 h deposition step with the magnetrons in UBM operation at a cathode power  $P_{CrAl}$  and  $P_{CrAlY} = 8$  kW. The plasma conditions in this case are a plasma density

$n_{pl} = 109 \text{ ion.cm}^{-2}$  and 90% of  $\text{N}_2^+$  ions [137].

Two sets of coatings were produced. For one set,  $U_b$  was varied at constant power  $P_{Cr}$  on the Cr target, for the second set,  $P_{Cr}$  was varied at constant  $U_b$ . The process changed parameters were:

- the substrate bias voltage  $U_b$  in a range of -75 V to -150 V
- the power  $P_{Cr}$  on the Cr target in a range of 2 kW to 8 kW

Tab. 3.2 to Tab. 3.4 summarise the process parameters of all deposition runs. The parameter set of specimen 1 is listed twice to directly identify the set of samples being mutually compared.

After the second set of experiments (variation of substrate bias voltage  $U_b$ ), the capacitor array at the bias power supply remained connected during the deposition step to stabilise the bias voltage  $U_b$  applied to the substrate.

Tab. 3.2: Process parameters for deposition of CrAlYN/CrN with substrate pre-treatment by CA and HIPIMS

Sample 1	Sample 2
Cr Substrate Pre-Treatment	
<b>HIPIMS</b>	<b>CA</b>
$U_d = 1000$ V	$I_d = 100$ A
$I_d = 2000$ A	
$t_{duty} = 0.6\%$	
$p = 0.11$ Pa	$p = 0.08$ Pa
$t = 40$ min	$t = 20$ min
$U_b = -500$ V	$U_b = -1200$ V
stabilised	stabilised
CrAlN Baselayer	
Reactive UBM	Reactive UBM
$P_{CrAl} = 8$ kW	$P_{CrAl} = 8$ kW
$p = 0.36$ Pa	$p = 0.36$ Pa
$N_2/Ar = 1:1$	$N_2/Ar = 1:1$
$t = 30$ min	$t = 30$ min
$U_b = -75$ V	$U_b = -95$ V
unstabilised	unstabilised
CrAlYN/CrN Nanoscale Multilayer	
Reactive UBM	Reactive UBM
$P_{CrAl} = 8$ kW	$P_{CrAl} = 8$ kW
$P_{CrAlY} = 8$ kW	$P_{CrAlY} = 8$ kW
$P_{Cr} = 8$ kW	$P_{Cr} = 8$ kW
$p = 0.36$ Pa	$p = 0.36$ Pa
$N_2/Ar = 1:1$	$N_2/Ar = 1:1$
$t = 180$ min	$t = 180$ min
$U_b = -75$ V	$U_b = -75$ V
unstabilised	unstabilised

Tab. 3.3: Process parameters for deposition of CrAlYN/CrN with variation in substrate bias voltage  $U_b$  (Sample 1 is reported from Tab. 3.2 for direct comparison)

Sample 1	Sample 3	Sample 4	Sample 5
Cr HIPIMS Substrate Pre-Treatment			
HIPIMS $U_d= 1000$ V $I_d= 2000$ A $t_{duty}=0.6\%$ $p=0.11$ Pa $t=40$ min $U_b= 500$ V stabilised	HIPIMS $U_d= 1000$ V $I_d= 2000$ A $t_{duty}=0.6\%$ $p= 0.11$ Pa $t= 40$ min $U_b= 500$ V stabilised	HIPIMS $U_d= 1000$ V $I_d= 2000$ A $t_{duty}=0.6\%$ $p= 0.11$ Pa $t= 40$ min $U_b= 500$ V stabilised	HIPIMS $U_d= 1000$ V $I_d= 2000$ A $t_{duty}=0.6\%$ $p= 0.11$ Pa $t= 40$ min $U_b= 500$ V stabilised
CrAlN Baselayer			
Reactive UBM $P_{CrAl}= 8$ kW $p= 0.36$ Pa $N_2/Ar= 1:1$ $t= 30$ min $U_b= -75$ V unstabilised	Reactive UBM $P_{CrAl}= 8$ kW $p= 0.36$ Pa $N_2/Ar= 1:1$ $t= 30$ min $U_b= -95$ V unstabilised	Reactive UBM $P_{CrAl}= 8$ kW $p= 0.36$ Pa $N_2/Ar= 1:1$ $t= 30$ min $U_b= -120$ V unstabilised	Reactive UBM $P_{CrAl}= 8$ kW $p= 0.36$ Pa $N_2/Ar= 1:1$ $t= 30$ min $U_b= -150$ V unstabilised
CrAlYN/CrN Nanoscale Multilayer			
Reactive UBM $P_{CrAl}= 8$ kW $P_{CrAlY}= 8$ kW $P_{Cr}= 8$ kW $p= 0.36$ Pa $N_2/Ar= 1:1$ $t= 180$ min $U_b= -75$ V unstabilised	Reactive UBM $P_{CrAl}= 8$ kW $P_{CrAlY}= 8$ kW $P_{Cr}= 8$ kW $p= 0.36$ Pa $N_2/Ar= 1:1$ $t= 180$ min $U_b= -95$ V unstabilised	Reactive UBM $P_{CrAl}= 8$ kW $P_{CrAlY}= 8$ kW $P_{Cr}= 8$ kW $p= 0.36$ Pa $N_2/Ar= 1:1$ $t= 180$ min $U_b= -120$ V unstabilised	Reactive UBM $P_{CrAl}= 8$ kW $P_{CrAlY}= 8$ kW $P_{Cr}= 8$ kW $p= 0.36$ Pa $N_2/Ar= 1:1$ $t= 180$ min $U_b= -150$ V unstabilised

Tab. 3.4: Process parameters for deposition of CrAlYN/CrN with variation in Cr target power  $P_{Cr}$

Sample 6	Sample 7	Sample 8	Sample 9
Cr HIPIMS Substrate Pre-Treatment			
HIPIMS $U_d= 1000$ V $I_d= 2000$ A $t_{duty}=0.6\%$ $p= 0.11$ Pa $t= 40$ min $U_b= 500$ V stabilised	HIPIMS $U_d= 1000$ V $I_d= 2000$ A $t_{duty}=0.6\%$ $p= 0.11$ Pa $t= 40$ min $U_b= 500$ V stabilised	HIPIMS $U_d= 1000$ V $I_d= 2000$ A $t_{duty}=0.6\%$ $p= 0.11$ Pa $t= 40$ min $U_b= 500$ V stabilised	HIPIMS $U_d= 1000$ V $I_d= 2000$ A $t_{duty}=0.6\%$ $p= 0.11$ Pa $t= 40$ min $U_b= 500$ V stabilised
CrAlN Baselayer			
Reactive UBM $P_{CrAl}= 8$ kW $p= 0.36$ Pa $N_2/Ar= 1:1$ $t= 30$ min $U_b= -75$ V stabilised	Reactive UBM $P_{CrAl}= 8$ kW $p= 0.36$ Pa $N_2/Ar= 1:1$ $t= 30$ min $U_b= -75$ V stabilised	Reactive UBM $P_{CrAl}= 8$ kW $p= 0.36$ Pa $N_2/Ar= 1:1$ $t= 30$ min $U_b= -75$ V stabilised	Reactive UBM $P_{CrAl}= 8$ kW $p= 0.36$ Pa $N_2/Ar= 1:1$ $t= 30$ min $U_b= -75$ V stabilised
CrAlYN/CrN Nanoscale Multilayer			
Reactive UBM $P_{CrAl}= 8$ kW $P_{CrAlY}= 8$ kW <b><math>P_{Cr}= 8</math> kW</b> $p= 0.36$ Pa $N_2/Ar= 1:1$ $t= 180$ min $U_b= -75$ V stabilised	Reactive UBM $P_{CrAl}= 8$ kW $P_{CrAlY}= 8$ kW <b><math>P_{Cr}= 6</math> kW</b> $p= 0.36$ Pa $N_2/Ar= 1:1$ $t= 180$ min $U_b= -75$ V stabilised	Reactive UBM $P_{CrAl}= 8$ kW $P_{CrAlY}= 8$ kW <b><math>P_{Cr}= 4</math> kW</b> $p= 0.36$ Pa $N_2/Ar= 1:1$ $t= 180$ min $U_b= -75$ V stabilised	Reactive UBM $P_{CrAl}= 8$ kW $P_{CrAlY}= 8$ kW <b><math>P_{Cr}= 2</math> kW</b> $p= 0.36$ Pa $N_2/Ar= 1:1$ $t= 180$ min $U_b= -75$ V stabilised

## 3.2 Microstructure and Phase Analysis

In the following, the characterisation techniques for the determination of the chemical composition, the microstructure and the phase structure of coatings, used during this study, are briefly reviewed.

### 3.2.1 Secondary Neutral Mass Spectrometry

Secondary neutral mass spectrometry (SNMS) is an extremely sensitive surface analysis technique used for quantification of the coating composition. In electron beam SNMS [138, 139], the coating is bombarded with  $\text{Ar}^+$  ions and a flux of neutral atoms is ejected from the coating surface. The sputtered material represents the stoichiometry of the coating due to the very high flux of neutrals (99.9% of the total flux). These neutral particles are then collected by a detector and subsequently ionized by electron impact. The analysis of the generated ion flux takes place in a mass spectrometer.

The SNMS measurements for the analysis of the CrAlYN/CrN were performed in a VG SIMSLAB instrument at Corus Swinden Technology Centre. The instrument was equipped with a VG Ionex DP5 duoplasmatron ion source for  $\text{Ar}^+$  ion beam generation and a  $90^\circ$  quadrupole mass spectrometer with HTP 2002 ioniser. Quantification of the chemical composition was carried out using certified reference materials as standard. The sputter depth was set to  $\sim 45 \text{ nm}\cdot\text{min}^{-1}$  to permit data collection over the total coating cross-section. This set-up with a relatively high sputter rate, however, limits the depth resolution and prevents the detection of the nanolayer structure.

### 3.2.2 X-Ray Diffraction Techniques

X-ray diffraction (XRD) provides a versatile technique to access various material characteristics as demonstrated in the following.

### 3.2.2.1 Functioning Principle of X-Ray Diffraction

The functioning principle of XRD is based on diffraction and interference phenomena when X-radiation penetrates a crystalline material [140]. Scattering at the lattice planes (hkl) causes constructive interference when the wavelength  $\lambda$  of the incident beam correlates with the  $d$ -spacing according to Bragg's law:

$$n\lambda = 2d\sin(\theta) \quad (3.1)$$

Here,  $n$  represents the order of diffraction,  $\lambda$  is the wavelength of the incident beam and  $\theta$  the Bragg angle (angle between the incident beam and the surface normal).

XRD experiments can be carried out in (i)  $\theta/2\theta$  Bragg-Brentano geometry or in (ii) parallel beam glancing angle (GA) geometry.

In the  $\theta/2\theta$  measurements, reflections takes place only at the (hkl) planes parallel to the surface (see Fig. 3.3). The X-rays penetrate deep into the material and reflections from the substrate are therefore detected in the diffractogram.

In GA-XRD, a low incident angle  $\gamma$  is held constant while only the detector moves on the  $2\theta$  angle (see Fig.3.4). Diffraction can only be obtained from planes

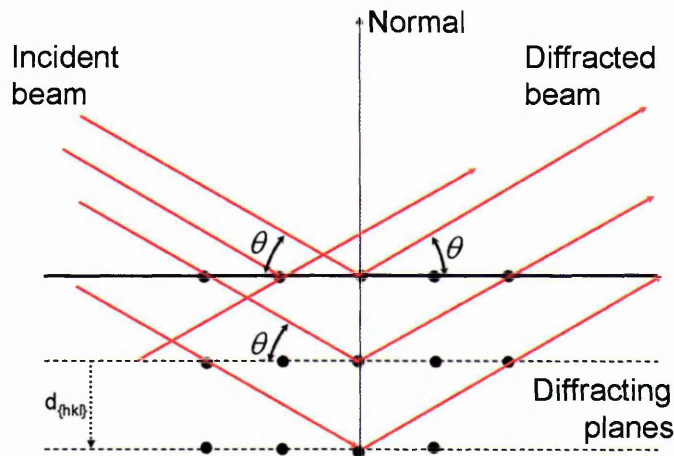


Fig. 3.3: Diffraction at planes parallel to the surface, measured in  $\theta/2\theta$  geometry

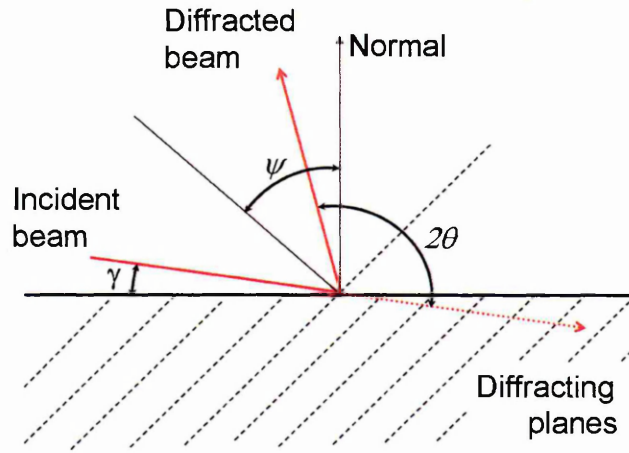


Fig. 3.4: Diffraction at lattice planes in a crystal inclined to the surface, measured in GA geometry

inclined by an angle  $\Psi = (\theta - \gamma)$  which is defined as the angle between the diffraction vector of (hkl) plane and the normal to the film surface. The penetration depth  $z_{1/e}$  of the incident X-rays into the material is calculated according to the following equation:

$$z_{1/e} = \frac{\sin(\gamma) \cdot \sin(2\theta - \gamma)}{\mu(\sin(\gamma) + \sin(2\theta - \gamma))} \quad (3.2)$$

Here,  $\mu$  represents the linear absorption coefficient which is estimated to be  $540 \text{ cm}^{-1}$  in CrAlYN/CrN. For an incident angle of  $\gamma = 2^\circ$ ,  $z_{1/e}$  corresponds to  $0.5 \mu\text{m}$ .

The equipment used for the all conducted XRD investigations was an automated Philips X'Pert MPD diffractometer with Cu-K $_{\alpha}$  ( $\lambda_{Cu} = 0.154056 \text{ nm}$ ) radiation driven at an acceleration voltage  $U_a$  of 40 kV. Measurements were taken with a step size in  $\theta$  of  $0.02^\circ$ .

### 3.2.2.2 Phase Analysis

The phase composition of CrAlYN/CrN in as-deposited state and after heat-treatment was determined in  $\theta/2\theta$  and GA-XRD geometry. The measurements

in GA-XRD geometry were performed to evaluate the formation of thin surface oxides in heat-treated specimens and avoid peak overlap between reflections of the coating and the substrate.

Peak positions and intensities were determined by a Gauss peak fitting routine. The phase identification was carried out by calculation of the  $d$ -spacing of the individual lattice planes (hkl) from  $2\theta$  peak positions and subsequent comparison with standard patterns retrieved from the JCPDS-database for crystallographic data [141]. The intensities listed in the database can only be compared with the intensities from the intensities obtained from measurements in the  $\theta/2\theta$  geometry. The intensities from scans taken in GA geometry were therefore not used as criteria for the phase identification.

$\theta/2\theta$  measurements permit the determination of the lattice parameter  $a_{o,\perp}$  [96,127]. In case of a nanolayered coating,  $a_{o,\perp}$  represents a virtual lattice parameter which is averaged from the individual layers. This measurement of  $a_{o,\perp}$  from lattice planes parallel to the coating normal gives an indication of the residual stress state in the coating [96]. Lattice parameters which are larger than those parameters of the unstressed reference material signify the compressive stresses in the lattice plane which cause an expansion of the lattice along the coating normal.

### 3.2.2.3 Texture Determination

The Harris texture factor  $T^*$  gives an indication whether the coatings grow with a preferred crystallographic orientation.  $T^*$  was calculated from a  $\theta/2\theta$  scan calculated according to the Harris inverse pole figure technique [142–144]. The proportion of grains with a certain orientation compared to a randomly oriented powder material of similar composition was calculated from the following equation:

$$T^* = \frac{\frac{I_{(hkl)}}{R_{(hkl)}}}{\frac{1}{n} \sum 1^n \frac{I_{(hkl)}}{R_{(hkl)}}} \quad (3.3)$$

In this equation,  $I_{(hkl)}$  represents the integral intensity of the individual reflections.  $R_{(hkl)}$  stands for the calculated intensities of the powder standard and  $n$  is

the number of considered reflections. A  $T^*$  of unity indicates random orientation, whilst  $T^*$  exceeding 1 a specific orientation of the corresponding (hkl) planes is given.

### 3.2.2.4 Nanoscale Bi-Layer Periodicity Determination

Low angle XRD (LA-XRD) in  $\theta/2\theta$  geometry ( $\theta = 1.7^\circ$  to  $10^\circ$ ) was conducted to determine the nanolayer modulation period  $\Lambda$  [145]. Here, the nanoscale bi-layer acts as a lattice plane at which the incident beam is diffracted. Thus,  $\Lambda$  is estimated from Bragg's law, according to the following equation (see Eq. 3.4):

$$\Lambda = \frac{n\lambda}{2\sin(\Theta)} \quad (3.4)$$

### 3.2.2.5 Stress Analysis

The coating stress was derived from GA-XRD measurements according to a modified  $\sin^2(\Psi)$ -method [146, 147].

This method uses the fact that stresses distort the  $d$ -spacing  $d_{(hkl),\Psi}$  of the individual lattice planes in the crystal.  $d_{(hkl),\Psi}$ , and hence, the lattice parameter  $a_{(hkl),\Psi}$  are deduced from the  $2\theta$  positions in a XRD scan obtained from a GA-XRD measurement (see Sec. 3.2.2.1).

The residual stress is then derived using a bi-axial stress model which links  $a_{(hkl),\Psi}$ , the stress free lattice parameter  $a_0$  and the stress  $\sigma$  according the following equation:

$$a_{(hkl),\Psi} = \sigma a_0 \left[ \left( \frac{1 - \nu}{E} \right) \sin^2(\Psi) - \frac{2\nu}{E} \right] + a_0 \quad (3.5)$$

Here,  $E$  represents Young's modulus and  $\nu$  gives Poisson's ratio. A plot of this equation with  $a_{(hkl),\Psi}$  versus  $\sin^2(\Psi)$  results in a straight line with the slope  $m$  from which  $\sigma$  can be derived if Young's modulus  $E$  and Poisson's ratio  $\nu$  are known:

$$m = \frac{1 + \nu}{E} \cdot \sigma \cdot a_0 \quad (3.6)$$

At a  $\sin^2(\Psi)$  value of  $2\nu/(1+\nu)$ ,  $a_{(hkl),\Psi}$  corresponds to the stress-free lattice parameter  $a_0$ .  $a_0$  in the nanoscale multilayer coating represents an average lattice parameter deduced from the combined CrN and CrAlYN layers. Here,  $a_0$  is a stress-free material parameter, in contrast to the stressed lattice parameter  $a_{0,\perp}$  (see Sec. 3.2.2.2).

The GA measurements were carried out with an incident angle  $\gamma = 2^\circ$ , corresponding to an X-ray penetration depth  $z_{1/e}$  of  $0.5 \mu\text{m}$  into the material.  $E$  was determined from a nanoindentation measurement (see Sec. 3.3.5.2). As  $\nu$  of CrAlYN/CrN is not known, it was estimated to 0.3.

### 3.2.3 Scanning Electron Microscopy and Energy Dispersive X-ray Analysis

Scanning electron microscopy (SEM) is a technique which permits the observation of a surface by means of rastering of an electron beam across the specimen surface [148]. This beam interacts with the sample material and causes various effects, such as the backscattering of primary electrons, the formation of secondary electrons and the generation of X-rays. The detection of these electrons allows imaging of the sample surface.

Energy dispersive X-ray Analysis (EDS) as technique to investigate the chemical composition of materials employs the generation of X-rays by an electron transition mechanism. This involves the ionisation of an atom by incident electrons and the subsequent transition of electrons from an excited state into the ground state. During this relaxation process, X-rays are emitted. These X-rays appear in an EDS spectra as characteristic lines which are element specific. Semi-quantitative analysis of the elemental composition is possible by calculating the integral intensity of the individual EDS lines.

A Philips XL40 SEM microscope with a W filament was used to investigate

the microstructure. Additionally, a FEI Nova NanoSEM 200 with a field emission gun (FEG) was used for high resolution imaging. The acceleration voltage  $U_a$  was chosen according to the surface features analysed. Both instruments were equipped with an Oxford EDS system for semi-quantitative analysis with N as the lightest detected element.

### 3.2.4 Transmission Electron Microscopy

Transmission electron microscopy (TEM) can be used as a powerful tool for microstructural investigations of a variety of materials [149,150].

A conventional transmission electron microscope consists of a condenser lens, objective lens and intermediate and projector lenses (see Fig. 3.5).

In a TEM, an electron transparent specimen is illuminated by a parallel electron beam. Imaging contrast arises from several sources, such as mass-thickness contrast and diffraction contrast. In crystalline samples, electrons diffracted from the lattice planes in the specimen are focused at the back focal plane of the objective lens forming a diffraction pattern (DP). The shape and the corresponding  $d$ -spacing of this DP give information about the crystal structure, the lattice parameter and the crystallographic orientation. A selected area diffraction pattern (SAD) is formed when the diffracting specimen volume is limited by an aperture. A bright field image (BF) is obtained by placing the objective aperture to restrict imaging to the undiffracted beam. Alternatively, using the diffracted beam for imaging, a dark field image (DF) is generated which, similar to the DP, contains information about crystal orientation.

In this study, electron transparent coating cross-sections were produced by mechanical grinding and polishing of the sample thickness to 30  $\mu\text{m}$ . Subsequently, an Ar ion beam milling (GATAN PIPS 691) was used to produce a small hole in the coating region with electron transparent areas (thickness <200 nm) on each side of the hole. During this process, Cu from the grid that holds the cross-section can re-deposit on the surface of the coating. This Cu re-deposit is frequently observed in the obtained TEM images (see Chapt. 4 to Chapt. 6).

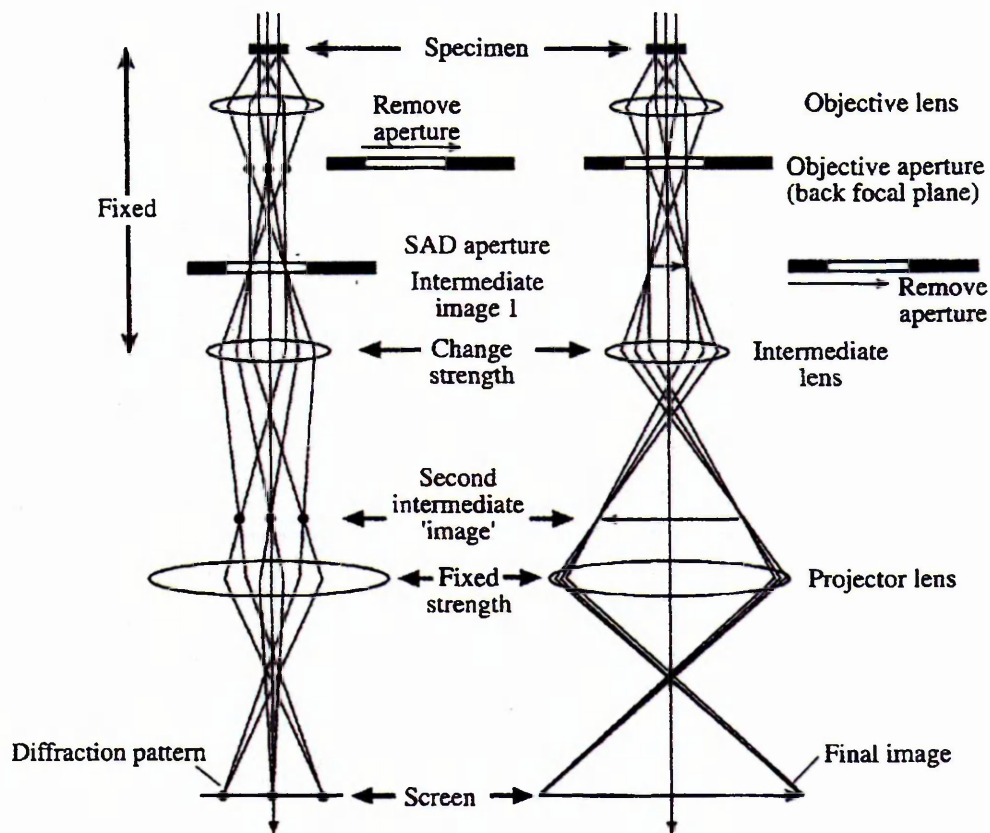


Fig. 3.5: Schematic of a TEM apparatus demonstrating the pathway of electrons from the specimen to the imaging system

A Philips EM420 TEM microscope, provided at the University of Sheffield, with W filament and an acceleration voltage  $U_a$  of 120 kV was used to investigate thin film microstructure. The instrument was equipped with an ultra-thin Si(Li)-EDS detector for semi-quantitative chemical analysis (TEM-EDS). TEM-EDS was constrained to detection of O as the lightest element and therefore did not permit the analysis of N. Semi-quantitative investigations of the chemical composition was performed by a calculation of the integrated line intensities in the TEM-EDS spectra and subsequent comparison with an instrument internal standard. The experimental error of TEM-EDS strongly depends on the measurement conditions during the analysis. This error is estimated to be in a range of a few % and is believed to be similar in all measurements as identical measurement conditions were used.

Moreover, a Philips CM-20 STEM microscope, equipped with a W filament and an acceleration voltage  $U_a = 200$  kV, was used in conventional TEM mode. A JEOL 2010F instrument, at the University of Sheffield, equipped with a FEG filament and an acceleration voltage  $U_a = 2$  kV, was utilised for analysis of the oxidised specimens. Furthermore, a JEOL 3010, provided at the Hungarian Academy of Sciences, with a LaB<sub>6</sub> filament,  $U_a = 300$  kV and a GATAN imaging filter for high resolution imaging was used for imaging of the lattice fringes.

### 3.2.5 Electron Energy Loss Spectroscopy

Electron energy loss spectroscopy (EELS) is a technique that permits the chemical analysis of materials from an electron transparent material in a transmission electron microscope (TEM) [149, 151, 152]. Here, a mono-energetic beam of electrons is scanned across the specimen. The electrons in the incident beam interact with the core electrons of the specimen material during this process. This interaction causes elastic and inelastic scattering of the incident electrons. Elastic scattering does not affect the electron energy whereas inelastically scattered electrons lose energy. The extent of this energy loss depends on the nature of the specimen electrons and their bonding states. The beam of transmitted electrons is then passed through a magnetic prism which disperses the electrons according to their energy. The electron energy loss is element specific for each transition and can be used to identify present elements. EELS permits the detection of light elements including N and is therefore a complementary technique to TEM-EDS.

Investigations were carried out in a JEOL 3010 high resolution TEM with a GATAN imaging filter at the Hungarian Academy of Sciences. Electron energy filtered elemental distribution maps were acquired with an analytical probe size fixed to 0.16 nm. These maps were taken from the N *K*-edge, the Cr *L*<sub>2,3</sub>-edge and the Al *K*-edge. It was necessary to use the Al *K*-edge for analysis as the Al *L*<sub>2,3</sub>-edge at 73 eV is superimposed on the Cr *M*<sub>1</sub> edge at 73.5 eV. Signals arising from any Y edges could not be detected suggesting relatively low Y concentrations.

### 3.3 Mechanical and Tribological Testing

This section shortly introduces the techniques used in this study to investigate the mechanical and tribological coating performance.

#### 3.3.1 Ball-Cratering Thickness Measurement

The coating thickness  $\Delta$  was measured using a ball cratering technique. A rotating steel ball, with known radius  $r_r$ , wears a crater, known as a calotte, through the coating revealing the substrate. Wear of the coating is promoted by adding diamond slurry to the touching surfaces. Inner and outer diameter  $r_o$  and  $r_i$ , respectively, of the calotte are measured using an optical microscope.  $\Delta$  can then be calculated based on the following equation:

$$\Delta = \frac{r_o^2 - r_i^2}{r_r} \quad (3.7)$$

The equipment used for analysing the coating thickness was a CSEM Calowear machine. The steel ball had a radius  $r_r$  of 10 mm and a diamond slurry with a particle size of 3  $\mu\text{m}$  was used.

#### 3.3.2 Surface Roughness Measurement

The surface roughness  $R_a$  was measured by surface stylus profilometer. The equipment used was a TAYLOR-HOBSON Talysurf-120L instrument with a 2  $\mu\text{m}$  radius diamond stylus. The diamond tip was pulled over the surface with a height resolution of 0.005  $\mu\text{m}$ .

#### 3.3.3 Adhesion Measurement

Two different methods were used to evaluate the substrate/coating adhesion: (i) the scratch test and (ii) the Rockwell C test.

### 3.3.3.1 Scratch Adhesion

In the scratch test [153–155], a Rockwell C diamond is drawn over the coated specimen surface (see Fig. 3.6). The applied normal force is continuously increased until the coating detaches from the substrate. The resulting damage is viewed by reflecting light microscopy. The critical load  $L_C$  is defined as the load at which the first adhesive failure emerges.

For the scratch test a CSEM REVETEST instrument equipped with a  $200\ \mu\text{m}$  Rockwell C tip, was used. The force  $F_N$  was subsequently increased with  $10\ \text{N}/\text{mm}$ .

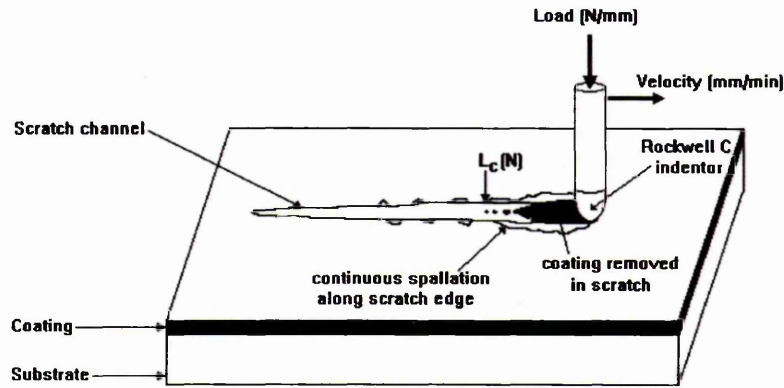


Fig. 3.6: Schematic arrangement of scratch test

### 3.3.3.2 Rockwell C ( $HR_C$ ) Indentation

A Rockwell C test [156, 157] is carried out in a conventional Rockwell C testing machine with a C-type diamond indenter. The indenter is pressed into the coated sample. The imprint is afterwards viewed by optical light microscopy and the coating surrounding the imprint is searched for cracks and spallation. Depending on the degree of cracking and/or spallation of the coating around the indentation, the adhesion is categorized with HF1-HF4 acceptable for minor cracking and low degree of spallation and HF5-HF6 (unacceptable) for failure of the coating. The test is limited to coated samples with a substrate hardness exceeding  $HR_C = 54$  and a maximum coating thickness of  $\Delta < 5\ \mu\text{m}$ .

### 3.3.4 Friction and Dry Sliding Wear Measurement

Friction is defined as the resistance to relative motion of bodies in contact [158]. The friction coefficient  $\mu$  can be expressed as the ratio of tangential force  $F_t$  and normal force  $F_N$  that presses the two surfaces together (see the following equation):

$$\mu = \frac{F_t}{F_N} \quad (3.8)$$

Wear, the removal of material from a solid surface, occurs as a result of mechanical action between two counterparts. The dry sliding wear rate  $k_S$  can be estimated via Archard's model (see the following equation):

$$k_s = \frac{V_r}{F_N l} \quad (3.9)$$

Here,  $V_r$  represents the loss in material volume and  $l$  the sliding distance.

Sliding wear tests are often conducted on a pin-on-disk tribometer [159]. During the test, a stationary ball is pressed on a rotating sample by a normal load  $F_N$ . The tangential force  $F_t$  is monitored as a function of sliding distance  $l$ . From this,  $\mu$  can be deduced. For the calculation of  $k_S$ , knowledge of the removed coating volume  $V_r$  is required (see the following equation):

$$V_r = 2\pi R_t A_t \quad (3.10)$$

Here,  $R_t$  represents the radius of the sliding circle and  $A_t$  the cross-sectional area of the wear track.

A CSEM tribometer was used to determine the friction coefficient and the wear rate of the coatings. A 6 mm  $\text{Al}_2\text{O}_3$  sliding ball was used as counterpart. The ball was sliding with a linear speed of  $10 \text{ cm.s}^{-1}$ , a normal load  $F_N$  of 5 N and a radius  $R_t$  of 10 mm on the coated HSS sample for  $l = 200\,000$  laps. The tests were carried out in an environment with a relative humidity  $H$  of 13-34% and temperatures  $T$  between 26-32 °C. The cross-sectional area of the wear track

$A_t$  was measured using a Talysurf profilometer 120L (see Sec. 3.3.2).

### 3.3.5 Micro- and Nano-Hardness, Young's Modulus

Hardness is a measure of the resistance of a material to deformation.

During a hardness measurement, a stylus is forced into the material being tested. The ratio between the total load and the projected area or depth of the permanent (plastic) indent provides a measure of hardness.

In this study, the hardness was evaluated by two methods: (i) Knoop micro-indentation and (ii) loading-unloading nano-indentation.

#### 3.3.5.1 Knoop Indentation

The Knoop hardness  $HK$  is a hardness measurement technique carried out with a Knoop indenter. This indenter has a pyramidal shape with a ratio of the diagonals of 1:7 and is commonly used for hardness measurements of coating systems [160].

Static micro-hardness measurements were performed using a Mitutoyo MVK/G1 tester with a Knoop indenter and a constant load  $F_N$  of 0.25 N. This normal force was applied for 10 s and the long length  $d_{ind}$  of the indenter footprint was measured by optical microscopy. From this,  $HK_{0.025}$  was calculated according to the following equation:

$$HK_{0.025} = 1.451 \cdot \frac{F_N}{d_{ind}^2} \quad (3.11)$$

#### 3.3.5.2 Nano-Indentation

Dynamic loading-unloading measurements allow insight into the elastic material properties [161, 162]. During such a measurement the load is stepwise increased and the penetration depth is recorded (see Fig. 3.7(a)). This causes plastic and elastic deformation. The hardness  $H_{IT}$  is then calculated from the maximum applied force  $F_{N,max}$  and the projected contact area  $A_p$  at the indentation depth  $h_c$  where the indenter has a maximum contact (see Fig. 3.7(b) for schematic of indent geometry):

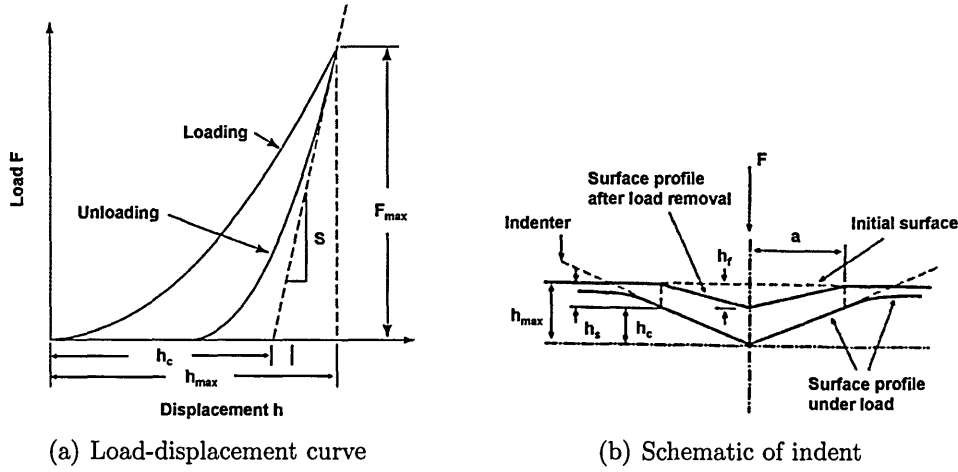


Fig. 3.7: Load-displacement curve obtained by nano-indentation with schematic of resulting indent

$$H_{IT} = \frac{F_{N,max}}{A_p} \quad (3.12)$$

$H_{IT}$  is independent of the substrate material when  $h_c$  is smaller than 10% of the coating thickness [161].

The Young's modulus  $E$  can be calculated by fitting the upper part of the unloading data with a power law relation after the Oliver & Pharr method [161] to obtain the reduced modulus  $E_r$ . Assuming, Poisson's ratio  $\nu$  and  $\nu_{ind}$  of coating and indenter, respectively, and Young's modulus  $E_{ind}$  of the indenter are known,  $E$  can be calculated according to following equation:

$$E = (1 - \nu^2) \cdot \frac{E_{ind} - (1 - \nu_{ind}^2) \cdot E_r}{E_r \cdot E_{ind}} \quad (3.13)$$

Dynamic loading-unloading experiments were performed with a CSM Nanoindenter equipped with a Berkovich type diamond tip. Analysis was performed using one loading-unloading cycle with a load  $F_{N,max} = 50$  mN and the loading time of 60 s. When indenting CrAlYN/CrN, typical indentation depths were of the order of 300 nm which was well below the recommended 10% rule for maximum indentation depth [161]. As the Poisson's ratio for the examined CrAlYN/CrN coatings is unknown, a value of 0.3 was estimated for all samples.

### **3.3.6 Dry High Speed Milling**

Dry high speed milling tests are a quick way to test the coatings in a real application environment. Such tests were performed in a MAZAK FJV-25 industrial cutting machine. 8 mm nose balled cemented carbide endmills were used for machining A2 steel with a hardness of 58 HRC in dry conditions using the following parameters: cutting speed 385 m/min, axial cutting depth 3.8 mm, stepover/radial cutting depth 0.4 mm and feed rate per tooth 0.05 mm/tooth. The end of tool life was defined by a 10% increase in cutting force.

## **3.4 Oxidation Texting**

The oxidation performance of the coating was assessed using different techniques which will be introduced in the following.

### **3.4.1 Thermogravimetric Analysis**

The high temperature oxidation behaviour of a material was determined by means of thermogravimetric (TG) analysis. In these TG measurements, the weight gain of a specimen under heating is recorded as a function of temperature. This allows determination of the extent of weight gain and the onset temperature of rapid oxidation (temperature at which weight gain increases rapidly).

TG measurements were carried out in a SETARAM Setsys 16/18 thermobalance. The tested specimen was heated up to 400°C with a ramp of 30°C/min. Further heating was carried out up to 1000°C with a rate of 1°C/min. Tests were performed in dry air with a flow rate of 12.5 mL/min. After reaching the final temperature, the samples were cooled down inside the furnace in flowing air.

### **3.4.2 Isothermal Oxidation Analysis**

Isothermal Oxidation tests were carried out in a Lenton Ltd. furnace. The samples were subjected to a heat-treatment in laboratory air at various temperatures and

exposure durations. The furnace was pre-heated to the required temperatures, then the samples were introduced. After the corresponding holding-time, the samples were removed from the furnace and cooled down in laboratory air. Short-term oxidation was carried for 1 h with temperatures in a range of 850° to 1000°C. Additionally, long-term tests were conducted at 850°C for up to 100 h.

# CHAPTER 4

---

---

## Influence of the Substrate Etching Pre-Treatment on the Coating Microstructure and Performance

---

---

Excellent substrate/coating adhesion is one of the key requirements for good functionality of the composite system in application. It is therefore required to engineer the substrate/coating interface in such a way that it provides high adhesion. One way to alter the interface structure is by bombarding the substrate surface with a flux of metallic ions. This treatment, the so called metal ion etching substrate pre-treatment, can forcefully remove contaminants from the surface and affect the growth structure of the subsequently deposited films. It is assumed that the effectiveness of the etching step is governed by the PVD technique used to pre-treat the substrate.

This chapter examines the influence of a HIPIMS pre-treatment on the interface structure and compares the generated morphology to one which forms after a conventional CA metal ion etching. Some selected mechanical properties will

also be investigated. A description of the experimental set-up and the employed process parameters for the pre-treatment step is given in Sec. 3.1.

## 4.1 Microstructural Characterisation

### 4.1.1 SEM Analysis

The visual appearance of the coating surface was examined by SEM analysis (see Sec. 3.2.3). Fig. 4.1 compares the surface morphology of CrAlYN/CrN coatings with a previous HIPIMS and a CA pre-treatment.

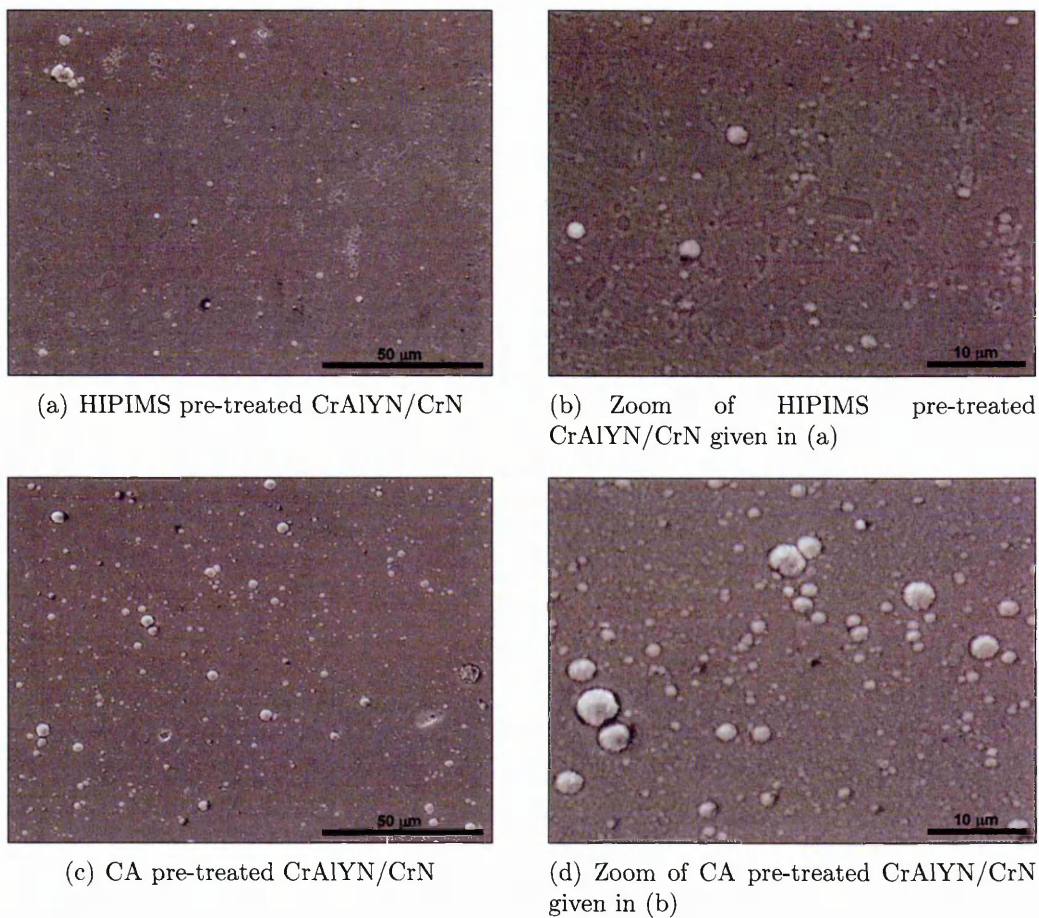


Fig. 4.1: SEM micrographs of CrAlYN/CrN pre-treated by (a), (b) HIPIMS and (c), (d) CA: The HIPIMS pre-treated specimen is nearly free of macro-particle induced growth defects

The specimen with HIPIMS pre-treatment reveals a smooth surface with only very few growth defects being present with a maximum size of  $\sim 1.6 \mu\text{m}$ . Defects with a diameter of  $\geq 1 \mu\text{m}$  emerge with a density of  $2.5 \times 10^{-3} \mu\text{m}^{-2}$ . The austenitic granular structure of the 304 stainless steel substrate material can be clearly observed. The surface roughness  $R_a$  of the film (see Fig. 4.2), evaluated using a stylus measurement technique (see Sec. 3.3.2), is measured to be  $0.043 \mu\text{m}$ . The coating can therefore be characterised as nearly free of macro-particle induced growth defects. Present defects can be generated by arcing on the target during the pre-treatment step [163] or by the presence of contamination in the vacuum chamber. The visibility of the stainless steel structure may be due to preferential sputtering of the some grains during the high energetic HIPIMS ion bombardment [164].

The surface of the CA pre-treated sample, in contrast, is completely covered with growth-defects with a size up to  $5 \mu\text{m}$ . The generation of these defects is induced by macro-particles ejected from the target during the pre-treatment step [57, 58, 165, 166]. The density of growth defects with a diameter exceeding

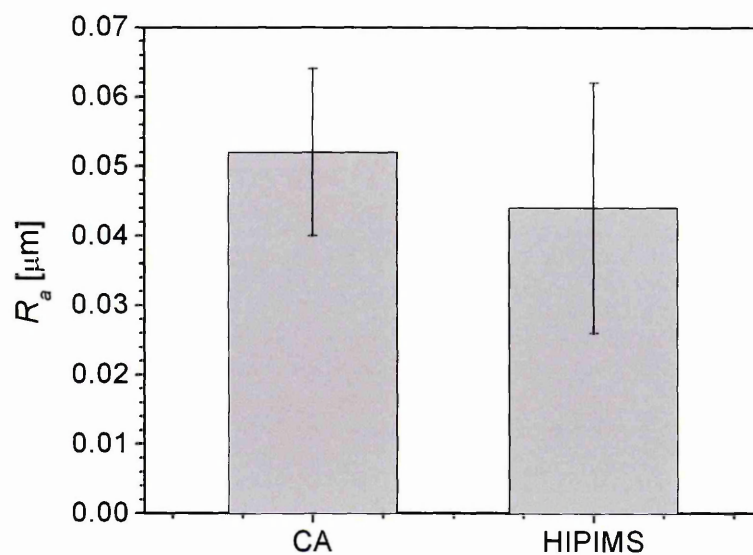


Fig. 4.2: Surface roughness  $R_a$  of CrAlYN/CrN with Cr HIPIMS and CA pre-treatment

1  $\mu\text{m}$  is calculated to be  $32.5 \times 10^{-3} \mu\text{m}^{-2}$  and therefore one order of magnitude higher than after HIPIMS treatment. In consequence,  $R_a$  is measured to be 0.53  $\mu\text{m}$  and is therefore significantly higher than in the coating with HIPIMS pre-treatment.

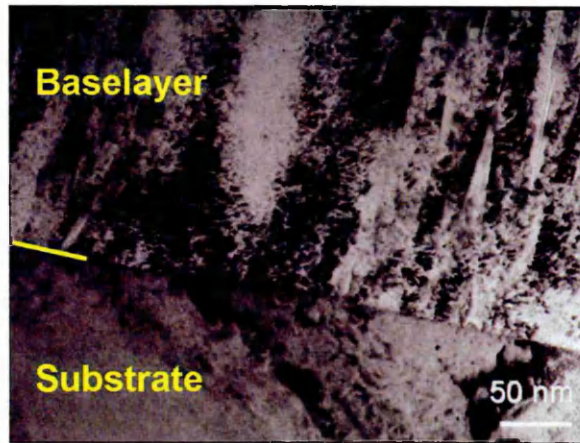
It can be concluded that the HIPIMS pre-treatment generates growth-defect free and smooth coatings.

#### 4.1.2 TEM Analysis

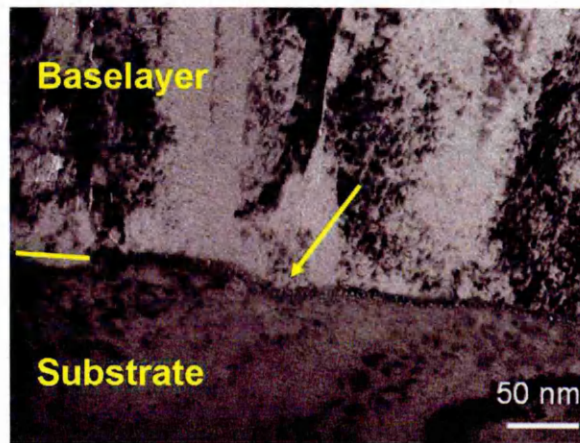
Cross-sectional TEM studies (see Sec. 3.2.4) permit the investigation of the substrate/coating interface. Fig. 4.3 shows BF-TEM micrographs of CrAlYN/CrN with a HIPIMS and CA pre-treated interface. The HIPIMS pre-treatment results in a sharp and clean interface without foreign or amorphous phases (see Fig. 4.3(a)). A dark line situated directly below the interface and may arise from lattice strains in the substrate. HIPIMS metal ion implantation into steel substrates is reported for particle bombardment ( $U_b = 600 \text{ V}$  to  $1000 \text{ V}$ ) by Cr and Nb ions [51, 71]. There, implantation of the metal ions into a depth of 5-15 nm causes lattice distortion and irradiation damage. It is believed that similar lattice strains are induced by particle bombardment at  $U_b = -500 \text{ V}$  due to the implantation of metal ions into the top surface layers of the substrate and, as a consequence, lead to the observation of a stress band in the BF-TEM micrograph.

In contrast to the HIPIMS pre-treated interface, the arc pre-treated interface appears more diffuse (Fig. 4.3(b)). In a few areas a thin layer with a fine grain structure, indicated by the arrow, can be observed. This suggests either the incomplete removal of the surface oxides, the deposition of a thin layer or the formation of a heavily distorted surface region as a result of radiation induced damage during the CA etching step.

Extensive TEM studies show that CA interfaces with Cr etch are highly clean and subsequently grown films have dense interfaces [75]. Treatment in a HIPIMS and CA plasma are both characterised by intense ion bombardment which, in turn, leads to interface with ion implantation. This structure represents essentially a



(a) HIPIMS pre-treated interface



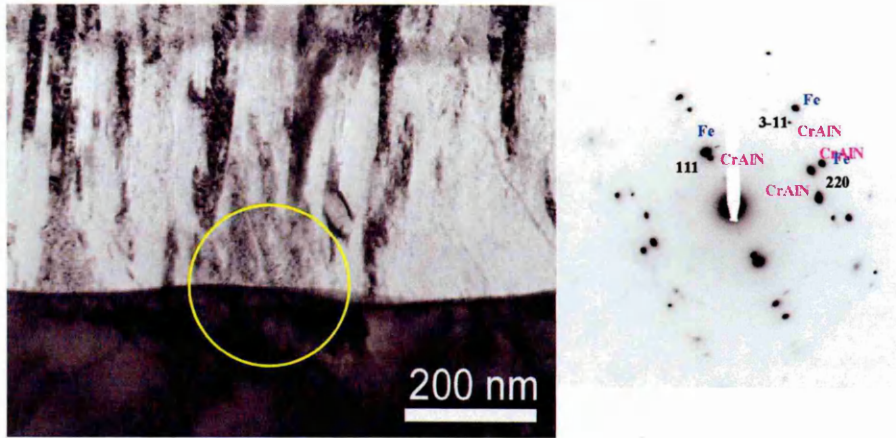
(b) CA pre-treated interface

Fig. 4.3: BF-TEM micrographs of the substrate/base layer interface of CrAlYN/CrN after (a) HIPIMS and (b) CA pre-treatment

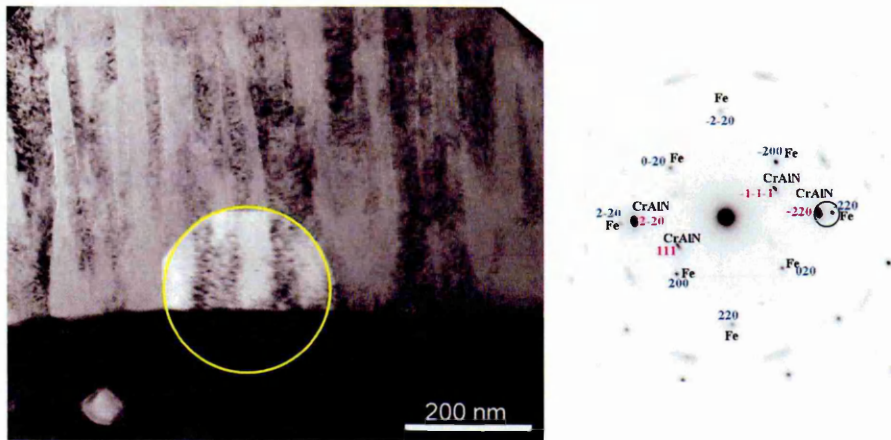
similarity between these techniques.

In the following, the crystallographic growth on a polycrystalline substrate material after HIPIMS pre-treatment is examined in detail. SAD patterns can give information about the crystallographic orientation of the substrate and coating crystals. Patterns are taken from different positions at the substrate/coating interface and analysed regarding the position of the individual diffraction spots and a possible alignment of the spots relating to the substrate and coating crystals.

The crystallographic orientation relationship between the substrate and base



(a) Substrate/base layer interface with epitaxial growth relation



(b) Substrate/base layer interface with axiotaxial growth relation

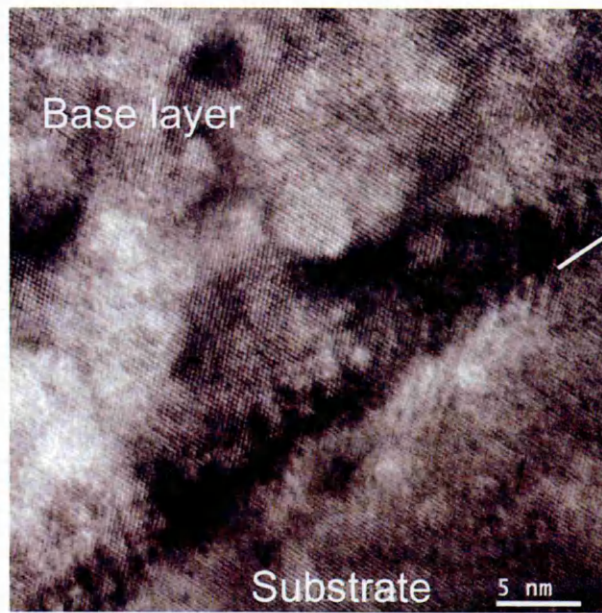
Fig. 4.4: BF-TEM micrographs and corresponding SAD pattern of HIPIMS-pre-treated CrAlYN/CrN with (a) epitaxial growth relation and (b) axiotaxial growth relation. The analysis was performed on two different substrate crystals of the same specimen

layer crystals after HIPIMS etching is analysed in Fig. 4.4. A BF-TEM micrograph of the HIPIMS pre-treated film with corresponding SAD pattern from the interface is given in Fig. 4.4(a). The BF-TEM image shows a substrate crystal with individual columns of the CrAlN base layer. The columnar growth of CrAlN is mainly governed by the energy of ion bombardment ( $U_b = -75$  V) during the deposition step and is characterised as a separate entity in Sec. 5.1. The SAD

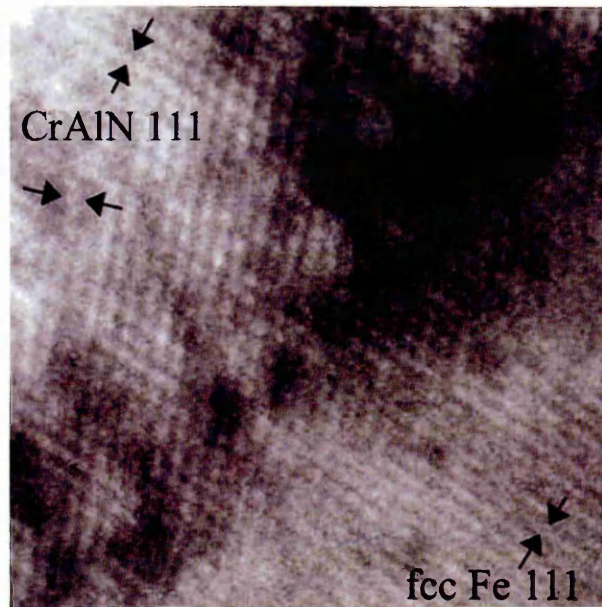
pattern is taken with the electron beam aligned along the  $[1\bar{1}2]$  zone axis. Two sets of reflections, indexed as diffraction spots from the (111), (220) and (311) planes, are visible with spots at a larger distance corresponding to reflections of the substrate crystal and those at a shorter distance to the CrAlN crystals. Reflections with identical (hkl) indices are mutually aligned, which is typically observed in hetero-epitaxially grown structures with lattice mismatch between the individual materials. Hetero-epitaxial growth is also referred to as cube-on-cube epitaxy where the crystalline and clean substrate surface serves as a template for the nucleation of the base layer and the growing CrAlN crystals adopt lattice structure and orientation of the substrate crystal [167].

A second type of orientation relationship is identified in Fig. 4.4(b) where a BF-TEM micrograph and the corresponding SAD pattern of the HIPIMS pre-treated specimen are given. The SAD pattern is taken with the  $[001]$  zone axis of the substrate crystal aligned parallel to the incident beam. The (220) reflections of the substrate are visibly in mutual alignment with the (220) reflections of the CrAlN crystals, as indicated by a circle, signifying alignment of the (220) planes in both materials. The (111) substrate reflections are not visible in the SAD pattern because they are forbidden reflections when aligning the beam along the  $[001]$  axis. The (111) reflections of CrAlN, however, are obvious in addition to the (220) CrAlN spots, giving a clear indication that the (111) planes of substrate and CrAlN are not aligned with each other. The SAD pattern with mutual alignment of diffraction spots on one axis attests that the atoms in the CrAlN crystals are oriented in only a single direction with the substrate atoms. The coating lattice planes are additionally tilted at a strong angle to the substrate lattice planes to minimise the difference in lattice spacing. This relation is referred to as axiotaxy [167]. The HIPIMS pre-treatment may cause both epitaxial and axiotaxial growth on large areas of the substrate surface.

High resolution BF-TEM imaging resolves the interface region on an atomic level (see Fig. 4.5). The phase contrast images reveal the clearly ordered atomic columns of substrate and base layer in close atomic registry between the individual



(a)



(b)

Fig. 4.5: BF-TEM micrographs of the lattice planes of a HIPIMS pre-treated interface with (a) BF-TEM micrograph and (b) zoom of the image presented in (a) (arrows mark the (111) lattice planes in substrate and coating)

lattices with the (111) planes of the substrate merging smoothly into the (111) planes of the CrAlN baselayer. The interface region appears to be crystalline and



Fig. 4.6: BF-TEM micrograph of CrAlN with epitaxial growth on a large area of the substrate surface. The epitaxial growth of the base layer merges into a growth structure governed by the process parameters

fully dense without misfit dislocations, amorphous regions or accumulation of gas atoms in form of bubbles. The atomic planes of base layer and the underlying substrate crystal seem to be in direct contact with each other. It is anticipated that the present interface structure provides strong adhesive bonding due to the formation of strong chemical forces, such as metallic, ionic or covalent bonds.

The crystallographic orientation between individual substrate crystals and the CrAlN base layer grains was investigated on various substrate grains analysing large substrate areas. Fig. 4.6 shows a BF-TEM micrograph of CrAlN with uniform diffraction contrast directly adjacent to the interface, implying local epitaxy of the base layer on a large analysed area of more than  $2 \mu\text{m}$  of the substrate crystal. Epitaxial growth is expected to be localised on the whole substrate crystal and to only change at the grain boundaries, depending on the orientation of the substrate grain.

Up to this point, a detailed examination of the effect of HIPIMS substrate pre-treatment on the appearance of the interface structure was given. As the relationship between a CA etching pre-treatment and the growth of subsequently sputtered thin films is already well established [72, 74, 168], this case will not be considered in detail. The Cr CA pre-treated interfaces, in general, provide a high degree of epitaxial growth which is comparable to that obtained on the

investigated Cr pre-treated HIPIMS interfaces. As a result of this examination, it can be concluded that both HIPIMS and CA pre-treatment with Cr ions generate interfaces on which highly epitaxial films can be grown. The interface structure of these films are comparable in nature, however, the HIPIMS pre-treatment permits to overcome the limitation of macro-particle ejection.

Axiotaxic/epitaxial growth may be a characteristic in sputtered films which are deposited after HIPIMS substrate pre-treatment. A similar crystallographic relationship could be shown in CrN films on both  $\gamma$ -TiAl and SS steel substrates after pre-treatment in a Cr or Nb HIPIMS plasma [71, 77, 169].

## 4.2 Influence of the Interface Structure on the Mechanical Properties

The macroscopic behaviour of thin films is often strongly governed by the microscopic film architecture. Investigations of the mechanical behaviour, according to the testing techniques described in Sec. 3.2, reveal that many properties, such as hardness  $H_{IT} = 35$  GPa and residual stress  $\sigma = -3.3$  GPa, are independent of the pre-treatment technology. Important aspects for coating performance though, namely adhesion, friction and wear, are significantly ruled by the pre-treatment method. A more complete characterisation of the film performance of HIPIMS pre-treated CrAlYN/CrN is given at a later stage in Chapt. 5.

### 4.2.1 Adhesion

The adhesion of a thin film is considered to be determined by the chemical and physical properties of the substrate/coating interface. Fig. 4.7 compares the adhesive behaviour between HIPIMS and CA pre-treated CrAlYN/CrN. The coating adhesion increases strongly from  $L_C = 55$  N to 61 N when the pre-treatment step is performed by HIPIMS.

The bonding strength between substrate and coating depends strongly on the

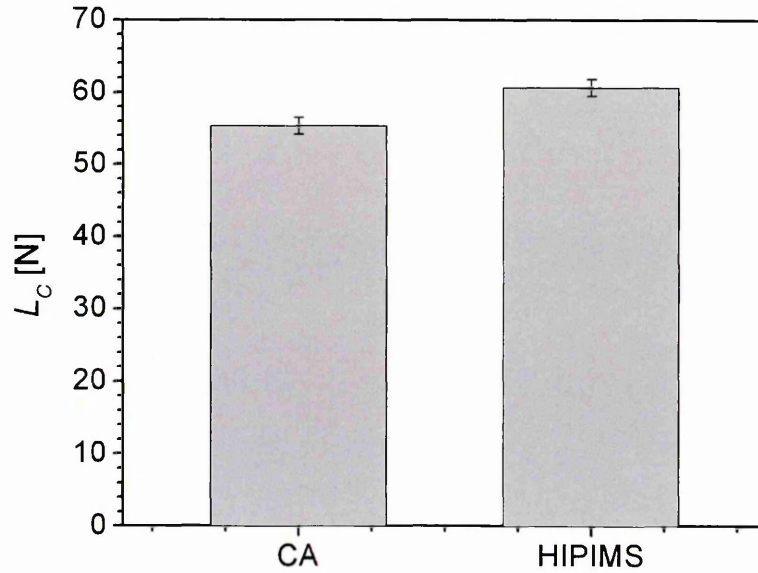
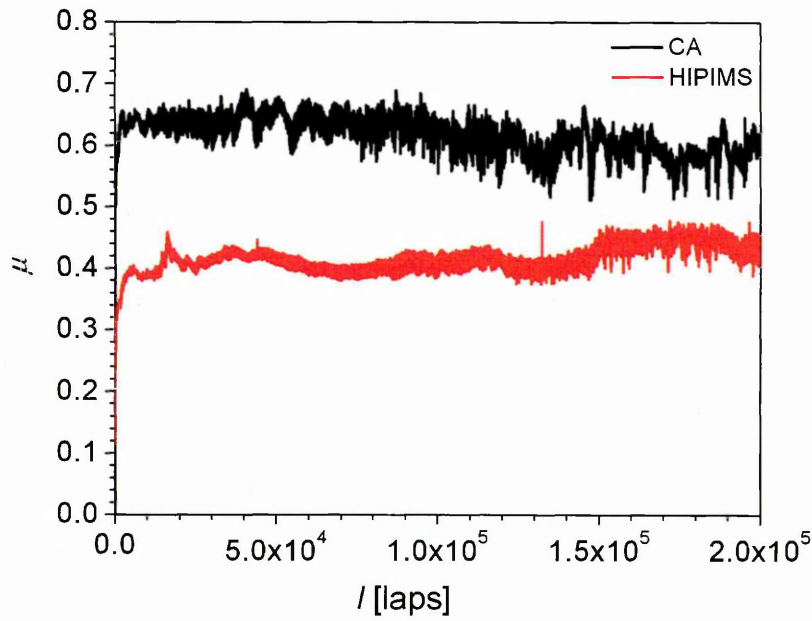


Fig. 4.7: Critical load value  $L_C$  of CrAlYN/CrN with Cr HIPIMS and CA pre-treatment

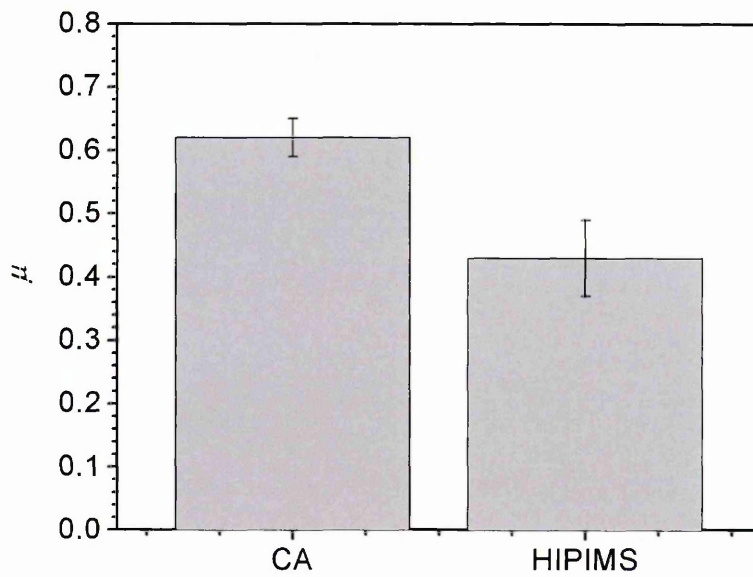
interface structure [75]. Coatings pre-treated by conventional Ar etching, for example, with highly strained and voided interfaces are clearly inferior in their adhesion compared to CA etched coatings with their clean and dense interfaces and a local epitaxial structure [75]. The present study can show that HIPIMS interfaces have a similar nature to those observed after CA pre-treatment [74]. Both techniques provide the base for local epitaxial growth on large substrate surface areas. These epitaxial structures provide a strong bonding and, in turn, enhance the substrate/coating adhesion. The adhesion measurements (see Fig. 4.7) additionally indicate that the implementation of HIPIMS can further improve the bonding property of the coating. The HIPIMS pre-treated film benefits from the contamination-free interface with direct contact of substrate and base layer atoms in atomic registry. These characteristics promote a high bonding strength and result in films with excellent adhesive properties.

## 4.2.2 Tribological Analysis

The friction behaviour of CrAlYN/CrN was analysed by a pin-on-disk wear test (see Sec. 3.3.4). Fig. 4.8 compares the friction curves obtained from nanoscale multilayered CrAlYN/CrN with CA and HIPIMS pre-treatment when sliding against an Al<sub>2</sub>O<sub>3</sub> counterpart. Both curves remain at a stable level up to very high sliding distances of 200,000 laps. The performance in dry sliding, however, differs remarkably with a friction coefficient  $\mu = 0.62$  in the CA pre-treated specimen compared to  $\mu = 0.43$  when implementing HIPIMS pre-treatment. A comparison of the wear coefficients (see Fig. 4.9(a)) clearly shows that the wear of the nanoscale multilayer coating is in a similar range with  $k_S$  at about  $2 \times 10^{-16} \text{ m}^3 \text{N}^{-1} \text{m}^{-1}$ . The wear rate  $k_{CP}$  of the Al<sub>2</sub>O<sub>3</sub> counterpart are by two orders of magnitude higher with  $2 \times 10^{-14} \text{ m}^3 \text{N}^{-1} \text{m}^{-1}$  (see Fig. 4.9(b)). In TiN coatings, friction and wear both decrease with decreasing surface roughness when sliding against Al<sub>2</sub>O<sub>3</sub> [170,171]. In CrAlYN/CrN, it is assumed that the smoother surface of the HIPIMS pre-treated coating causes reduced wear of the alumina ball and thus brings less debris into the sliding contact. This, in turn, may give rise to lower friction. Thus CA pre-treated CrAlYN/CrN is outperformed by a similar coating with HIPIMS substrate surface etching pre-treatment.

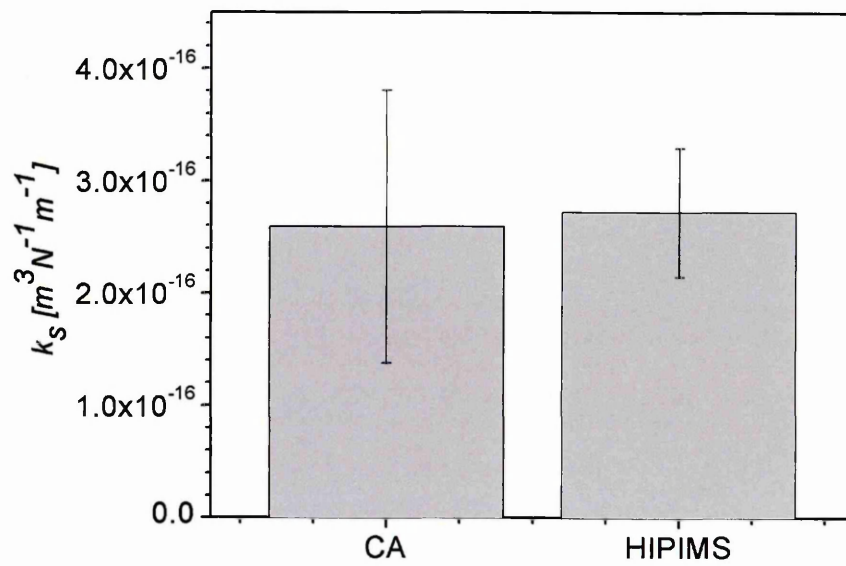


(a)

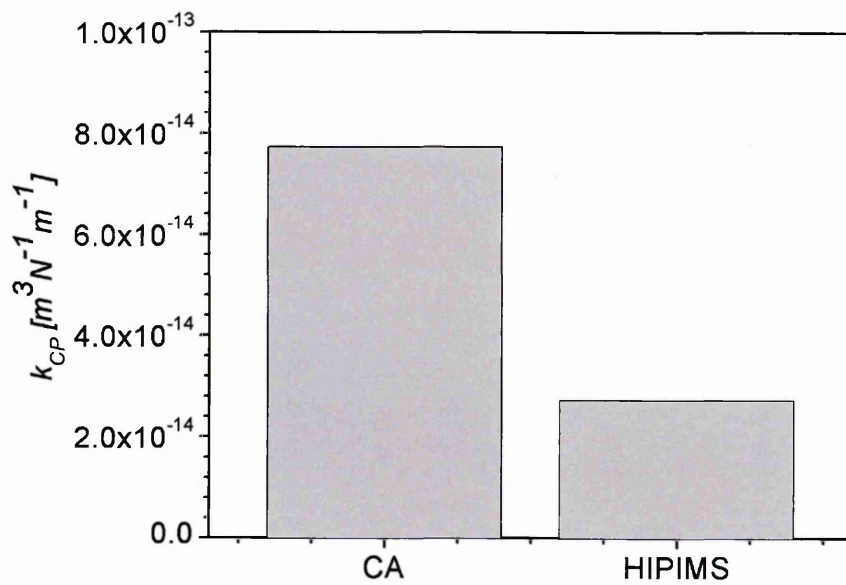


(b)

Fig. 4.8: (a) Friction coefficient  $\mu$  of CrAlYN/CrN with Cr HIPIMS and CA pre-treatment as a function of sliding distance  $l$  and (b) average friction coefficient  $\mu$ , evaluated after sliding against a  $\text{Al}_2\text{O}_3$  counterpart



(a)



(b)

Fig. 4.9: (a) Sliding wear coefficient  $k_S$  of the coating and (b) Sliding wear coefficient  $k_{CP}$  of CrAlYN/CrN after sliding against  $Al_2O_3$

### 4.3 Chapter Summary

Substrate surface pre-treatment in a Cr/Ar HIPIMS plasma generates films which have smooth surfaces and are free of macro-particle induced growth defects. The ion bombardment during the etching step effectively cleans the substrate surface and removes contaminations. Subsequently grown films can nucleate in a local epitaxy or axiotaxy directly on the atomically clean surface and form high density interfaces providing high adhesive bonding strength between the base layer columns and the underlying substrate grains. Local epitaxial growth can be preserved on a large scale on areas of several  $\mu\text{m}$  in length. CrAlYN/CrN coatings with HIPIMS pre-treatment are superior to those with CA pre-treatment with enhanced adhesion, reduced surface roughness and remarkably lower friction coefficient. The supremacy of the HIPIMPS pre-treatment can be associated to the complete removal of surface contamination which may compromise the adhesive bonding strength of CA pe-treated samples as well as the absence of macro-particle induced growth defects which are detrimental for the friction behaviour when removed from the thin film.

In summary, a HIPIMS substrate etching pre-treatment prior to coating deposition generates highly dense and defect-free thin films with superior mechanical properties when compared to a CA pre-treatment.

# CHAPTER 5

---

---

## Development of a Novel CrAlYN/CrN Coating

---

---

### 5.1 Influence of Energetic Particle Bombardment on the Microstructure and Mechanical Prop- erties

It was previously shown that the deposition conditions during thin film growth have a pronounced effect on the microstructure and the subsequently arising properties (see Sec. 2.3). One such deposition parameter affecting the growth structure is the energy of the ions bombarding the growing film. It is possible to relate this energy directly to the substrate bias voltage  $U_b$  applied to the substrate when all other process parameters are kept constant [66].

In the following, the effect of the substrate bias voltage  $U_b$  in a range of -75 V to -150 V on microstructure, mechanical and tribological performance of novel CrAlYN/CrN nanoscale multilayer coatings is described. The deposition conditions for these coatings are described in Sec. 3.1.

### 5.1.1 SNMS Analysis

Coating composition was analysed by SNMS depth profiling (see Sec. 3.2.1). Fig. 5.1 shows a typical depth profile, here obtained from CrAlYN/CrN grown at  $U_b = -75$  V. Three distinct zones can be distinguished. The CrAlYN/CrN is characterised by high atomic fractions of Cr ( $\sim 28.7\text{at}\%$ ), Al ( $\sim 31.5\text{at}\%$ ) and N ( $\sim 38.1\text{at}\%$ ) (see Fig. 5.1(a)). Additionally, low concentrations of Y ( $\sim 0.5\text{at}\%$ ) and contaminations of O ( $< 0.9\text{at}\%$ ) are found (see Fig. 5.1(b)). The composition of the Y-free CrAlN base layer was determined from an individual sample which only comprised the base layer. The CrAlN base layer is represented by a slight enrichment in Al ( $\sim 44.6\text{at}\%$ ) and a reduction in both Cr ( $\sim 31.3\text{at}\%$ ) and N ( $\sim 31.3\text{at}\%$ ) (see Fig. 5.2). The substrate region is distinguished by the appearance of Fe and Ni in the profile and a decrease in signals related to the coating elements. Due to the characteristics of the SNMS technique, the transition between these zones is gradual and does not mirror the presumably sharp interfaces of the individual zones. The SNMS studies clearly reveal the non-stoichiometry of both the coating and the base layer with an excess in metal component.

Analysis of the chemical composition in all investigated specimens (see Fig. 5.3) reveals that the coatings consist of  $27.7 \pm 1.4$  at% Cr,  $30.8 \pm 1.6$  at% Al, a low Y of  $0.5 \pm 0.1$  at% and a N content of  $40.0 \pm 3.0$  at%. It can be shown that the composition is constant within the experimental error when analysed in  $U_b$  between  $-75$  V and  $-150$  V. CrN<sub>x</sub> [100], in contrast, depletes by  $\sim 2.8\text{at}\%$  in N and Ti<sub>1-x</sub>Al<sub>x</sub>N [93] diminishes by  $\sim 2.3\text{at}\%$  in Al when investigated in a similar range of analysed bias voltages. In these cases, preferred re-sputtering of the light element N or Al was found responsible for variations in chemical composition. The error in the measurement of the chemical composition of CrAlYN/CrN prevents the determination of a similar effect in this material.

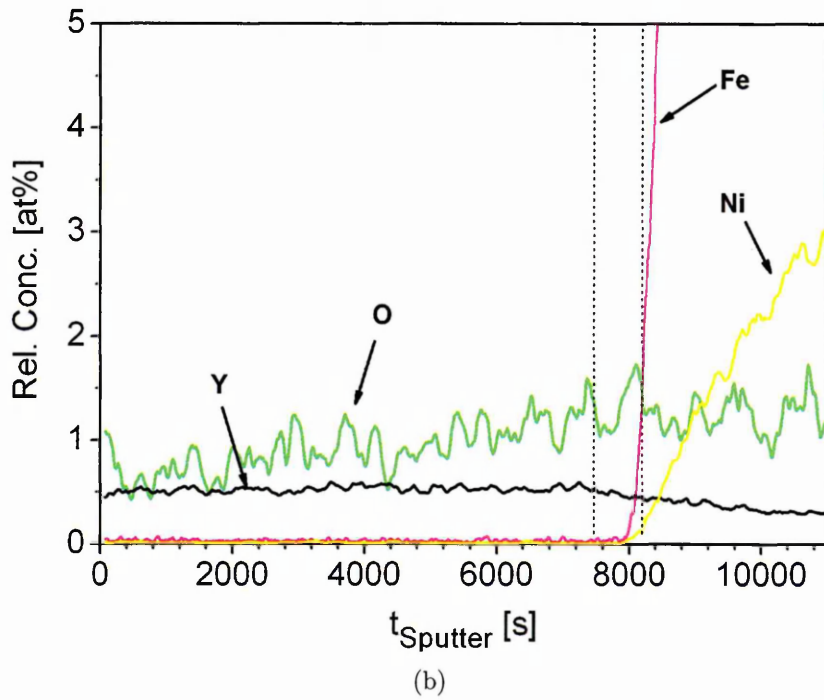
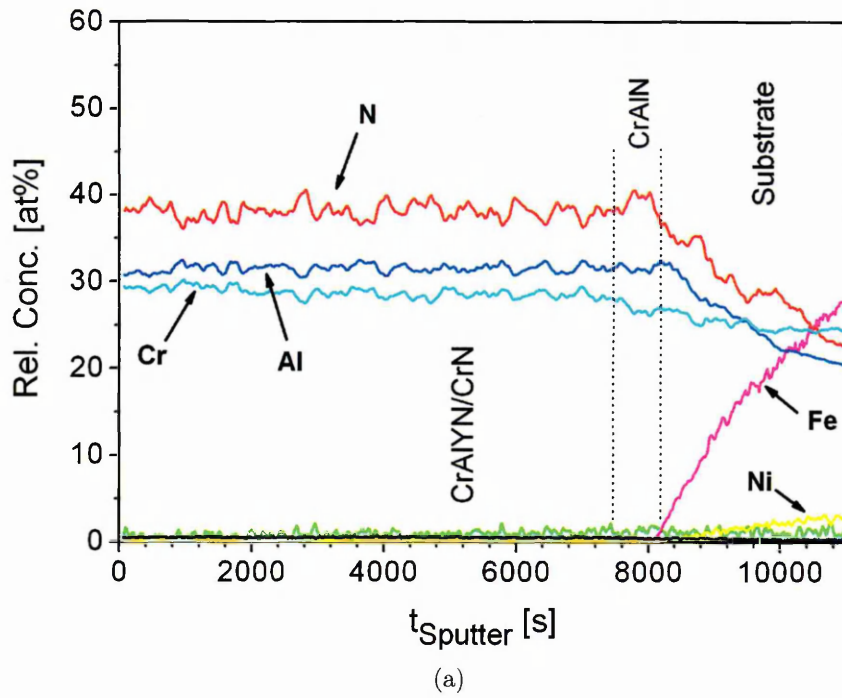


Fig. 5.1: SNMS profile of CrAlYN/CrN deposited  $U_b = -75$  V: (a) High concentration regime and (b) Zoom in the concentration region of 0-5at%

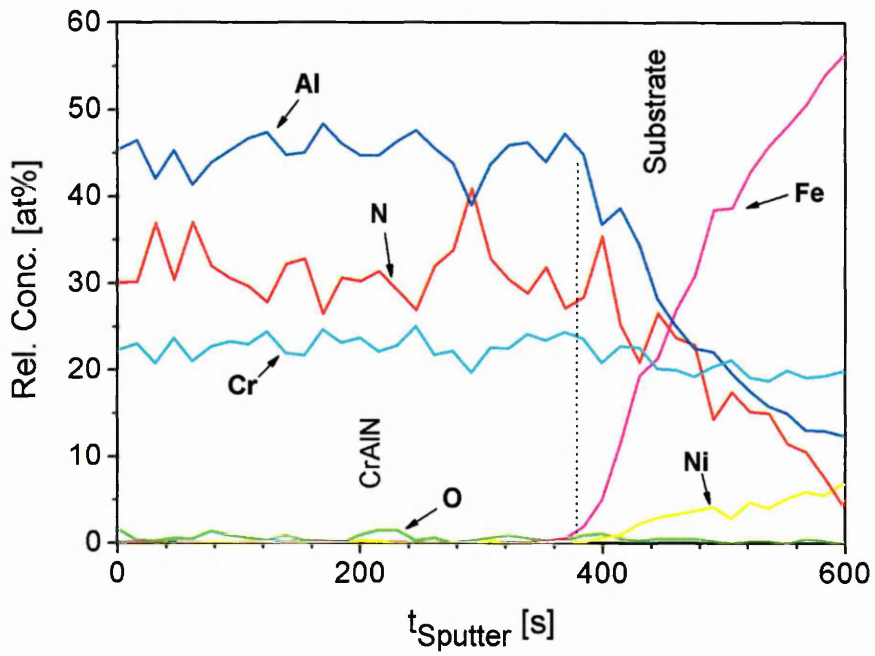


Fig. 5.2: SNMS profile of CrAlN base layer deposited at  $U_b = -75$  V

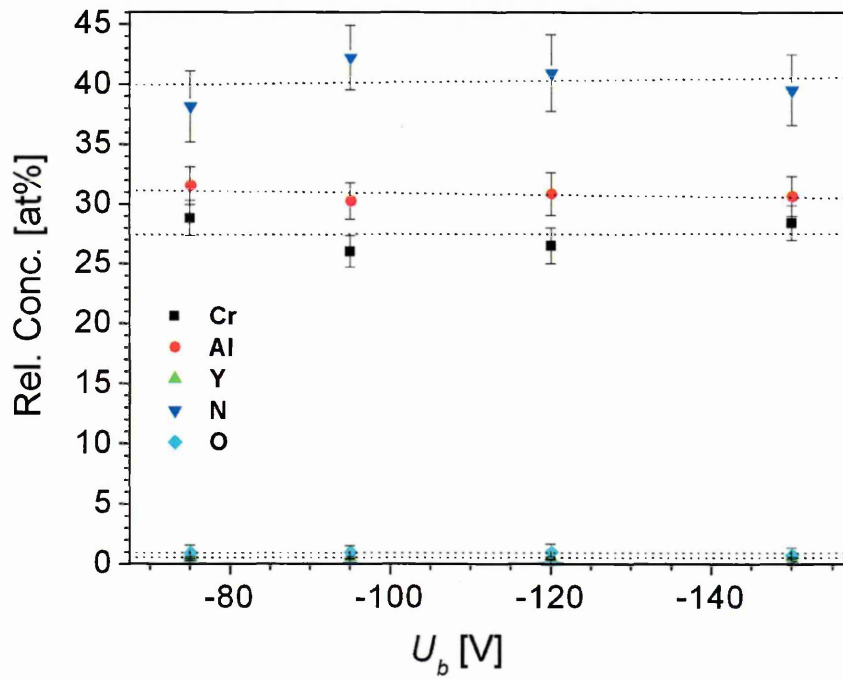


Fig. 5.3: Chemical composition of CrAlYN/CrN as function of bias voltage  $U_b$

## 5.1.2 XRD Analysis

Phase analysis was carried out by XRD measurements in  $\theta/2\theta$ -geometry (see Sec. 3.2.2.2).

Fig. 5.4 represents a scan of CrAlYN/CrN deposited at  $U_b = -75$  V. Only one set of reflections is present signifying a single-phase NaCl B1 fcc lattice structure for CrAlYN/CrN. Individual peaks for fcc-CrN (JCPCD 76-2494, listed in the database [141]) and fcc-AlN (JCPCD 25-1495) are not found. Reflections are labelled according to their corresponding crystal lattice plane. Peaks labels 'S' refer to reflections contributed from the 304 stainless steel (SS) substrate material. Although the chemical analysis demonstrates that the coating is non-stoichiometric with an excess in metal (see Fig. 5.3), no other phases, such as Cr<sub>2</sub>N (JCPCD 35-0803) or hcp-AlN (JCPCD 25-1133), are evident by XRD. This is in good agreement with literature. CrN<sub>x</sub> thin films with similar metal/N ratio were found to consist of single phase CrN<sub>x</sub> [118]. hcp-AlN is not found indicating an Al concentration in the CrAlYN layers either below the maximum theoretical solu-

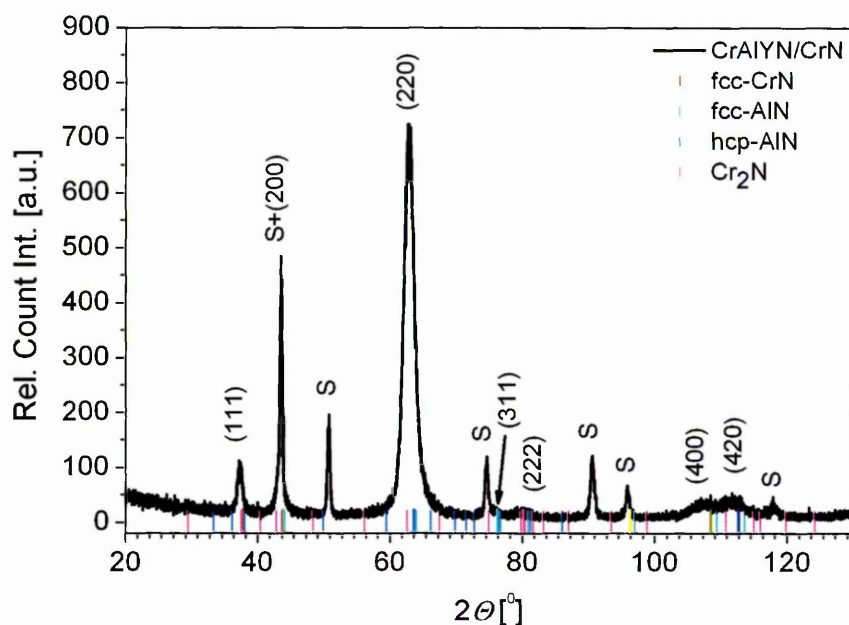


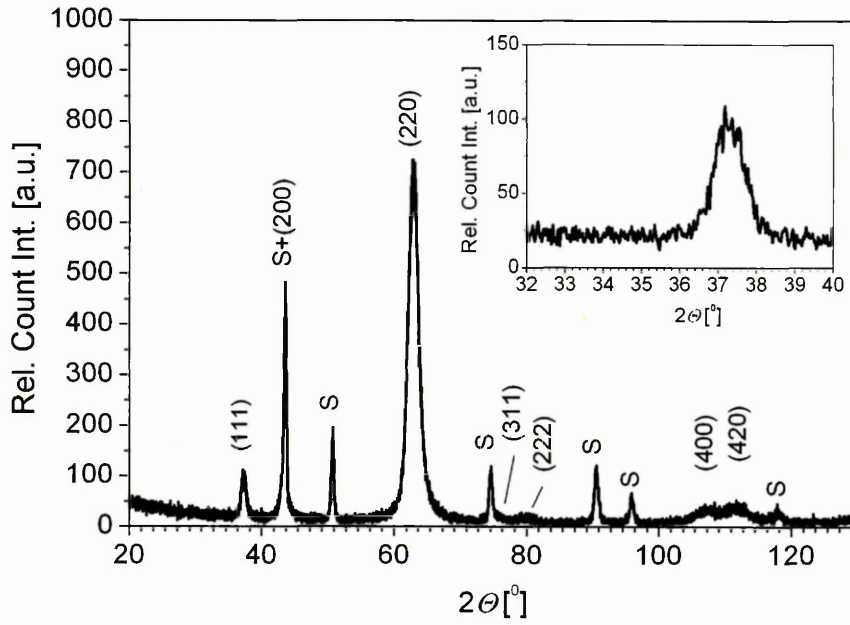
Fig. 5.4:  $\theta/2\theta$ -XRD scan of CrAlYN/CrN deposited at  $U_b = -75$  V with peak positions of standard CrN, fcc-AlN, Cr<sub>2</sub>N and hcp-AlN from the JCPCD database [141]

bility of  $\sim 77.2$ at% Al in a CrN lattice structure [115] or may be forced into the fcc-lattice of the nanolayer structure.

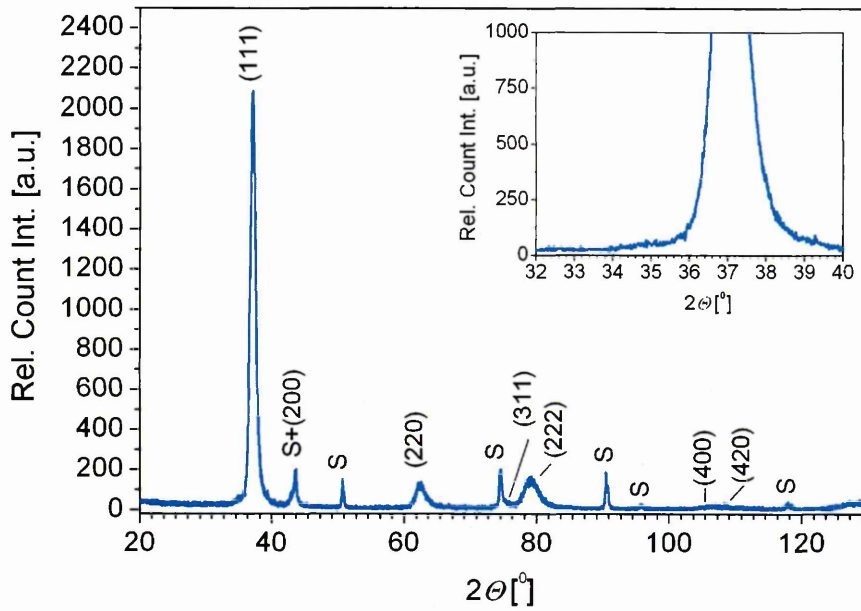
A comparison of the obtained  $\theta/2\theta$ -XRD diffractograms is shown in Fig. 5.5. All scans reveal a similar pattern of reflections as described above signifying a fcc single phase lattice structure for CrAlYN/CrN deposited in a range of  $U_b$  between -75 V and -150 V. Satellite peaks (see insert in Fig. 5.5(a)) due to a well defined multilayer structure are absent in coatings deposited at low  $U_b$ . Such satellite peaks of the (111) reflection, in contrast, are present when deposition was carried out at  $U_b \geq -120$  V (see insert in Fig. 5.5(c)). The presence of high order satellite peaks is usually attributed to a reduced interface roughness between the individual layers [172].

The unstressed lattice parameter  $a_0$  of CrAlYN/CrN, which gives an average lattice parameter in the combined CrN and CrAlYN layers, determined by GAXRD (see Sec. 3.2.2.5), is calculated to be  $0.415 \text{ nm} \pm 0.001 \text{ nm}$  and is not affected by the applied  $U_b$  during deposition. This value is slightly higher than those in single phase fcc-CrN (JCPCD 76-2494) with  $a_{0,\text{CrN}} = 0.414 \text{ nm}$  and fcc-AlN (JCPCD 25-1495) with  $a_{0,\text{AlN}} = 0.412 \text{ nm}$ , respectively.  $a_0$  was also larger than observed in stoichiometric arc-deposited CrAlN with  $a_{0,\text{CrAlN}} = 0.413 \text{ nm}$  and similar Cr/Al ratio [114]. A comparison with a theoretical lattice parameter  $a_{0,t}$ , which can be calculated from the weighted fraction of the individual components CrN, fcc-AlN and YN according to Vegard's law [173], is not possible. Prediction of  $a_{0,t}$  of CrAlYN/CrN would assume the knowledge of  $a_0$  of compounds with similar substoichiometry. Discrepancies between lattice parameters found by experiment and JCPCD standards may be related to the non-stoichiometry of CrAlYN/CrN. It is well known that the solid solution lattice parameter  $a_0$  of fcc-materials is a function of chemical composition [116, 121]. A constant  $a_0$  for CrAlYN/CrN in the investigated  $U_b$  range indicates a stable and constant chemical composition. This is in good agreement with the results obtained by SNMS (see Fig. 5.3).

XRD analysis reveals that both the chemical and the phase composition of CrAlYN/CrN are independent of variations in  $U_b$  in the range of -75 V to -150 V.

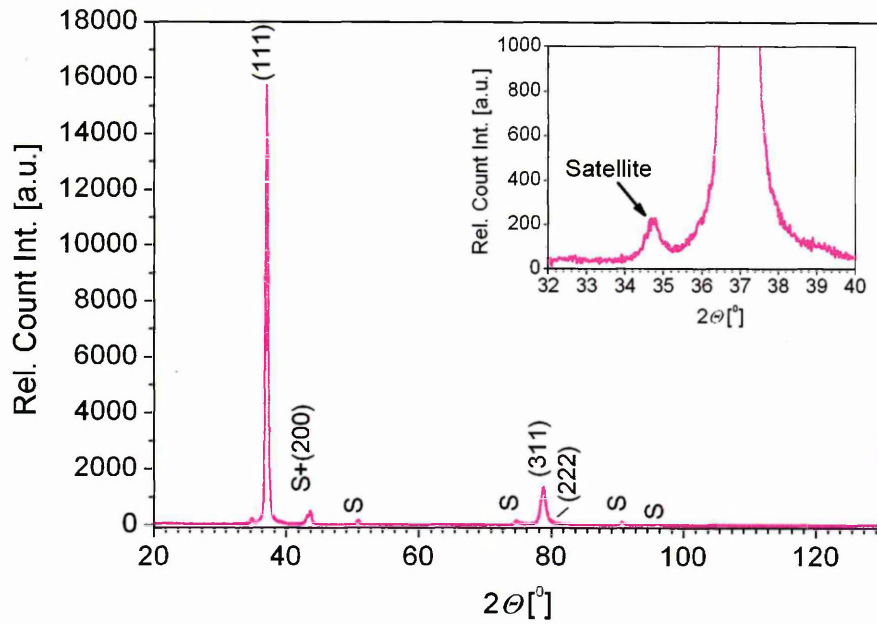


(a)  $U_b = -75$  V

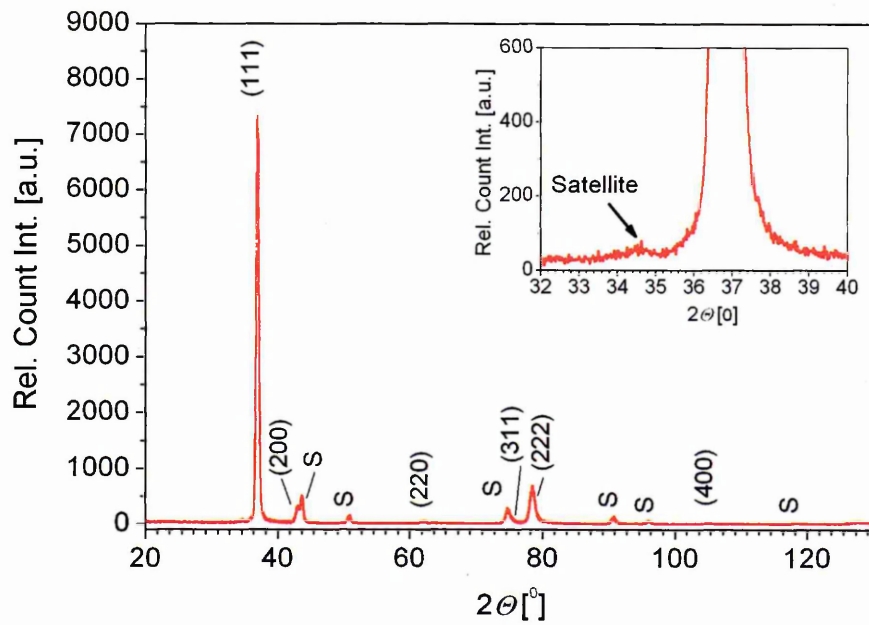


(b)  $U_b = -95$  V

Fig. 5.5:  $\theta/2\theta$ -XRD pattern of CrAlYN/CrN deposited at various bias voltages  $U_b$



(c)  $U_b = -120$  V



(d)  $U_b = -150$  V

Fig. 5.5: Continued

### 5.1.3 Texture Analysis

Texture factors were determined by  $\theta/2\theta$ -XRD analysis (see Sec. 3.2.2.3) and are compared in Fig. 5.6. A strong (110) fibre texture with a texture coefficient  $T_{(220)}^* = 4.89$  is observed in CrAlYN/CrN deposited at  $U_b = -75$  V. A mixed (110)/(111) texture occurs when increasing  $U_b$  to  $-95$  V with  $T_{(220)}^* = 1.12$  and  $T_{(111)}^* = 4.91$ . Increasing  $U_b$  further to  $-120$  V intensified the (111) texture with  $T_{(111)}^* = 5.62$ .

The texture evolution in nitride coatings is often explained in terms of a surface energy model [174, 175]. This model proposes that low surface energy crystal planes align normal to the growth direction if the surface energy is minimised. The lowest surface energy planes in B1-fcc structures are the (100) plane, followed by (110) and (111) with the next higher energies [175]. In case of CrAlYN/CrN grown at  $U_b = -75$  V, in contrast, the (110) texture is dominant. The growth of CrAlYN/CrN grown at  $U_b = -75$  V is therefore not governed by the surface energy as driving force. A different model [176] explains the growth of (110) textures by the incorporation of tetrahedrally located dumb-bell  $N_2$  molecules along the [220] direction of the lattice. This model is also assumed to be valid in TiAlN/CrN, TiAlN/VN and CrN [177]. In highly stressed coatings, the strain energy model is often applied to explain the texture development [178]. In this model, the lowest strain energy becomes the major driving force in determining the preferred growth orientation [178]. In this case, the lattice plane whose elastic modulus is minimum will be oriented parallel to the surface. In B1-fcc structures, this corresponds to the (111) plane. It is therefore likely that (111) texture in CrAlYN/CrN films deposited at higher  $U_b \leq -95$  V is controlled by the strain energy.

### 5.1.4 SEM Analysis

The surface topography of CrAlYN/CrN was studied by SEM with results shown in Fig. 5.7. When depositing CrAlYN/CrN at low  $U_b = -75$  V, a rough surface topography with cellular features is found (see Fig. 5.7(a)). This surface morphology is presumably attributed to columnar growth structures with dome-shaped

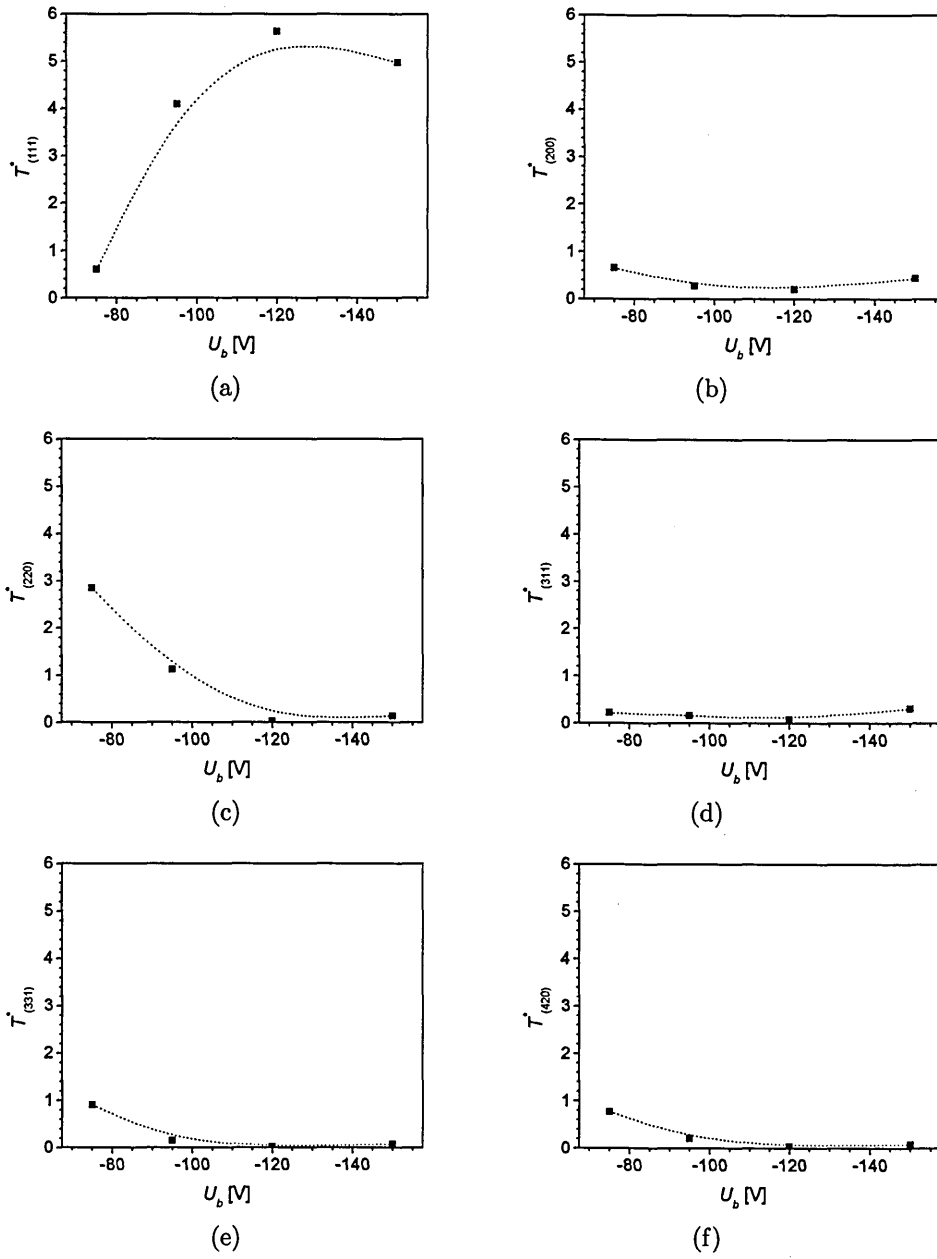
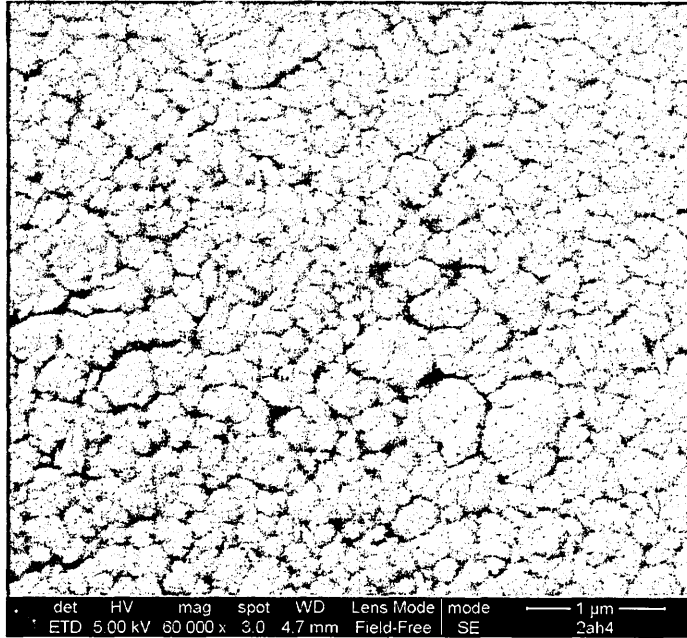
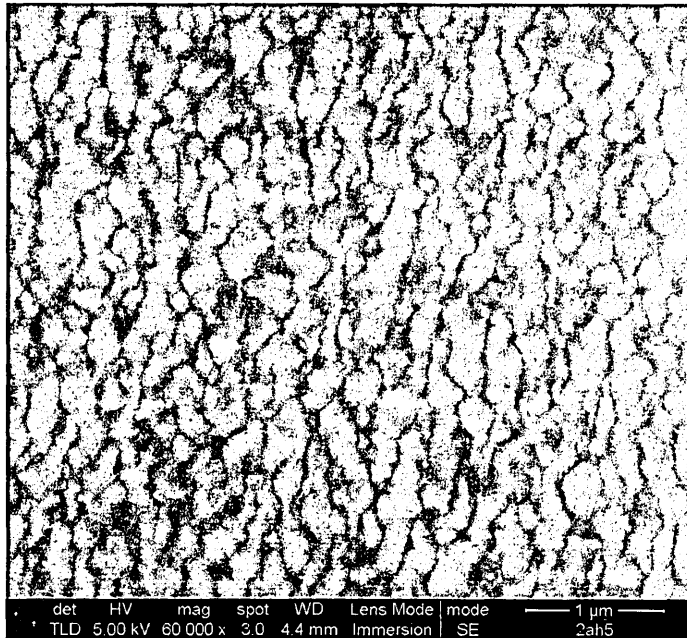


Fig. 5.6: Texture coefficients  $T^*$  as function of bias voltage  $U_b$

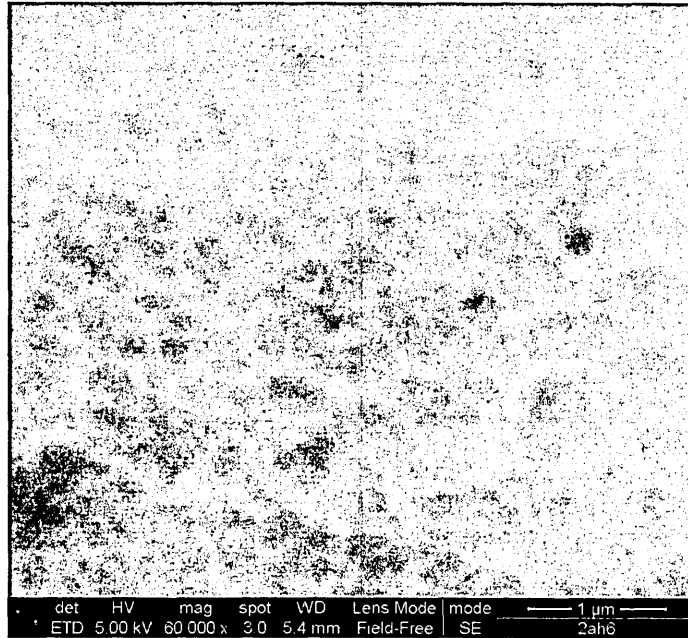


(a)  $U_b = -75$  V

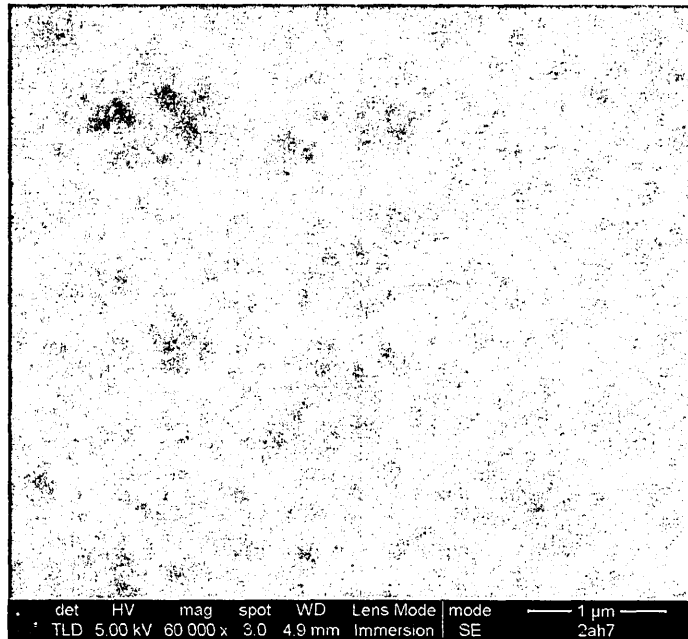


(b)  $U_b = -95$  V

Fig. 5.7: Surface morphology of CrAlYN/CrN deposited at varying bias voltages  $U_b$ , observed by SEM: The morphology changes from a surface with a network of interconnected cells to a smooth surface as  $U_b$  increases



(c)  $U_b = -120$  V



(d)  $U_b = -150$  V

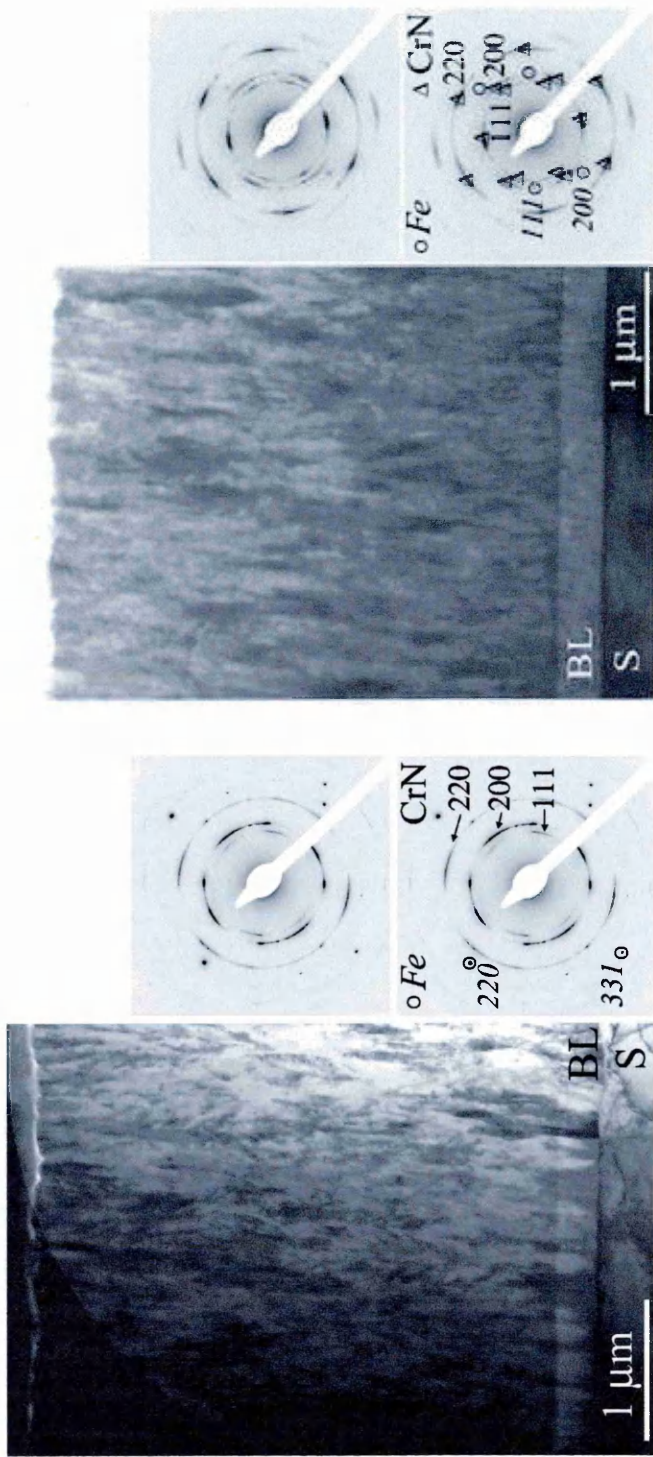
Fig. 5.7: Continued

column tops. The cell boundaries form a network of valleys which may arise from the so-called 'shadowing effect' (see Sec. 2.3) during the growth process. Similar structures are commonly observed in columnar PVD coatings grown at low  $U_b$  [179,180].

At  $U_b = -95$  V, the coating surface becomes smoother with a network of interconnected cells. This morphology suggests a structure which is grown in conditions of energetic ion bombardment which is not high enough to completely eliminate shadowing effects. The surface topology of CrAlYN/CrN deposited at  $U_b \geq -120$  V (see Fig. 5.7(c) and 5.7(d)) demonstrates a very flat surface with 2-dimensional equiaxial cells. Evidence for shadowing effects are not found. This morphology indicates an erosion-like effect due to re-sputtering as well as coating densification during the high-energy bombardment. A decreased coating roughness  $R_a$  as a result of an increase in  $U_b$  and, hence, in energetic particle bombardment were previously reported in CrN [100], TiAlN [180] and ZrAlN [179]. These data are in agreement with the results found in CrAlYN/CrN.

### 5.1.5 TEM Analysis

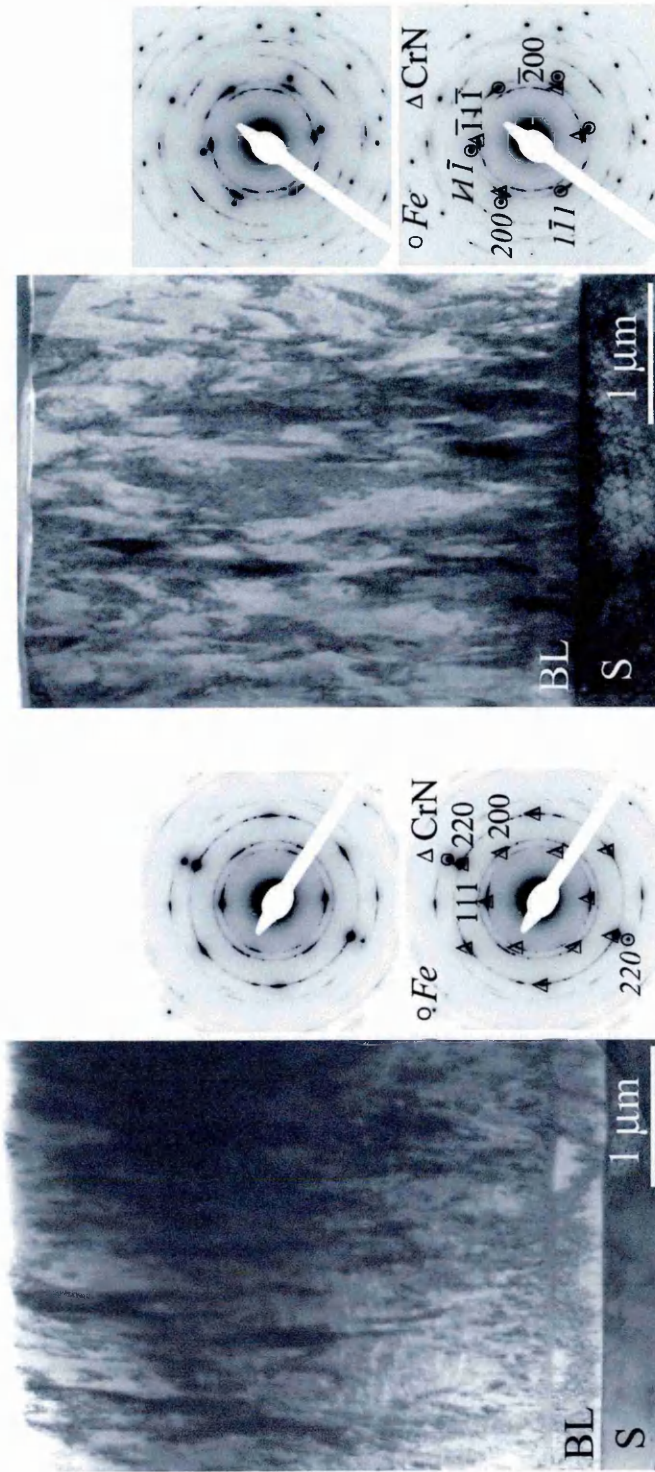
The effect of ion bombardment on the microstructure of CrAlYN/CrN deposited at different  $U_b$  was investigated by TEM analysis with (see Sec. 3.2.4). An overview of the coating cross-sections including corresponding SAD pattern is given in Fig. 5.8.



(a)  $U_b = -75$  V, polycrystalline columnar, (220) texture

(b)  $U_b = -95$  V, polycrystalline columnar, (111) texture

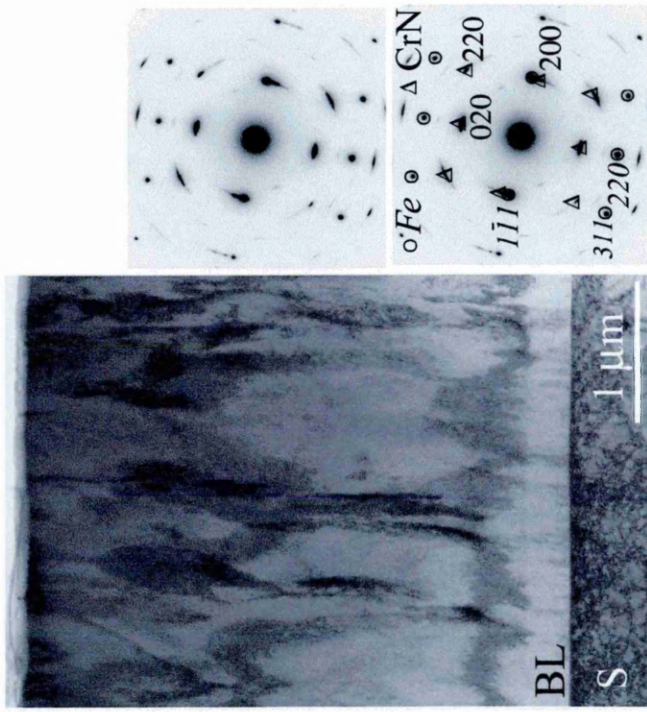
Fig. 5.8: BF-TEM micrographs and corresponding SAD pattern of CrAlYN/CrN deposited at various bias voltages  $U_b$  (The SAD pattern are taken from an area across the total coating cross-section including the underlying substrate crystal)



(c)  $U_b = -120$  V, polycrystalline columnar, partially single crystalline in the CrAlN base layer, (111) texture

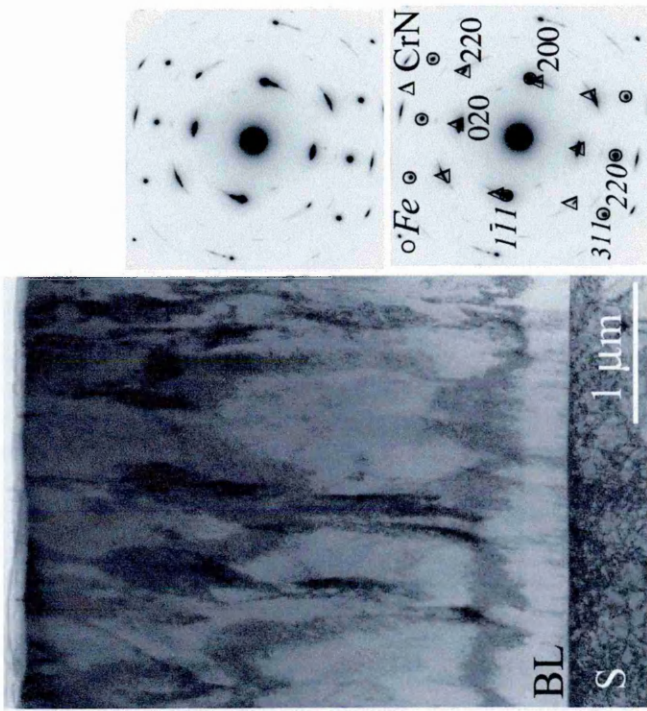
(d)  $U_b = -150$  V, polycrystalline columnar, (111) texture

Fig. 5.8: Continued



(e)  $U_b = -150$  V, single crystalline, (010) texture corresponding to substrate crystal

Fig. 5.8: Continued



(e)  $U_b = -150$  V, single crystalline, (010) texture corresponding to substrate crystal

Fig. 5.8: Continued

Fig. 5.9 shows details of CrAlYN/CrN deposited at  $U_b = -75$  V. Base layer and coating are polycrystalline with a columnar morphology. There are domains in which the columns of the multilayer are continuations of the base layer crystals. Columns grow in a competitive manner up to the column tops and exhibit dome-shaped column tops (see Fig. 5.10) and are responsible for the the surface morphology observed by SEM (see Fig. 5.7(a)). Voids and under-dense areas are present at the column boundaries (see Fig. 5.11). The presence of these low density zones can be related to atomic shadowing processes occurring in films which are prepared by low energetic ion bombardment [66]. The ion bombardment provided by  $U_b = -75$  V is not sufficiently high to densify the CrAlYN/CrN film and generates a structure which can be associated with a zone T structure in Messier's SZM [66].

SAD patterns were taken from different positions of the film cross-section (not shown). The mutual alignment of the diffraction spots of the CrAlN base layer and the underlying substrate crystal identify coating growth in local epitaxy or

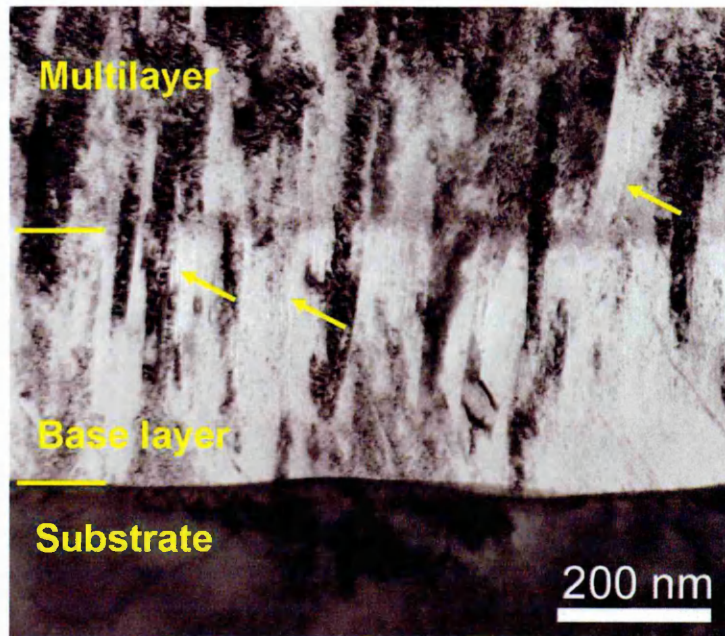


Fig. 5.9: BF-TEM micrograph of the CrAlN base layer region in CrAlYN/CrN deposited at  $U_b = -75$  V (Arrows indicate the presence of voids and under-dense areas)

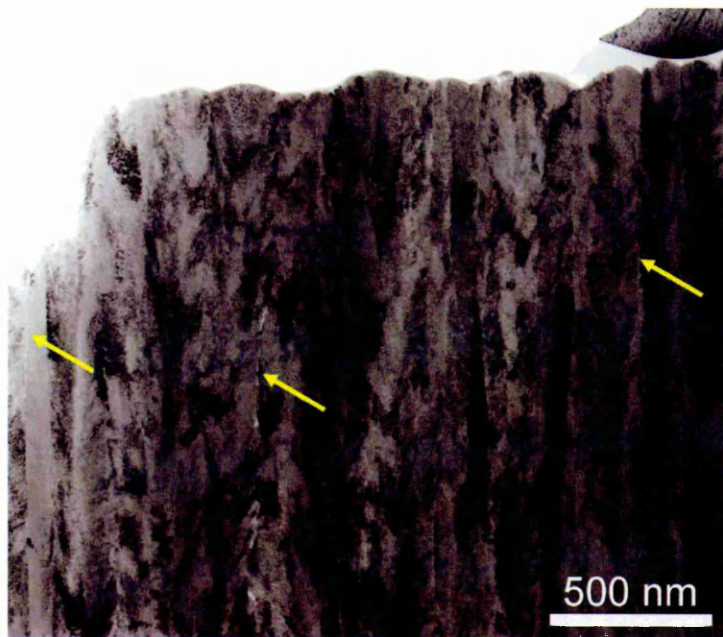


Fig. 5.10: BF-TEM micrograph of the upper part of CrAlYN/CrN deposited at  $U_b = -75 V$  with under-dense column boundaries and dome-shaped column tops (Arrows indicate the presence of voids and under-dense areas)

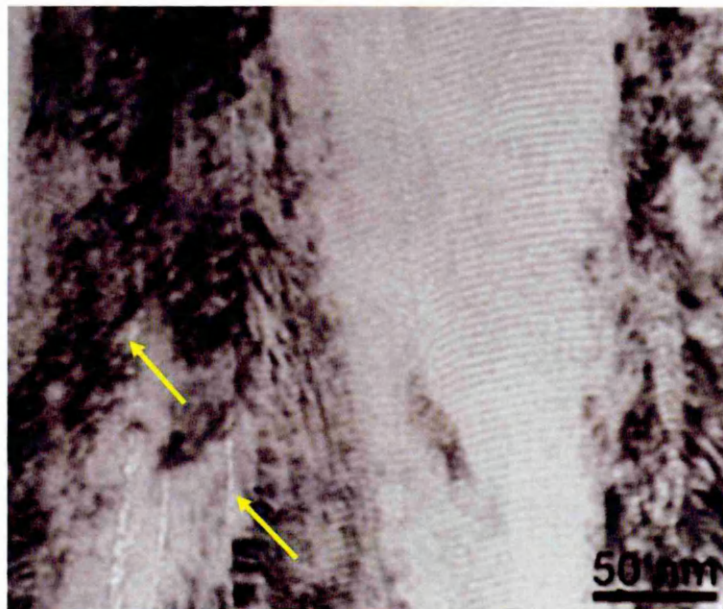


Fig. 5.11: BF-TEM micrograph of the curved nanolayers with under-dense column boundaries in CrAlYN/CrN deposited at  $U_b = -75 V$  (Arrows indicate low density regions at the column boundaries)

axiotaxy which is mainly governed by the orientation of the substrate crystal (see Sec. 4.1.2). The initial orientation gradually turns into an orientation determined by the deposition parameter  $U_b$ . The SAD pattern obtained across the coating section (see insert in Fig. 5.8(a)) indicates the development of the (220) texture. This is in good agreement with the results obtained by  $\theta/2\theta$ -XRD investigation (see Fig. 5.5(a)).

In CrAlYN/CrN deposited at  $U_b = -95$  V (see Fig. 5.8(b)), the base layer and coating are both polycrystalline columnar. The base layer columns continuously grow into the nanolayer region (see Fig. 5.12). The column boundaries are dense and free of inter-columnar voids. The nanolayers (see Fig. 5.13) are grown slightly convex evolving into dome-shaped column tops (see Fig. 5.8(b)). Bombardment with higher energetic particles causes the observed coating densification and eliminates inter-columnar voids. The emerging morphology may be classified as a zone 2 structure according to Messier's SZM [66].

Analysis of the SAD pattern (not shown) reveals local axiotactic or epitactic growth of the base layer on large substrate surface areas with an increased lateral

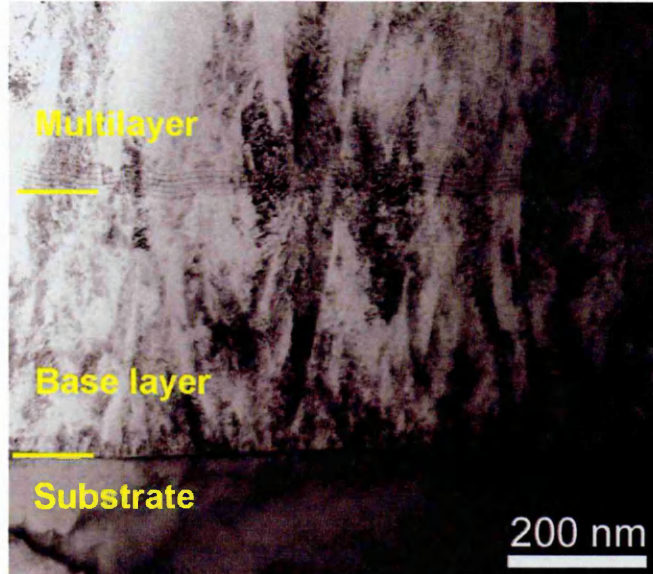


Fig. 5.12: BF-TEM micrograph of the CrAlN base layer region in CrAlYN/CrN deposited at  $U_b = -95$  V with dense column boundaries

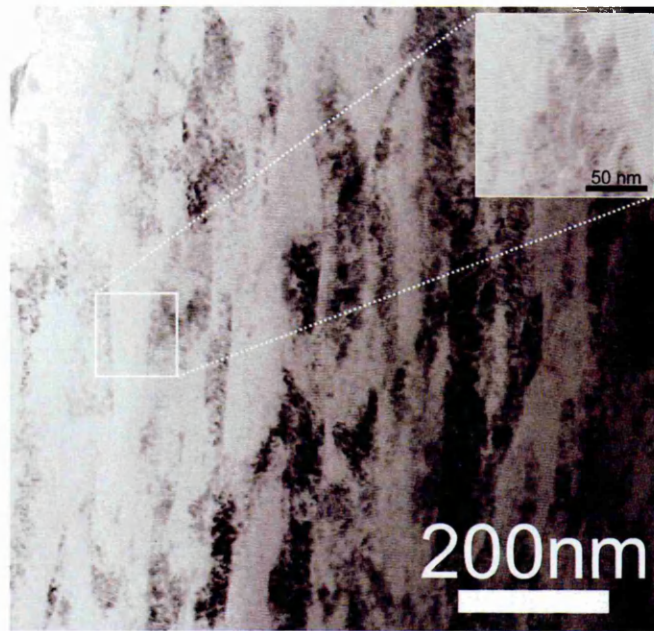


Fig. 5.13: BF-TEM micrograph of the slightly curved nanolayers in CrAlYN/CrN deposited at  $U_b = -95$  V with dense column boundaries

extent of the epitaxial growth compared to the base layer growth at  $U_b = -75$  V. The SAD pattern taken from the middle of the coating, containing both diffraction spots from substrate and coating, suggest a (111) crystallographic orientation (see insert in Fig. 5.8(b)). This is in good agreement with the XRD results and indicates a transition in growth mechanism energy according to the strain energy model [175].

As  $U_b$  during deposition is increased to -120 V, a change in microstructure becomes obvious (see Fig. 5.8(c)). The base layer contains both columnar as well as large single crystal domains which strongly pronounced epitaxial growth (see Fig. 5.14). A BF-TEM image of the interface with the corresponding SAD pattern (see Fig. 5.15) in a selected single crystal CrAlN clearly reveals the alignment of diffraction spots and identifies an epitaxial growth relationship between substrate and CrAlN. The nanoscale multilayer (see Fig. 5.16) grows in dense, columnar morphology. The layers are nearly parallel to the interface with only a minimal curvature. The individual columns are large with nearly flat column tops. An indication for increased column sizes is also given by the sharp and well defined

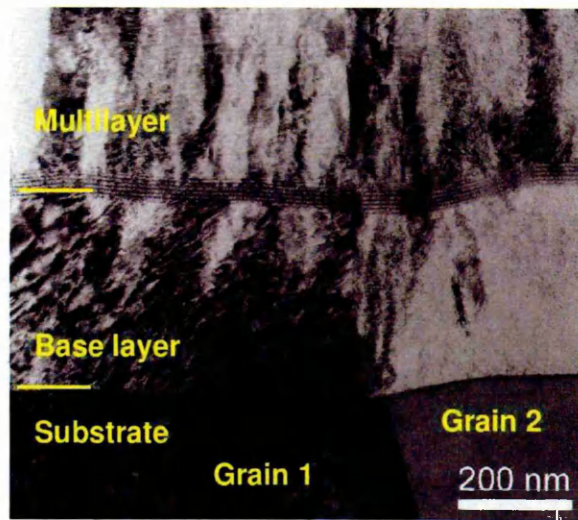


Fig. 5.14: BF-TEM micrograph of the CrAlN base layer in CrAlYN/CrN deposited at  $U_b = -120$  V: CrAlN grown on substrate grain 1 reveals single crystalline growth whereas CrAlN grown on substrate grain 2 grows in a polycrystalline structure

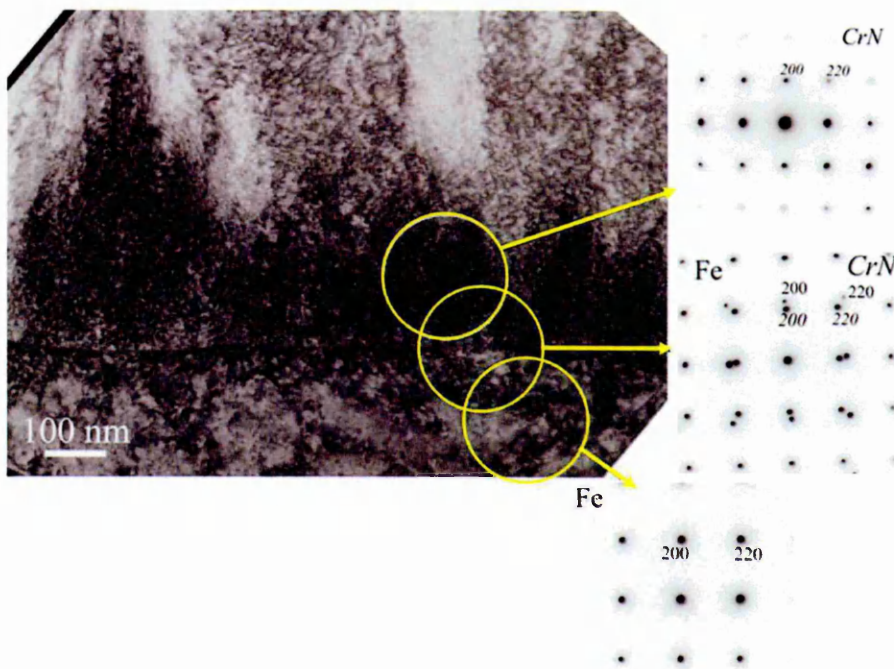


Fig. 5.15: BF-TEM micrograph of the single crystalline CrAlN base layer deposited at  $U_b = -120$  V with the corresponding SAD pattern of the substrate/base layer interface indicating local epitaxial growth

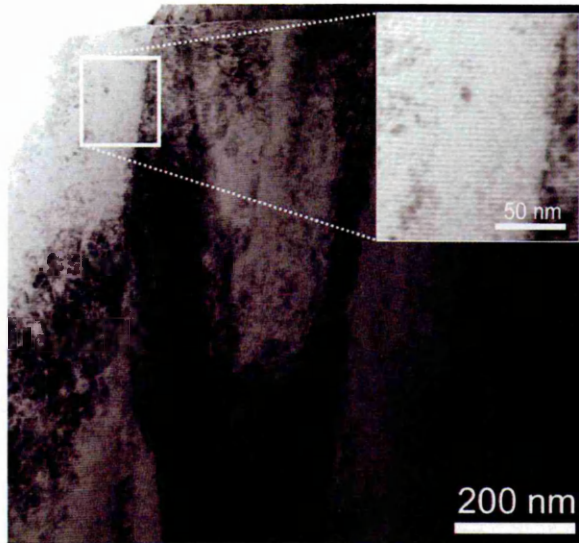


Fig. 5.16: BF-TEM micrograph of the nanolayers of CrAlYN/CrN deposited at  $U_b = -120$  V: The nanolayers are curvature-free and the column boundaries are dense

diffraction peaks in the  $\theta/2\theta$ -XRD scan (see Fig. 5.5(c)). The dense and void-free coating morphology compares to a zone 2 structure in Messier's SZM [66] and is obtained by high energetic ion bombardment.

When applying  $U_b = -150$  V, a mixed coating structure with either columnar domains (see Fig. 5.8(d)) or single crystalline domains (see Fig. 5.8(e)) is found. The CrAlN base layer grains grow with high quality epitaxy fitting to the size and orientation of the local substrate crystal (see Fig. 5.17). In the columnar domains, these base layer grains continue growth into a polycrystalline multilayer with (111) preferential orientation which is governed by  $U_b$  (see insert in Fig. 5.8(d)). New crystals, also with (111) orientation, may grow as a result of repeated, ion bombardment induced re-nucleation (see Fig. 5.18). Re-nucleation points are found at various positions over the whole film thickness. In the single crystalline domains, in contrast, the coating grows as a single crystal from the interface (see Fig. 5.8(e)). Re-nucleation does not take place at a higher thickness. The original orientation of base layer at the substrate/base layer interface is preserved and governed only by the alignment of the substrate crystal (see SAD pattern

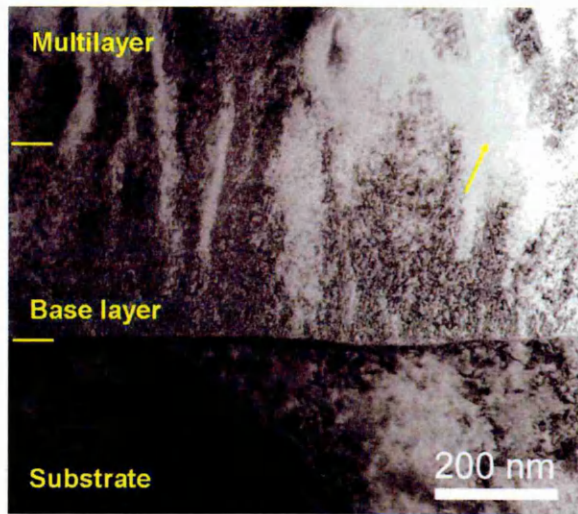


Fig. 5.17: BF-TEM micrograph of the single crystalline CrAlN base layer region in CrAlYN/CrN deposited at  $U_b = -150\text{ V}$  transforming into a single crystalline multilayer structure

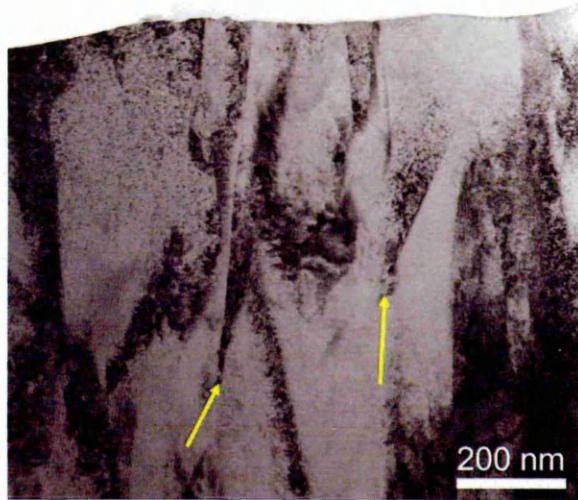


Fig. 5.18: BF-TEM micrograph of the upper part of CrAlYN/CrN deposited at  $U_b = -150\text{ V}$ : Re-nucleation takes place with the growth of new crystals at a higher coating thickness (Arrows indicate re-nucleation points)

in Fig. 5.8(e)). The nanoscale layers (see Fig. 5.19) are curvature-free, clearly defined with sharp interfaces. These structures are found independently of the single or polycrystalline growth character of the coating and give strong evidence for high coating densification due to energetic particle bombardment.

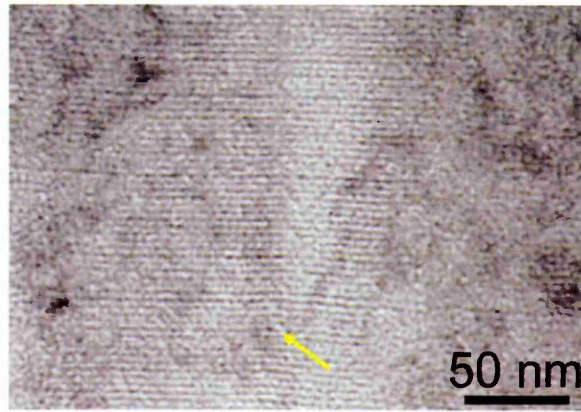


Fig. 5.19: BF-TEM micrograph of the nanolayers in two different columns of CrAlYN/CrN deposited at  $U_b = -150$  V: The boundaries are highly dense and the nanolayers are curvature-free

The texture analysis (see Fig. 5.6(a)) reveals a slight decrease in  $T_{(111)}^*$  when increasing  $U_b$  from -120 V to -150 V. The TEM additionally shows the presence of single crystal grains which grow accordingly to the crystallographic orientation of the substrate grain (see Fig. 5.8(e)). It is believed that these single crystal domains with rather random orientation contribute to the slight decrease in  $T_{(111)}^*$  found in CrAlYN/CrN deposited at  $U_b = -150$  V.

To conclude, the film microstructure of CrAlYN/CrN is found to be highly affected by changing the ion energy during deposition by applying  $U_b$ . Tab. 5.1 directly summarises these results as function of  $U_b$ .

The ball-cratering thickness test (see Sec. 3.3.1) gives a measure of the coating thickness  $\Delta$  which linearly decreases from  $5.3 \mu\text{m}$  to  $4.1 \mu\text{m}$  as  $U_b$  is increased (see Fig. 5.20). This reduction in coating thickness can be related to the observed coating densification as well as increased re-sputtering of atoms already deposited at the substrate. These results are in well agreement with those obtained from cross-sectional TEM investigations (see Fig. 5.8) which confirm thinner coatings when deposition takes place at high  $U_b$ .

Tab. 5.1: Microstructure and texture of CrAlYN/CrN as function of substrate bias  $U_b$

Base layer	-75 V	-95 V	-120 V	-150 V
Microstructure	poly-crystalline columnar		poly-crystalline columnar + single crystalline	
	voided		void-free	

Coating	-75 V	-95 V	-120 V	-150 V
Microstructure	poly-crystalline, columnar, dome-shaped		poly-crystalline, columnar + single crystalline, flat	
	voided		void-free	

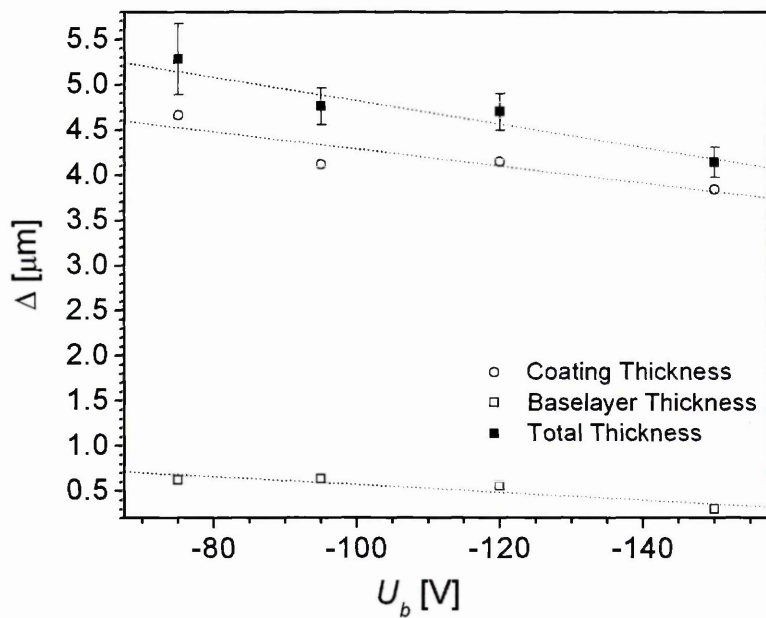


Fig. 5.20: Coating thickness  $\Delta$  as function of the substrate bias voltage  $U_b$ , determined by the ball-cratering test

### 5.1.6 Nanoscale Bi-Layer Periodicity

LA-XRD scans (see Sec. 3.2.2.4) were performed to determine the nanolayer periodicity  $\Lambda$  (see Fig. 5.21(a)). 1st order reflections at  $2\theta = 2.1^\circ$  and, additionally, 2nd order reflections at  $2\theta = 4.1^\circ$  are present in all coatings. These reflections become sharper and have a higher intensity as  $U_b$  is increased. When  $U_b$  is increased to -150 V, a third reflection appears in the scan at  $2\theta = 2.9^\circ$ . The appearance of a third reflection clearly gives evidence that, as  $U_b$  is increased, the interfaces between the individual component layers in the film become flatter and sharper. The observed peak itself may result from diffraction of the incident beam at layers that do not coincide with the combination CrAlYN/CrN as a bi-layer but may result from reflection of a different layer combination. Assuming that the reflection represents a 2nd order peak, the correlated total thickness would be  $\sim 6$  nm. In Sec. 5.3.1, the thickness ratio of the individual layers CrN and CrAlYN in CrAlYN/CrN (Cr target power  $P_{Cr} = 8$  kW) is calculated to be 0.95. Assigning these data to CrAlYN/CrN deposited at  $U_b = -150$  V, CrAlYN and CrN have a roughly equal thickness of  $\sim 2$  nm. The observed reflection in the LA-XRD may result from one of two possible reflecting systems, namely CrAlYN/CrN/CrAlYN or CrN/CrAlYN/CrN, which both have an approximative thickness of  $\sim 6$  nm.

The nanolayer periodicity  $\Lambda$  (see Fig. 5.21) is calculated to be  $\sim 4$  nm in all coatings. A clear indication for a reduced  $\Lambda$ , as expected from reduced coating thickness  $\Delta$  (see Fig. 5.20, measured by ball-cratering), cannot be confirmed and may be due to limitations of the LA-XRD method when analysing curved surfaces.

### 5.1.7 Residual Stress

The stressed lattice parameter  $a_{0,\perp}$  was measured from the  $\theta/2\theta$ -XRD diffractogram and gives the lattice constant for planes which are normal to the coating surface (see Sec. 3.2.2.2).  $a_{0,\perp}$  is found to steadily expand from 0.416 nm at  $U_b = -75$  V to 0.422 nm at higher  $U_b$  of -150 V (see Fig. 5.22). The lattice expansion normal to the surface may indicate the presence of compressive stresses in the coating plane.

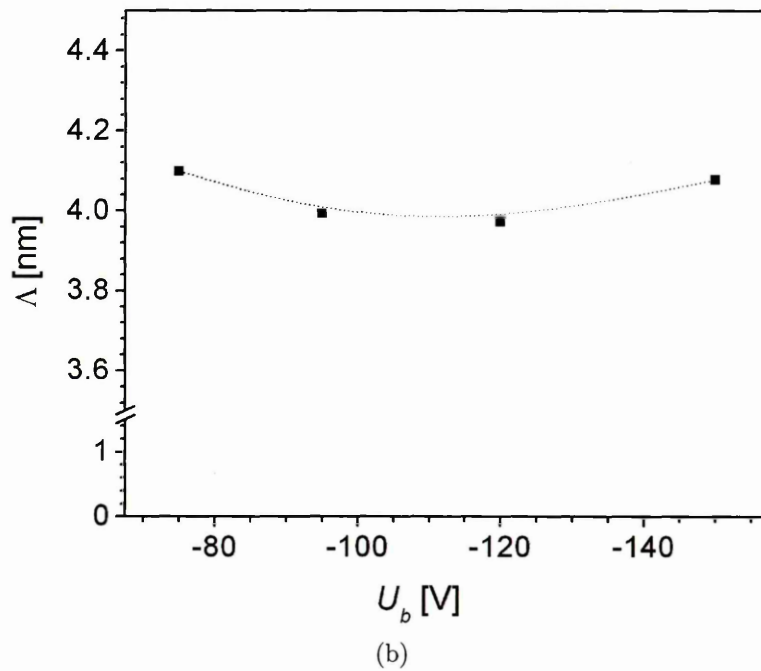
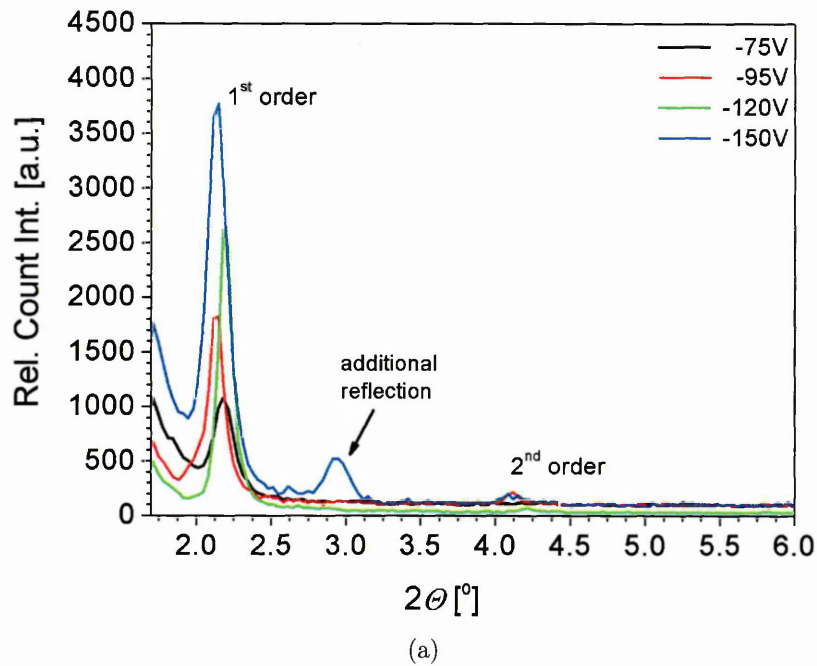


Fig. 5.21: Nanoscale bi-layer thickness  $\Lambda$  of CrAlYN/CrN deposited at various bias voltages  $U_b$ , investigated by LA-XRD: (a) LA-XRD scans with high order reflections from the nanolayers and (b) Bi-layer periodicity  $\Lambda$

The stress state in the coatings was analysed by the XRD analysis according to the  $\sin^2(\Psi)$  method (see Sec. 3.2.2.5). From this, a plot of  $a_{\Psi(hkl)} - \sin^2(\Psi)$  is obtained. A positive slope of this plot signifies tensile stresses whereas a negative slope represents compressive stresses in the coating. The negative slope of this plot obtained from the investigated CrAlYN/CrN indicates that the nanoscale multilayer coatings are in a compressive stress state (see Fig. 5.23(a)). Medium compressive stresses  $\sigma$  in a range of -3.3 GPa at  $U_b = -75$  V and -9.5 GPa at  $U_b = -150$  V are present in the investigated coatings (see Fig. 5.23(b)). This strong increase in  $\sigma$  of  $\sim 300\%$  may be attributed to the fact that the coating is composed mainly of light elements. High residual stress levels are generally associated with higher defect densities induced by energetic ion bombardment [57]. During this bombardment two competing processes occur with (i) an energy transfer to condensing atoms and (ii) the generation of defects. Thin films containing light atoms (Cr, Al: atomic weight  $< 52$  amu) require less activation energy for surface diffusion which is necessary to move the atoms to their equilibrium position [181]. The excess energy is therefore available for defect formation and can generate high

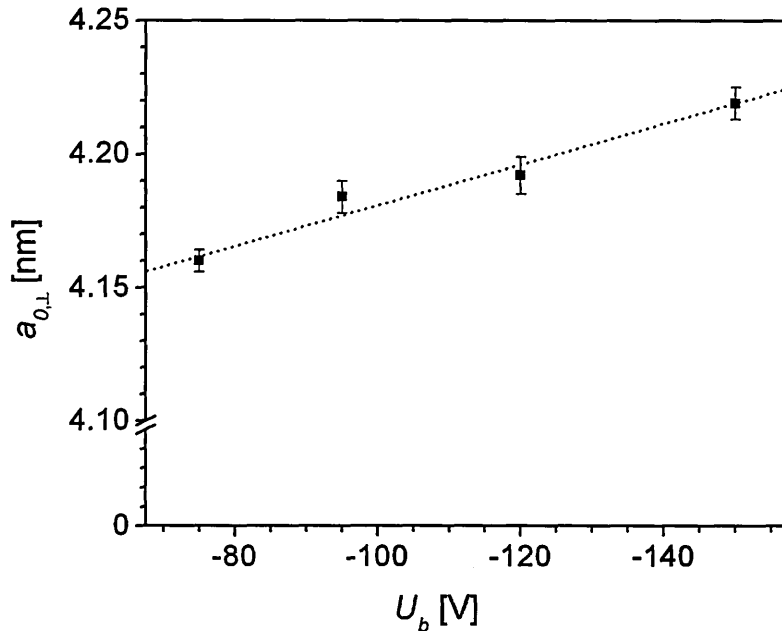


Fig. 5.22: Stressed lattice parameter  $a_{0,\perp}$  of CrAlYN/CrN deposited at various bias voltage  $U_b$

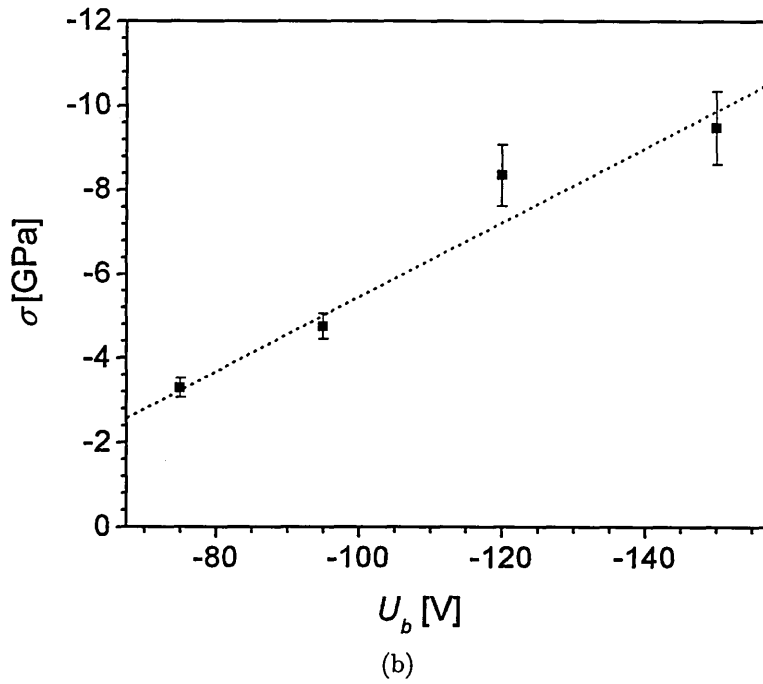
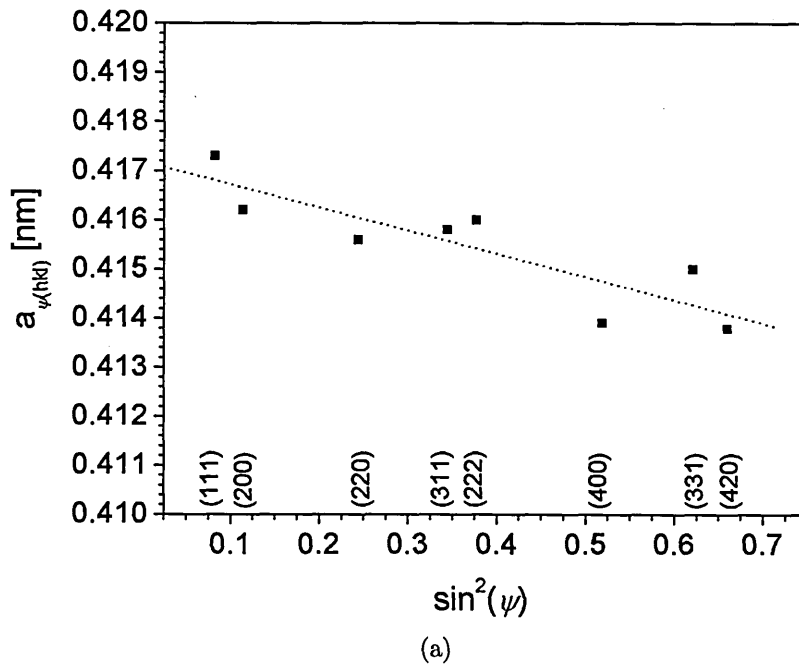


Fig. 5.23: (a) Typical  $\sin^2(\Psi)$  plot (CrAlYN/CrN grown at  $U_b = -75$  V) and (b) Residual stress  $\sigma$  of CrAlYN/CrN deposited at various bias voltages  $U_b$

defect densities and, hence, high residual stress levels.

### 5.1.8 Hardness and Young's Modulus

The nano-hardness  $H_{IT}$  (see Sec. 3.3.5.2) is at a level of 35 GPa to 52 GPa and rises strongly as  $U_b$  is increased (see Fig. 5.24(a)). Additionally, a similar rise in hardness from HK 3170 to HK 4290 (see Fig. 5.24(b)) is observed when analysing the Knoop hardness  $HK_{0.025}$  (see Sec. 3.3.5.1).  $H_{IT}$  of CrAlYN/CrN grown at  $U_b \geq -95$  V exceeds 40 GPa. Coatings with higher hardness are often categorised as superhard coatings [87]. It can therefore be concluded that CrAlYN/CrN grown at  $U_b \geq$  are superhard coatings.

Several strengthening mechanisms, all providing obstacles for dislocation movements, contribute to enhanced hardness of CrAlYN/CrN. Growth-defect hardening is one such growth mechanism [182]. The high energetic ion bombardment induces high defect densities. One indication for these defects are high residual stresses (see Fig. 5.23). These defects also provide obstacles for dislocation movements [182] and therefore enhance the hardness of CrAlYN/CrN. Microstructural changes caused by variations in  $U_b$  during deposition also affect  $H_{IT}$ . At high  $U_b$ , the nanolayer structure becomes more pronounced and less wavy (see Fig. 5.19). These better-defined interfaces, with sharp transitions between the individual layers, hinder dislocation movements more effectively [14] and contribute to the remarkable increase in hardness.

The elastic properties were determined by means of Young's modulus  $E$  (see Sec. 3.3.5.2).  $E$  is found with  $380 \pm 25$  GPa in all CrAlYN/CrN coatings analysed in the range of  $U_b = -75$  V to  $-150$  V.

### 5.1.9 Adhesion

The substrate/coating adhesion was determined by means of the critical load  $L_C$  obtained from scratch testing (see Sec. 3.3.3.1).  $L_C$  exceeds high levels of 45 N in all coatings (see Fig. 5.25). The low bias CrAlYN/CrN ( $U_b = -75$  V) reveals a high  $L_C$  value of 61 N which linearly decreases to 45 N at high  $U_b = -150$  V.

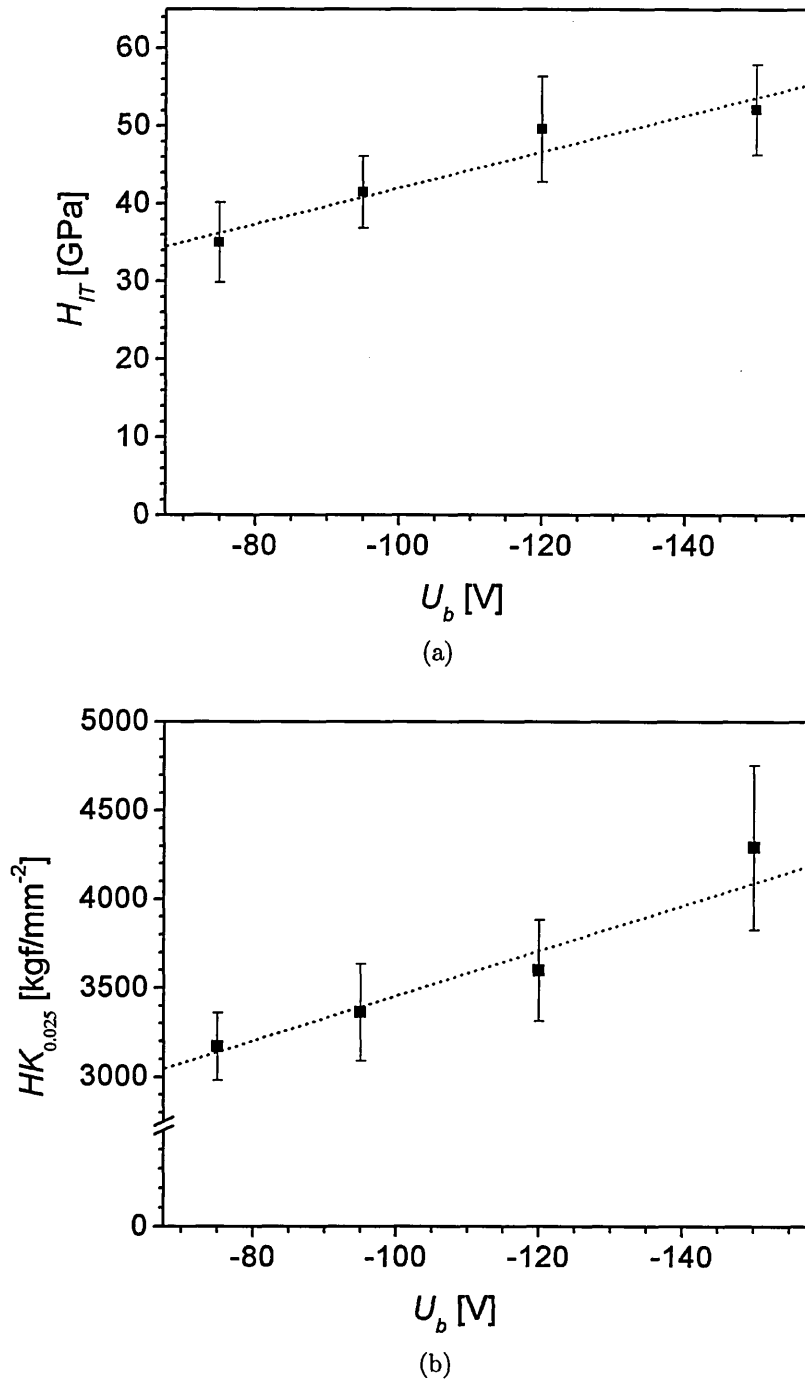


Fig. 5.24: Hardness of CrAlYN/CrN deposited at various substrate bias voltages  $U_b$ : (a) Nano-hardness  $H_{IT}$  and (b) Microhardness  $HK_{0.025}$

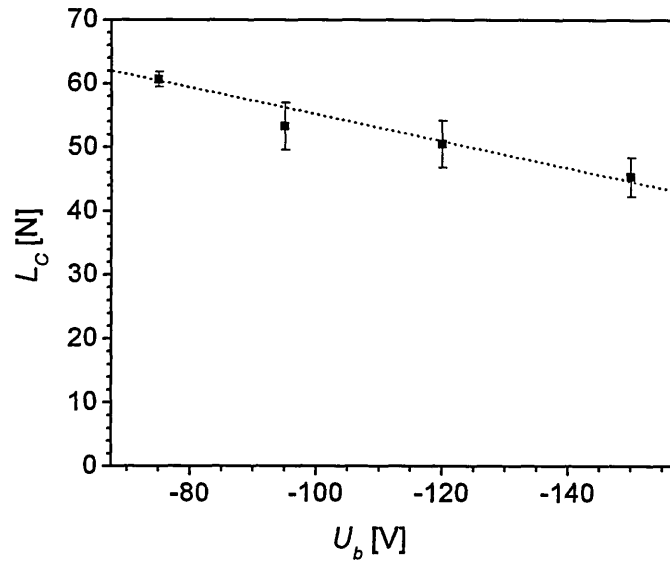


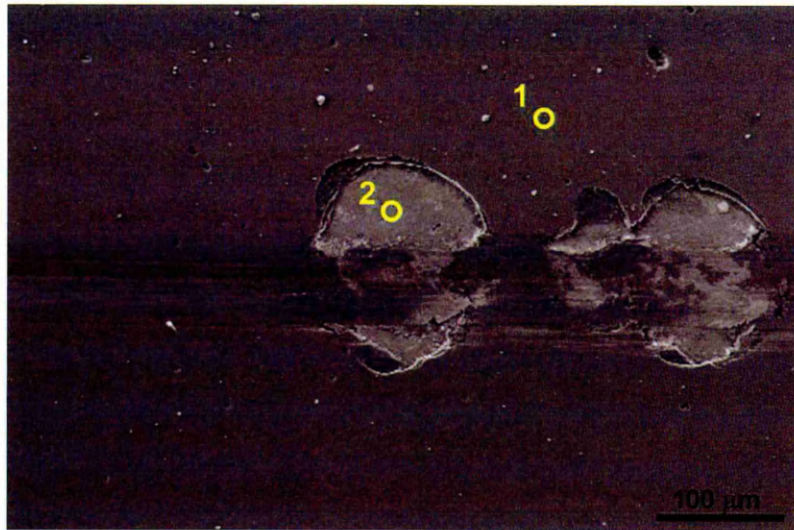
Fig. 5.25: Critical Load values  $L_C$  as a function of bias voltage  $U_b$

Fig. 5.26(a) shows, for CrAlYN/CrN deposited at  $U_b = -75$  V, a SEM image of a typical scratch scar produced by the moving stylus. EDS analysis in an area in which chipping failure occurred exhibits only the presence of substrate elements and confirms adhesive thin film failure. Similar results are found in all analysed coatings.

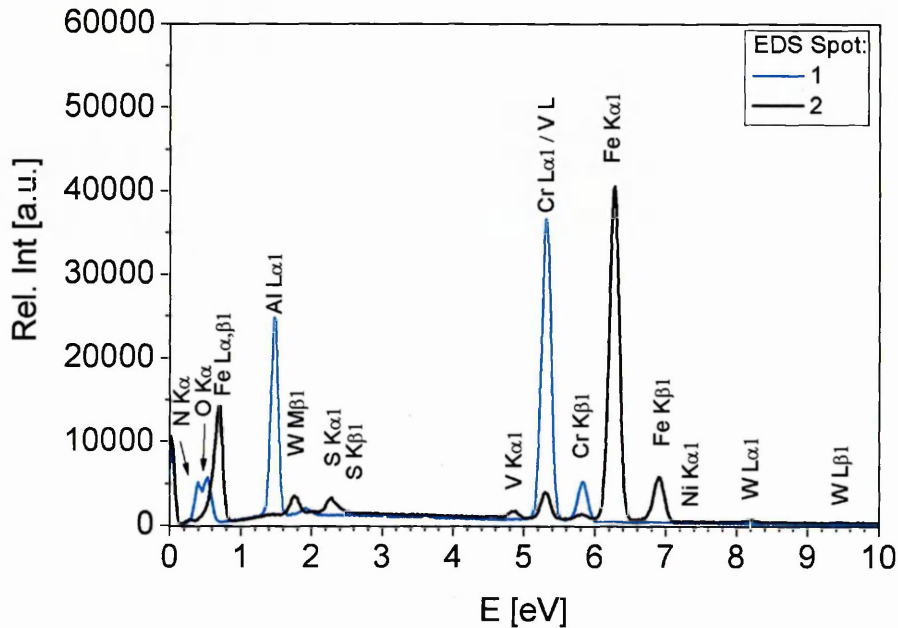
Further adhesion measurements were carried out in accordance to the Rockwell C indentation test (see Sec. 3.3.3.2). Fig. 5.27 presents the Rockwell C indents for CrAlYN/CrN deposited at various  $U_b$ . The imprint of CrAlYN/CrN grown at  $U_b = -75$  V reveals cracking of the coating at the rim (see Fig. 5.27(a)). As  $U_b$  is steadily increased, first spallation of coating segments takes place in the medium  $U_b$  coatings ( $U_b = -95$  V (see Fig. 5.27(c)) and  $-120$  V (see Fig. 5.27(e)). Further increase in  $U_b$  results in complete coating spallation at the rim of the indent (see Fig. 5.27(g)). The adhesion grades are classified as HF1 to HF4 with increasing  $U_b$ .

The results of scratch adhesion testing and Rockwell indentation are consistent and show a similar trend of degrading substrate/coating adhesion as  $U_b$  is increased.

Excellent adhesion with values as high as  $L_C = 61$  N and a HF1 classification



(a)



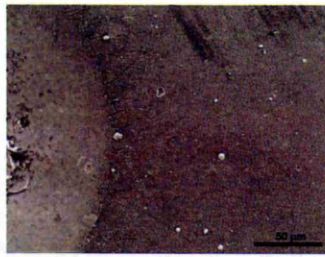
(b)

Fig. 5.26: Analysis of adhesive failure in CrAlYN/CrN grown at  $U_b = -75$  V on a HSS substrate: (a) scratch scar with coating spallation at the rim and (b) EDS spectra taken from the positions indicated in (a)

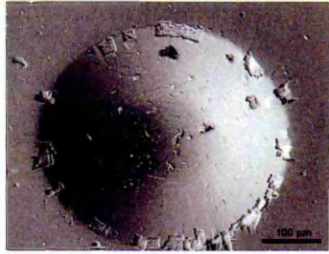
are obtained as result of the HIPIMS etching pre-treatment. Residual stresses  $\sigma$  as high as -9.5 GPa (see Fig. 5.23(b)) can induce large forces at the substrate/base layer interface and, in turn, reduce the level of additional external loading that



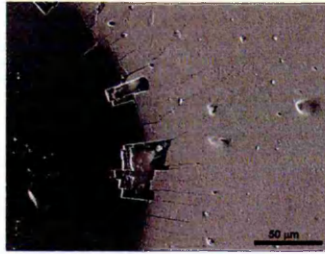
(a)  $U_b = -75$  V



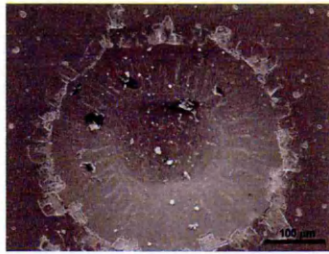
(b)  $U_b = -75$  V, zoom of (a)



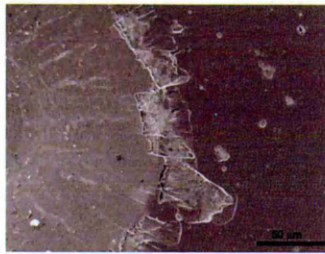
(c)  $U_b = -95$  V



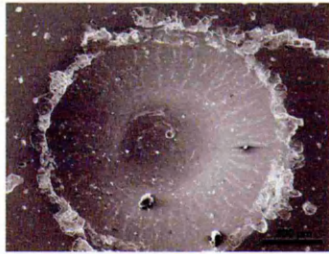
(d)  $U_b = -95$  V, zoom of (c)



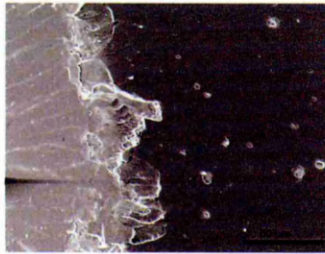
(e)  $U_b = -120$  V



(f)  $U_b = -120$  V, zoom of (e)



(g)  $U_b = -150$  V



(h)  $U_b = -150$  V, zoom of (g)

Fig. 5.27: Rockwell indentation imprints of CrAlYN/CrN deposited at various bias voltages  $U_b$

can be tolerated by the coating. In this case, delamination occurs and, as a result, the adhesion decreases.

### 5.1.10 Friction and Dry Sliding Wear

The friction behaviour of CrAlYN/CrN was assessed by testing the samples on a pin-on-disk equipment (see Sec. 3.3.4).

Fig. 5.28 compares the friction coefficients of CrAlYN/CrN. The friction coefficient  $\mu$  is in a range of 0.43 to 0.55 and varies only slightly with  $U_b$ . The dry sliding wear coefficient  $k_S$  (see Fig. 5.29(a)) signifies generally low wear rates  $k_S$  in a range of  $2.7 \times 10^{-16}$  to  $3.7 \times 10^{-17} \text{ m}^3 \text{N}^{-1} \text{m}^{-1}$ . Strongly decreasing wear rates  $k_S$  are observed as  $U_b$  is increased. The wear rate  $k_{CP}$  of the  $\text{Al}_2\text{O}_3$  counterpart (see Fig. 5.29(b)) is in a range of  $10^{-14} \text{ m}^3 \text{N}^{-1} \text{m}^{-1}$  and with this at least two orders of magnitude higher than  $k_S$  of the coating.

The friction curves of CrAlYN/CrN deposited at different  $U_b$  demonstrate the evolution of  $\mu$  up to high sliding distances (see Fig. 5.30). After a short running

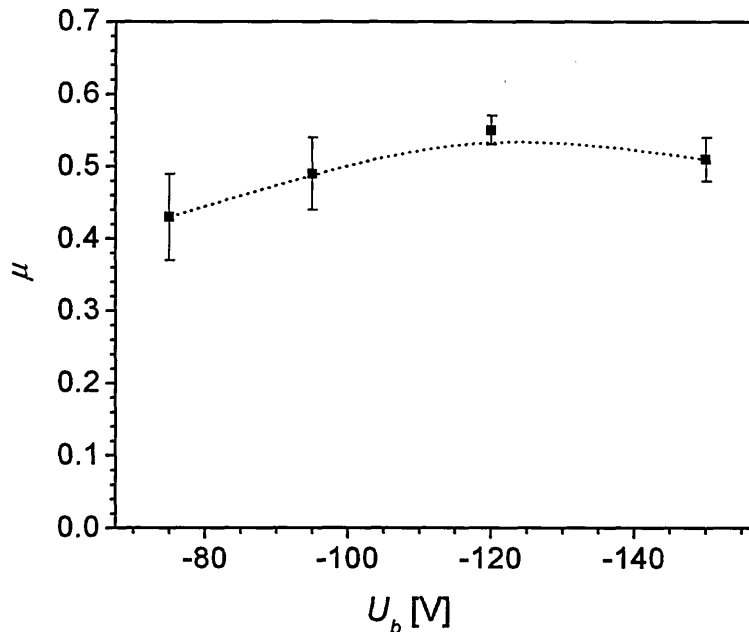


Fig. 5.28: Friction coefficient  $\mu$  of CrAlYN/CrN as function of substrate bias voltage  $U_b$

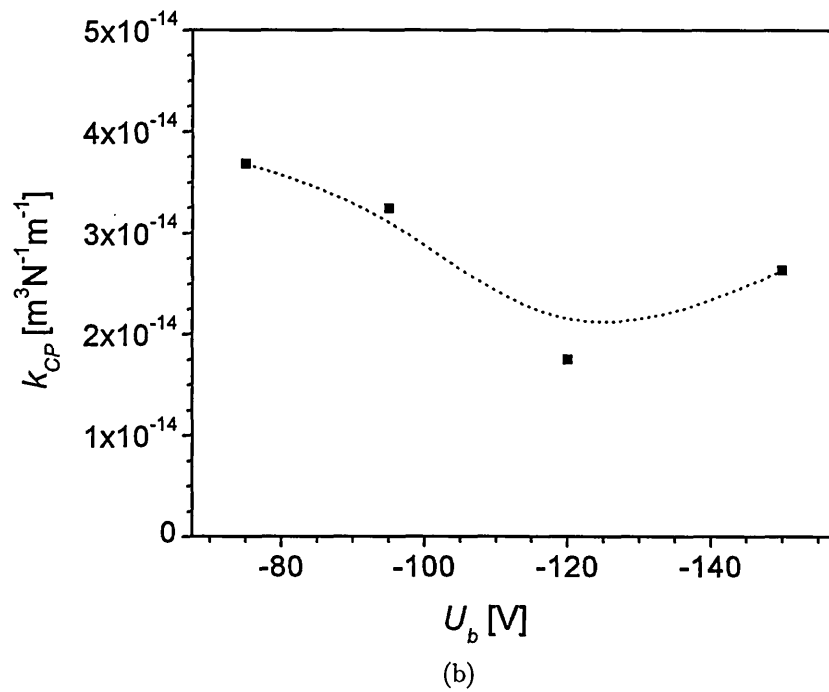
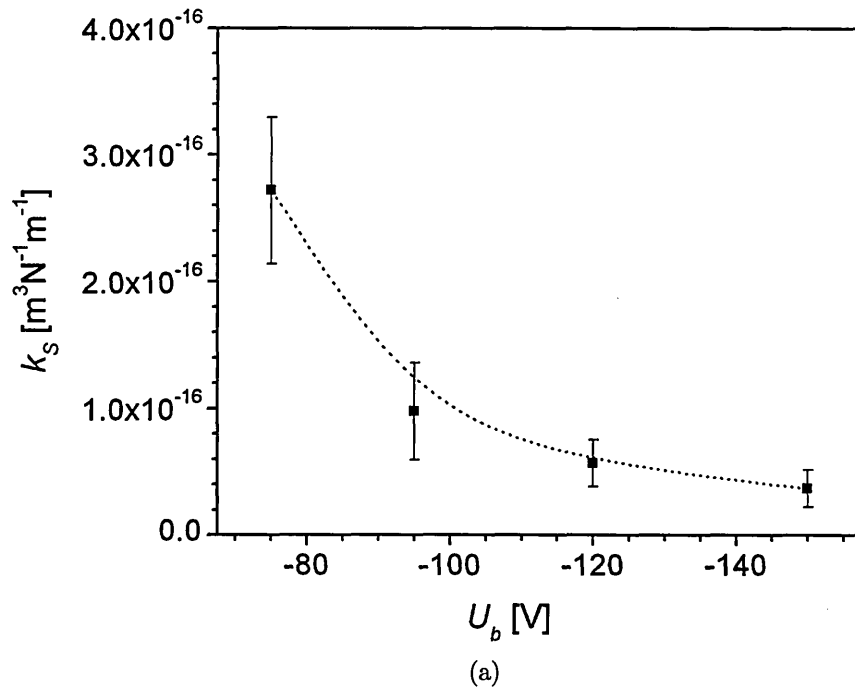
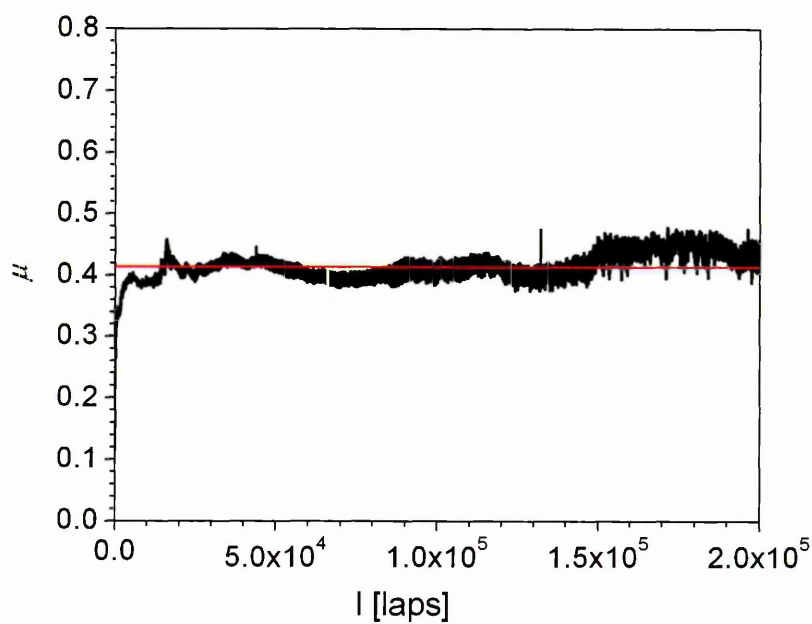
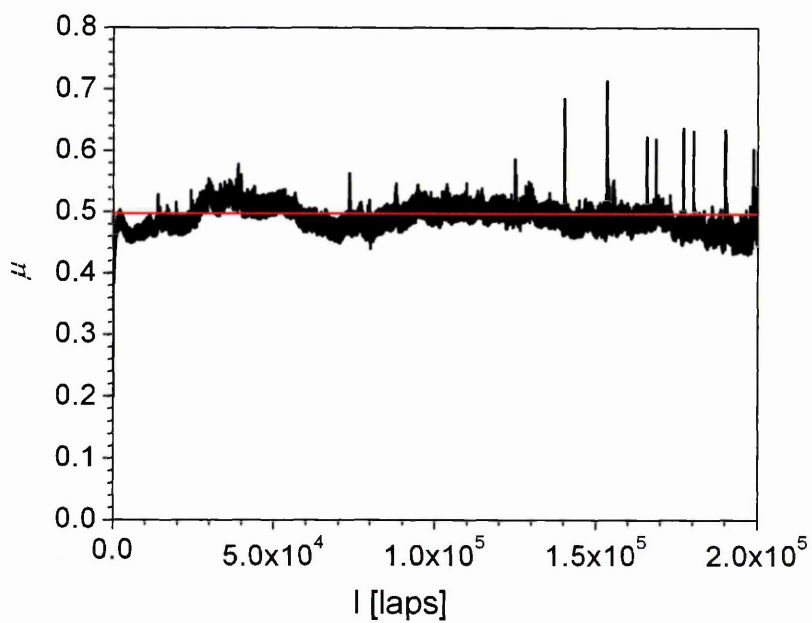


Fig. 5.29: (a) Sliding wear coefficient  $k_S$  of the coating and (b) Sliding wear coefficient  $k_{CP}$  of the counterpart as function of the bias voltage  $U_b$

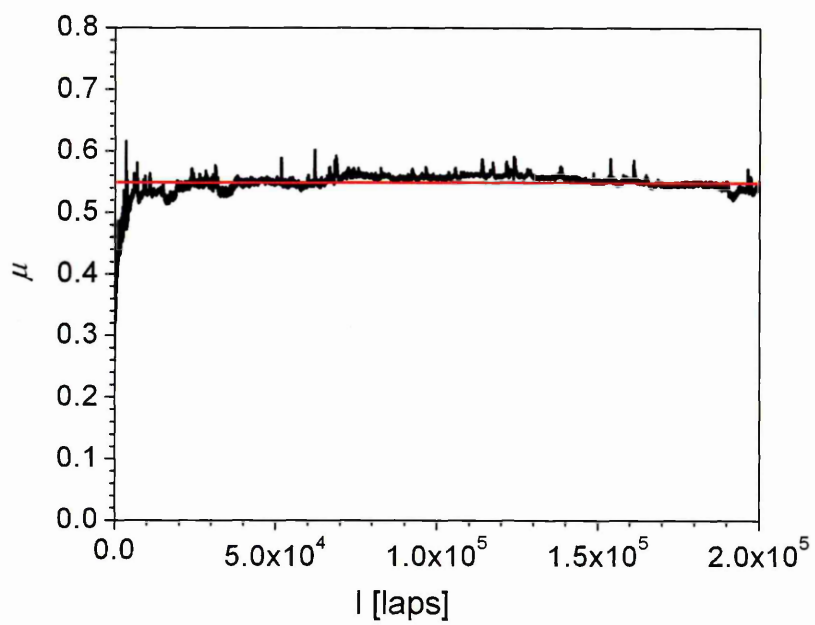


(a)  $U_b = -75$  V

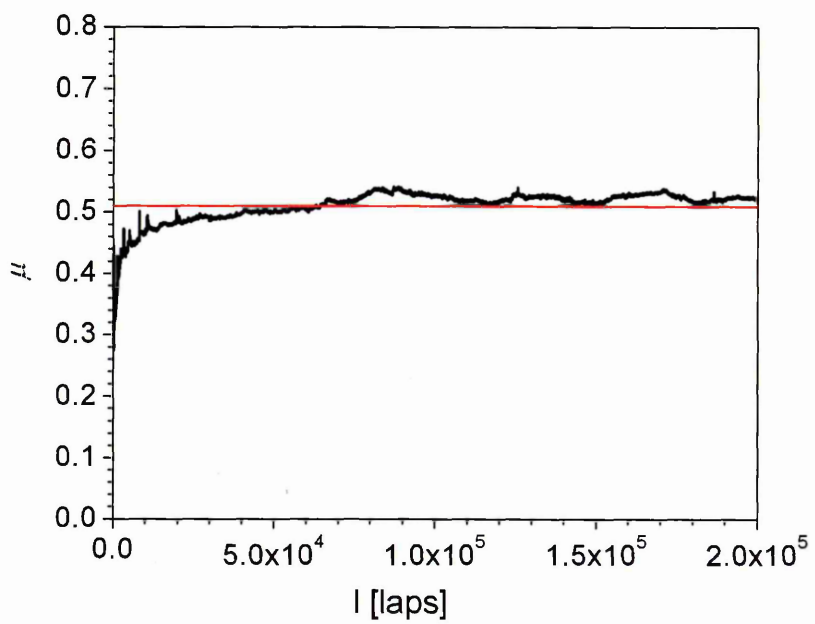


(b)  $U_b = -95$  V

Fig. 5.30: Friction curves of CrAlYN/CrN deposited at various bias voltages  $U_b$



(c)  $U_b = -120$  V



(d)  $U_b = -150$  V

Fig. 5.30: Continued

in-period,  $\mu$  remains at constant levels up to high sliding distances. This is true for all analysed coatings. The stability of  $\mu$  up to high distances indicates steady-state wear.

In order to understand how to optimize the wear properties of CrAlYN/CrN coatings, it is important to identify the operating wear mechanisms. Analysis of the wear track is necessary before further discussion as different wear mechanism can be active.

The surface of CrAlYN/CrN ( $U_b = -75$  V) (see Fig. 5.31) reveals 3 distinct areas after dry sliding: the wear track, a transition zone between wear scar and coating and the unaffected thin film with loose accumulation of wear particles. The wear scar shows a smooth, defect free surface without wear particles on the wear track. Additionally, no signs of micro-cracking or coating spallation are observed. Wear takes place in a mild wear regime. In the transition zone at the rim of the wear scar (see Fig. 5.32), two different phenomena can be observed (i) the removal of the column tops (see Fig. 5.33) and a material transfer zone (see Fig. 5.34). An EDS spectrum of this material shows the presence of all coating elements including N and also a substantial O signal (see Fig. 5.35, spectrum 1). Large amounts of wear debris are found outside the wear track (see Fig. 5.36). These particles are flake-shaped and have a variety of sizes in the sub-micron range. In the EDS

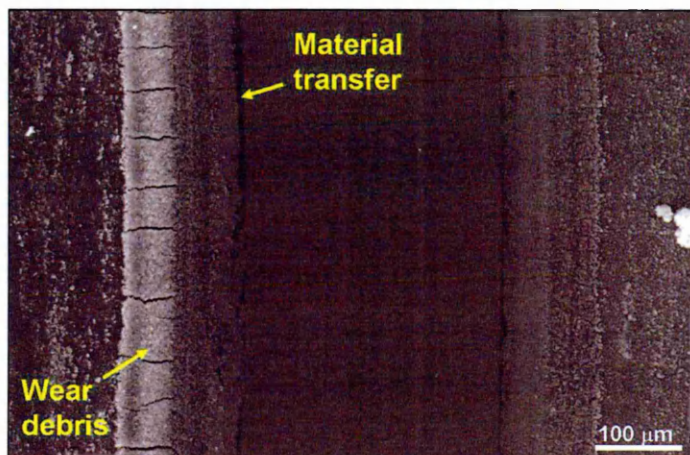


Fig. 5.31: SEM micrograph of the wear scar and the wear debris of CrAlYN/CrN deposited at  $U_b = -75$  V after sliding for 200,000 laps against  $Al_2O_3$

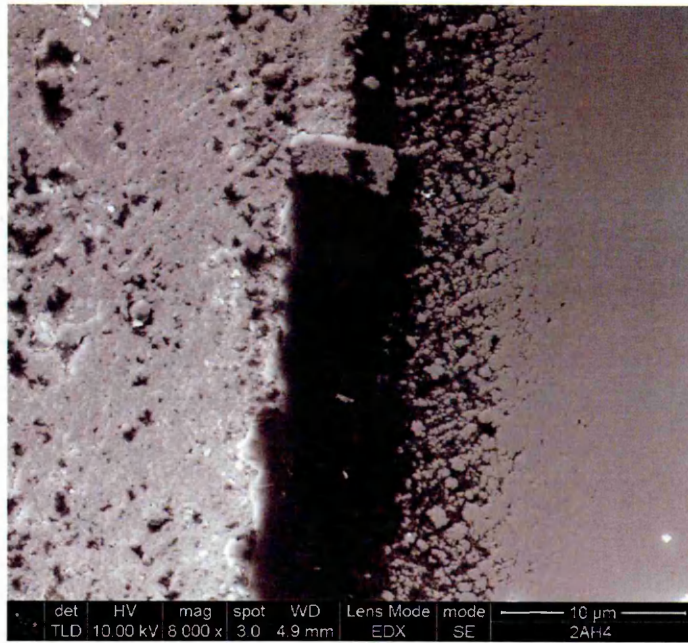


Fig. 5.32: SEM micrograph of the transition zone between the wear scar and undamaged CrAlYN/CrN coating deposited at  $U_b = -75$  V after sliding for 200,000 laps against  $\text{Al}_2\text{O}_3$

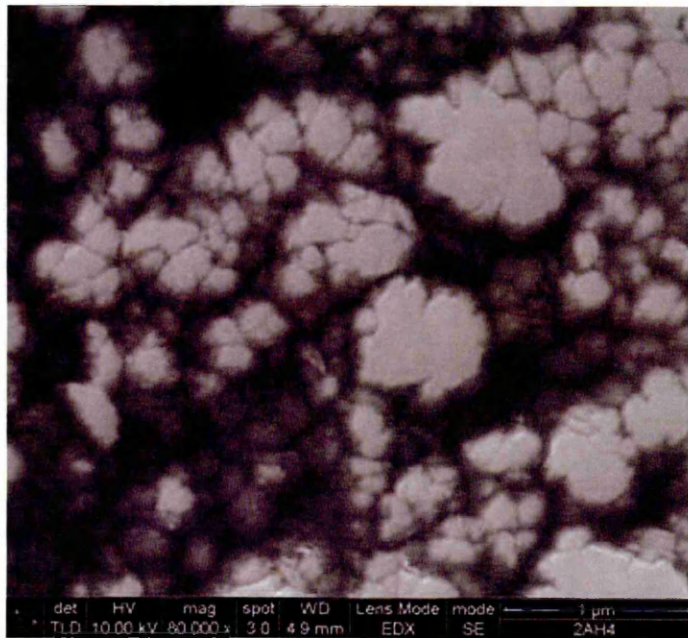


Fig. 5.33: SEM micrograph of the worn-off column tops CrAlYN/CrN deposited at  $U_b = -75$  V after sliding for 200,000 laps against  $\text{Al}_2\text{O}_3$

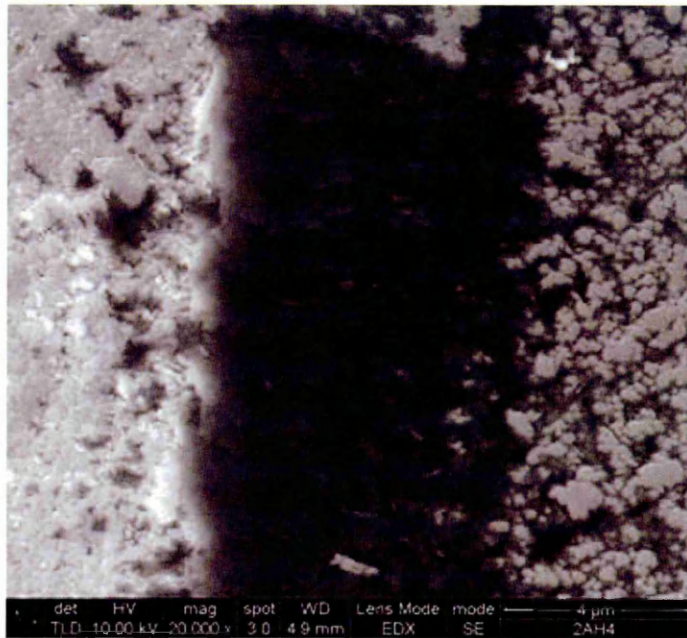


Fig. 5.34: SEM micrograph of the transferred material in the transition zone between the wear scar and the undamaged CrAlYN/CrN coating deposited at  $U_b = -75$  V after sliding for 200,000 laps against  $Al_2O_3$  (higher magnification compared to Fig. 5.32)

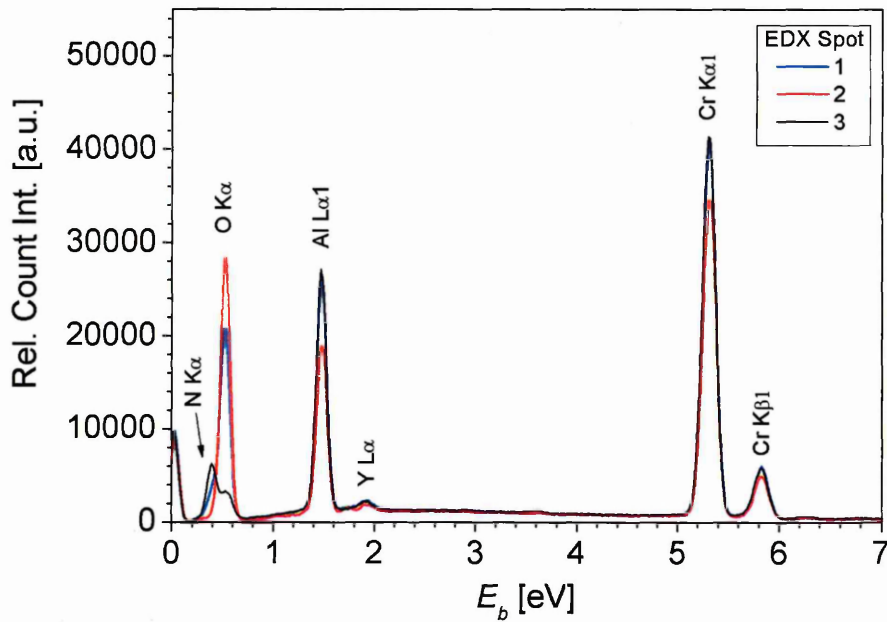


Fig. 5.35: EDS spectra of (1) transferred material in the transition zone (see Fig. 5.34) and (2) of the wear particles outside the wear track (see Fig. 5.36) and (3) as-deposited coating

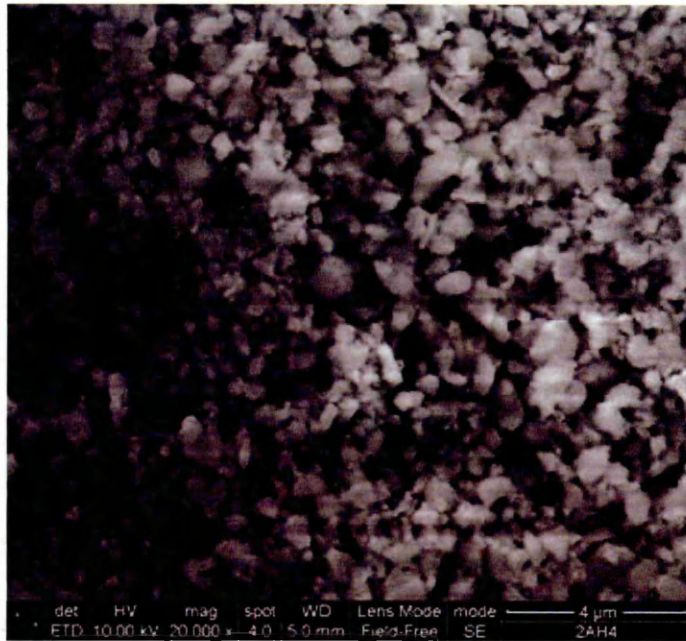


Fig. 5.36: SEM micrograph of the wear particles which have accumulated outside the wear track of CrAlYN/CrN deposited at  $U_b = -75$  V after sliding against  $Al_2O_3$

spectrum, a high O signal is measured from this debris whereas N is absent (see Fig. 5.36, spectrum 2). This absence of N implies the complete oxidation of these wear particles.

CrAlYN/CrN deposited at  $U_b = -75$  V is characterised by columnar structure with inter-columnar voids and dome-shaped column tops (see Fig. 5.10). This morphology result in the dome-shaped column tops (see Fig. 5.7(a)). These column tops provide places for high asperity contact between coating and sliding counterpart. When in moving contact, plastic deformation can be induced at these places and result in the removal of the column tops by mechanical wear (see Fig. 5.33). Additionally, material is also removed from the ball (see Fig. 5.29(b)). These wear particles are then entrapped at the moving interface between the sliding interfaces. Here, they act as third body wear particle and oxidise under the high temperatures (flash temperatures) that arise during sliding. Debris generated in this tribo-oxidation condition is then either transferred to the rim of the wear track, sticks to the sliding counterpart or accumulates to form the large scale debris. From this, it may be concluded that the wear mechanism in

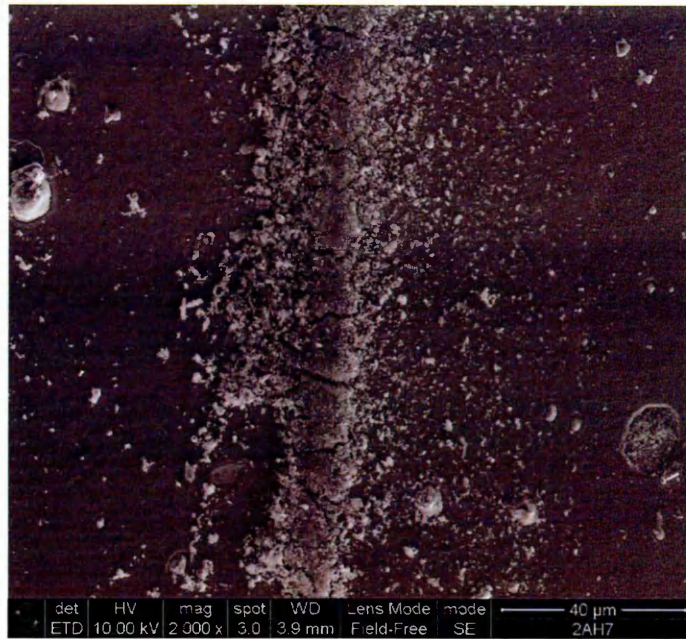


Fig. 5.37: SEM micrograph of the wear debris accumulated outside the wear track in CrAlYN/CrN deposited at  $U_b = -150$  V after sliding for 200,000 laps against  $\text{Al}_2\text{O}_3$

CrAlYN/CrN grown at low  $U_b = -75$  V takes place via combined mechanical wear and tribo-oxidation. As CrAlYN/CrN is a nanoscale multilayer, it is likely that the mechanical wear takes place via the previously described nanolayer de-lamination wear (see Sec. 2.14 or [89, 183]).

The tested CrAlYN/CrN deposited at high  $U_b = -150$  V (see Fig. 5.37) reveals a smooth wear track, material transfer and, moreover, wear debris. This is consistent with the observations made from the low  $U_b$  coating (see Fig. 5.31). The high  $U_b$  coating, however, shows a significantly reduced amount of transferred material at the track rim and wear debris outside the track. The wear debris, moreover, appears to consist of smaller agglomerates (see Fig. 5.38). From this, it is concluded that the wear of the high  $U_b$  coatings also takes place by mechanical wear and tribo-oxidation. This coating, however, reveals a better resistance to wear.

These observations may be in close relation to the microstructure of the coating. As  $U_b$  is increased, the structure becomes more dense, inter-columnar voids are eliminated and the coating surface becomes very smooth (see Sec. 5.1.5). These

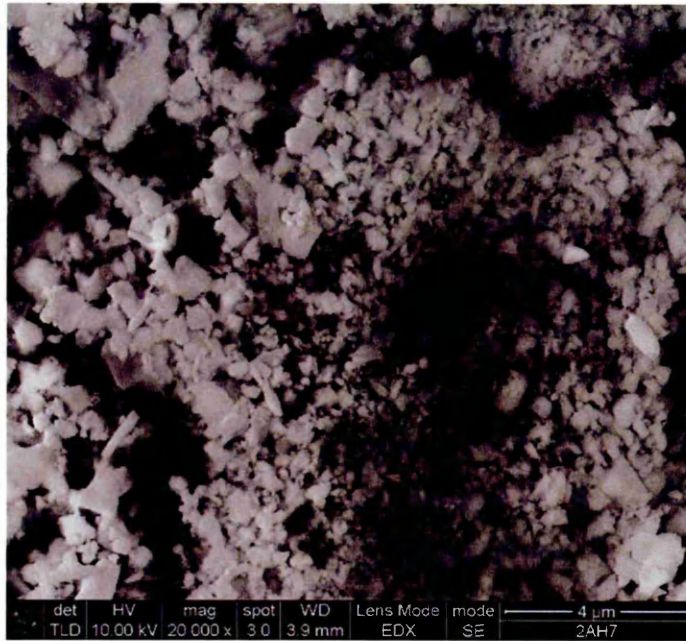


Fig. 5.38: SEM micrograph of the wear particles of CrAlYN/CrN deposited at  $U_b = -150$  V after sliding for 200,000 laps against  $\text{Al}_2\text{O}_3$

smooth surfaces (see e.g. Fig. 5.7(d)) reduce the coating wear as they lack the wear-promoting column tops (see Fig. 5.7(a)). Moreover, the nanolayer structure with its curvature-free structure (see Fig. 5.18) may have a higher resistance to the layer-by-layer delamination. Furthermore, the coating hardness increases with  $U_b$  (see Fig. 5.24(a)). This rising hardness ( $H_{IT} = 35.0$  GPa to 52.1 GPa) provides with a higher resistance against mechanical wear and therefore significantly reduces  $k_S$  (see Fig. 5.29(a)).

### 5.1.11 Dry High Speed Milling

Dry high speed milling was performed in a A2 hardened steel (see Sec. 3.3.6). A tool life time  $t_{Lifetime}$  (see Fig. 5.39) up to 45 min can be achieved when  $U_b$  is -75 V. This life time drastically declines to 19 min for  $U_b = -150$  V.

The failure mechanism during the milling process was investigated in detail in CrAlYN/CrN deposited at  $U_b = -75$  V (see Fig. 5.40). On the flank side (see Fig. 5.40(a)), the coating is spalled off from the cutting edge revealing the tool. Additionally, material is removed from the tool by abrasive and sliding wear. In

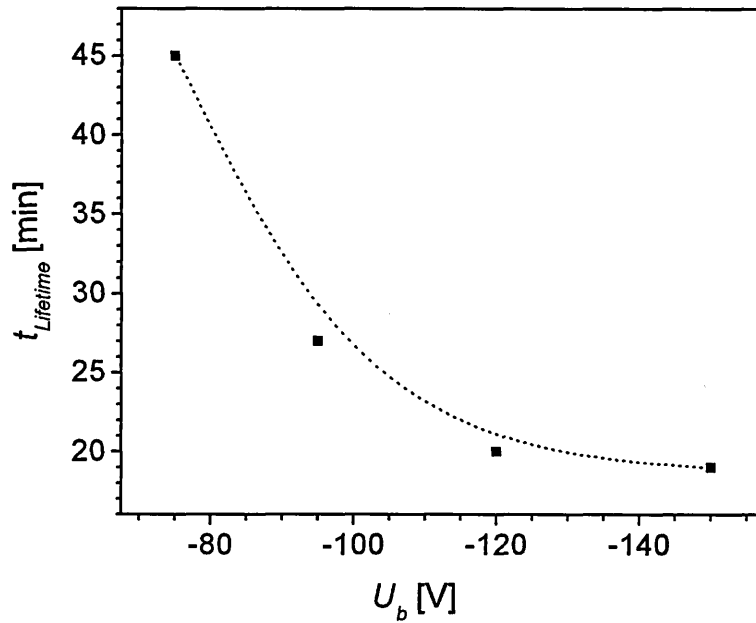
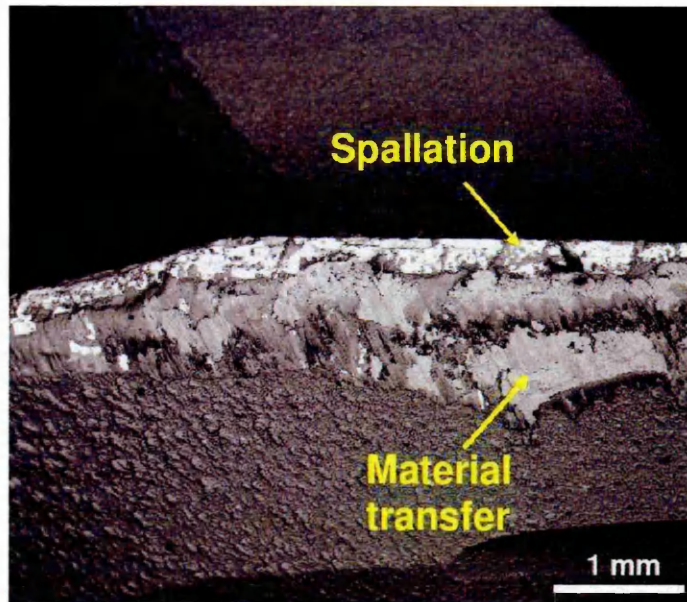


Fig. 5.39: Lifetime  $t_{Lifetime}$  of a CrAlYN/CrN coated endmill in dry high speed milling as function of substrate bias voltage  $U_b$

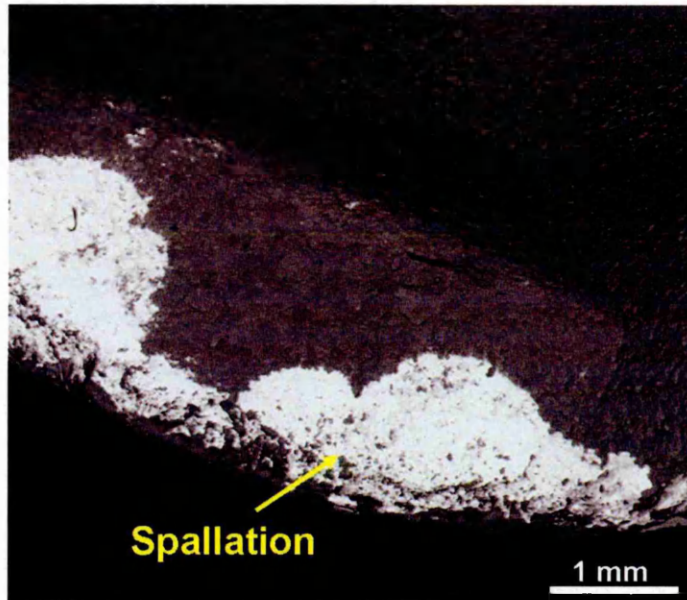
other regions, a build-up of material can be observed. Abrasive and sliding wear occur at the same time. On the rake side (see Fig. 5.40(b)), in contrast, spallation of material is found on large areas.

EDS elemental distribution maps were taken from the cutting edge, showing the distribution of various elements present in either tool, coating or workpiece (see Fig. 5.41). Large quantities of work piece material, such as Fe, Si and V, are transferred to the build-up edge of the tool. O is found on large areas of the tool surface, mainly in conjunction with Fe and Si. W is mainly distributed at the cutting edge. From these distribution maps, it can be concluded that material is transferred from the workpiece to the cutting tool. Additionally, coating and transferred material oxidise during the milling process in which temperatures up to 1000°C can be generated [184]. Oxidation mainly occurs in regions with a high amount of transferred work piece material. W at the cutting edge indicates the removal of the protective coating due to adhesive failure.

In summary, identified failure mechanisms during dry high speed milling are transfer of work piece material, oxidation as well as adhesive coating failure. These



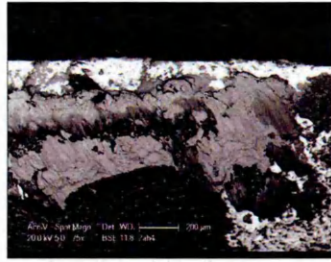
(a) Flank side



(b) Rake side

Fig. 5.40: SEM micrographs of a CrAlYN/CrN coated cutting tool after dry high speed milling of A2 HSS (The coating was grown at  $U_b = -75$  V)

tool failure mechanism are observed in all coatings and therefore dependent of variations in  $U_b$ .



(a) BSE micrograph



(b) Cr  $K_{\alpha}$ -map



(c) Al  $K$ -map



(d) O  $K$ -map



(e) Fe  $K_{\alpha}$ -map



(f) Si  $K$ -map



(g) V  $K$ -map



(h) W  $L_{\alpha}$ -map

Fig. 5.41: EDS elemental distribution mapping of a CrAlYN/CrN coated endmill after dry high speed milling in A2 steel

## 5.2 Influence of the Stabilisation of Bias Voltage on the Microstructure and Mechanical Properties

A change of the experimental set-up was necessary to stabilise the bias voltage  $U_b$  applied to the substrates during the deposition step (see Sec. 3.1).

The effect of additional stabilisation of  $U_b$  on microstructure and thin film performance was only marginal and will therefore not be discussed in detail. Two aspects, however, are worth mentioning.

Firstly, this bias stabilisation lead to a film densification which is obvious at the column boundaries. The open columnar structure, as found in CrAlYN/CrN when deposited without stabilisation (see Sec. 5.1.5) is replaced by a dense structure without voids being present at the column boundaries (see Sec. 5.3.4).

Most coating properties are not influenced by this structural change. The sliding wear behaviour, however, is significantly affected with a remarkable reduction of wear rate  $k_S$  by nearly one order of magnitude from  $2.7 \times 10^{-16} \text{ m}^3 \text{N}^{-1} \text{m}^{-1}$  to  $4.5 \times 10^{-17} \text{ m}^3 \text{N}^{-1} \text{m}^{-1}$ . This behaviour was most probably related to the delamination wear mechanism found in nanoscale multilayer thin films [185] which predicts reduced wear rates for films with dense column boundaries and flat superlattice layers.

Other film properties were similar and will not be explicitly itemised.

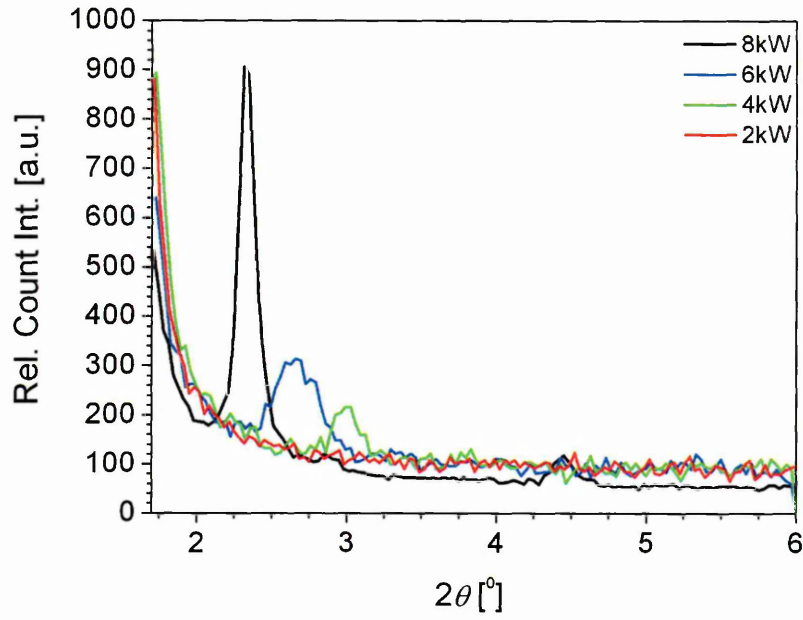
## 5.3 Influence of the Chemical Composition on the Microstructure and Mechanical Properties

The chemical composition of a coating is of crucial importance for many coating properties (see Chapt. 2.4). In multilayer coatings, different options of manipulating the chemical concentration are given by either a change of composition within the individual layer or by a variation in relative concentration of one layer component, i.e. by means of thickness alteration.

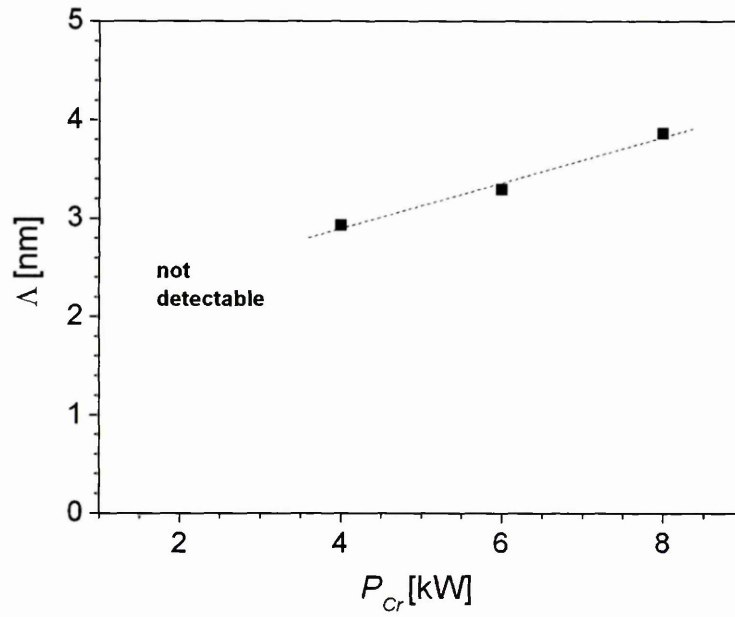
This section describes the manipulation of chemical composition by a variation in the power  $P_{Cr}$  on the Cr target during the nanolayer deposition step. The microstructure as well as the mechanical and tribological properties of these coatings will be discussed. Details of the process parameters are given in Sec. 3.1.

### 5.3.1 Nanoscale Bi-Layer Periodicity

The nanolayer periodicity  $\Lambda$  was determined from LA-XRD diffractometry (see Sec. 3.2.2.4). The obtained LA-XRD scans (see Fig. 5.42(a)) show a first and second order reflection ( $2\theta = 2.3^\circ$  and  $4.4^\circ$ ) obtained from CrAlYN/CrN grown at  $P_{Cr} = 8$  kW. Coatings grown in a medium  $P_{Cr}$  range of 4-6 kW show only a first order reflection ( $2\theta = 2.6^\circ$  at  $P_{Cr} = 6$  kW and  $2\theta = 3.0^\circ$  at  $P_{Cr} = 4$  kW). As  $P_{Cr}$  is decreased, the reflections become less sharp and decline in peak intensity. CrAlYN/CrN deposited at  $P_{Cr} = 2$  kW, in contrast, does not reveal any reflections. The peak shift to higher  $2\theta$  positions at lower  $P_{Cr}$  indicates a reduction in the nanolayer periodicity  $\Lambda$  (see Fig. 5.42(b)). The peak broadening and the reduction in relative count intensity may be due to some level of interfacial mixing and roughness in the film [186]. In coatings with smaller lattice period, the interface represents a greater proportion of the period thickness and, hence, peaks are broader with less relative intensity. The absence of a nanolayer reflection in CrAlYN/CrN grown at  $P_{Cr} = 2$  kW may indicate a very fine layered layer struc-



(a)



(b)

Fig. 5.42: Low angle  $\theta/2\theta$  scans and bi-layer thickness  $\Lambda$  of CrAlYN/CrN deposited at various Cr target powers  $P_{Cr}$ , analysed by LA-XRD

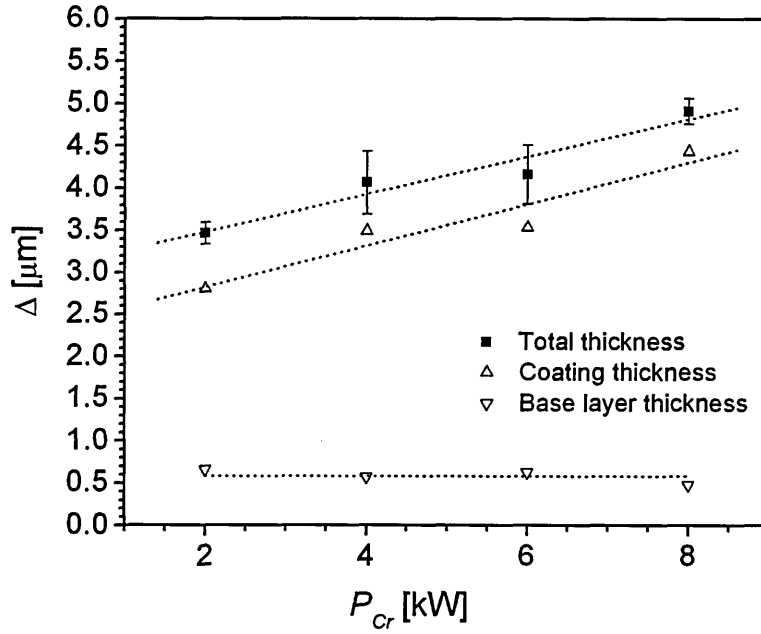


Fig. 5.43: Coating thickness  $\Delta$  as function of Cr target power  $P_{Cr}$

ture with extremely low reflection intensity or could be caused by a limitation in the LA-XRD technique. Further investigations by TEM analysis (see Sec. 3.2.4) is necessary to verify one of these assumptions.

The nanolayer periodicity  $\Lambda$  is calculated (see Eq. 3.4, Sec.3.2.2.4) and decreases from 3.9 nm to 2.9 nm as  $P_{Cr}$  is decreased (see Fig. 5.42). From this, an approximately linear relationship can be found when only accounting for reflections of coatings grown at  $P_{Cr}$  between 4 kW and 8 kW:

$$\Lambda = 0.23 \cdot P_{Cr} + 1.96 \text{ nm} \quad (5.1)$$

Extrapolation of Eq. 5.1 to  $P_{Cr} = 0$  kW gives the thickness of the CrAlYN layer of 1.96 nm. Thus, when deposition is carried out at  $P_{Cr} = 8$  kW, the CrN and CrAlYN components of the multilayer have an approximately equal thickness with a ratio of 0.95. This value may have an effect on mechanical thin film behaviour. A maximum hardness, for example, is expected when the individual components of the nanolayers have an equal thickness [14].

Direct evidence of a reduced CrN layer thickness is also presented when plotting the total coating thickness  $\Delta$  (see Fig. 5.43), measured by ball cratering thickness measurement (see Sec. 3.3.1). Here, a reduction in  $\Delta$  of the nanoscale multilayer from 4.9  $\mu\text{m}$  to 3.5  $\mu\text{m}$  is found.

### 5.3.2 SNMS Analysis

SNMS depth profiling was carried out to determine the coating composition (see Sec. 3.2.1). All plots reveal a steady composition across the nanolayers (see Fig. 5.44).

A direct comparison of the coating atomic fractions (see Fig. 5.45(a)) shows that the Cr content of the coatings decreases from  $\sim 32.8\text{at}\%$  to  $\sim 21.5\text{at}\%$  as  $P_{Cr}$  is reduced. The metal/N ratio (see Fig. 5.45(b)) significantly decreases from 1.9 to 1.5 as  $P_{Cr}$  is reduced. This signifies that films deposited at low  $P_{Cr}$  are closer to a stoichiometric composition. CrN coatings are known for their affinity to form sub-stoichiometric nitrides [118]. In CrAlYN/CrN, minimising the CrN component therefore improves the coating stoichiometry. During thin film growth, numerous ions contribute to the energy transfer to the substrate and cause both densification and re-sputtering of the coating. Light elements, such as N, are especially prone to be re-sputtered [179]. Cr as a heavy atom (52 atu) significantly adds to ion-induced re-sputtering effects of the growing film. With the reduction of  $P_{Cr}$ , it is expected that Al as a much lighter element becomes more dominant in the bombardment process. Due to its lower weight (27 atu), its effect on the re-sputtering of N from the growing coating may be less pronounced than for Cr. Therefore, a reduction in Cr inside the plasma may generate thin films with higher N contents. Similar behaviour was reported for CrAlN where higher N concentrations were found in low Cr containing films [119].

The Cr/Al ratio (see Fig. 5.45(b)), which is 0.90 at  $P_{Cr} = 8 \text{ kW}$ , decreases to 0.56 when  $P_{Cr}$  is reduced to 2 kW. The changing ratio is directly related to the reduction in the Cr atomic fraction.

The sputtering time in the depth profiles (see Fig. 5.44) required until substrate

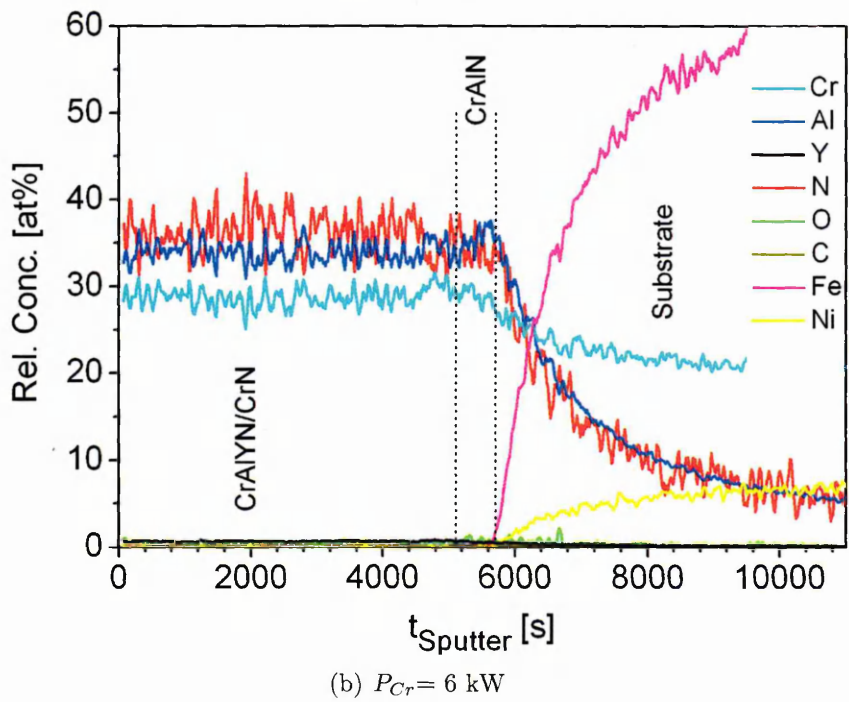
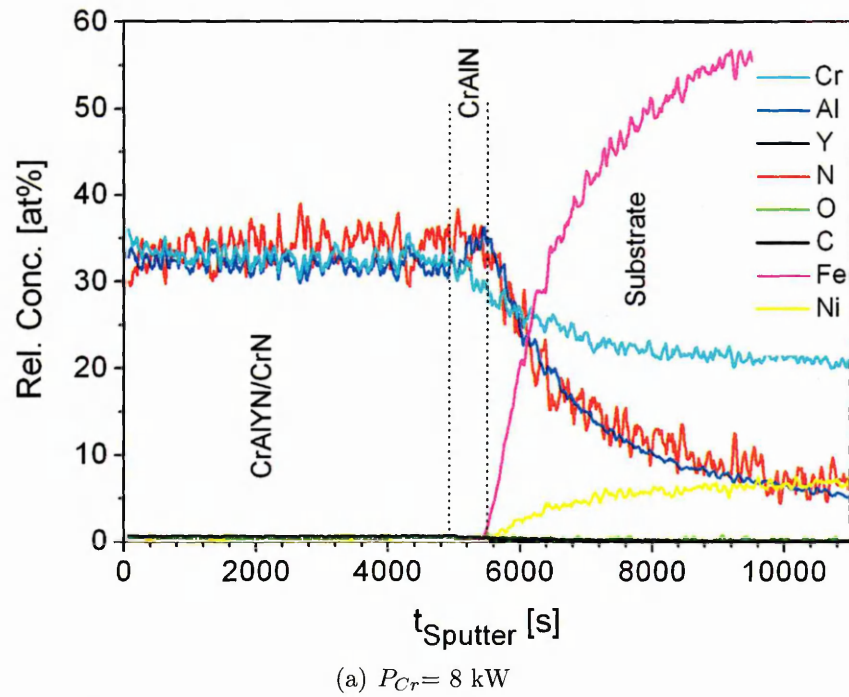
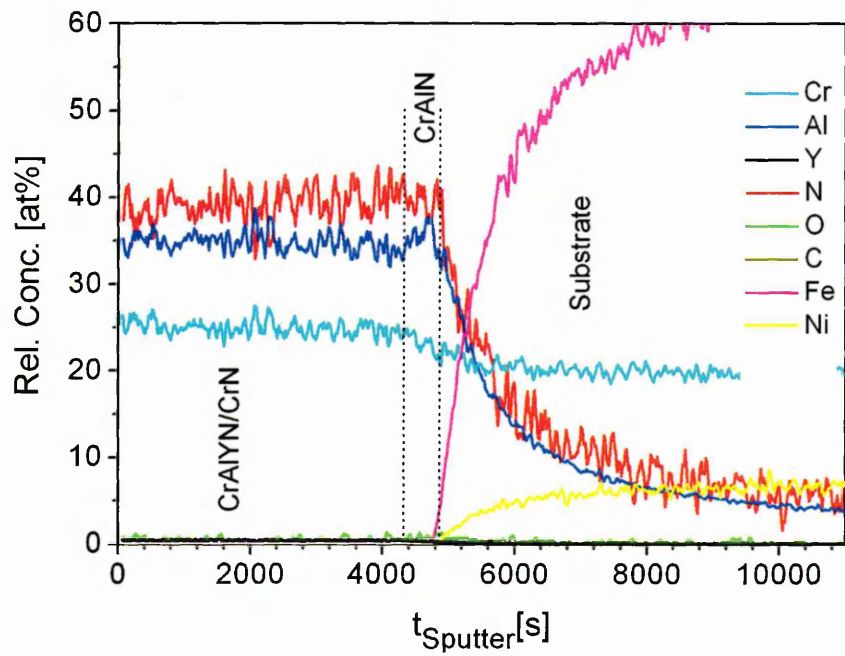
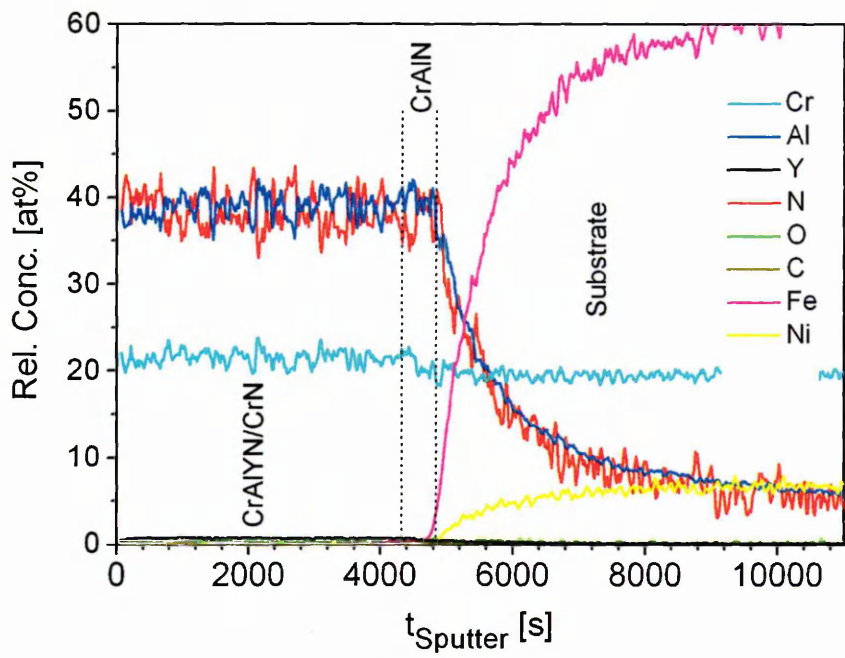


Fig. 5.44: SNMS depth profiles of CrAlYN/CrN deposited at different Cr target powers  $P_{Cr}$

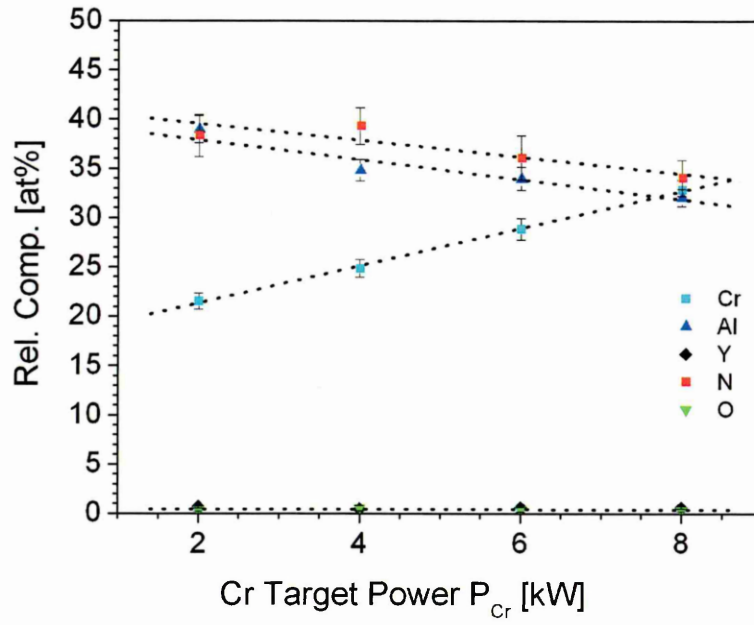


(c)  $P_{Cr} = 4 \text{ kW}$

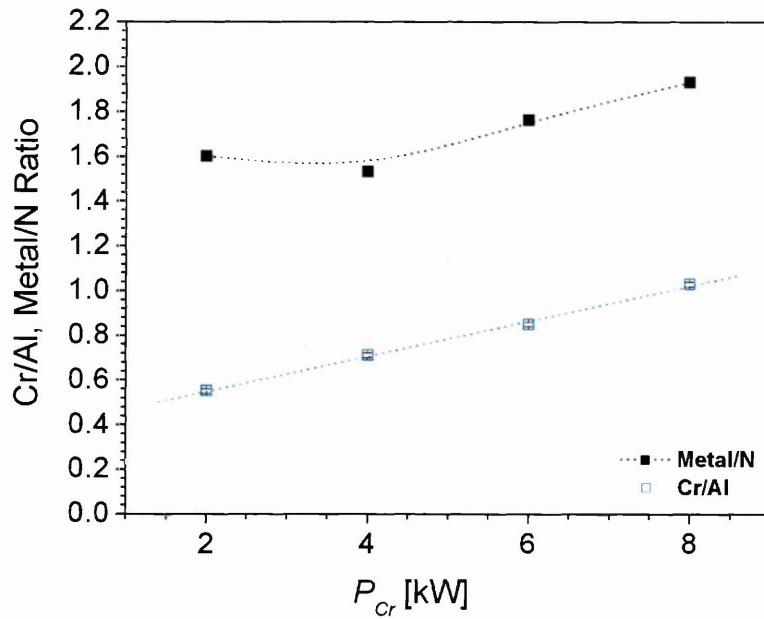


(d)  $P_{Cr} = 2 \text{ kW}$

Fig. 5.44: Continued



(a)



(b)

Fig. 5.45: Chemical composition of CrAlYN/CrN as function of Cr target power  $P_{Cr}$ : (a) Relative composition of all coating elements and (b) Compositional ratios of Cr/Al and metal/N

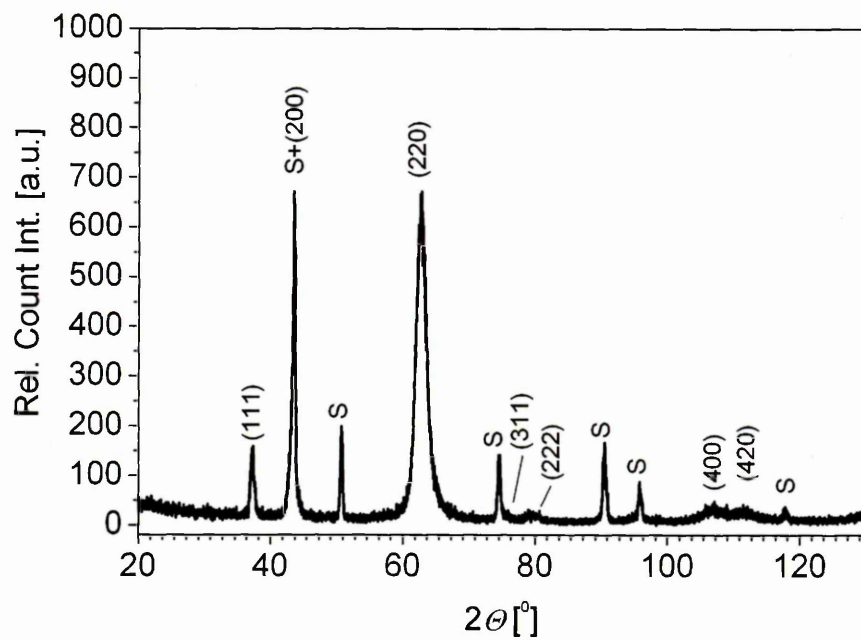
elements Fe and Ni were detected decreases from  $\sim 6000$  s from  $P_{Cr} = 8$  kW to  $\sim 4000$  s at  $P_{Cr} = 2$  kW. Assuming constant sputtering rates, the reduction in sputtering time is another indication of reduced film thickness. This is in good agreement with the analysis of the bi-layer periodicity (see Fig. 5.42) and the coating thickness (see Fig. 5.43).

### 5.3.3 XRD Analysis

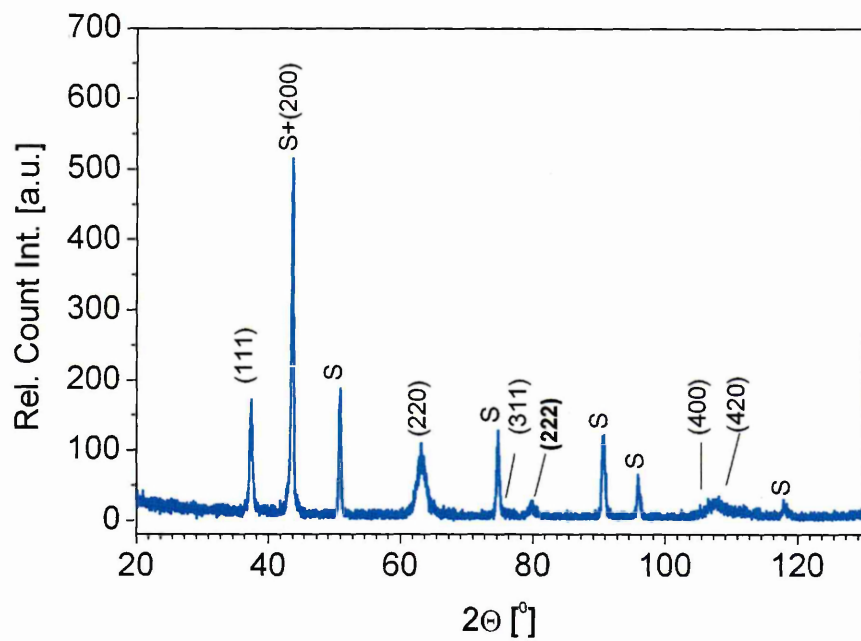
Phase analysis was carried out by  $\theta/2\theta$ -XRD measurements (see Sec. 3.2.2.2). Single phase NaCl (B1)-fcc CrAlYN/CrN is the only phase present in all coatings (see Fig. 5.46). The individual reflections are indexed according to their corresponding (hkl) lattice planes. Reflections labeled 'S' correlate to the substrate material. A strong contribution of substrate peaks is found in all diffractograms.

It is shown that the phase composition is not affected by a variation in  $P_{Cr}$ . This is related to the fact that, by changing  $P_{Cr}$ , only the thickness of the CrN layer is affected. The elemental composition of the individual layers CrAlYN and CrN, in contrast, is not changed. The expected phases are therefore similar in all coatings and do not vary with  $P_{Cr}$ . This B1-fcc phase is also obtained when  $P_{Cr}$  is fixed to 8 kW and the bias voltage  $U_b$  is varied in a range of -75 V to -150 V (see Sec. 5.1).

The unstressed lattice parameter  $a_0$  (see Fig. 5.47) is found to decrease linearly from 0.4158 nm at  $P_{Cr} = 8$  kW to 0.4144 nm in case of  $P_{Cr} = 2$  kW. This behaviour may be explained by the correlation between lattice parameter  $a_{0,CrAlYN}$  and  $a_{0,CrN}$  of the individual nanolayers. Shrinkage of the lattice spacing is a well reported phenomenon in fcc-CrAlN coatings and relates to the replacement of Cr by Al atoms [119, 121]. The measured lattice parameter  $a_0$  is composed of the weighted fraction in lattice parameter of CrAlYN and CrN. Removal of CrN as component with the larger spacing therefore may result in coating system with smaller lattice parameters  $a_0$ , as  $P_{Cr}$  is reduced. It is expected that the lattice spacing  $a_{0,CrAlYN}$  of CrAlYN is smaller than  $a_{0,CrN}$  of CrN as Al is introduced into the lattice.

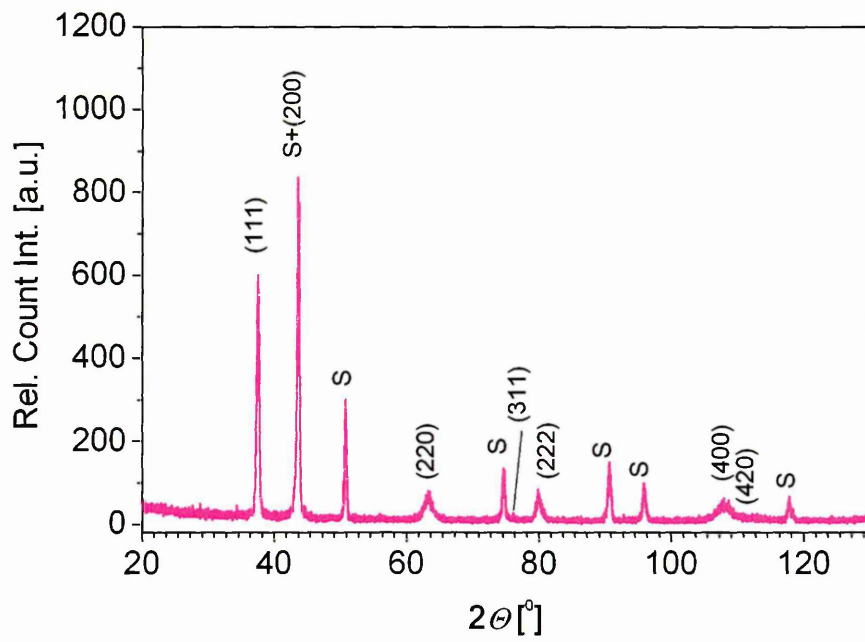


(a)  $P_{Cr} = 8 \text{ kW}$

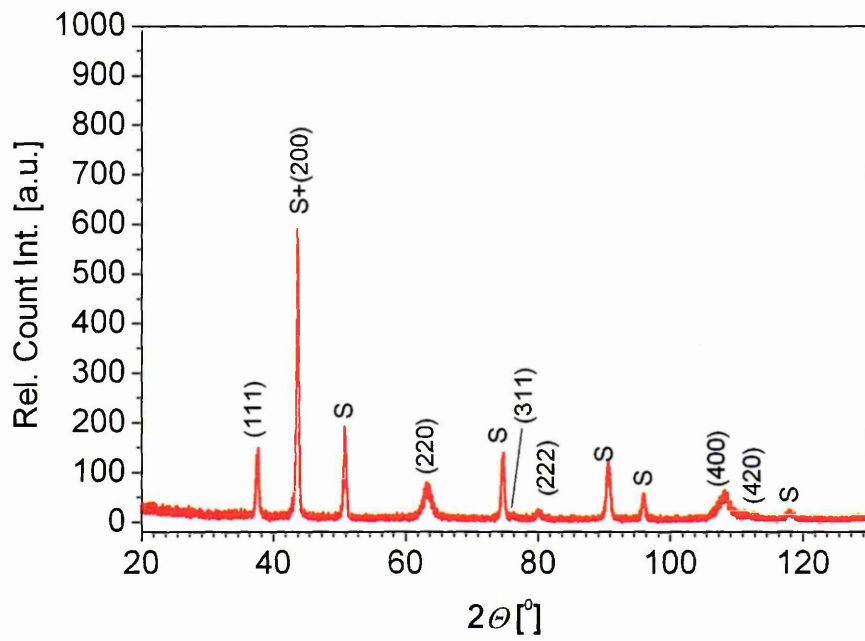


(b)  $P_{Cr} = 6 \text{ kW}$

Fig. 5.46:  $\theta/2\theta$ -XRD pattern of CrAlYN/CrN deposited at various Cr target powers  $P_{Cr}$



(c)  $P_{Cr} = 4$  kW



(d)  $P_{Cr} = 2$  kW

Fig. 5.46: Continued

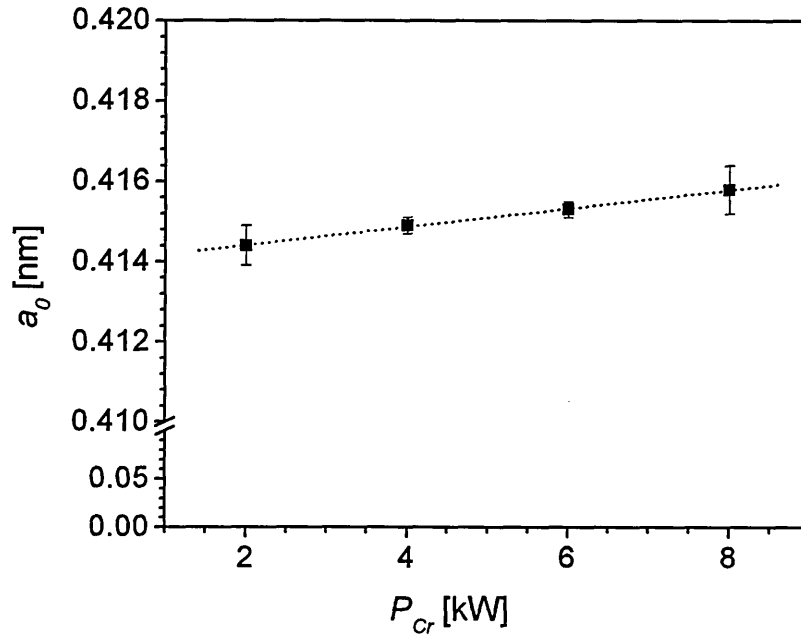


Fig. 5.47: Unstressed lattice parameter  $a_0$  of CrAlYN/CrN as function of the Cr target power  $P_{Cr}$

### 5.3.4 TEM Analysis

Microstructural analysis was carried out by TEM studies (see Sec. 3.2.4). All coatings (see Fig. 5.48) grow in a columnar competitive structure with columns nucleating in the CrAlN base layer and growing continuously up to the column tops. The film thickness  $\Delta$  is found to decrease as  $P_{Cr}$  was reduced due to the reduction of CrN layer thickness inside the coating, confirming the result of the ball cratering thickness measurement (see Fig. 5.43).

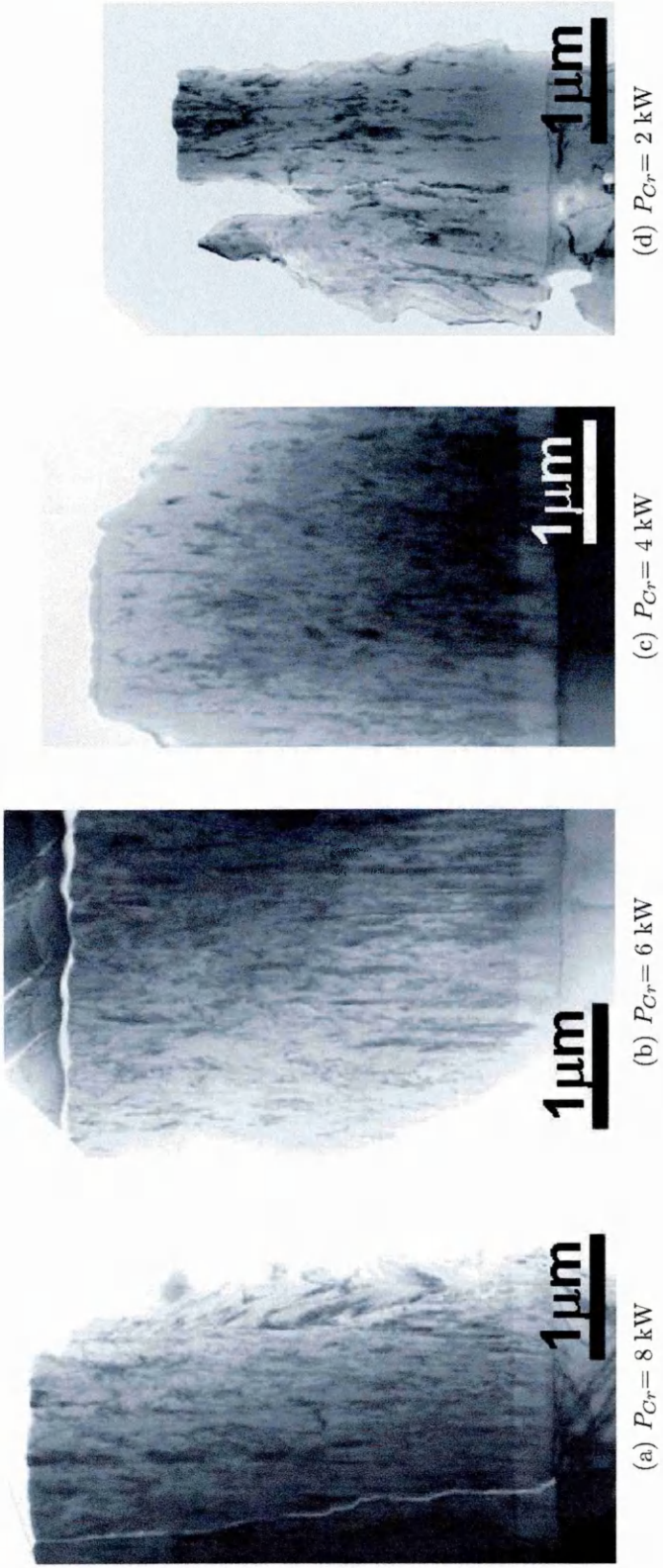


Fig. 5.48: BF-TEM images of CrAlYN/CrN deposited at various Cr target power  $P_{Cr}$

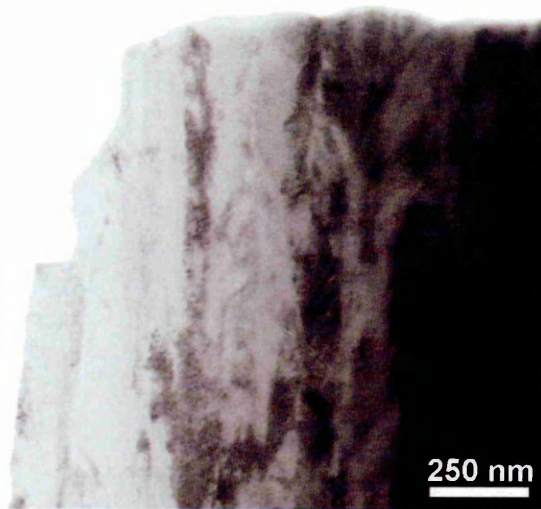


Fig. 5.49: BF-TEM micrograph of the upper part of CrAlYN/CrN deposited at  $P_{Cr} = 8$  kW

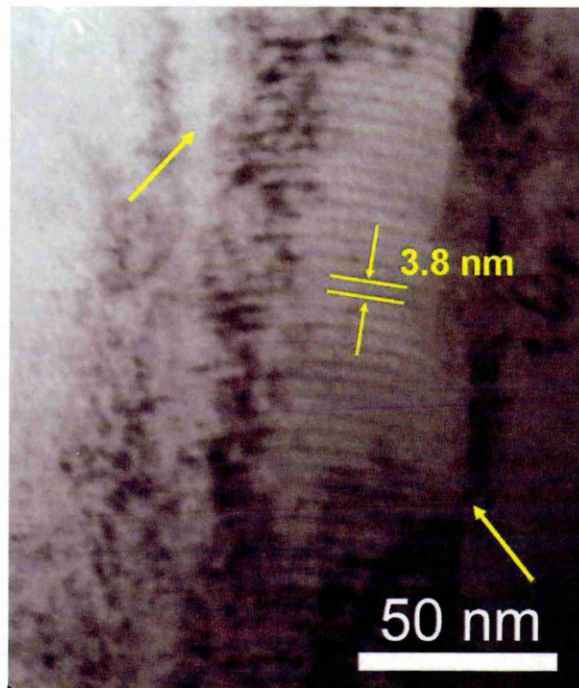


Fig. 5.50: BF-TEM micrograph of the nanolayers in CrAlYN/CrN deposited at  $P_{Cr} = 8$  kW: The column boundaries are dense and void-free (Arrow indicates a dense column boundary)

CrAlYN/CrN grown at  $P_{Cr} = 8$  kW shows a dense columnar structure (see Fig. 5.48(a) and Fig. 5.49). The nanolayers (see Fig. 5.50) are well defined and

clearly reveal a bi-layer periodicity  $\Lambda = 3.8$  nm. The column boundaries are dense and free of inter-columnar voids.  $\Lambda$  measured from the BF-TEM micrograph corresponds well to  $\Lambda$  determined by LA-XRD (see Fig. 5.42(b)).

A reduction of  $P_{Cr}$  to 6 kW results in a coating with similar structural details (see Fig. 5.48(b), further details not shown) compared to those obtained at  $P_{Cr} = 8$  kW.

The coating deposited at  $P_{Cr} = 4$  kW grows in a competitive columnar structure (see Fig. 5.48(c)). Here, less dense structures with inter-columnar voids are found (see Fig. 5.51). The nanoscale multilayers are clearly visible on a nanometer scale (see Fig. 5.52). Additionally, low density regions are found at the column boundaries.

During the deposition process, the samples are subjected to three-fold rotation and deposition from four different targets (see Sec. 3.1). These low density zones are possibly related to the previously mentioned reduction in particle bombardment at lower  $P_{Cr}$ . It is expected that, as  $P_{Cr}$  is reduced, less Cr particles are ejected into the plasma and, hence, reduced numbers of ions/atoms arrive at the substrate to bombard the growing surface. It is therefore suggested that less energy is transferred into the growing coating and less dense coatings form. Ac-

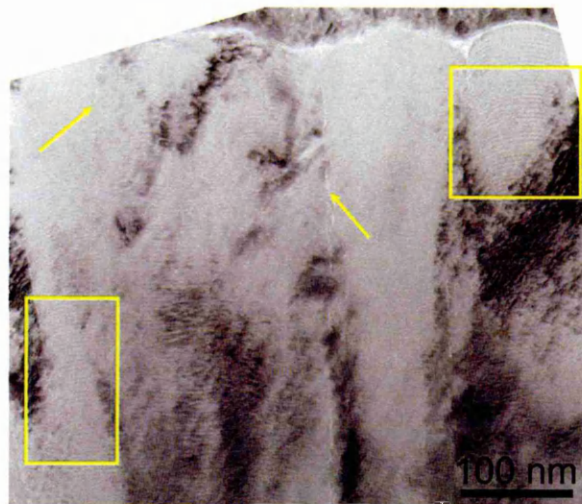


Fig. 5.51: BF-TEM micrograph of the upper part of CrAlYN/CrN deposited at  $P_{Cr} = 4$  kW: The column boundaries are voided (Arrows indicate a dense column boundary, a box hints to the nano-layer structure)

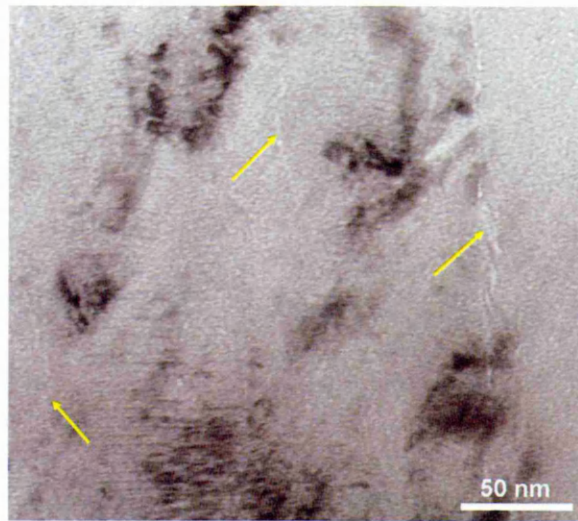


Fig. 5.52: BF-TEM micrograph of the nanolayers in CrAlYN/CrN deposited at  $P_{Cr} = 4$  kW with the image taken at higher magnification: The column boundaries are under-dense (Arrows indicate low density regions)

cording to Messier's SZM, a reduction in ion bombardment causes the growth of less dense coatings. This, in turn, could explain the formation of coatings with inter-columnar voids.

CrAlYN/CrN which was prepared at  $P_{Cr} = 2$  kW reveals a columnar structure (see Fig. 5.48(d)). In this structure, layered features in the bulk of the column as well as low-density regions can be observed on a nanolayer scale (see Fig. 5.54). The thickness of these layers is measured to a value of  $\sim 1.8$  nm. At  $P_{Cr} = 2$  kW, a theoretical CrN thickness of 0.46 nm is estimated (see Eq. 5.1), resulting in a theoretical bi-layer thickness  $\Lambda$  of 2.4 nm. The measured  $\Lambda$ , however, is therefore somewhat thinner than expected and corresponds roughly to the thickness of the CrAlYN layer (1.96 nm after Eq. 5.1). The observed structure is possibly arising from the previously mentioned decrease in ion bombardment at lower  $P_{Cr}$ . It is suggested that, as the specimens pass in front of the Cr target, only a limited number of particles arrive at the substrate. The condensing ions/atoms may only form layers with a thickness of a few atomic layers. Additionally, subsequent re-sputtering of these layers could partially remove these layers when the substrates are subjected to ion bombardment in front of one of fully powered targets. As a

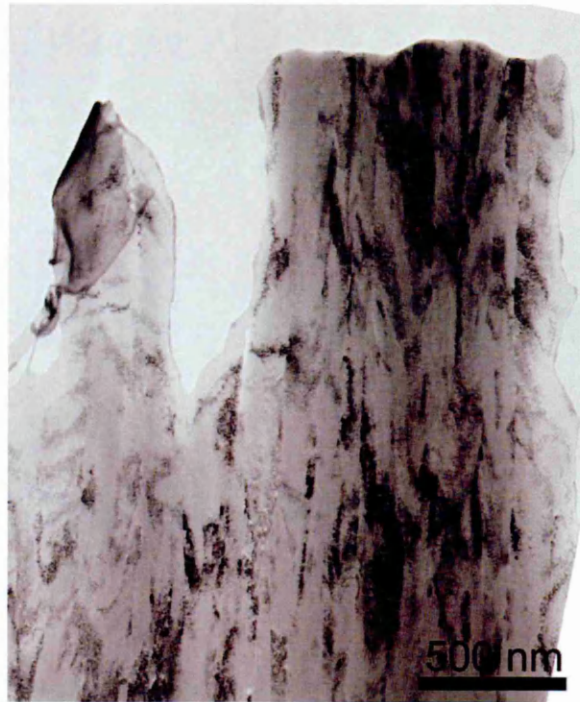


Fig. 5.53: BF-TEM micrograph of the upper part of CrAlYN/CrN deposited at  $P_{Cr} = 2$  kW: The coating grows in a columnar structure

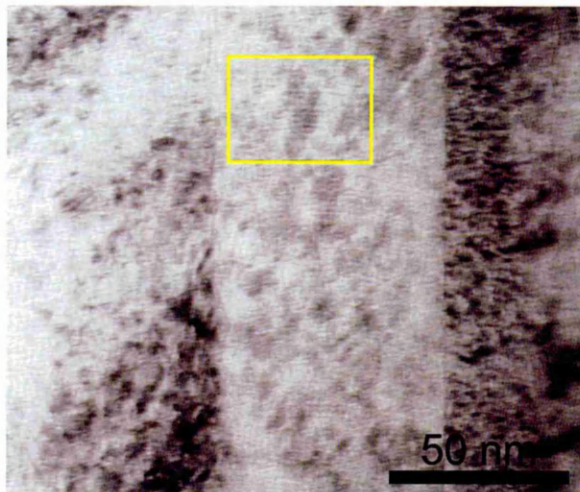


Fig. 5.54: BF-TEM micrograph of the layered "near-monolithic" features in CrAlYN/CrN deposited at  $P_{Cr} = 2$  kW

result, a layered structure with high and low density zones could be generated. These zones may be imaged by TEM analysis due to mass-thickness contrast arising from the under-dense layers at the position of the CrN layers. The resulting

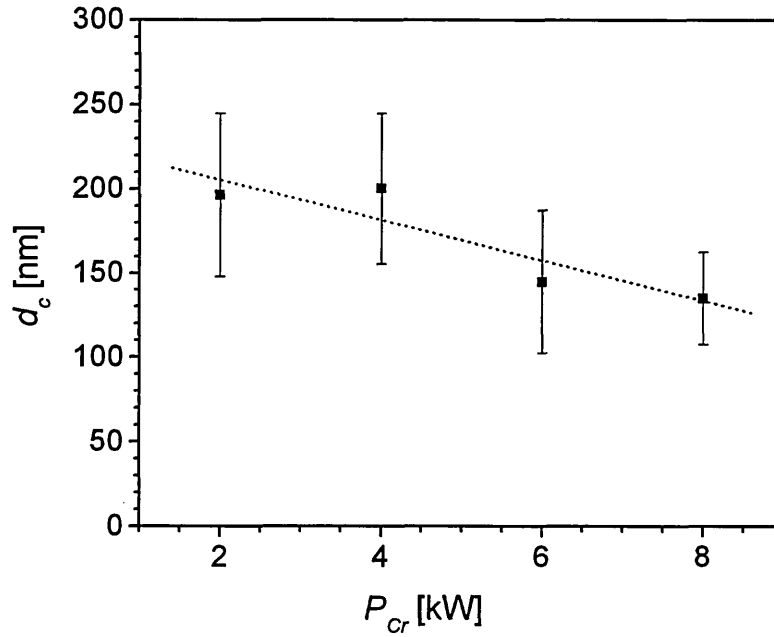


Fig. 5.55: Average column diameter  $d_c$  of CrAlYN/CrN as function of Cr target power  $P_{Cr}$

coatings could be referred to as "near-monolithically" grown. This hypothesis is supported by the absence of a reflection in the LA-XRD scan (see Fig. 5.42(a)) which suggests a structure without clearly defined nanolayers.

TEM imaging allows the determination of the average column diameter  $d_c$ , measured at the column top (see Fig. 5.55).  $d_c$  decreases linearly from  $\sim 200$  nm to  $\sim 130$  nm as a function of  $P_{Cr}$ . In Ag/Cu coatings,  $d_c$  was found to increase as function of the thicker layer [187]. In the case of CrAlYN/CrN, this does not seem to be the case, as the CrAlYN layer as thicker layer is constant at 1.9 nm (see Sec. 5.3.1). In the former case, however, the deposition time of the thicker layer was the variable process parameter for deposition which may explain discrepancies in the findings.

It can be concluded from TEM analysis that CrAlYN/CrN grows in a polycrystalline columnar structure with distinct nanolayers. The initially dense coatings ( $P_{Cr}= 6$  kW to 8 kW) become less dense with inter-columnar voids ( $P_{Cr}= 4$  kW), as  $P_{Cr}$  is reduced. With a further reduction in  $P_{Cr}$  to 2 kW, a "near-monolithic" structure without clearly developed nanolayers forms.

### 5.3.5 Texture Analysis

Texture coefficients  $T^*$  (see Sec. 3.2.2.3) were calculated to investigate the presence of a preferred crystallographic growth direction (see Fig. 5.56). A (110) texture is observed in CrAlYN/CrN with  $P_{Cr} = 8$  kW ( $T_{(110)}^* = 4.7$ ). Reducing to  $P_{Cr}$  results in a relative decrease of the (110) preferred orientation ( $T_{(110)}^* = 2.9$  at  $P_{Cr} = 4$  kW) and becomes more randomly oriented ( $T_{(111)}^* = 1.8$ ,  $T_{(110)}^* = 1.0$  and  $T_{(100)}^* = 1.5$ ). Deposition at  $P_{Cr} = 2$  kW results in a film with mixed (110), (331) texture ( $T_{(110)}^* = 2.5$  and  $T_{(100)}^* = 1.6$ ).

It can be seen that the coating grows in a more random orientation as  $P_{Cr}$  and, hence, the CrN layer thickness decreases. CrN deposited under similar conditions is known to be strongly (110) textured [100]. In CrAlYN/CrN, thick CrN nanolayers would therefore favour the development of (110) crystallographic orientation as the CrN contributes significantly to the growth characteristics of the nanolayer composite. With the removal of this (110) textured component, this favoured orientation is expected to decrease. The “near-monolithic” CrAlYN ( $P_{Cr} = 2$  kW) does not follow this trend towards higher random structuring but has a mixed preferred orientation. The drastic change in texture in CrAlYN deposited at low  $P_{Cr}$  may be a result of changed microstructure without the presence of a nanoscale multilayer structure. Identical results were found for TiAlN/CrN superlattice coatings with similar microstructure and bi-layer period [188]. The texture development as described above may be characteristic for nanoscale multilayer coatings with a CrN component.

### 5.3.6 Residual Stress

The lattice parameter  $a_{0,\perp}$  (see Sec. 3.2.2.5) and the residual stresses  $\sigma$  in the coating (see Sec. 3.2.2.5) were analysed by XRD measurements.

The lattice parameter  $a_{0,\perp}$  (see Fig. 5.57(a)) decreases from 0.4174 nm to 0.4149 nm when  $P_{Cr}$  is reduced to 4 kW and then slightly increases again to 0.4157 nm as  $P_{Cr}$  is further reduced ( $P_{Cr} = 2$  kW). These values are up to 0.4% higher than the unstressed lattice parameter  $a_0$  (see Fig. 5.47) and indicate com-

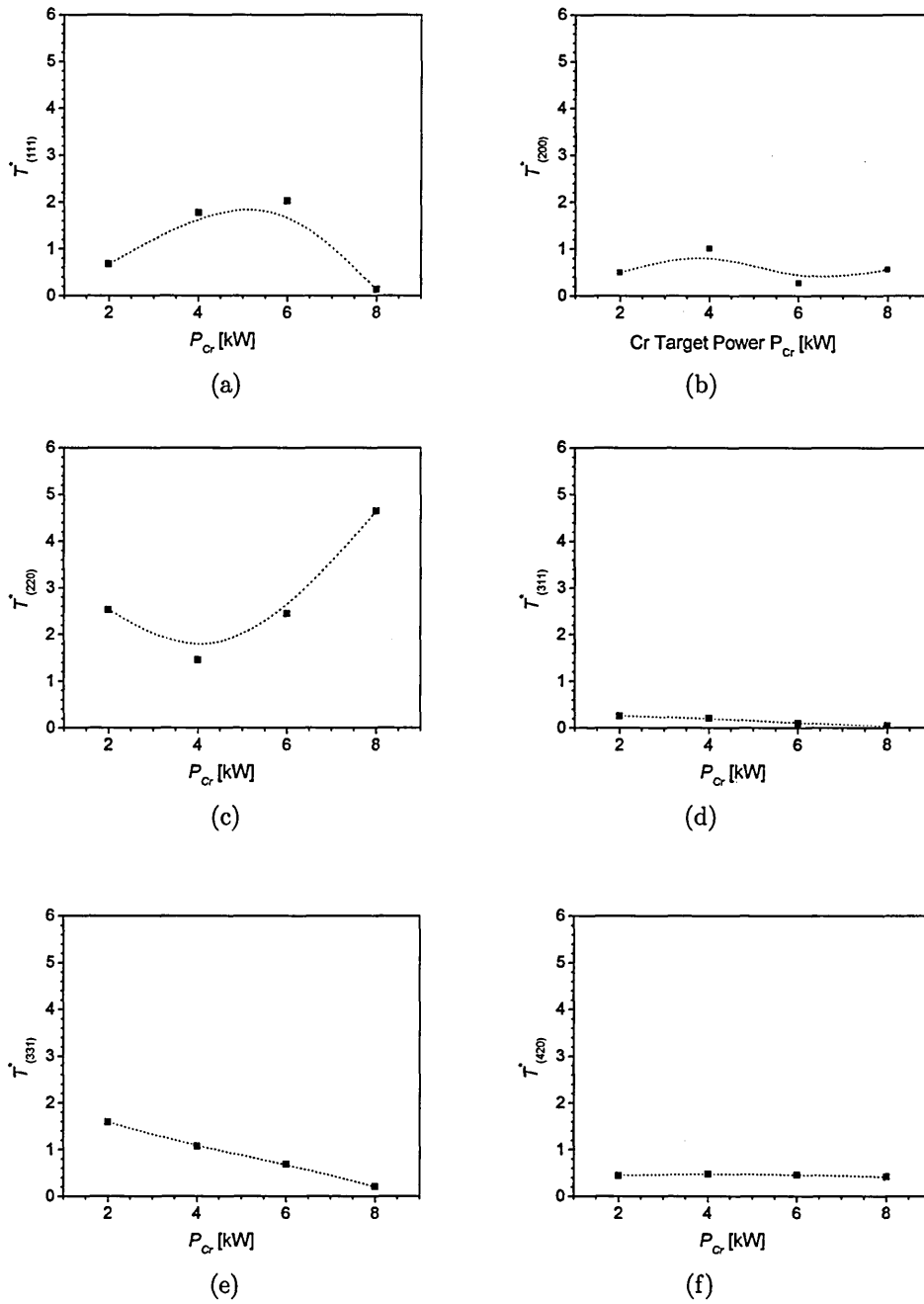
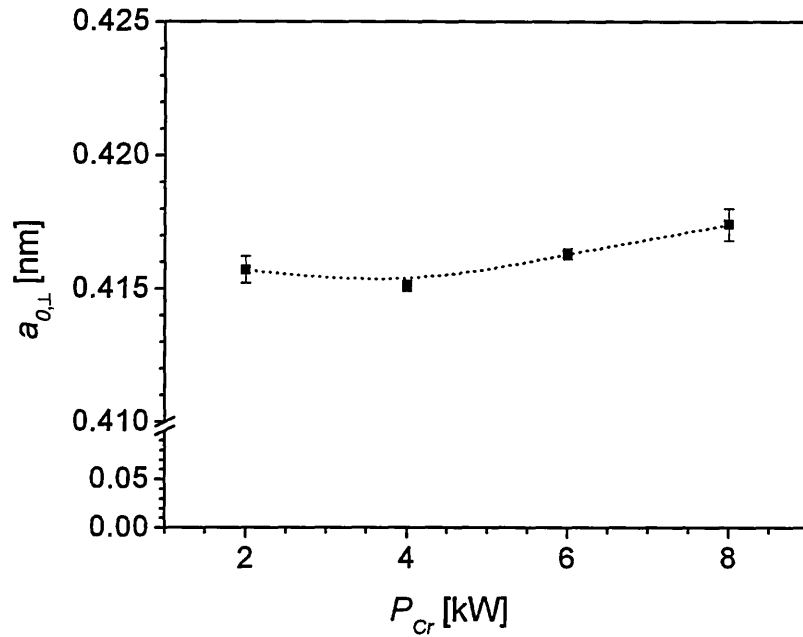
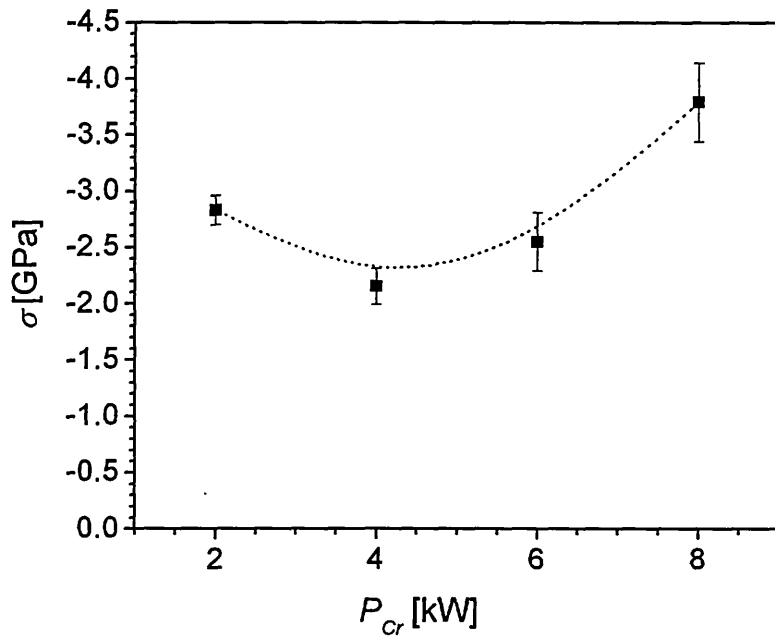


Fig. 5.56: Texture coefficients  $T^*_{(hkl)}$  as function of Cr target power  $P_{Cr}$



(a) Stressed lattice parameter  $a_{0,\perp}$



(b) Residual stresses  $\sigma$

Fig. 5.57: Stressed lattice parameter  $a_{0,\perp}$  and residual stress  $\sigma$  of CrAlYN/CrN deposited at various Cr target powers  $P_{Cr}$

pressive stresses within the films as the lattice expands perpendicular to the surface.

Determination of the residual stresses  $\sigma$  (see Fig. 5.57(b)) reveals compressive stresses in all coatings. The stress levels are in a medium range decreasing from -3.8 GPa for deposition at high  $P_{Cr}$  to -2.2 GPa for  $P_{Cr}= 4$  kW. The coating deposited at  $P_{Cr}$ , however, shows slightly higher  $\sigma$  of -2.8 GPa.

The ion bombardment can significantly affect the stress state of the coating, as shown in CrAlYN/CrN coatings grown at various substrate bias voltages  $U_b$  (see Fig. 5.23(b), Sec. 5.1.7). The TEM investigations of CrAlYN/CrN deposited under various  $P_{Cr}$  conditions reveal a reduction in coating densification, especially at the column boundaries (see Fig. 5.3.4). From this, it is suggested that the ion bombardment during deposition drops as  $P_{Cr}$  decreases. This diminution in ion bombardment is expected to introduce less defects in the growing structure and, hence, generate lower stresses. The increased stress in CrAlYN/CrN grown at  $P_{Cr}= 2$  kW may be related to the “near-monolithic” coating structure which significantly differs from the nanoscale multilayers. A similar correlation between  $P_{Cr}$  and the residual stresses was reported for TiAlN/CrN nanoscale multilayer films [188].

### 5.3.7 Hardness and Young’s Modulus

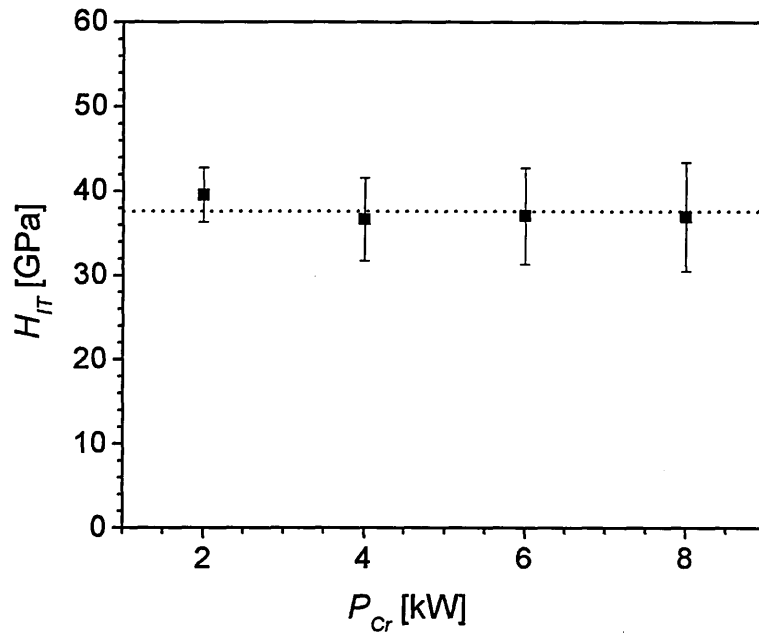
In the present study,  $H_{IT}$  is found to be in a range of 36 GPa to 39 GPa (see Fig. 5.58(a)). These values are constant within the error of the measurement.  $H_{IT}$ , therefore, seems to be independent of the variation in  $P_{Cr}$ .

Many factors can influence the coating hardness, such as residual stress  $\sigma$  and bi-layer thickness  $\Lambda$  as well as the grain or column size, respectively. Effects on hardness may act to oppose and compensate each other. Hardness may be induced by residual stresses  $\sigma$  in the film (see Sec. 5.1.7). Stress and hardness both originate from lattice defects and, for this reason, usually occur in combination [57]. In CrAlYN/CrN,  $\sigma$  decreases as  $P_{Cr}$  is lowered (see Fig. 5.57(b)). Thus,  $\sigma$  was mainly governing the hardness, a reduction in hardness would be

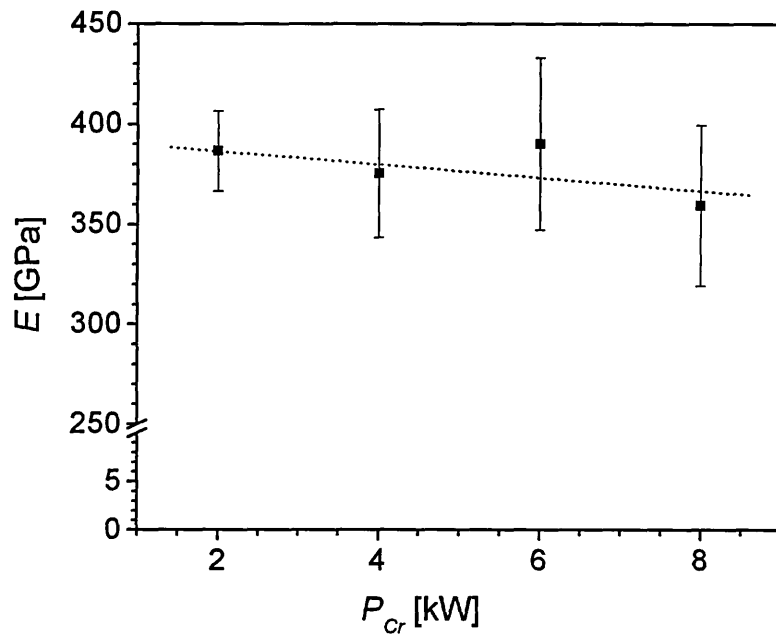
expected. Another important mechanism determining hardness in nanoscale superlattice coatings is the bi-layer thickness  $\Lambda$  [14]. The optimum film hardness is expected in films with a  $\Lambda$  between 5 nm and 12 nm and a thickness ratio of 1:1 between the individual layers. In CrAlYN/CrN, both parameters are changed by variation in  $P_{Cr}$  and, hence, CrN layer thickness.  $\Lambda$  is between 3.8 nm and 2.7 nm (see Fig. 5.42(b)). This is well below optimum reported in literature [14]. Additionally, the thickness ratio between CrN and CrAlYN is close to the optimum of 1 (0.97 in  $P_{Cr}= 8$  kW) but shifts further away from the designated ratio to a minimum value of 0.17 ( $P_{Cr}= 2$  kW) as  $P_{Cr}$  is reduced. If the layer structure is too thin, the resistance to the indenting body is only low as dislocation movements are only hindered inadequately and, thus, the nanolayer hardness is compromised. Assuming  $\Lambda$  was the only parameter determining the hardness, a decrease in hardness would be expected as  $P_{Cr}$  is reduced. Grain refinement as a hardening mechanism after the Hall-Petch relation is a well documented phenomenon [182]. In CrAlYN/CrN, the average column diameter  $d_c$  decreases with reduced  $P_{Cr}$  (see Fig 5.55). Assuming hardening due to grain refinement as only hardening mechanism, the hardness of CrAlYN/CrN would therefore increase with reduced  $P_{Cr}$ .

The fact, however, that the nano-hardness  $H_{IT}$  is not affected by a variation in  $P_{Cr}$  (see Fig. 5.58(a)) indicates joint action of different hardening mechanism with opposing effects. A possible decrease in hardness due to reduction in residual stresses  $\sigma$  and bi-layer thickness  $\Lambda$  may possibly be compensated by an increase in hardness caused by grain refinement at the same time. This, in turn, could result in constant hardness values which is independent of  $P_{Cr}$ .

The coating stiffness, characterised by of Young's modulus  $E$  (see Sec. 3.3.5.2), is found in a range of 385 GPa ( $P_{Cr}= 8$  kW) to 360 GPa ( $P_{Cr}= 2$  kW) (see Fig. 5.58(b)). It is known that CrN films have a lower elastic modulus  $E$  than CrAlN when deposited under similar conditions [119]. If a similar relation is true for CrN and CrAlYN, it is suggested that  $E$  increases as  $P_{Cr}$  is reduced and less CrN is introduced into the composite.



(a) Nano-hardness  $H_{IT}$



(b) Elastic modulus  $E$

Fig. 5.58: Nano-hardness  $H_{IT}$  and Young's modulus  $E$  of CrAlYN/CrN deposited at various Cr target powers  $P_{Cr}$

### 5.3.8 Adhesion

The coating adhesion was determined by means of scratch adhesion testing (see Sec. 3.3.3.1). High critical load values  $L_C$  rise from 65 N to 72 N as  $P_{Cr}$  is reduced (see Fig. 5.59). The scratch adhesion is determined by numerous factors, such as residual stresses and ductility. It is shown previously that high residual stresses  $\sigma$  lead to early adhesive failure at the substrate/coating interface (see Sec. 5.1.9). In the present case,  $\sigma$  decreases slightly from -3.8 GPa to -2.2 GPa as  $P_{Cr}$  is lowered (see Fig. 5.59). As a consequence, these coatings are better adherent. CrAlYN/CrN produced at  $P_{Cr}=2$  kW is unexpectedly well adherent with  $L_C=72$  N despite higher  $\sigma$  than in the coatings grown at  $P_{Cr}=4$  kW and 6 kW. Monolithic (Cr,Al)N coatings reveal improved adhesion, as the Cr atomic fraction is lowered and Young's modulus  $E$  increased [189]. This is due to the fact that thin films with higher elastic modulus are more resistant to plastic deformation and therefore exhibit higher  $L_C$  values [155]. CrAlYN/CrN coatings also have a higher stiffness with lower  $P_{Cr}$  and, consequently, lower Cr content (see Fig. 5.58(b)). It is suggested that the increase in  $L_C$  values for deposition at  $P_{Cr}$  is related to this

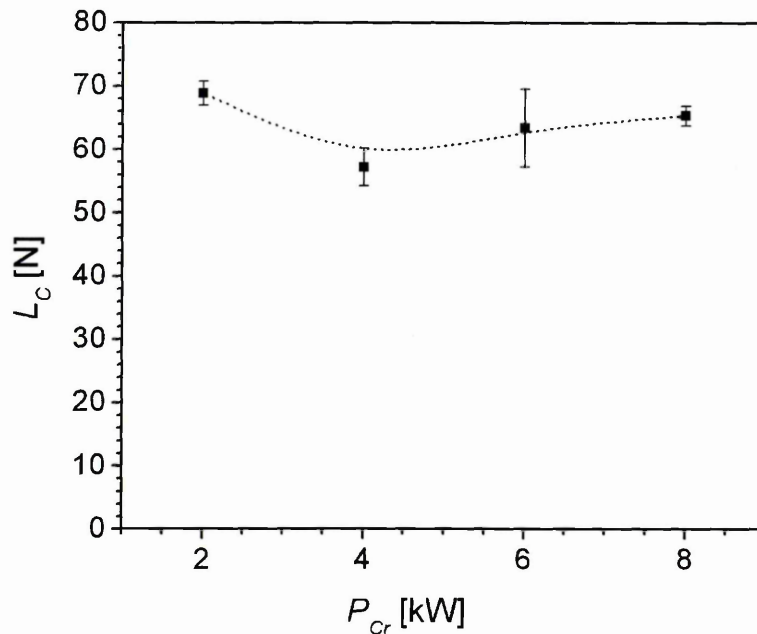


Fig. 5.59: Critical Load values  $L_C$  as a function of Cr target power  $P_{Cr}$

enhanced stiffness.

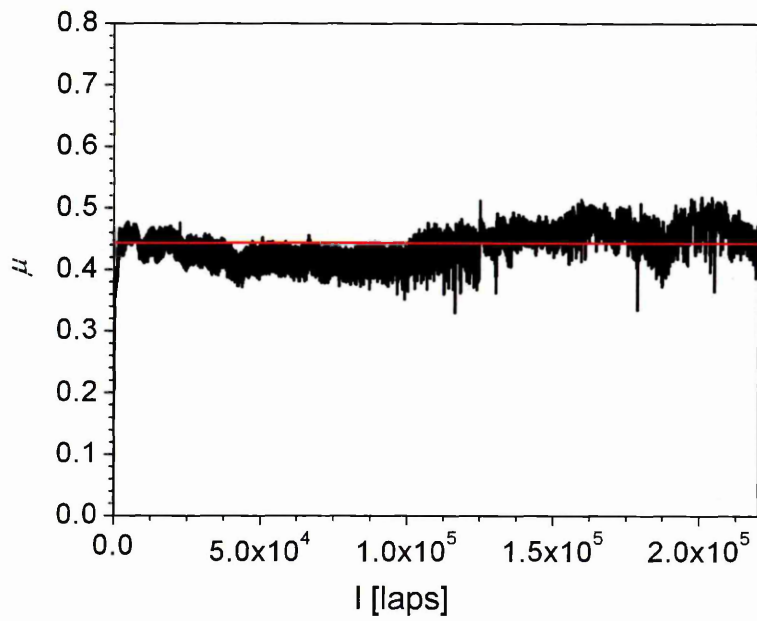
### 5.3.9 Friction and Dry Sliding Wear

CrAlYN/CrN coatings were tested on a pin-on-disk tribometer in dry sliding conditions (see Sec. 3.3.4). All obtained friction curves (see Fig. 5.60) show smooth and steady friction values up to very high sliding distances  $l= 200.000$  laps. The friction coefficient  $\mu$  is in a range of 0.45 to 0.5 for sliding contact against a  $\text{Al}_2\text{O}_3$  counterpart (see Fig. 5.61). The lowest value is obtained for deposition at  $P_{Cr}= 8$  kW. The sliding wear coefficient  $k_S$  is on a very low level of  $4.5 \times 10^{-17} \text{ m}^3 \text{ N}^{-1} \text{ m}^{-1}$  at  $P_{Cr}= 8$  kW (see Fig. 5.62). This values slightly increases for a change in  $P_{Cr}$  to 4 kW and then shows a strong rise by nearly one order of magnitude to  $2.2 \times 10^{-16} \text{ m}^3 \text{ N}^{-1} \text{ m}^{-1}$  for  $P_{Cr}= 2$  kW.

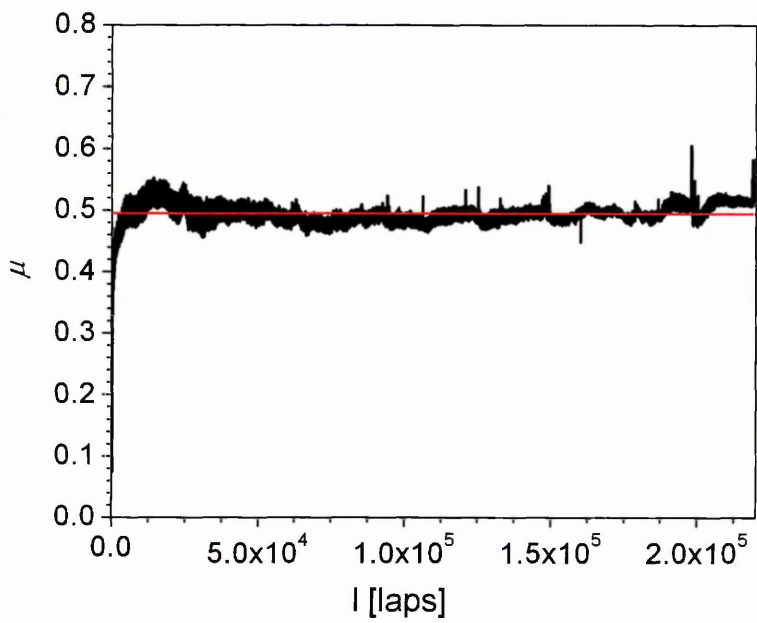
Wear particles found on the surface of the coating after testing have a variety of sizes with the dimensions ranging from a few tens up to several hunderends of nanometers (see Fig. 5.63).

Relating the wear behaviour to the coating microstructure, it is known that CrAlYN/CrN grown at  $P_{Cr}= 8$  kW reveals a dense columnar microstructure (see Fig. 5.50) with a pronounced nanolayer structure. This structure has been defined as beneficial for low wear rates [190]. Few wear particles are generated during the test and, hence, a low  $\mu$  is achieved. As  $P_{Cr}$  decreases to 4 kW, the coating changes to an open columnar structure (see Fig. 5.49). The interspaces between the individual columns are in range of hundreds of nanometers. In such structures, the very small wear particles can become canted at the inter-columnar spaces. This cant can then increase the adhesion between the sliding partners and, as a result, cause enhanced adhesive wear [190].

CrAlYN/CrN grown at  $P_{Cr}$  with its “near-monolithic” growth structure reveals the highest wear rate. A comparison of monolithic and nanolayered coatings [185] suggests that monolithic coatings reveal higher wear rates as wear particles are removed from the coating due to crack propagation along the column boundaries. It is assumed that a similar mechanism is responsible for the some-

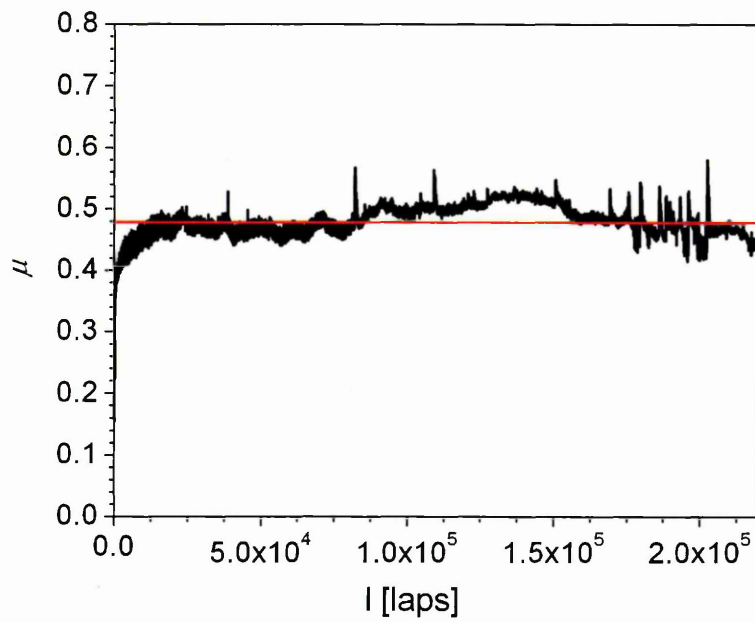


(a)  $P_{Cr} = 8 \text{ kW}$

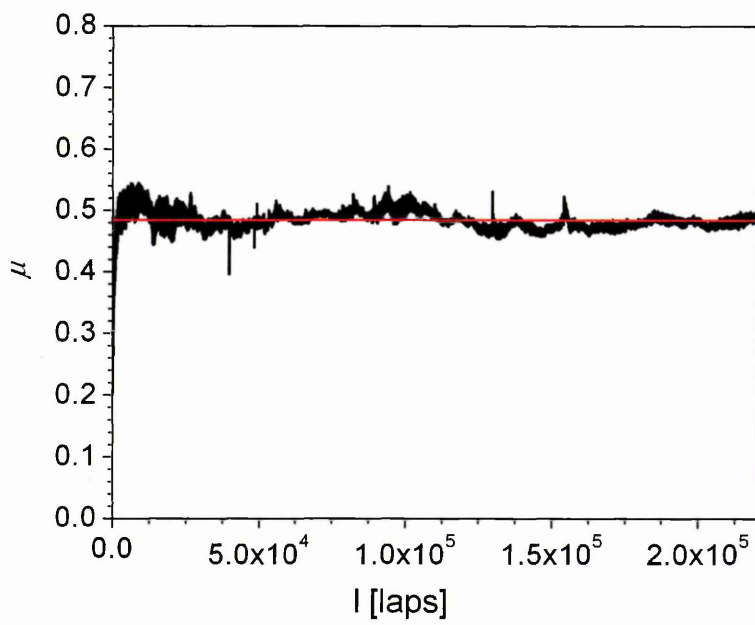


(b)  $P_{Cr} = 6 \text{ kW}$

Fig. 5.60: Friction curves of CrAlYN/CrN deposited at various Cr target powers  $P_{Cr}$



(c)  $P_{Cr} = 4$  kW



(d)  $P_{Cr} = 2$  kW

Fig. 5.60: Continued

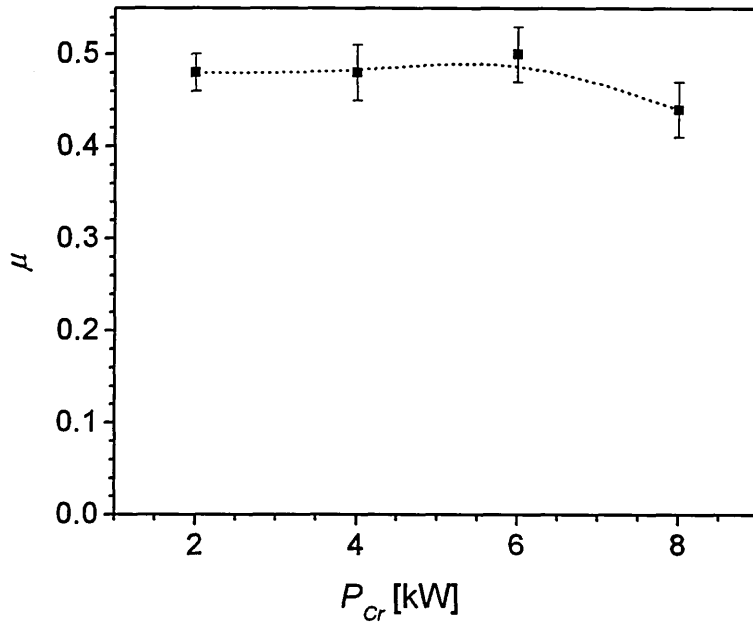


Fig. 5.61: Friction coefficient  $\mu$  of CrAlYN/CrN as function of Cr target power  $P_{Cr}$

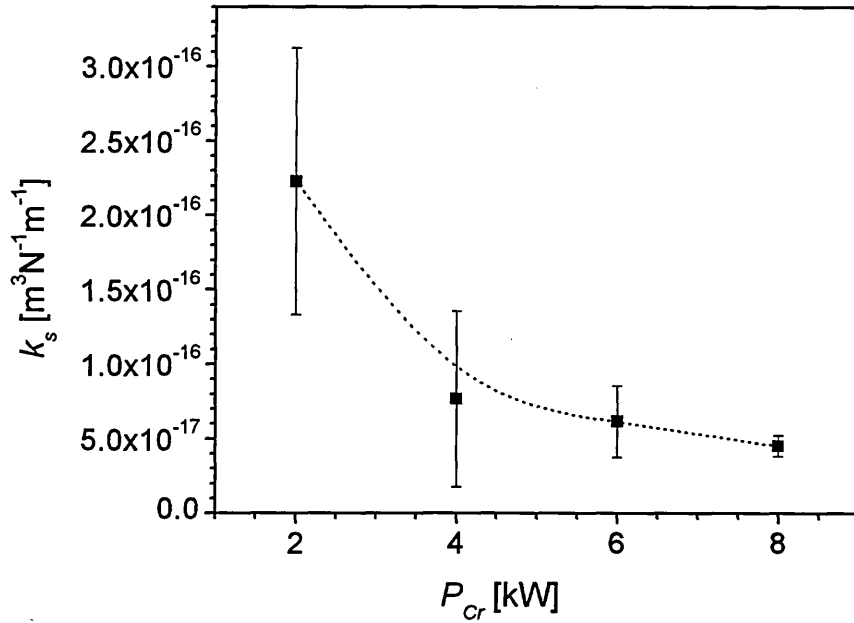


Fig. 5.62: Dry sliding wear coefficient  $k_s$  of CrAlYN/CrN as function of Cr target power  $P_{Cr}$

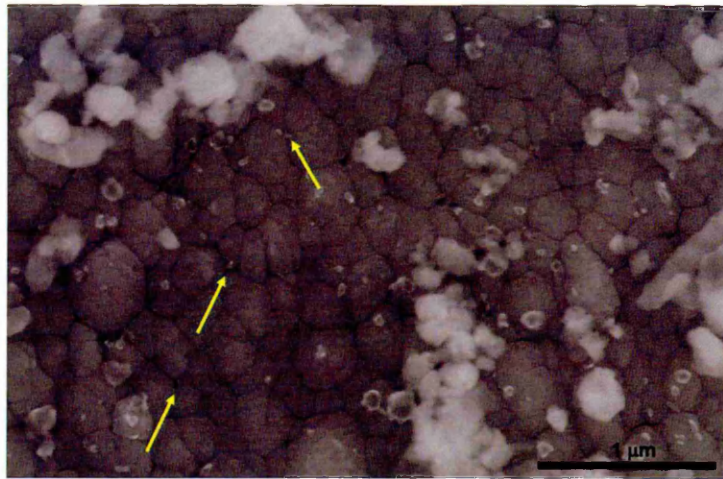


Fig. 5.63: Wear particles on the surface of CrAlYN/CrN grown at  $P_{Cr} = 2$  kW after sliding against  $Al_2O_3$  for 200,000 laps

what increased  $k_S$  in CrAlYN/CrN grown at  $P_{Cr} = 2$  kW.

## 5.4 Chapter Summary

This section gives a summary of the structure and properties of CrAlYN/CrN grown under various deposition conditions. Here, two process parameters were changed during the deposition: (i) the energy of the bombarding ions during the growth process and (ii) the chemical composition of the coating.

The energy of the impinging ions at the growing films was changed by a variation in the substrate bias voltage  $U_b$  between -75 V and -150 V. The investigated CrAlYN/CrN are sub-stoichiometric in their chemical composition and have an excess in the metal component (metal/N ratio  $\sim 1.5$ ) and have an approximately equal Cr and Al atomic fraction (Cr/Al ratio  $\sim 0.90$ ). These coatings contain only low atomic fractions of Y ( $\sim 0.5\text{at}\%$ ). CrAlYN/CrN with this composition forms a pseudo-binary B1 fcc single phase lattice structure. The chemical composition and the phase composition are therefore not affected by  $U_b$  and, hence, the energetic ion bombardment. CrAlYN/CrN deposited at low  $U_b = -75$  V exhibits a polycrystalline columnar morphology with inter-columnar voids. As  $U_b$  is increased to -95 V, the coating is densified, the column boundaries are void-free and the curvature of the nanolayers decreases. When further increasing  $U_b$ , a coating structure with coexisting polycrystalline columnar and single crystal domains form. These single crystals are limited to the CrAlN base layer region at  $U_b = -120$  V, but extend all the way to the column tops for  $U_b = -150$  V. The novel CrAlYN/CrN coatings exhibit a coating morphology which is strongly dependent on  $U_b$ . The observed structures are consistent with those predicted by Messier's structure zone model [66]. An increase in  $U_b$  causes a change in the preferred crystallographic orientation of CrAlYN/CrN from (110) at  $U_b = -75$  V to (111) at higher  $U_b \geq -95$  V. The increase in  $U_b$  also causes high compressive residual stresses up to -9.5 GPa ( $U_b = -150$  V) which are accompanied by a strong increase in hardness. This higher hardness, combined with the curvature-free nanolayer structure, is beneficial for the wear resistance and results in a reduction in the wear rate  $k_S$  by one order of magnitude from already low  $2.7 \times 10^{-16} \text{ m}^3 \text{ N}^{-1} \text{ m}^{-1}$  to extremely low  $4.7 \times 10^{-17} \text{ m}^3 \text{ N}^{-1} \text{ m}^{-1}$ . The excellent substrate/coating adhesion,

which is provided by the HIPIMS substrate pre-treatment, ranges from critical load values  $L_C$  of 41 N to 61 N with the lower  $L_C$  values in the highly stressed coatings. In summary, the analysis of the coating microstructure, the mechanical and tribological properties reveals that the performance of CrAlYN/CrN is strongly dependent on  $U_b$  and, hence, the energy of the impinging ions during the growth process.

The chemical composition of CrAlYN/CrN was controlled by a variation in the power  $P_{Cr}$  on the Cr target in a range of 8 kW to 2 kW during the nanolayer deposition. Coatings grown at high  $P_{Cr}= 8$  kW have an equal atomic fraction of Cr and Al (Cr/Al ratio  $\sim 0.90$ ) whereas coatings grown at low  $P_{Cr}= 2$  kW are rich in Al (Cr/Al ratio  $\sim 0.56$ ). This reduction in Cr content goes along with thinner CrN nanolayers in the multilayer structure. The deposition at  $P_{Cr}$  reduced the Cr thickness by an extent that the layers are not clearly defined and a “near-monolithic” structure forms. All investigated CrAlYN/CrN grow in a B1-fcc lattice structure. The phase composition is therefore not influenced by the change in  $P_{Cr}$  in the investigated range. High  $P_{Cr}$  CrAlYN/CrN coatings have a pronounced (110) crystallographic orientation. This orientation diminishes and the crystals grow in nearly random orientations as  $P_{Cr}$  is reduced. This change in texture is caused by the removal of the (110) growth promoting CrN. Regarding the mechanical performance, all studies CrAlYN/CrN coatings have medium residual stresses  $\sigma$  in a range of -2.8 GPa to -3.7 GPa, an equal hardness  $H_{IT}$  of  $\sim 3000$  GPa and identical friction coefficients  $\mu$  of  $\sim 0.47$ . These properties are therefore only marginally affected by a change in  $P_{Cr}$  and, hence, chemical composition. The wear rates, in contrast, strongly increase as  $P_{Cr}$  is reduced. This declining wear resistance may be caused by a reduction in the CrN layer thickness and a possibly occurring change in the wear mechanism from nanolayer delamination to crack propagation. To conclude, the investigation of the CrAlYN/CrN coatings show that the microstructure and most mechanical and tribological properties remain unaffected by a change in  $P_{Cr}$  and the resulting variation in chemical composition.

# CHAPTER 6

---

---

## Oxidation Behaviour of CrAlYN/CrN

---

---

This chapter presents a study of the oxidation behaviour of CrAlYN/CrN. In the first part, the short term isothermal oxidation of 1 h up to high temperatures of 1000°C is analysed. Following this, the long term oxidation for up to 100 h exposure time at 850°C is investigated. Subsequently, the impact of various process parameters, including ion bombardment and chemical composition, on the oxidation performance of CrAlYN/CrN films is discussed.

### 6.1 Thermogravimetric Analysis

Dynamic thermogravimetric (TG) analysis (see Sec. 3.4.1) was performed to investigate the oxidation behaviour of CrAlYN/CrN (standard deposition parameters  $U_b = -75$  V and  $P_{Cr} = 8$  kW) grown on 304 stainless steel (SS) substrates. TG analysis can be used for a fast and exact comparison of the oxidation performance of various coating/substrate systems, as it gives information on the rate of weight gain  $\rho$  as well as the transition temperatures  $T$  at which changes in the fitted linear slope of  $\rho$  occur.

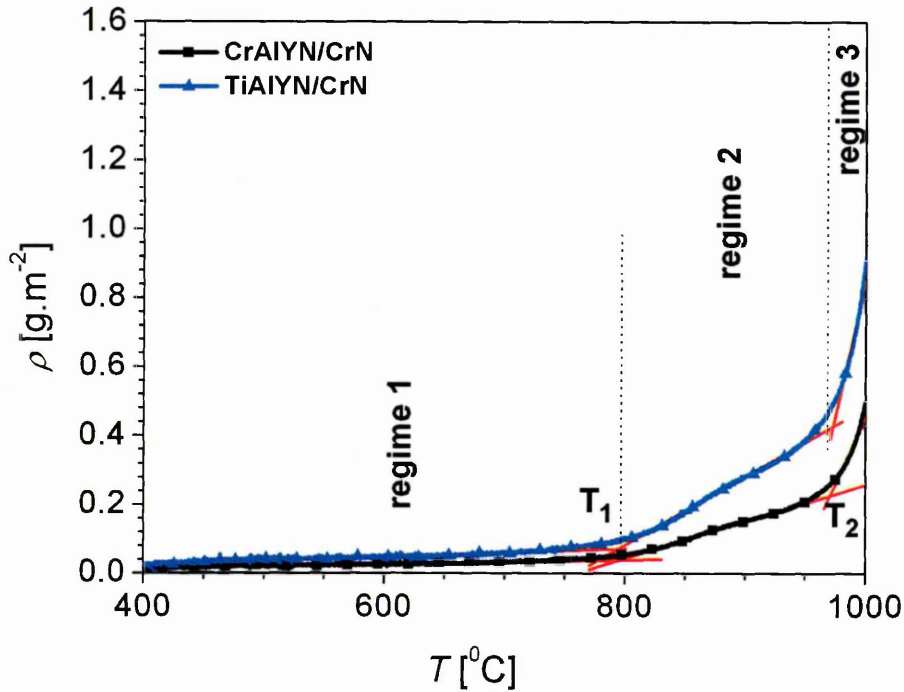


Fig. 6.1: Dynamic thermogravimetric data of CrAlYN/CrN and TiAlYN/CrN on 304 stainless steel substrates for thermal ramping at  $5 \text{ K}\cdot\text{min}^{-1}$  in dry air

The weight gain  $\rho$  of CrAlYN/CrN as a function of temperature  $T$  is presented in Fig. 6.1. In this, three distinct regions can be clearly distinguished. Below a transition temperature of  $T_1 = 800^\circ\text{C}$ , weight gain takes place at a low rate of  $0.6 \times 10^{-5} \text{ g}\cdot\text{m}^{-1}\text{K}^{-1}$ . Above  $800^\circ\text{C}$ , a higher rate of  $1.1 \times 10^{-3} \text{ g}\cdot\text{m}^{-1}\text{K}^{-1}$  can be observed. This rate increases furthermore to  $5.2 \times 10^{-3} \text{ g}\cdot\text{m}^{-1}\text{K}^{-1}$  above  $T_2 = 970^\circ\text{C}$ . From this, the onset temperature of rapid oxidation can be derived to  $970^\circ\text{C}$ . It is assumed that the different weight gain rates are associated with different oxidation processes occurring upon heating. A discussion will be given at a later stage (see Sec. 6.2.5) after detailed analysis of these processes in isothermal testing.

Additionally, Fig. 6.1 compares the weight gain of CrAlYN/CrN to a recently developed TiAlYN/CrN film [191] used as coating for cutting tools. The weight gain  $\rho$  of TiAlYN/CrN (weight gain rates of  $1.5 \times 10^{-4} \text{ g}\cdot\text{m}^{-1}\text{K}^{-1}$  below  $585^\circ\text{C}$ ,  $2.0 \times 10^{-3} \text{ g}\cdot\text{m}^{-1}\text{K}^{-1}$  between  $585^\circ\text{C}$  and  $950^\circ\text{C}$ ,  $5.2 \times 10^{-2} \text{ g}\cdot\text{m}^{-1}\text{K}^{-1}$ ) is higher by up to one order of magnitude and, moreover, the onset of rapid oxidation is at  $950^\circ\text{C}$

lower than in CrAlYN/CrN. This significantly improved oxidation resistance of CrAlYN/CrN is related to the removal of the highly reactive Ti from the thin film. Superior oxidation behaviour in Ti-free films was already reported when comparing CrN/AlN and TiN/AlN films [192].

In conclusion, TG analysis as a fast oxidation experiment permits the identification of three different oxidation regimes as a function of temperature. However, no information about the actual oxidation processes in the coating can be retrieved. The following sections describe a more detailed investigation of the oxidation behaviour at high temperatures.

## 6.2 Short Term Oxidation for 1 h up to 1000°C

This section investigates the oxidation mechanisms taking place during short term isothermal oxidation testing of CrAlYN/CrN for 1 h at different temperatures between 850°C and 1000°C. The knowledge of oxidation processes in the chosen exposure and temperature regime is of importance in applications such as dry high speed milling where the typical tool life time are in a range of 1 h [193] and temperatures at the tool surface exceed  $\geq 950^\circ\text{C}$  [191].

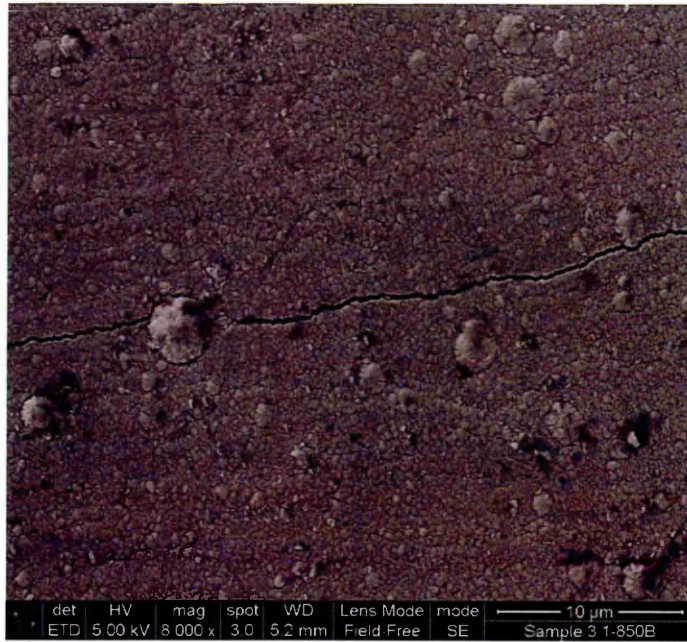
### 6.2.1 Reactions after 1 h at 850°C

The oxidation performance of CrAlYN/CrN coatings exposed to air for 1 h at 850°C was investigated after the heat-treatment using a variety of different analysis techniques.

SEM surface observations (see Sec. 3.2.3) can give information on the appearance of the film surface before and after heat-treatment. The chemical composition can be determined by means of EDS analysis (see Sec. 3.2.3). The film surface was investigated after heat-treatment (see Fig. 6.2). After 1 h heat-treatment at 850°C, the initial film surface remains smooth and does not oxidise visibly (see Fig. 6.2(a)). However, network of cracks is observed (see Fig. 6.2(a)). Despite the appearance of cracks, the heated coating is well adherent and does not spall off.

The presence of O in the film is demonstrated by EDS analysis with an O content of  $\sim 5\text{at}\%$  (see Fig. 6.3). Additionally, a Cr/Al ratio of  $\sim 1.66$  is found which increases from  $\sim 1.63$  (measured from the CrK-AlK line ratio obtained by EDS) in the as-deposited state (see Fig. 6.3(c)). The presence of O in the coating signifies that surface oxidation takes place after heat-treatment for 1 h at 850°C. The increasing Cr/Al ratio implies an increase in Cr atomic fraction which may arise from Cr diffusion from the substrate into the coating.

The crack propagation in the coating may be correlated to the generation of thermal stresses  $\sigma_{th}$  which arise due to the mismatch in thermal expansion coefficient  $\alpha$  between the individual components [19].  $\sigma_{th}$  can be estimated according

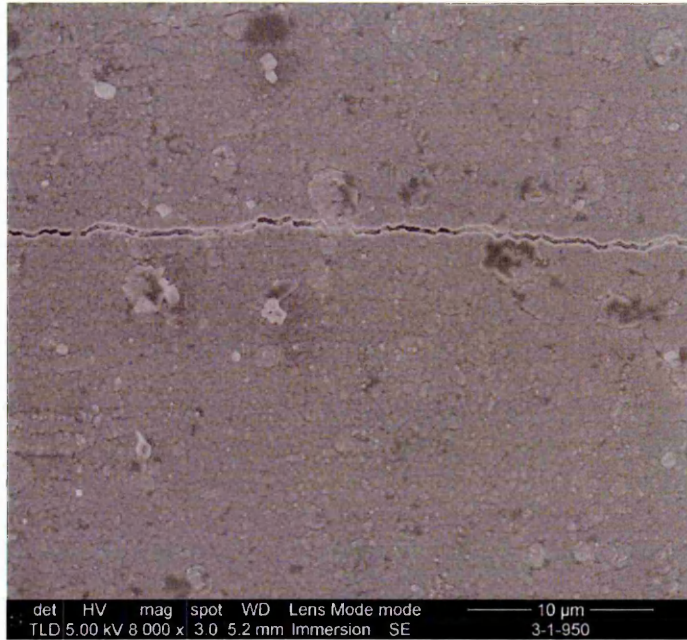


(a) 850°C

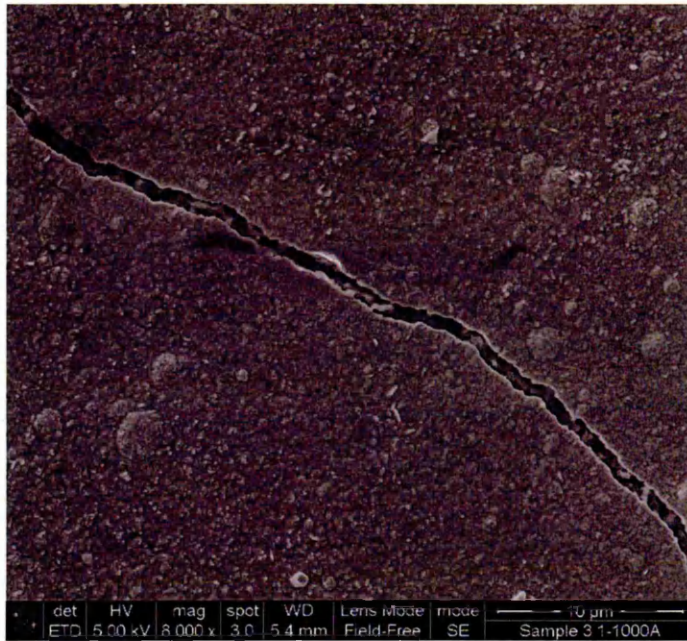


(b) 900°C

Fig. 6.2: SEM micrographs of the coating surface after isothermal heat-treatment in laboratory air for 1 h at different temperatures: Cracks open in the coating and small oxide crystals form on the surface as the temperature is increased



(c) 950°C



(d) 1000°C

Fig. 6.2: Continued

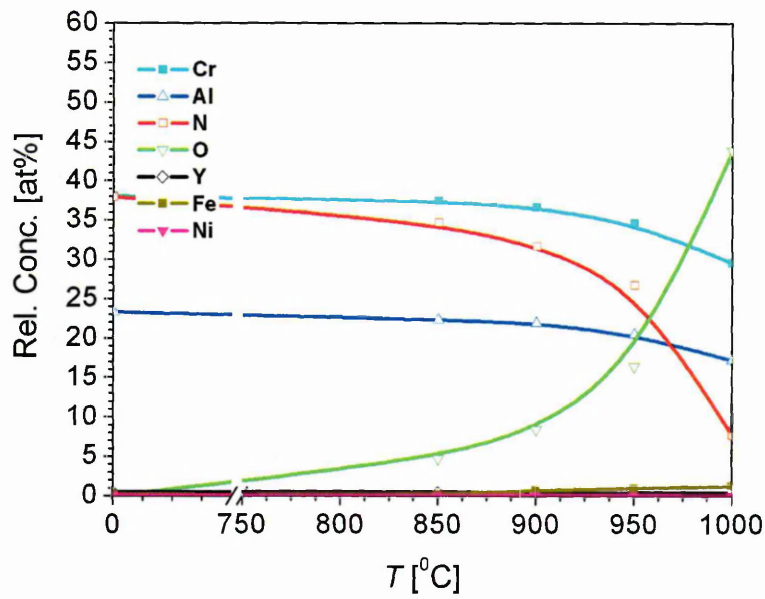
to the following equation:

$$\sigma_{th} = \frac{E_{CrAlYN/CrN}}{1 - \mu_{CrAlYN/CrN}} - \frac{\alpha_{CrAlYN/CrN} - \alpha_{304SS}}{T_d - T} \quad (6.1)$$

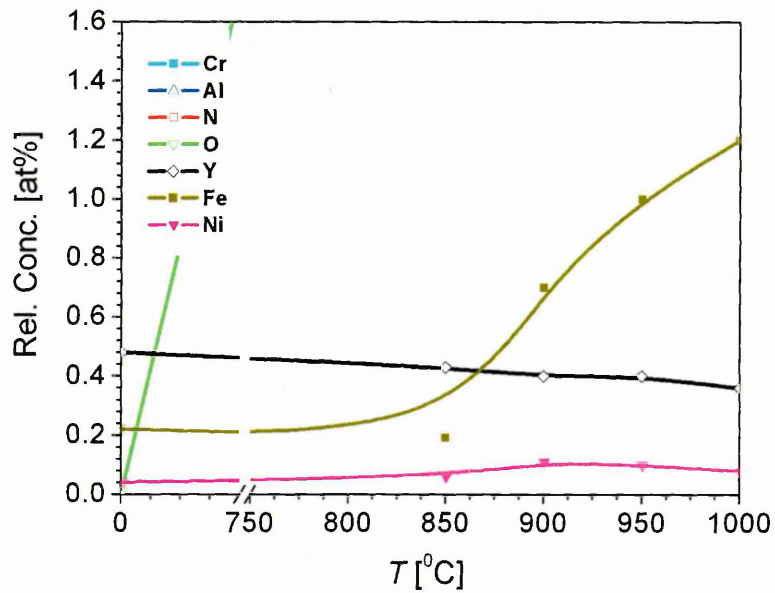
Here,  $\alpha$  represents the thermal expansion coefficient of coating and substrate ( $\alpha_{CrAlYN/CrN}$  and  $\alpha_{304SS}$ , respectively),  $T_d$  the deposition temperature and  $T$  the heat-treatment temperature.  $\mu_{CrAlYN/CrN}$  is the Poisson's ratio and  $E_{CrAlYN/CrN}$  is the Young's modulus (see Sec. 5.1.8) of the coating.  $\alpha_{CrAlYN/CrN}$  is derived to be  $4.6 \times 10^{-6} \text{K}^{-1}$  from linear extrapolation of the expansion coefficients of the binary components CrN ( $\alpha_{CrN} = 3.5 \times 10^{-6} \text{K}^{-1}$  [103]) and AlN ( $\alpha_{AlN} = 5.5 \times 10^{-6} \text{K}^{-1}$  [194]).  $\alpha_{304SS}$  is  $17.3 \times 10^{-6} \text{K}^{-1}$  [195].  $\mu_{CrAlYN/CrN}$  is estimated to 0.3 as no other data is available. If tensile stresses  $\sigma_{th}$  exceed the residual stresses  $\sigma$  of the coating, cracking occurs. These cracks then permit fast pathways for the oxidising medium to the substrate and allow the oxidation of the substrate. For purely theoretical considerations, i.e. ignoring stress relief, the temperature at which cracking in CrAlYN/CrN is expected to appear is estimated to 830°C. Cracks in the coating are observed after heating to 850°C (see Fig. 6.2) and therefore in well agreement with the above estimation.

XRD analysis at a glancing angle  $\gamma = 2^\circ$  and an X-ray penetration depth  $z_{1/e}$  of  $\sim 560$  nm allows the determination of changes in the phase composition (see Sec. 3.2.2). GA-XRD patterns of the as-deposited coating and films after a 1 h heat-treatment at different temperatures are shown in Fig. 6.4. At 850°C, all observed reflections can be unambiguously identified as reflections of the CrAlYN/CrN phase (see Fig. 5.4, Sec. 5.1.2). CrAlYN/CrN is therefore the only phase.

Cross-sectional TEM investigations (see Sec. 3.2.4) give information on the thin film microstructure after heat-treatment. Imaging of the bulk coating (see Fig. 6.5) reveals large columnar grains. A SAD pattern (see insert in Fig. 6.5) clearly reveals only reflections related to the CrAlYN/CrN phase. The nanolayers (not shown) are similar to the structure in as deposited state (see Fig. 5.11, Sec. 5.1). The preservation of the coating features gives evidence of low interdif-

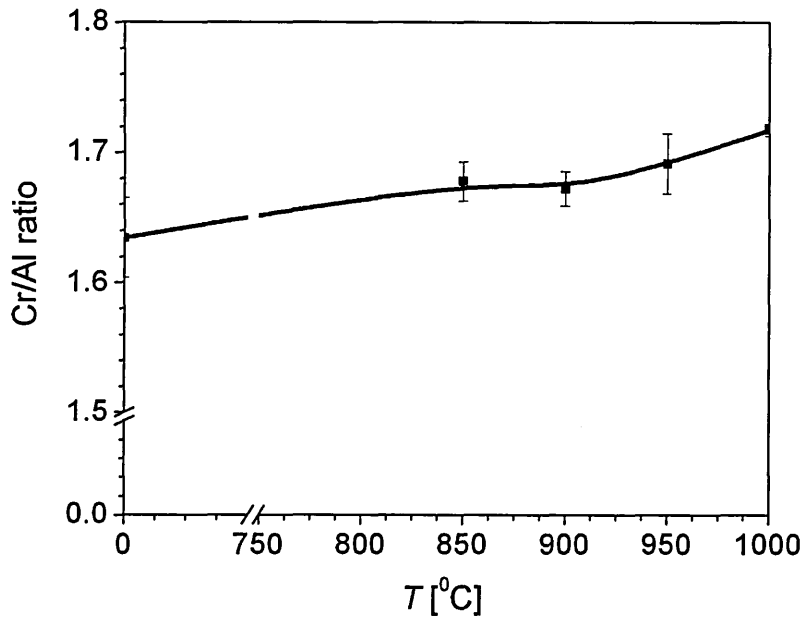


(a)



(b)

Fig. 6.3: (a) Relative coating composition after O uptake after isothermal heat-treatment in laboratory air for 1 h up to 1000°C and (b) zoom in the concentration range 0-1.6 at% and (c) Cr/Al ratio as a function of temperature  $T$ , analysed by EDS



(c)

Fig. 6.3: Continued

fusion between the individual layers and bulk CrAlYN/CrN after heat-treatment at 850°C remains unaltered by the heat-treatment. The TEM analysis confirms the thermal stability of CrAlYN/CrN at 850°C which was already shown in the GA-XRD investigation (see Fig. 6.4).

Fig. 6.6 shows a BF micrograph taken from the top region of the CrAlYN/CrN film with a  $20 \pm 7$  nm thick layer, located underneath the previously mentioned Cu-redeposit (see Sec. 3.2.4). TEM-EDS analysis shows that this layer consists of Cr, Al and O and is an oxide scale that formed during the high temperature heat-treatment. N as a light element cannot be detected as the TEM-EDS analysis is restricted to O as the lightest element (see Sec. 3.2.4). In the bulk coating, in contrast, only Cr and Al are detected indicating that the O uptake is limited to the top surface and diffusion into the bulk via volume diffusion processes does not take place after 1 h heat-treatment at 850°C.

It is evident that TEM can verify the presence of a nano-scale oxide on top of the thin film whereas GA-XRD cannot identify new phases in the film after the

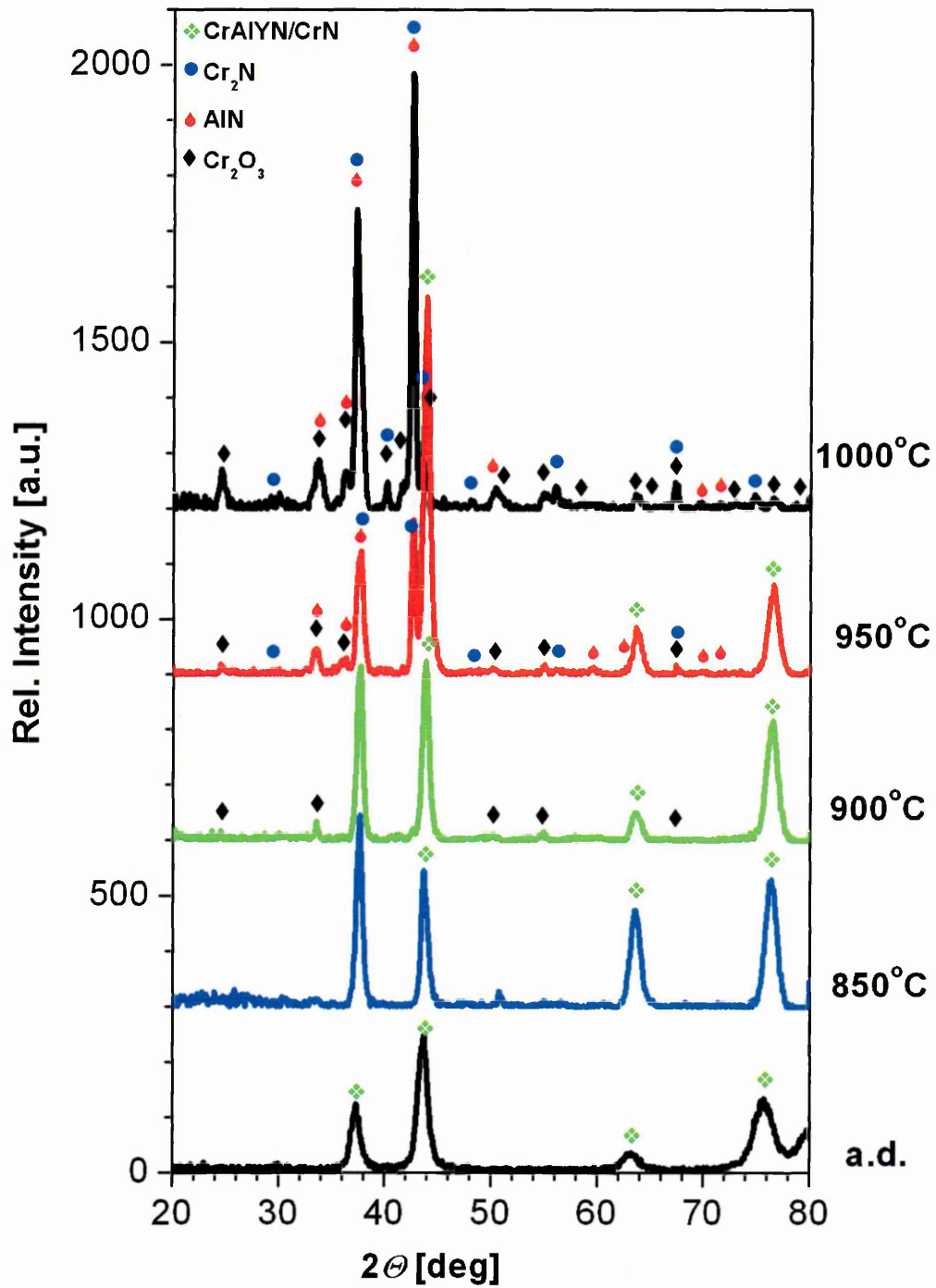


Fig. 6.4: GA-XRD pattern (incident angle  $\gamma = 2^\circ$ ) obtained from CrAlYN/CrN after heat-treatment in laboratory air for 1 h up to 1000°C

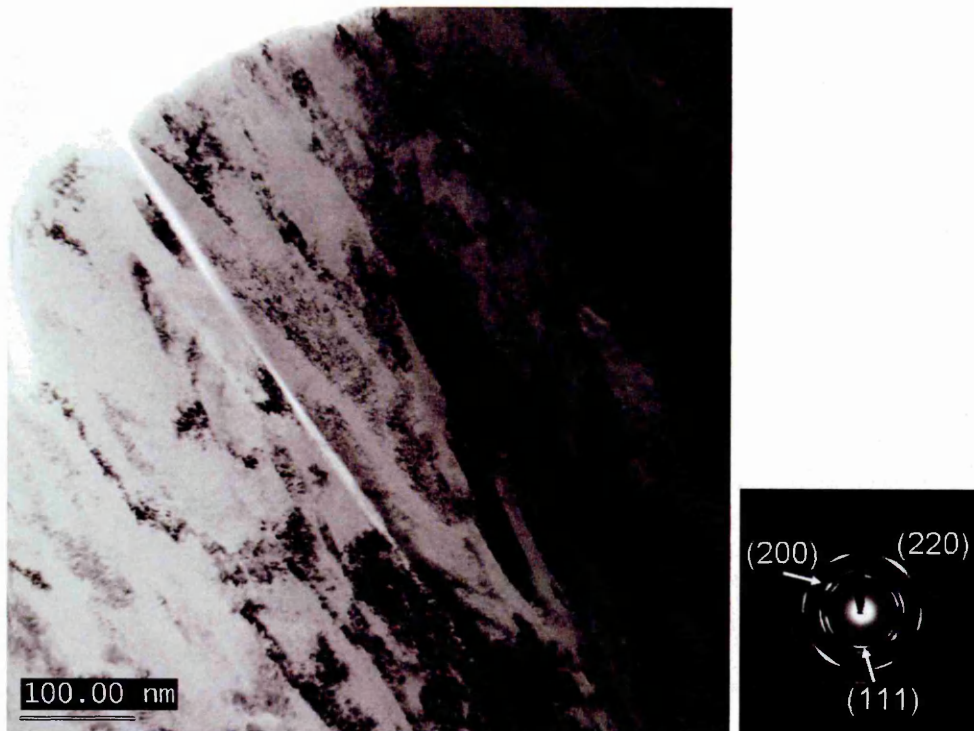


Fig. 6.5: BF-TEM micrograph and the corresponding SAD pattern taken from the bulk CrAlYN/CrN after heat-treatment in laboratory air at 850°C: A columnar coating structure with a pronounced texture is present

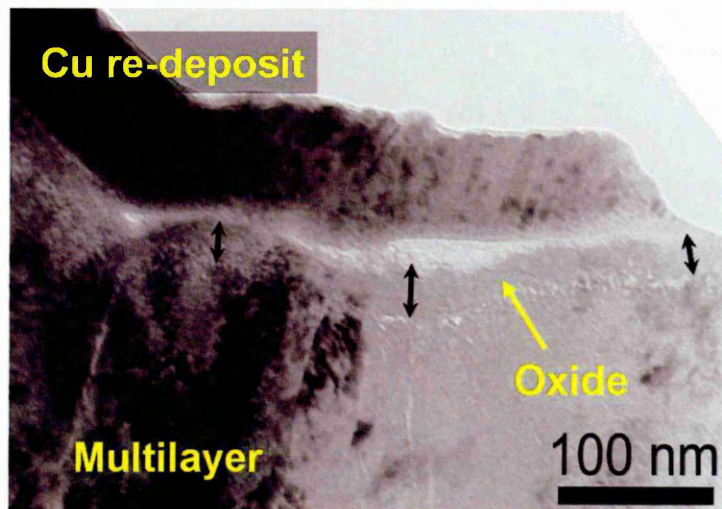


Fig. 6.6: BF-TEM micrograph of the oxide scale grown on CrAlYN/CrN after heat-treatment in laboratory air at 850°C (A Cu-redeposit forms on top of the oxides as an artifact from the TEM preparation)

heat-treatment. The discrepancy between these results are most probably due to the limitations in the GA-XRD method to detect phases with extremely small volumes if their relative contribution in reflection intensity of the oxide phases is extremely low.

To summarise, CrAlYN/CrN retains its nanoscale multilayer upon heating to 850°C. During this treatment, a thin, dense (Cr,Al)-oxide scale forms on the coating surface. Importantly, heating result in the formation of cracks which can act as fast access pathways for the oxidising medium.

### 6.2.2 Reactions after 1 h at 900°C

The study of dynamic TG data of CrAlYN/CrN (see Fig. 6.1) with its increase in weight gain in regime 2 (measured to 60% between 850°C and 900°C) gives strong evidence of accelerated oxidation processes at the higher temperature.

The effect of isothermal heat-treatment at 900°C on the oxidation performance of CrAlYN/CrN was analysed from SEM surface observations (see Fig. 6.2(b)). Large numbers of cracks appear inside the coating (see Fig. 6.2(b)). The higher extent of cracking is most probably related to higher thermal stresses that are present in CrAlYN/CrN at 900°C compared to 850°C (see Eq. 6.1). CrAlYN/CrN remains attached to the substrate and indicates good coating adhesion after the heat-treatment. Despite the presence of cracks, the coating surface remains relatively smooth and free of large oxide crystals (see Fig. 6.2(b)), indicating good oxidation performance. EDS analysis, however, confirms an increase in O content ( $\sim 9.5\text{at}\%$ ) (see Fig. 6.3). It is therefore suggested that surface oxidation takes place at a very low rate. The detection of Fe ( $\sim 0.6\text{at}\%$ ) (Fig. 6.3(b)) and the increase in Cr/Al ratio (from  $\sim 1.63$  in the as-deposited state to  $\sim 1.67$ ) (see Fig. 6.3(c)) implies the diffusion of Fe and Cr from the 304 stainless steel substrate into the coating.

The GA-XRD pattern (see Fig. 6.4) reveals numerous reflections. From the measured  $2\theta$  positions, the corresponding lattice spacing  $d$  (see Eq. 3.1, Sec. 3.2.2) is calculated and then used to identify the phases which are present (see Tab. 6.1).

Tab. 6.1: Possible phases identified by GA-XRD (see Fig.6.4) in CrAlYN/CrN heat-treated for 1 h at 900°C (Multiple listing indicates more than one possible candidate per peak and/or peak overlap)

No.	$2\theta$ [°]	$d$ [nm]	Candidates	
			fcc-CrN (JCPCD 76-2494) $d_{(hkl)}$ [nm] (hkl)	romb-Cr <sub>2</sub> O <sub>3</sub> (JCPCD 74-0326) $d_{(hkl)}$ [nm] (hkl)
1	24.40	0.360		0.363 (012)
2	33.48	0.267		0.266 (104)
3	37.54	0.239	0.239 (111)	
4	41.05	0.219		0.218 (113)
5	43.73	0.207	0.207 (200)	
6	58.88	0.156		0.158 (018)
7	63.50	0.146	0.146 (220)	0.146 (214)

The typical reflections of the pseudo-binary CrAlYN/CrN phase (see Fig. 5.4, Sec. 5.1.2) are detected. Additional reflections are observed (e.g. at  $2\theta = 24.40^\circ$ ,  $41.05^\circ$  and  $58.88^\circ$ ) and can be clearly matched to a corundum-type Cr<sub>2</sub>O<sub>3</sub> phase (rhombohedral Eskolaite, JCPCD 74-0326). The Cr<sub>2</sub>O<sub>3</sub> Eskolaite phase is believed to form during surface oxidation of CrAlYN/CrN. The oxidation of CrN films is suggested to take place via a replacement mechanism during which the N in the CrN phase is replaced by O to form Cr<sub>2</sub>O<sub>3</sub> and N<sub>2</sub> is released into the gas phase [105]. It is assumed that a similar reaction process takes place in CrAlYN/CrN films. As no Al or Y containing phases are found, it is believed that these elements may dissolve in the Cr<sub>2</sub>O<sub>3</sub> phase to form (Cr,Al)<sub>2</sub>O<sub>3</sub>.

Structural investigations by TEM (see Fig. 6.7) reveal an intact nanoscale layer structure in the bulk coating. The columnar structure is also retained, although voids form at the column boundaries. The preservation of the nanolayers implies that interdiffusion between the individual layers is only limited at 900°C. The void formation at the boundaries can occur due to annihilation and annealing processes with the accumulation of point defects, e.g. vacancies in the lattice, at the column boundaries [92].

At the coating top (see Fig. 6.8), a compact single layer oxide scale with a thickness of  $36 \pm 5$  nm can be observed. TEM-EDS confirms the presence of Cr,

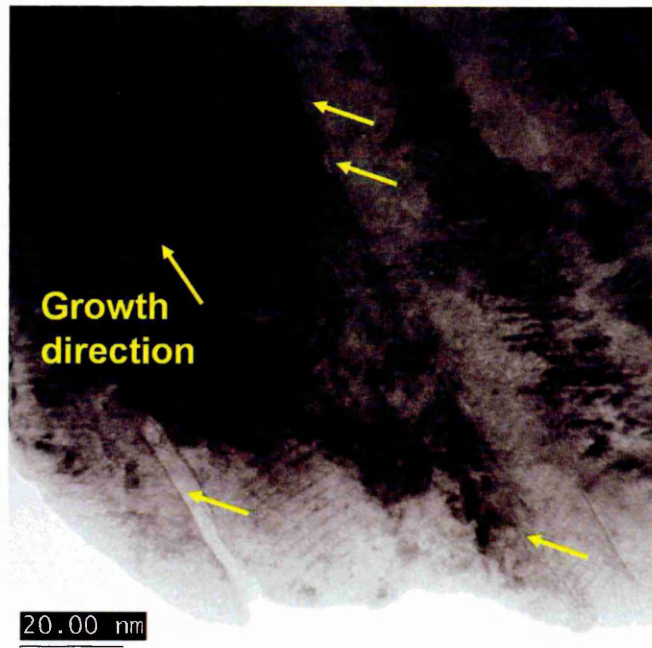


Fig. 6.7: BF-TEM micrograph of the bulk CrAlYN/CrN after 1 h heat-treatment in laboratory air at 900°C: Pores form at the column boundaries

Al and O within this layer. The combined results of XRD and TEM-EDS allow an estimation on the structure of the  $\text{Cr}_2\text{O}_3$  phase. As no phase related to Al, such as  $\text{Al}_2\text{O}_3$ , is present the film and the oxide scale is known to contain Al, it can be suggested that the oxides consist of a  $(\text{Cr,Al})_2\text{O}_3$  solid solution.

### 6.2.3 Reactions after 1 h at 950°C

The TG measurements strongly indicated accelerated surface oxidation at temperatures above 950°C (see Fig. 6.1). The reactions taking place at these temperatures are examined in detail after heat-treatment of CrAlYN/CrN for 1 h at this temperature.

The surface morphology, investigated by SEM, (see Fig. 6.2(c)) with a relatively smooth surface and the previously described crack network, remains largely unaffected by the increase in temperature to 950°C. A considerable amount of O ( $\sim 17\%$ ) is taken up by the coating (see Fig. 6.3) and signifies an increased oxidation rate. Additionally, the Fe content ( $\sim 1.3 \text{ at}\%$ ) (see Fig. 6.3(b)) and the Cr/Al

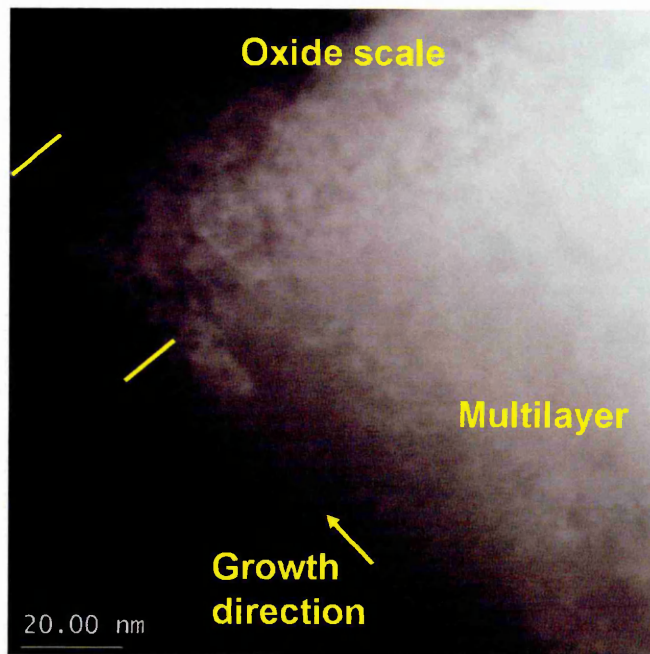


Fig. 6.8: DF-TEM micrograph of a dense oxide scale grown on CrAlYN/CrN after 1 h heat-treatment in laboratory air at 900°C: An oxide scale forms on the coating top; an under-dense structure forms underneath the compact top oxide scale

ratio ( $\sim 1.69$ ) (see Fig. 6.3(c)) further increase and indicate more pronounced diffusion of Fe and Cr into the coating.

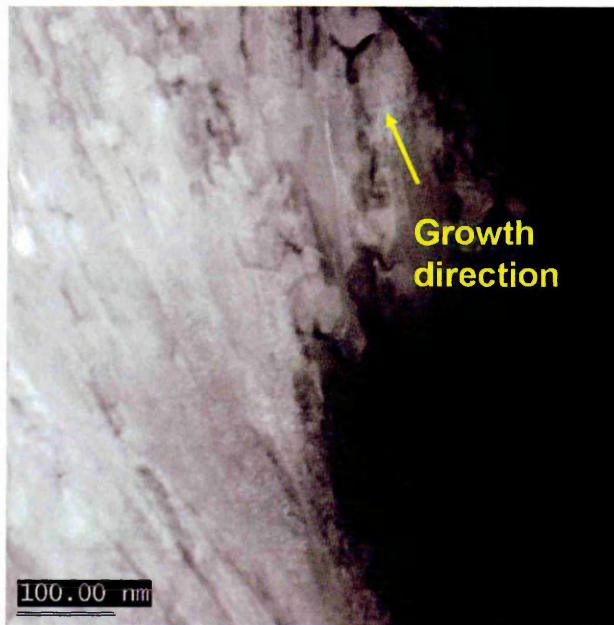
The GA-XRD diffractogram (see Fig. 6.4) reveals numerous reflections. Tab. 6.2 lists all measured reflections and suggests possible candidates for the phase identification. A detailed analysis allows the identification of the CrAlYN/CrN phase which is represented by the CrN reflections. Additionally, Cr<sub>2</sub>N (hexagonal, JCPCD 35-0803, reflection e.g. at  $2\theta = 56.10^\circ$ ) and AlN (hexagonal, JCPCD 76-1620, reflection e.g. at  $2\theta = 35.98^\circ$ ) are found. Corundum-type Cr<sub>2</sub>O<sub>3</sub> (rhombohedral Eskolaite, JCPCD 74-0326) can also be unambiguously matched (e.g. reflections at  $2\theta = 24.73^\circ$  and  $41.53^\circ$ ). In summary, GA-XRD reveals the presence of CrAlYN/CrN, Cr<sub>2</sub>N, hcp-AlN together with Cr<sub>2</sub>O<sub>3</sub> after heat-treatment for 1 h at 950°C. The formation of the Cr<sub>2</sub>N and AlN phases is in agreement with thermodynamic predictions (see Tab. 2.1, Sec. 2.1) as the formation enthalpy of these compounds ( $-126 \text{ kJ}\cdot\text{mol}^{-1}$  and  $-318 \text{ kJ}\cdot\text{mol}^{-1}$ ) is more negative than the for-

Tab. 6.2: Possible phases identified by GA-XRD (see Fig. 6.4) in CrAlYN/CrN heat-treated for 1 h at 950°C (Numbers in bold indicate reflections which can be unambiguously matched)

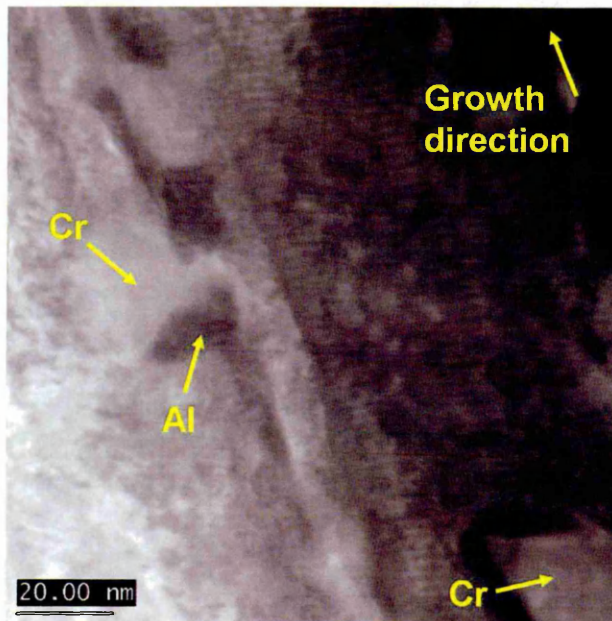
No.	$2\theta$ [°]	$d$ [nm]	Candidates			
			fcc-CrN (JCPCD 76-2494) $d_{(hkl)}$ [nm]	hcp-Cr <sub>2</sub> N (JCPCD 35-0803) $d_{(hkl)}$ [nm]	hcp-AlN (JCPCD 25-1133) $d_{(hkl)}$ [nm]	romb-Cr <sub>2</sub> O <sub>3</sub> (JCPCD 74-0326) $d_{(hkl)}$ [nm]
1	24.73	0.360				0.363
2	33.55	0.267			0.270	0.266
3	35.98	0.250				0.248
4	37.15	0.242		0.241		
5	37.69	0.239	0.239	0.224	0.237	
6	41.53	0.217				0.218
7	42.60	0.212		0.212		
8	43.79	0.207	0.207			
9	50.13	0.182			0.183	
10	56.10	0.164		0.164		
11	58.60	0.158				0.158
12	59.38	0.156			0.156	
13	63.50	0.146	0.146			0.146
14	66.18	0.141			0.146	
15	67.28	0.139		0.139		0.139
16	69.73	0.135			0.135	
17	76.21	0.125			0.125	
18	76.53	0.124				0.124
19	79.44	0.121		0.120		

mation energy of CrN (and supposedly CrAlN) ( $-118 \text{ kJ.mol}^{-1}$ ) and a phase transformation is therefore favoured. Additionally, the growth of Cr<sub>2</sub>O<sub>3</sub> was also to be expected due to the highly negative formation energy of  $-1135 \text{ kJ.mol}^{-1}$ . Al<sub>2</sub>O<sub>3</sub>, in contrast, which has an even higher negative formation energy of  $-1621 \text{ kJ.mol}^{-1}$  and would therefore be expected to preferably form in comparison with Cr<sub>2</sub>O<sub>3</sub> is not detected. It is therefore suggested that the Al content in the coating material is too low to form an individual Al<sub>2</sub>O<sub>3</sub> phase after a heat-treatment for 1 h at 950°C.

TEM analysis of the coating heat-treated at 950°C (see Fig. 6.9) clearly shows pronounced microstructural changes in the material. The initially columnar grains



(a)



(b)

Fig. 6.9: DF-TEM micrograph of the bulk CrAlYN/CrN after 1 h heat-treatment in laboratory air at 950°C: (a) The coating renucleates starting from at the bottom of the columns; (b) Cr-rich and Al-rich crystals segregate at the column boundaries

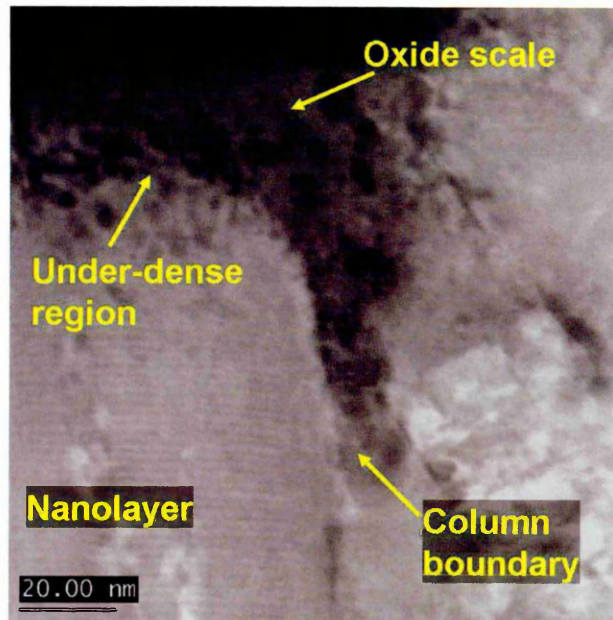


Fig. 6.10: DF-TEM micrograph of the oxide scale grown on CrAlYN/CrN after 1 h heat-treatment in laboratory air at 950°C: Column boundaries permit access of O into the coating and lead to oxide formation

recrystallise (see Fig. 6.9(a)) with nucleation points located preferentially at bottom of the columns. The new grains largely follow the growth direction of the initial columns, but globular crystals accumulate at the former column boundaries. These crystals (see Fig. 6.9(b)) with a size of  $\sim 10\text{-}15$  nm are identified by TEM-EDS as grains rich in either Cr or Al. Although the presence of N cannot be analysed using TEM-EDS, a comparison with XRD results indicate that the grains may consist of  $\text{Cr}_2\text{N}$  and hcp-AlN. The nanoscale multilayer structure remains intact in large areas, mainly located towards the column tops (see Fig. 6.10) indicating that the recrystallisation process is not completed after 1 h heat-treatment at 950°C.

The formation of  $\text{Cr}_2\text{N}$  and hcp-AlN, known to appear in monolithic CrN [104, 196] and CrAlN [114, 197], also seem to take place in the CrAlYN/CrN nanoscale multilayer. Whereas the phase segregation in CrAlN [114] takes place at temperatures between 950°C and 1000°C, the degradation of the CrAlYN/CrN films is here, in contrast, already in an advanced stage at 950°C. Different explanations

may be given for this behaviour. The phase transition in CrAlN [114] is known to shift to lower temperatures when the coating is higher Cr containing (see Fig. 2.15, Sec. 2.4.3.2). In CrAlYN/CrN, the coating becomes higher Cr containing as diffusion from the substrate occurs (see Fig. 6.3(c)). Assuming the phase transition in CrAlN and CrAlYN/CrN takes place with similar reactions, it is suggested that the diffusion of Cr from the substrate is one of the main mechanisms promoting the observed phase transformation. Another explanation may be given with the non-stoichiometry of CrAlYN/CrN with an excess of metal. It may also be the case that the nanolayer structure with a combination of two unstable systems CrN and CrAlYN mutually influence each other and accelerate the phase decomposition. The phase transition may, furthermore, be affected by the presence of Y in the multilayer coating.

TEM microscopy shows the formation of a  $35\pm 9$  nm thick, dense oxide scale covering the film (see Fig. 6.10). This oxides also propagates along the column boundaries into the coating. Additionally, an under-dense structure is observed at the coating/oxide interface. The oxide formation at the column boundaries is caused by O diffusion along the columns [21, 131, 198]. The formation of under-dense regions and voids at the interface is often attributed to vacancy condensation. These vacancies can accumulate as a result of outward ion transport [199]. Interfacial voids in CrN coatings, for example, were reported as a result of outward Cr diffusion [30]. Voids in CrAlYN/CrN may therefore occur due to diffusion of Cr and Al through the scale. In CrN coatings, the trapping of  $N_2$  at the interface due to reduced diffusivity through the scale was identified as a mechanism for the formation of interfacial voids [30]. In CrAlYN/CrN, two reactions can be identified as a source for  $N_2$ : (i) the phase transformation from CrAlYN/CrN into  $Cr_2N$  and hcp-AlN and (ii) the oxidation of CrAlYN/CrN into  $(Cr,Al)_2O_3$ . Trapping of  $N_2$  may therefore contribute to void formation.

In summary, XRD and TEM investigations suggest two simultaneously occurring processes in CrAlYN/CrN isothermally heat-treated at  $950^\circ C$  with, firstly with a partial coating decomposition into  $Cr_2N$  and AlN and, secondly, elevated

surface oxidation with the formation of  $(\text{Cr,Al})_2\text{O}_3$ .

#### 6.2.4 Reactions after 1 h at 1000°C

In this section, the reaction processes taking place after isothermal heat-treatment for 1 h at 1000°C are investigated in detail.

SEM surface observations after heat-treatment at 1000°C (see Fig. 6.2(d)) reveal a smooth coating surface without coating spallation or other defects except the formerly mentioned crack network after 1h heat-treatment at 1000°C. Crystals grow inside these cracks. EDS investigations (see Fig. 6.3(a)) show a strong increase in O atomic fraction ( $\sim 45$  at%) and give clear evidence of faster oxidation. Increased Fe contents ( $\sim 1.2\%$ ) and a higher Cr/Al ratio ( $\sim 1.71$  at%) are also detected (see Fig. 6.3(b)). The diffusion of Fe, Cr and other substrate elements can take place via surface diffusion through the cracks and via diffusion along grain and column boundaries, as reported in TiAlCrN [131]. As previously mentioned, cracks permit fast access of the oxidising medium to the substrate and promote the growth of oxides. It is therefore suggested that the crystals growing in the cracks are oxides from the substrate.

Investigations of the phase structure by GA-XRD (see Fig. 6.4) exhibit numerous reflections at similar  $2\theta$  positions to those reported after heat-treatment at 950°C and therefore confirm the presence of the previously observed phases  $\text{Cr}_2\text{N}$ ,  $\text{AlN}$ ,  $\text{Cr}_2\text{O}_3$ . The strongest increase in reflection intensity is related to the  $\text{Cr}_2\text{O}_3$  reflections whereas the reflections of  $\text{CrAlYN/CrN}$  are below the detection limit. This increase in  $\text{Cr}_2\text{O}_3$  intensity implies a higher  $\text{Cr}_2\text{O}_3$  volume fraction in the sampled volume and therefore signifies the growth of thicker oxides.

Cross-sectional TEM investigations were carried out to determine possible changes in the microstructure after heating (see Fig. 6.11). The columnar structure of the as-deposited state (see Fig. 5.8(a), Sec. 5.1.5) is replaced by a globular polycrystalline structure. At the coating top, a layered structure can be seen which is presumably an oxide scale.

The microstructure in the bulk after demonstrates a fine-grained globular crys-

tal structure (see Fig. 6.12). TEM-EDS identifies these grains as either Cr- or Al-rich. An SAD pattern from this region (see insert in Fig.6.12) reveals a variety of discrete diffraction spots. Different phases can be identified from the corresponding  $d$ -spacing (see Tab. 6.3). These are CrN, Cr<sub>2</sub>N and hcp-AlN. The CrN phase is believed to represent an fcc-CrAlN phase as a remaining of the initial CrAlYN/CrN structure. These combined findings of XRD, TEM-EDS and SAD signify that the recrystallisation of CrAlYN/CrN at 1000°C takes place with a phase transformation into Cr<sub>2</sub>N and AlN. It is concluded that initial as-deposited nanoscale multilayer structure (see Fig. 5.11, Sec. 5.1.5) is completely replaced by a globular coating structure after heat-treatment for 1 h at 1000°C.

The oxide formation was investigated in more detail by TEM (see Fig. 6.13(a)) showing the presence of an oxide consisting of two distinct layers with a total thickness of ~50 nm at the very outer surface. The scale consists of grains with

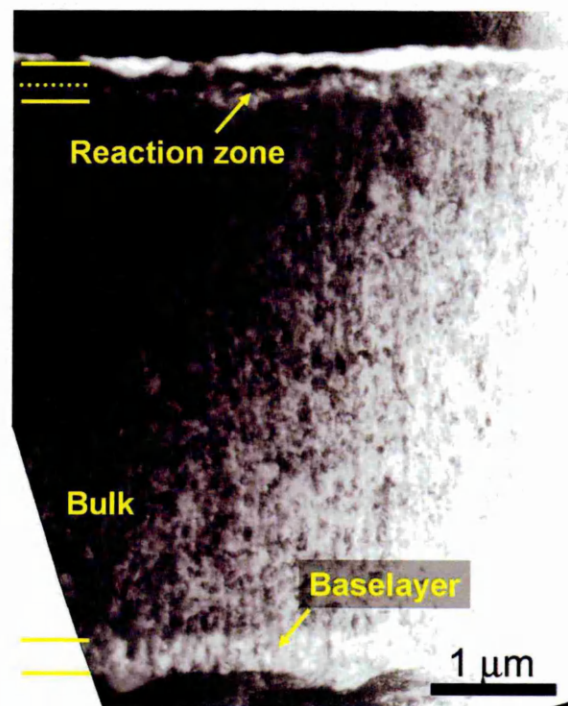


Fig. 6.11: BF-TEM cross-sectional micrograph of CrAlYN/CrN after 1 h heat-treatment in laboratory air at 1000°C: The coating has a polycrystalline structure with a reaction zone at the coating top

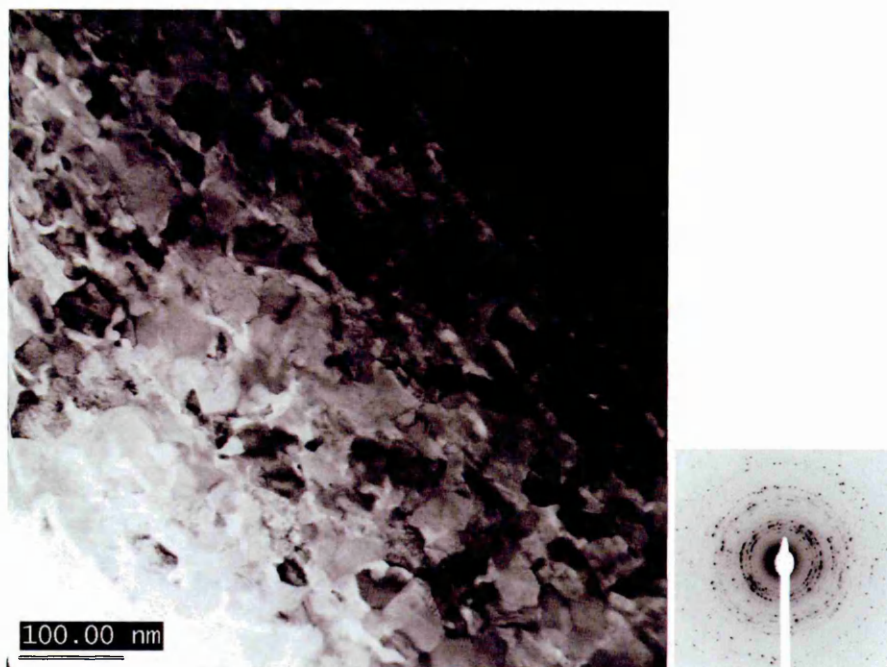


Fig. 6.12: BF-TEM micrograph and the corresponding SAD pattern from the bulk CrAlYN/CrN after heat-treatment in laboratory air at 850°C (Reflections of the SAD pattern are listed and indexed in Tab. 6.3)

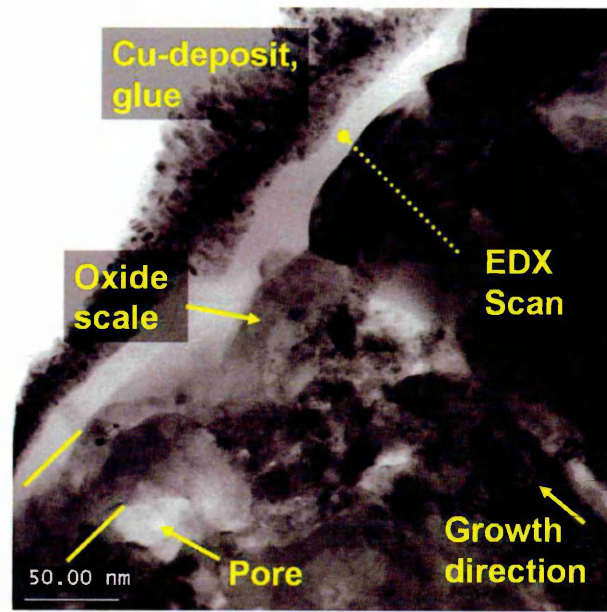
a lateral size of up to 100 nm and appears to be dense and void-free. A TEM-EDS line scan was performed across the scale cross-section and the calculated normalised Cr/Al and O/(Cr+Al) ratios are summarised in Fig. 6.13(b) with 3 distinct regions found. The first 6 nm are discarded as the signal in this region is an artefact from the TEM specimen preparation. Within the first 30 nm at the very scale top, both constant Cr/Al ( $\sim 1.5$ ) and O/(Cr+Al) ratios ( $\sim 2.7$ ) are found. Proceeding further towards the bulk, the Cr/Al ratio more than triples ( $\sim 4.2$ ) whereas the O/(Cr+Al) ratio drops ( $\sim 2.1$ ). The higher Cr/Al ratio signifies a higher local presence of Cr in the inner oxide layer. The stepwise increase of Al closer to the coating top suggests outward diffusion of Al, leaving Cr in its initial position and generating a duplex-oxide with an Al-rich outer oxide and a Cr-rich inner oxide. The Al-rich layer also binds higher O contents which may be related to a high O affinity of Al compared with Cr. Although the calculation of count ratios gives only qualitative information on the elemental distribution of the

Tab. 6.3: Possible phases identified from the SAD pattern (see insert in Fig.6.12) in the bulk of CrAlYN/CrN coating heat-treated at 1000°C

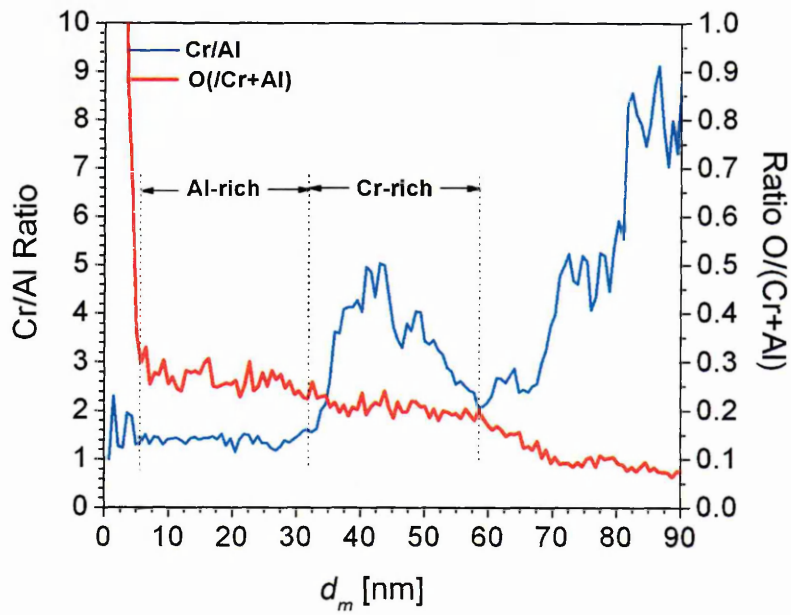
No.	$d$ [nm]	Candidates		
		fcc-CrN (JCPCD 76-2494) $d_{(hkl)}$ [nm], (hkl)	hcp-Cr <sub>2</sub> N (JCPCD 35-0803) $d_{(hkl)}$ [nm], (hkl)	hcp-AlN (JCPCD 25-1133) $d_{(hkl)}$ [nm], (hkl)
1	0.305		0.305 (101)	
2	0.265			0.270 (100)
3	0.249		0.241 (110)	
4	0.239	0.239 (111)	0.224 (002)	
5	0.212		0.212 (111)	
6	0.197	0.207 (200)		
7	0.187			0.182 (102)
8	0.162		0.164 (112)	
9	0.157			0.156 (110)
10	0.183	0.146 (220)		
11	0.140	0.138 (300)	0.138 (300)	
12	1.173	0.119 (222)		0.185 (202)
13	0.116		0.118 (302)	

individual elements, it gives clear evidence that these processes are taking place.

Electron energy filtered elemental distribution maps (see Sec. 3.2.5) were taken to investigate the effect of heat-treatment on the element distribution within the thin film (see Fig. 6.14). A comparison of the N and O distribution maps shows a high intensity O signal in the region of the oxide scale and the porous layer with a combined total thickness of  $\sim 180$  nm receding deeper into the bulk coating. The N signal becomes strong proceeding into the bulk after  $\sim 550$  nm. These findings indicate surface oxidation and O diffusion into the thin film with a large O diffusion zone. The N in this region may be partially replaced by O according to the oxidation reactions discussed previously. The Al and Cr distribution maps show a high Al distribution in the oxide scale whereas Cr is found to a lesser extent in the very top outer scale but mostly located directly underneath the Al-rich zone. The results signify the formation of an Al-rich outer oxide and a Cr-rich inner oxide and confirm the TEM-EDS data obtained from the oxide scale. Regions

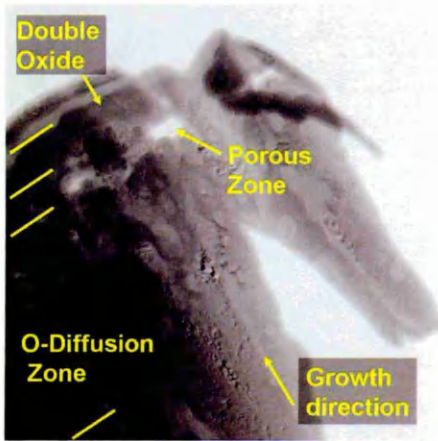


(a)

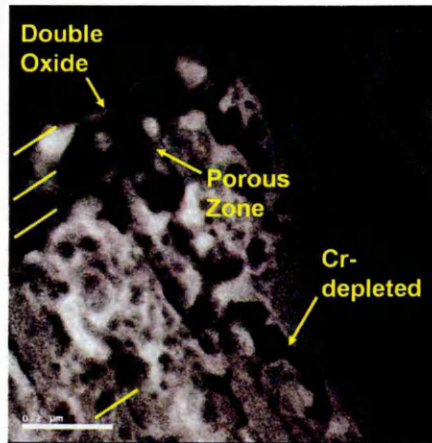


(b)

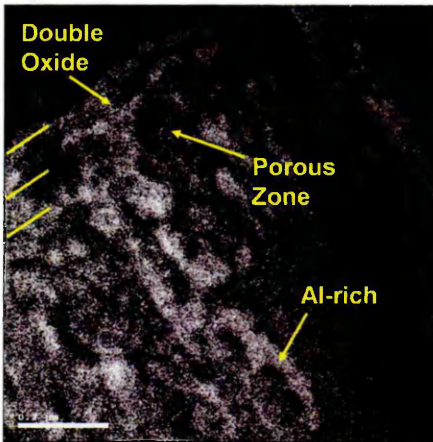
Fig. 6.13: Analysis of oxide scale formation on top of CrAlYN/CrN after 1 h heat-treatment in laboratory air at 1000°C: (a) BF-TEM micrograph with a double layered oxide scale and pores at the coating/scale interface; (b) EDS line scan across the oxide scale



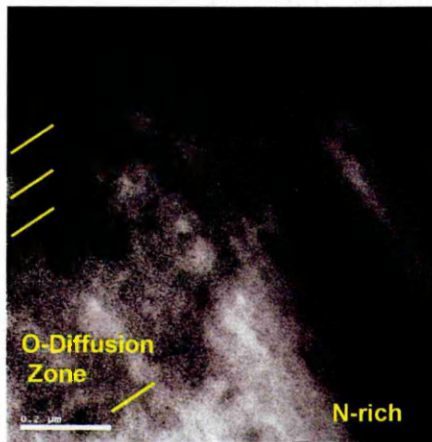
(a) BF micrograph



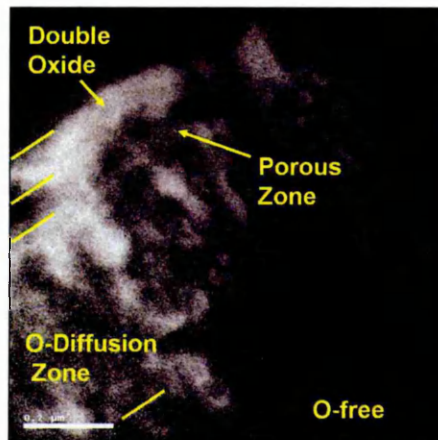
(b) Cr map, from L<sub>2,3</sub> edge



(c) Al map, from K-edge



(d) N map, from K-edge



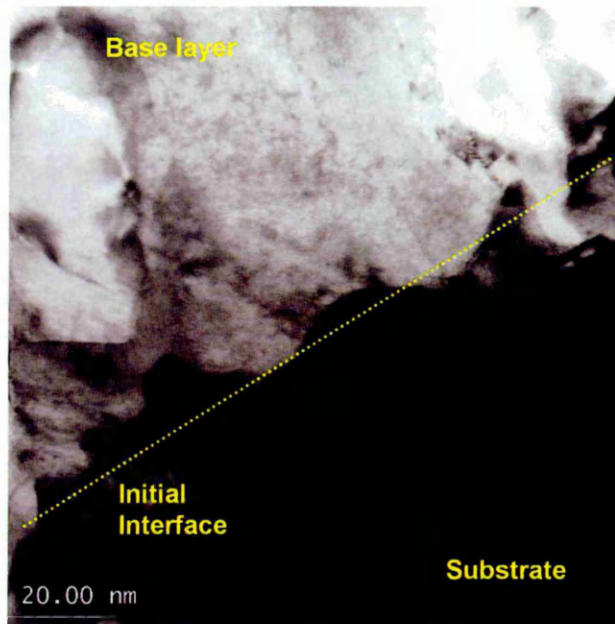
(e) O map, from K-edge

Fig. 6.14: Electron energy filtered elemental distribution maps of the top region of CrAlYN/CrN after 1 h heat-treatment in laboratory at 1000°C

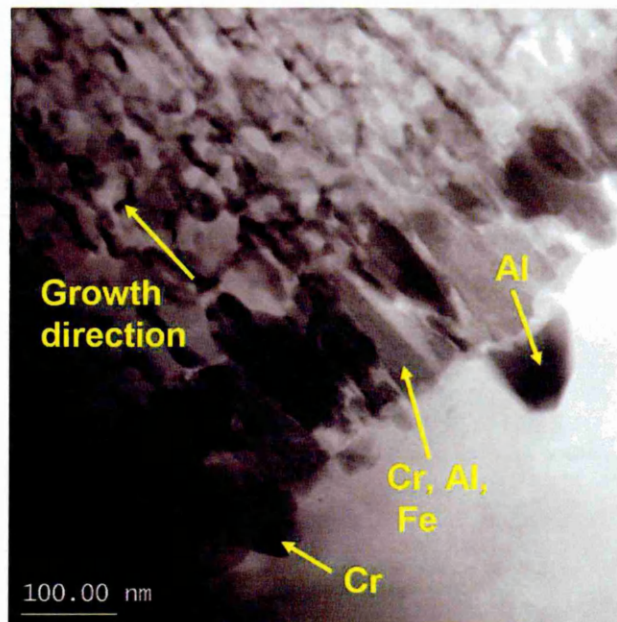
without signal in the porous zone arise from voids in the material. In general, Cr accumulates in some grains whereas the Al signal is distributed more evenly in the layer. The segregation of Cr and Al becomes more pronounced in the O diffusion zone where large grains rich in either Cr or Al are detected. Coating grains within the O diffusion zone which are rich in Cr are also rich in O, whereas grains with high Al content were O deficient in comparison. An explanation for this behaviour may be found in decomposition of CrAlYN/CrN into Cr<sub>2</sub>N and AlN. The coating degradation can result in the formation of two components with different oxidation resistance. Cr<sub>2</sub>N is known to start oxidising at temperatures above ~675°C [30] whereas hcp-AlN remains stable up to ~850°C [200, 201]. A direct comparison of these materials under similar testing conditions is not available but literature gives an indication for better oxidation resistance of AlN at 1000°C. Therefore, O is preferentially accumulated in grains consisting of Cr<sub>2</sub>N whereas AlN remains nearly oxygen-free.

Fig. 6.15 shows TEM micrographs of the substrate/baselayer interface after heat-treatment. The initially sharp and clearly defined interface becomes wavy and the recrystallisation of the baselayer results in grains which protrude and intermix with the substrate grains (see Fig. 6.15(a)). Mutual inter-diffusion between substrate and base layer takes place at the interface. TEM-EDS analysis confirms the presence of grains rich in Al and Cr within the substrate close to the interface region (maximum distance 80 nm) and, at the same time, Fe is found within individual base layer grains (see Fig. 6.15(b)). These findings indicate that interdiffusion at the interface occurs.

The reactions taking place in CrAlYN/CrN nanoscale multilayer coatings upon heating to 1000°C can be identified as (i) diffusion of substrate elements through cracks and, additionally, into the coating, (ii) a phase transformation into Cr<sub>2</sub>N and hcp-AlN and (iii) the formation of a duplex-oxide layer with a Al-rich outer layer and a Cr-rich inner layer.



(a)



(b)

Fig. 6.15: DF-TEM micrographs of structural changes at the substrate/base layer interface of CrAlYN/CrN after 1 h heat-treatment in laboratory air at 1000°C: (a) rough substrate/coating interface and (b) a recrystallised base layer with interdiffusion of elements

## 6.2.5 Thermogravimetric Analysis vs. Isothermal Heat-Treatment

In the continuous TG measurements (see Fig. 6.1) it was shown that CrAlYN/CrN gains weight at three different rates (regime 1 to regime 3). After extensive analysis of the reactions taking place in isothermally heated CrAlYN/CrN, these reactions can now be linked to the observed weight gain in the TG curve.

Below 800°C (regime 1), slow oxidation of the CrAlYN/CrN coating is suggested to be the main oxidation mechanism of CrAlYN/CrN.

In isothermally heated CrAlYN/CrN, cracks are observed in the coating at 850°C (see Fig. 6.2(a)). These cracks provide fast access paths of the oxidising medium to the substrate and allow oxidation of the substrate material. The first appearance of such cracks was estimated at 830°C. This temperature is close to 800°, the temperature at which a significant increase in weight gain is observed in the TG curve (regime 2). The surface of CrAlYN/CrN additionally oxidises with the formation of a steadily growing (Cr,Al)<sub>2</sub>O<sub>3</sub> scale. It is therefore believed that substrate oxidation through the cracks and relatively low coating oxidation contribute to higher weight gain.

When increasing the temperature of the isothermal heat-treatment from 950°C to 1000°C, accelerated substrate oxidation is observed. Furthermore, the coating structure undergoes a phase transformation and a layered oxide scale forms. This duplex-oxide suggests high oxidation of the substrate. The onset temperature of rapid oxidation in CrAlYN/CrN is estimated to 970°C from the TG measurement (see Fig. 6.1). The weight gain above 970°C (regime 3) is therefore caused by high substrate oxidation and accelerated coating oxidation.

## 6.3 Long term oxidation up to 100 h at 850°C

Oxidation experiments were conducted on larger time scales at medium temperatures. These tests were implemented to study the behaviour of CrAlYN/CrN at a temperature which could represent a real service environment, e.g. a low temperature stage of a gas turbine or a molding tool. This section describes the oxidation behaviour of CrAlYN/CrN at comparatively low temperatures of 850°C between 1 h and 100 h heat-treatment duration.

### 6.3.1 Reactions after 1 h

The oxidation processes of CrAlYN/CrN taking place after oxidation for 1 h at 850°C were previously discussed in Sec. 6.2 and will only be shortly summarised. It is shown that the as-deposited columnar coating structure is retained after heat-treatment (see Fig. 6.18(a)). The only visible sign of surface oxidation is presence of a  $\sim 23$ nm thick, dense oxide layer (see Fig. 6.6, Sec. 6.2).

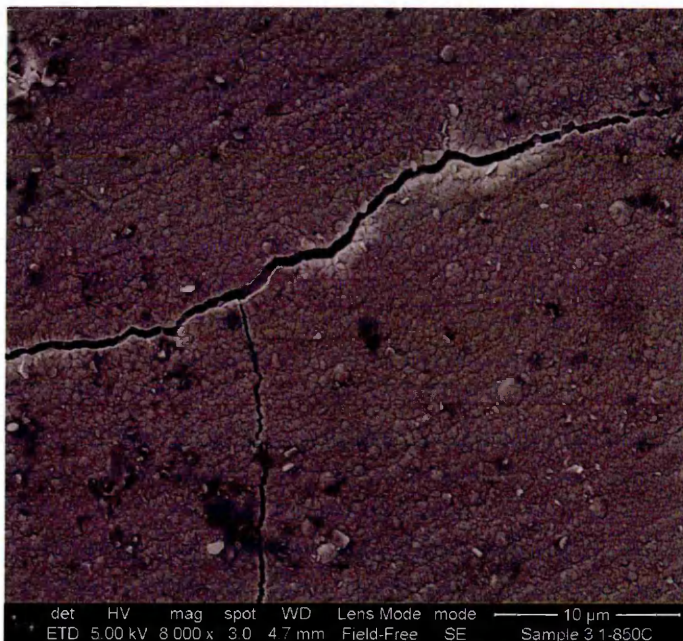
### 6.3.2 Reactions after 5 h

SEM analysis of the specimen surface after 5 h exposure to laboratory air reveals a relatively smooth coating surface with randomly propagating cracks (see Fig. 6.16(b)). The surface observations suggest only marginal surface reactions after heating for 5 h.

The GA-XRD pattern (see Fig. 6.17) shows the typical reflections of the CrAlYN/CrN single phase (see Fig 5.4, Sec. 5.1). Additionally, low intensity reflections of other phases appear. These phases are identified and indexed from the calculated lattice spacing  $d$  (see Eq. 3.1, Sec. 3.2.2) which corresponds to the measured  $2\theta$  positions (see Tab. 6.4). Reflections of hexagonal Cr<sub>2</sub>N (e.g. at  $2\theta = 29.07^\circ$  and  $42.55^\circ$ , JCPCD 35-0805), hexagonal AlN (e.g. at  $2\theta = 37.74^\circ$  and  $59.64^\circ$ , JCPCD 25-1133) and rhombohedral corundum type Cr<sub>2</sub>O<sub>3</sub> (e.g. at  $2\theta = 24.40^\circ$  and  $55.02^\circ$ , JCPCD 74-0326) are positively identified. The GA-XRD analysis therefore distinguishes the CrAlYN/CrN phase, Cr<sub>2</sub>N, hcp-AlN and Cr<sub>2</sub>O<sub>3</sub>

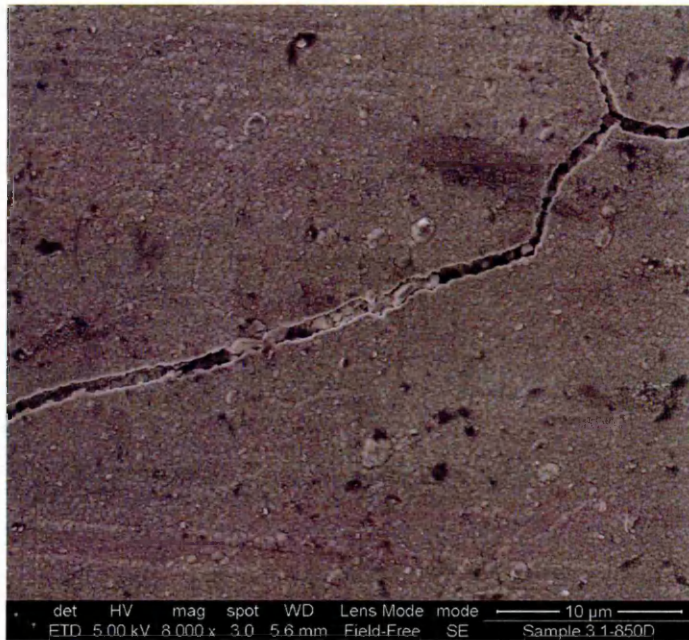


(a) 1 h

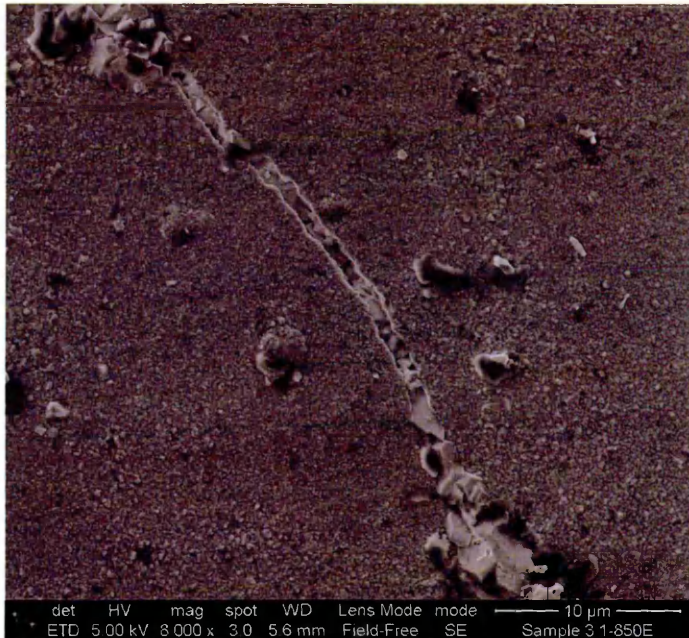


(b) 5 h

Fig. 6.16: SEM micrographs of the surface of CrAlYN/CrN after exposure for up to 100 h to laboratory air at 850°C: Crystals with increasing size grow on top of the coating surface and above 20 h exposure time also inside cracks

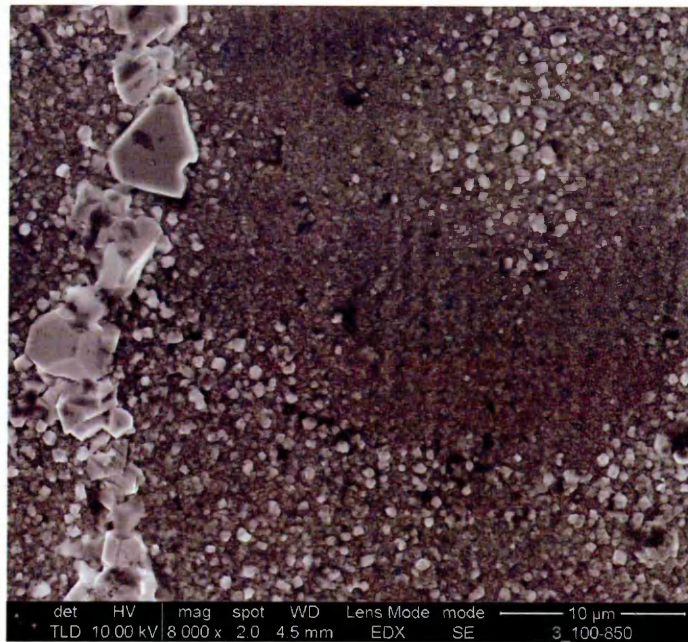


(c) 20 h



(d) 50 h

Fig. 6.16: Continued



(e) 100 h

Fig. 6.16: Continued

after 5 h heat-treatment.

TEM analysis was carried out to study the effect of heat-treatment on the microstructure of CrAlYN/CrN. A BF-TEM micrograph of CrAlYN/CrN (see Fig. 6.18(b)) demonstrates that the columnar structure (see Fig. 5.8(a), Sec. 5.1) is retained after heat-treatment for 5 h at 850°C. At this magnification, no microstructural changes or oxidation processes can be observed.

Possibly occurring diffusion processes in the coating can be investigated by analysing the distribution of elements across the coating cross-section. For this, semi-quantitative TEM-EDS spot analysis of Cr, Al and Fe was carried out at different positions to obtain a concentration profile of these elements (see Fig. 6.19). Fe (with  $\sim 78\text{at}\%$  in the substrate) is also present in the base layer ( $\sim 1.6\text{at}\%$ ) and the coating ( $< 1\text{at}\%$  at a distance of  $1.8\ \mu\text{m}$  from the substrate/base layer interface). A high Cr atomic fraction is detected in the substrate ( $\sim 22\ \text{at}\%$ ), in the base layer ( $\sim 34\text{at}\%$ ) and in the multilayer structure ( $\sim 53\text{at}\%$ ). Al is not present in the substrate but is detected in the base layer ( $\sim 63\text{at}\%$ ) and in the

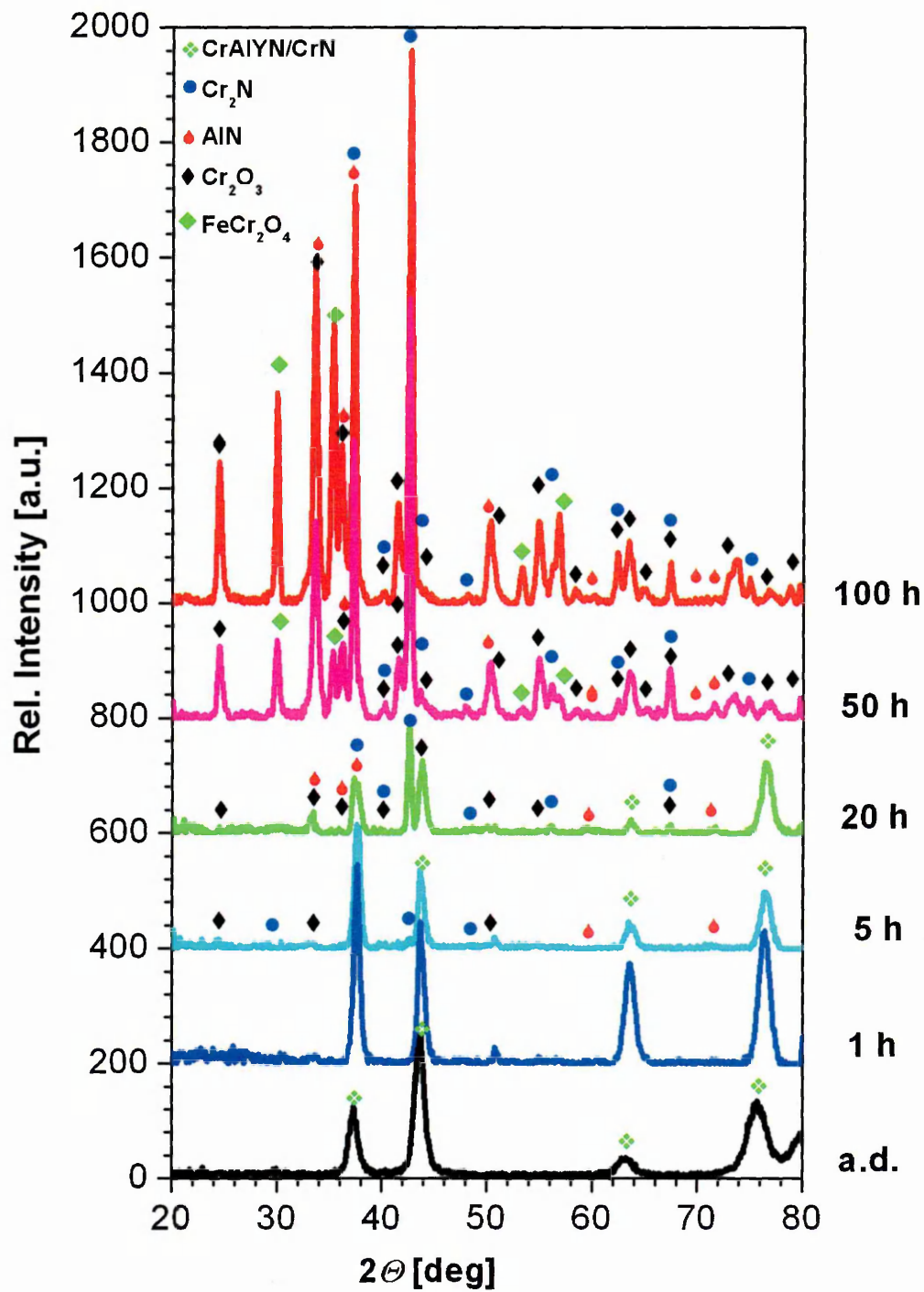


Fig. 6.17: GA-XRD pattern (incident angle  $\gamma = 2^\circ\text{C}$ ) obtained from CrAlYN/CrN after heat-treatment in laboratory air for up to 100 h at  $850^\circ\text{C}$

Tab. 6.4: Possible phases identified from the GA-XRD diffractogram (see Fig. 6.17) of CrAlYN/CrN heat-treated for 5 h at 850°C (Numbers in bold indicate reflections which can be unambiguously identified)

No.	$2\theta$ [°]	$d$ [nm]	fcc-CrN (JCPCD 76-2494) $d_{(hkl)}$ (hkl)	hcp-Cr <sub>2</sub> N (JCPCD 35-0803) $d_{(hkl)}$ (hkl)	hcp-AlN (JCPCD 25-1133) $d_{(hkl)}$ (hkl)	romb-Cr <sub>2</sub> O <sub>3</sub> (JCPCD 74-0326) $d_{(hkl)}$ (hkl)
1	24.40	0.365				0.366 (012)
2	29.07	0.307		0.305 (101)		
3	33.28	0.269			0.249 (002)	
4	37.48	0.240	0.239 (111)			
5	37.74	0.238			0.237 (101)	
6	39.79	0.227				0.226 (006)
7	42.55	0.212		0.212 (111)		
8	43.55	0.208	0.207 (200)			
9	49.97	0.183			0.183 (102)	
10	50.65	0.180				0.182 (024)
11	55.02	0.167				0.167 (116)
12	59.64	0.155			0.156 (110)	
13	63.45	0.147	0.146 (220)			
14	64.01	0.145				0.146 (214)
15	72.01	0.131			0.132 (112)	
16	76.34	0.125	0.125 (311)		0.125 (004)	
17	76.67	0.124				0.124 (217)
18	78.60	0.122				0.121 (306)

nanoscale multilayer ( $\sim 46\text{at}\%$ ). From this, a Cr/Al ratio of  $\sim 1.15$  is derived in the nanolayer structure. With the presence of Fe inside the bulk coating, evidence is given for the diffusion of Fe from the 304 stainless steel substrate into the coating. Additionally, the increase in Cr/Al ratio of  $\sim 1.15$  after heat-treatment compared to  $\sim 1.04$  in the as-deposited state indicates diffusion of Cr into the coating.

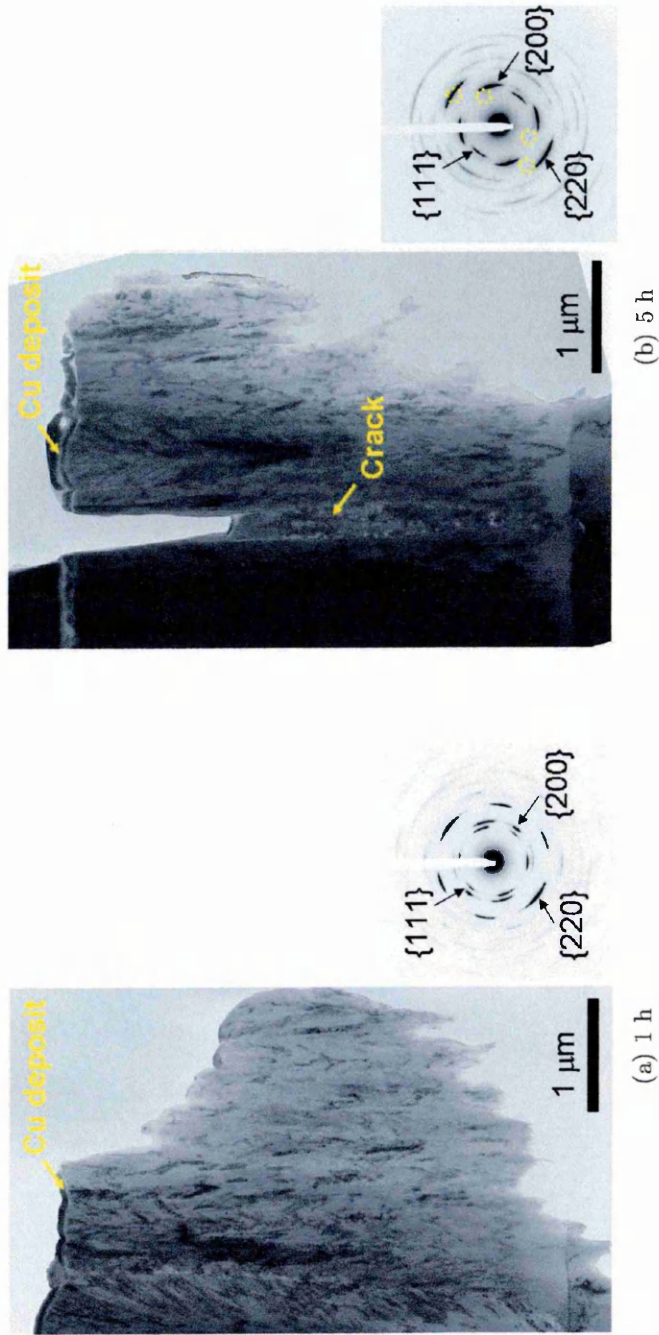


Fig. 6.18: BF-TEM micrographs and the corresponding SAD pattern of CrAlYN/CrN after isothermal heat-treatment at 850°C in air up to 100 h (The SAD pattern were taken from the middle of the bulk coating and are indexed with the main CrN reflections)

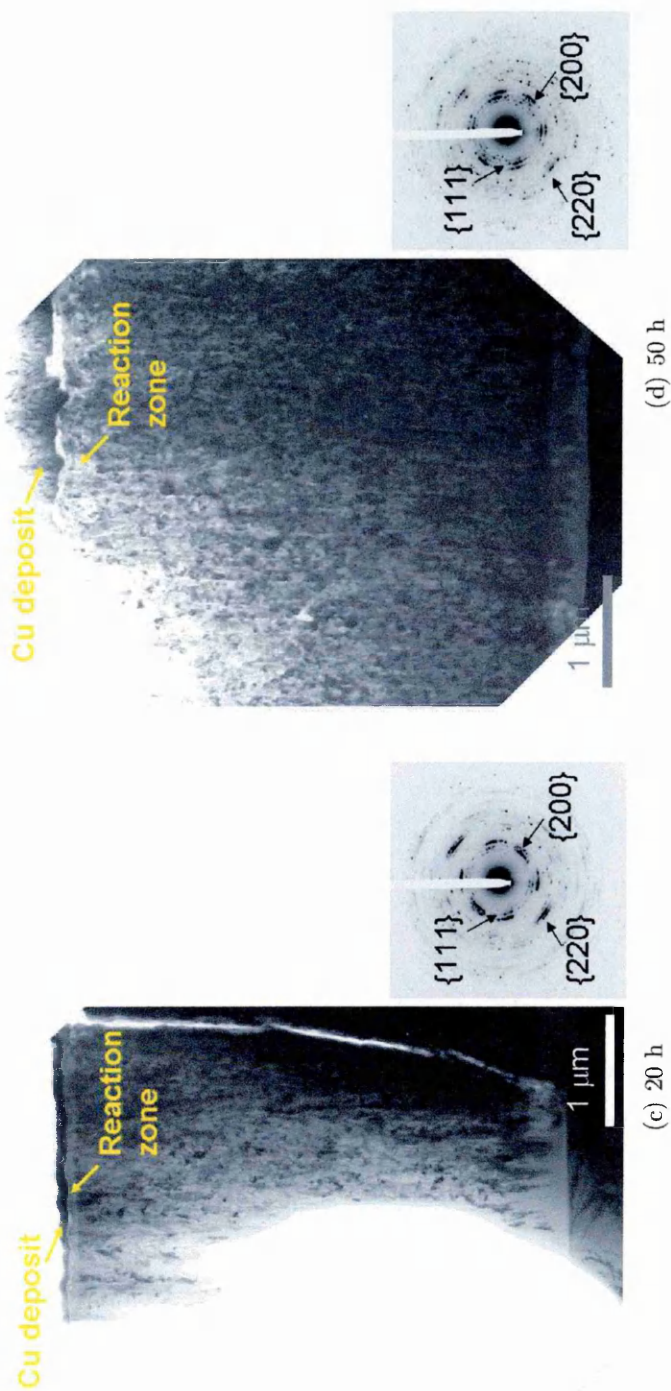
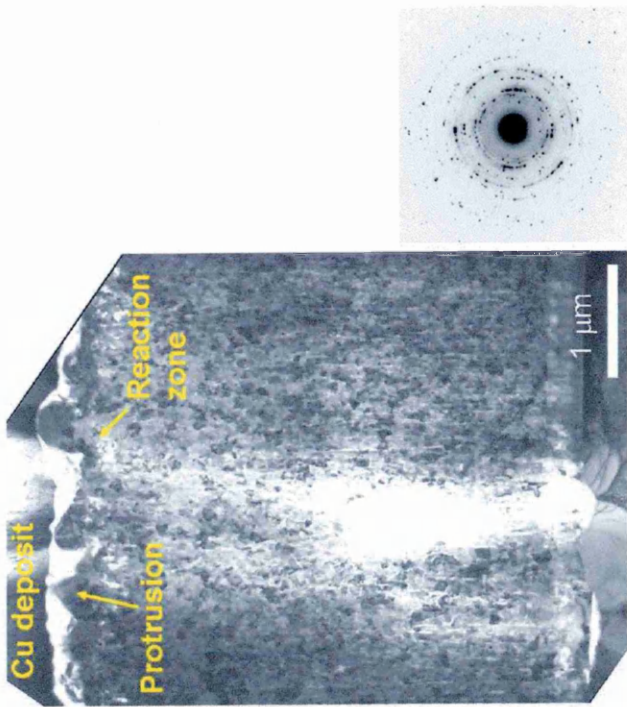


Fig. 6.18: Continued



(e) 100 h

Fig. 6.18: Continued

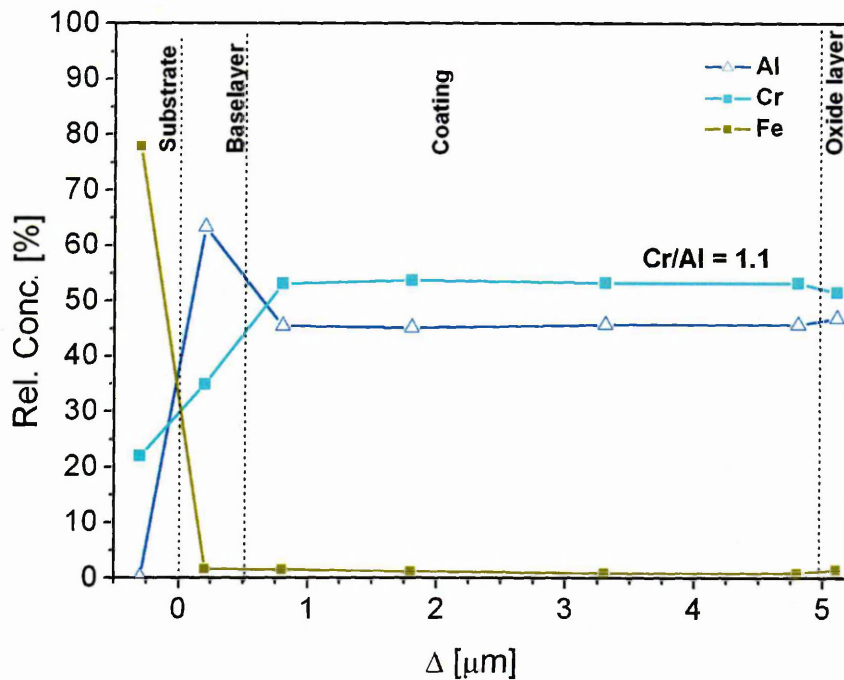


Fig. 6.19: TEM-EDX spot analysis profile for the metallic components Cr, Al and Fe over the total coating cross-section after 5 h heat-treatment in laboratory air at 850°C: In the multilayer structure, the Fe content is ~2.5at% and the Cr/Al ratio is ~1.1

In TEM imaging (see Fig. 6.20), the nanolayers are clearly visible in the thin film multilayer region. Additionally, pores are discovered at the column boundaries. These voids may form as point defects in the coating, e.g. vacancies in the lattice, excess N<sub>2</sub> or incorporated inert gas atoms (Ar) precipitate at the grain boundaries during the heat-treatment [92].

A SAD pattern taken from the nanolayers in the middle of the coating cross-section (see insert in Fig. 6.18(b)) shows the typical diffraction arcs of the textured CrAlYN/CrN. Additionally, a number of discrete diffraction spots are found. From the *d*-spacing of these spots (see Tab. 6.5), the individual phases CrN (JCPCD 76-2494), Cr<sub>2</sub>N (JCPCD 35-0803) and AlN (JCPCD 25-1133) are identified. These diffractions arcs of the CrN phase were already observed in the as-deposited coating and after 1 h at 850°C (see insert in Fig. 6.18(a)). These arcs of the CrN phase therefore represent the pseudobinary CrAlYN/CrN nanolayer

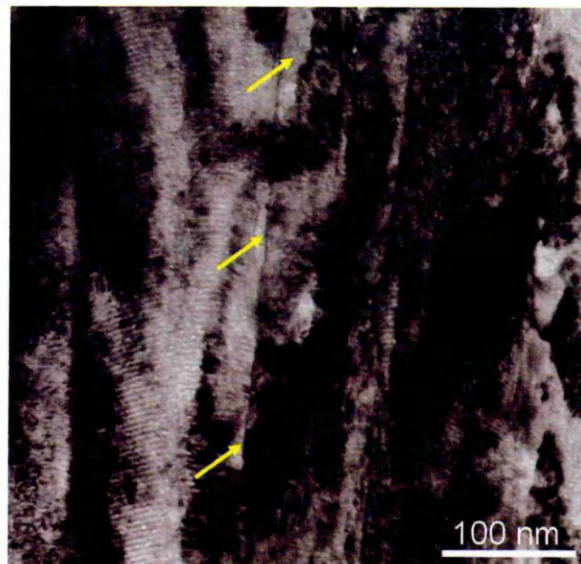


Fig. 6.20: BF-TEM micrograph of the bulk CrAlYN/CrN after 5 h heat-treatment in laboratory air at 850°C: Pores form at the column boundaries (indicated by arrows)

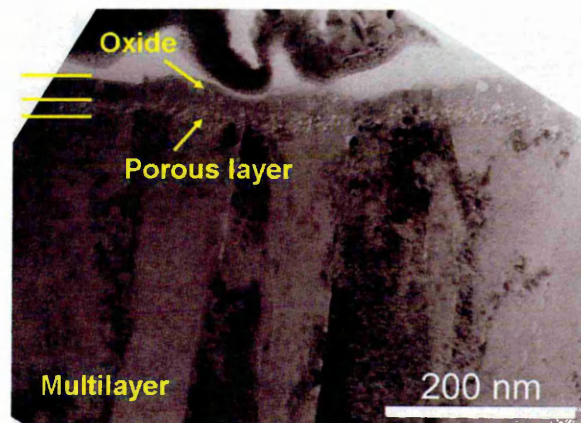
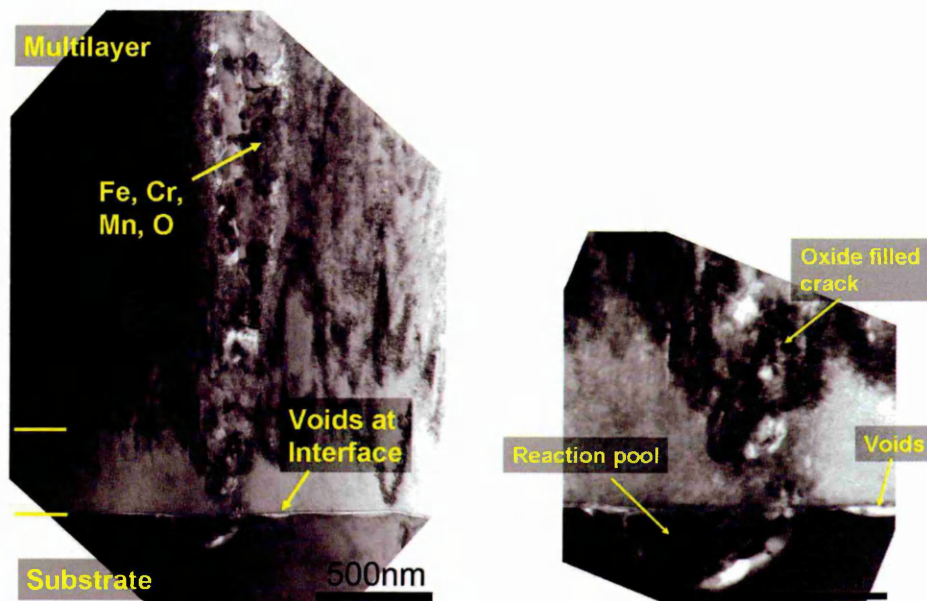


Fig. 6.21: BF-TEM micrograph of the oxide scale on CrAlYN/CrN after 5 h heat-treatment in laboratory air at 850°C: A low density layer is situated underneath the oxide scale at the coating/scale interface

structure. These findings confirm the results obtained from the GA-XRD scans (see Fig. 6.17) in which reflections of CrAlYN/CrN, Cr<sub>2</sub>N and AlN were found.

At the very column top, a  $26 \pm 5$  nm thin, dense oxide layer forms at the coating (see Fig. 6.21). Underneath the dense oxide, a region with speckled contrast is found. This contrast may arise from a material with low density. Determination of



(a) Through-thickness crack with formation of various oxides

(b) Crack at interface with large reaction pool and void formation

Fig. 6.22: BF-TEM micrographs of a through-thickness crack in the CrAlYN/CrN after 5 h heat-treatment in laboratory air at 850°C

the chemical composition by TEM-EDS shows the presence of Cr, Al and O in the oxide scale. The growth of oxide scales often takes place via outward migration of coating material [199,202]. Coating elements can diffuse into/through the oxide and provide material for the oxide growth. This element migration may leave a zone with low density and/or pores at the coating/oxide interface. It is likely that similar diffusion processes of Cr and Al also occur in CrAlYN/CrN. The previously mentioned mechanism of N<sub>2</sub> trapping at the coating/oxide interface (see Sec. 6.2.3) and the precipitation of defects, e.g. incorporated Ar atoms [92], may also contribute to the formation of a low density zone. Previously performed GA-XRD investigations (see Fig. 6.17) affirm a Cr<sub>2</sub>O<sub>3</sub> phase as reaction product. The TEM-EDS investigation, in contrast, reveals the presence of Al in the thin oxide. It is therefore suggested that the detected Cr<sub>2</sub>O<sub>3</sub> phase incorporates Al into the lattice to form a (Cr,Al)<sub>2</sub>O<sub>3</sub> solid solution. Thermodynamic predictions of the Cr<sub>2</sub>O<sub>3</sub>-Al<sub>2</sub>O<sub>3</sub> phase system postulate the formation of two co-existing corundum type solid solution of which one is Al-rich and one Cr-rich [203–205] for a Cr/Al

Tab. 6.5: Possible phases identified from the SAD (see insert in Fig. 6.18(b)) in the bulk of CrAlYN/CrN coating heat-treated for 5 h at 850°C

No.	$d$ [nm]	Candidates		
		fcc-CrN (JCPCD 76-1684) $d_{\{hkl\}}$ [nm], (hkl)	hcp-Cr <sub>2</sub> N (JCPCD 35-0803) $d_{\{hkl\}}$ [nm], (hkl)	hcp-AlN (JCPCD 25-1133) $d_{\{hkl\}}$ [nm], (hkl)
1	0.269		0.269 (100)	
2	0.239	0.239 (111)		0.241 (110)
3	0.224			0.224 (002)
4	0.205	0.207 (200)		
5	0.163			0.164 (112)
6	0.156		0.156 (110)	
7	0.147			
8	0.140			0.139 (300)
9	0.126	0.125 (311)		0.127 (113)

ratio of  $\sim 1$  and a temperature of 850°C. In the present CrAlYN/CrN system, however, only one corundum type (Cr,Al)<sub>2</sub>O<sub>3</sub> is found. It may be expected that the heat-treatment time of 5 h is not sufficiently long for these two phases to form. Exposure for longer times may therefore be necessary to clarify this point.

Through-thickness cracks are observed in the coating (see Fig. 6.22). The existence of such cracks is already known from the SEM surface observations (see Fig. 6.16(b)). Large crystals form inside the crack (see Fig. 6.22(a)). TEM-EDS identifies these crystals as a mixture of grains with varying Cr, Fe, Mn and Al content. A large reaction pool (see Fig. 6.22(b)) is located at the bottom of the crack and consists mainly from Fe, Cr and Ni with traces of Mn and O. Furthermore large voids are observed at the substrate/base layer interface. Atoms can, for example, migrate along the interface into the crack and form oxides there. Moreover, TEM-EDS depth profiling (see Fig. 6.19) shows that a substantial amount of substrate elements are present in the bulk coating. The chemical composition of the crystals in the crack with Cr, Fe and O as main components suggests that various (Cr, Fe)-oxides form. Fe and Mn can be classified as elements originating from the substrate. This suggests that the less oxidation resistant substrate oxi-

disappears rapidly when exposed to open air and fills the crack with porous oxides. The presence of Al in these oxides additionally hints that coating oxidation contributes to the crack closure and, hence, coating elements accumulate in the crack. The observed voids at the interface can develop when material is removed from these regions by either surface diffusion of material through cracks or volume diffusion into the bulk coating.

To sum up, the CrAlYN/CrN retains largely a nanolayer structure. XRD and TEM investigations reveal the additional presence of Cr<sub>2</sub>N and hcp-AlN in the coating. Oxidation of the coating causes the formation of a (Cr,Al)<sub>2</sub>O<sub>3</sub> scale.

### 6.3.3 Reactions after 20 h

SEM observations of coating surface of CrAlYN/CrN after 20 h heat-treatment (see Fig. 6.16(c)) shows cracks in the coating with crystals growing inside these cracks, presumably oxides from the substrate. The coating surface itself remains relatively smooth with the typical dome-shaped morphology, however, first facet-shaped crystals are visible (see Fig. 6.23) and give macroscopic evidence of surface oxidation.

The GA-XRD diffractogram (see Fig. 6.17) shows low intensity reflections of CrN representing the CrAlYN/CrN phase (e.g. at  $2\theta = 37.52^\circ$  and  $43.63^\circ$ ). Additionally, Cr<sub>2</sub>N reflections (e.g. at  $2\theta = 42.53^\circ$ ) and AlN (e.g. at  $2\theta = 33.25^\circ$ ) are found. Furthermore, reflections of Cr<sub>2</sub>O<sub>3</sub> are present (e.g. at  $2\theta = 24.50^\circ$  and  $50.54^\circ$ ). For each phase, more than one reflection is present which is unambiguously identifiable. Consequently, the phases in CrAlYN/CrN after 20 h heat-treatment at 850°C are CrAlYN/CrN, Cr<sub>2</sub>N and hcp-AlN as well as Cr<sub>2</sub>O<sub>3</sub>. These phases were already observed after heat-treatment for 5 h at 850°C (see Tab. 6.4, Sec. 6.3.2).

A TEM micrograph of the coating cross-section is shown in Fig. 6.18(c). The micrograph reveals a columnar coating structure and shows a thin and dense reaction layer at the top of the coating. The nanolayer structure can be observed in the bulk coating (see Fig. 6.24). Furthermore, large pores form at the column

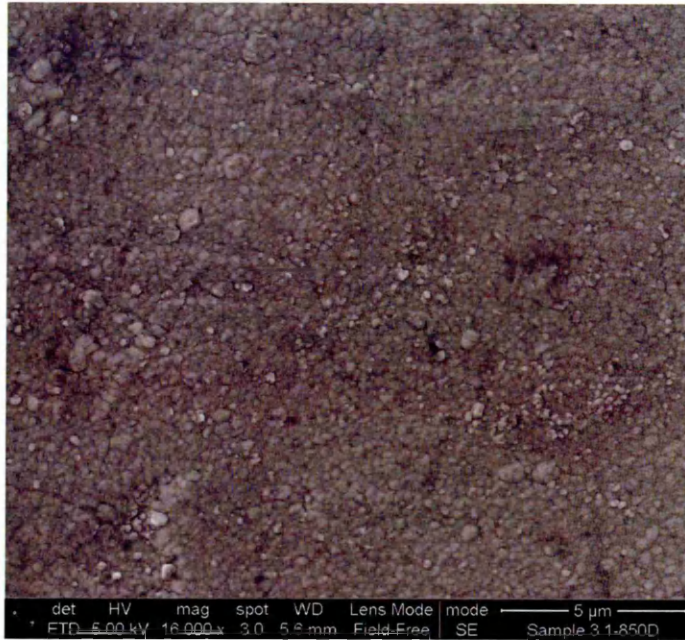


Fig. 6.23: High resolution SEM micrograph of the CrAlYN/CrN surface after 20 h heat-treatment in laboratory air at 850°C: First oxide crystals appear on the dome-shaped morphology of the as-deposited coating

boundaries which extend across the total coating thickness and interconnect the substrate and the coating tops. Additionally, foreign crystals with sizes of 100-200 nm in diameter are found. These crystals are either rich in Cr or in Al with traces of Y (<2at%), as evidenced by TEM-EDS. The highly Al-containing crystals incorporate higher contents of Y whereas Y detection in the Cr-rich regions is rather limited. A SAD pattern of these structures (see insert in Fig. 6.18(c)) shows a mixture of diffraction arcs and discrete spots. Analysis of the  $d$ -spacing reveals the CrAlYN/CrN phase (represented by CrN), Cr<sub>2</sub>N and AlN. The earlier observed diffraction arcs of the CrAlYN/CrN phase are weaker in comparison with the SAD pattern taken after 5 h heat-treatment (see insert in Fig. 6.18(b)). Additionally, more spots relating to the previously observed Cr<sub>2</sub>N and AlN phases are present. The reduction of the CrAlYN/CrN diffraction arcs with the simultaneous increase in diffraction spots of Cr<sub>2</sub>N and AlN suggest that the initial CrAlYN/CrN is partially replaced by these new phases. As the TEM-EDS analysis of individual grains always shows a mixture of Cr and Al, it can be expected that the Cr<sub>2</sub>N

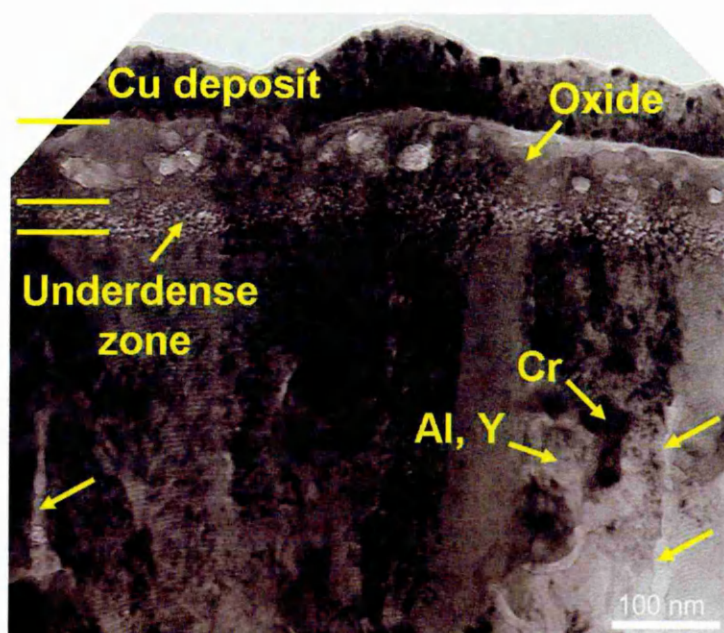


Fig. 6.24: BF-TEM micrograph of oxide scale on CrAlYN/CrN after 20 h heat-treatment in laboratory air at 850°C with the formation of microcrystals inside the bulk as well as an oxide scale on the coating surface (Arrows indicate pores at the column boundaries)

and AlN phases incorporate a substantial amount of the complementary element.

The TEM verifies that the bulk CrAlYN/CrN preserves a nanolayer structure which is replaced in few places by polycrystalline globular Cr<sub>2</sub>N and Y-containing hcp-AlN.

The growth of a dense oxide layer is observed at the film surface (see Fig. 6.24). These oxide crystals have an average size of 16-25 nm and form a smooth surface morphology. A low density region underneath the scale, already characterised after 5 h by speckled contrast layer (see Fig. 6.21), becomes more pronounced and thicker when heat-treatment is carried out for 20 h. TEM-EDS identifies Cr, Al and O in the scale (Cr/Al ratio ~2.13) and reveals the presence of the substrate elements Fe and Mn (both <1at% metal content) in some of the oxide crystals. These substrate elements can migrate to the coating surface either by surface diffusion through cracks in the coating (see Fig. 6.16) or by grain boundary diffusion through the voided boundaries in the bulk material (see Fig. 6.24). When reaching

the surface, these substrate elements are then incorporated into the growing oxide.

In the GA-XRD diffractogram (see Fig. 6.17), a  $\text{Cr}_2\text{O}_3$  phase is detected. This  $\text{Cr}_2\text{O}_3$  as only oxide phase. Other phases are not present. The previously mentioned TEM-EDS studies show that this oxide consists of predominantly Cr and Al as well as low concentrations of Fe and Mn. The XRD studies indicate that no Al-based oxides form in the scale. The presence of Al in the scale, however, suggests that Al is incorporated in the  $\text{Cr}_2\text{O}_3$  forming a  $(\text{Cr,Al})_2\text{O}_3$  solid solution with incorporation of Fe and Mn.

In conclusion, the CrAlYN/CrN remains intact in large regions of the coating. However, the coating degradation cumulatively proceeds with a phase transformation of CrAlYN/CrN into  $\text{Cr}_2\text{N}$  and Y-rich AlN and the formation of a Fe- and Mn- containing  $(\text{Cr,Al})_2\text{O}_3$  oxide scale.

### 6.3.4 Reactions after 50 h

SEM surface observations after 50 h heat-treatment (see Fig. 6.16(d)) demonstrate the growth of surface oxides at a larger scale compared to that observed after shorter heat-treatment experiments. The initially dome-shaped coating surface (see Fig. 5.7(a), Sec. 5.1) is completely replaced by small facet-shaped oxides (see Fig. 6.25). Additionally, cracks open up with an extensive growth of crystals inside are observed. This strongly increased amount of oxides both on the coating surface and inside the cracks gives direct evidence of accelerated oxidation of coating and substrate.

The XRD diffractogram (see Fig. 6.17) shows numerous reflections. The phases  $\text{Cr}_2\text{N}$ , hcp-AlN and  $\text{Cr}_2\text{O}_3$ , which already form after heat-treatment for 5 h, are again identified. Additionally to these reflections, further reflections are found. Additionally,  $\text{FeCr}_2\text{O}_4$  (reflections e.g. at  $2\theta = 35.25^\circ$ , monoclinic, JCPCD 24-0511) can be identified. The formation of this phase signifies oxidation of the substrate. The growth of (Fe,Cr)-oxides was already observed after 5 h (see Fig. 6.22). At this stage, it was not possible to identify the phase structure of these crystals. After 50 h, in contrast, a Fe-containing phase is evidenced by GA-XRD mea-



Fig. 6.25: High resolution SEM micrograph of the CrAlYN/CrN surface after 50 h heat-treatment in laboratory air at 850°C: Fine grained oxides grow on the coating surface

surements (see Fig. 6.17) and therefore implies that the oxides crystals inside the cracks grow in a  $\text{FeCr}_2\text{O}_4$  phase structure.

TEM investigations were conducted to identify microstructural changes occurring upon heating. The cross-sectional view (see Fig. 6.18(d)) shows that the initially columnar structure in the bulk coating is replaced to a large extent by small polycrystalline grains. A small band of inhomogeneously distributed crystals (reaction zone) with a rough surface appearance can be observed at the coating top. It is suggested that this structure arises from surface oxidation.

A TEM-EDS spot analysis profile was taken from the thin film cross-section (see Fig. 6.26). Fe is observed in the base layer ( $\sim 3.1\text{at}\%$  metal content) and the coating ( $\sim 2.5\text{at}\%$ ). Additionally, a higher Cr content ( $\sim 36\text{at}\%$  in the base layer and  $\sim 54\text{at}\%$  in the multilayer region) is also present over the total cross-section resulting in a Cr/Al ratio of 1.32. Furthermore, small amounts of Mn are detected ( $< 1\text{at}\%$ , below quantification limit). A comparison of the Fe content and the Cr/Al ratio after 5 h (see Fig. 6.19) and 50 h heat-treatment shows an

increase in Fe (from  $\sim 1.5\text{at}\%$  to  $\sim 3.1\text{at}\%$ ) and in Cr/Al ratio (from  $\sim 1.15$  to  $\sim 1.32$ ). This increase in Fe signifies accelerated Fe diffusion into the coating at longer heat-treatment times. The increase in Cr/Al ratio, in addition, suggests the diffusion of Cr from the substrate into the coating and, in consequence, an increase in the Cr atomic fraction. The presence of Mn in the coating, moreover, implies the diffusion of Mn from the substrate into the coating.

Microstructural TEM observations reveal the presence of a polycrystalline morphology over the complete cross-section (see Fig. 6.18(d)). Some of these crystals can reach dimensions of up to  $\sim 50$  nm in diameter (see Fig. 6.27). The initial column boundaries are still present, despite the obvious changes in morphology. Additionally, a very faint nanolayer structure is found in isolated grains (not shown). The preservation of the nanolayers in isolated grains suggests that the phase decomposition process is in an advanced stage but nevertheless incomplete

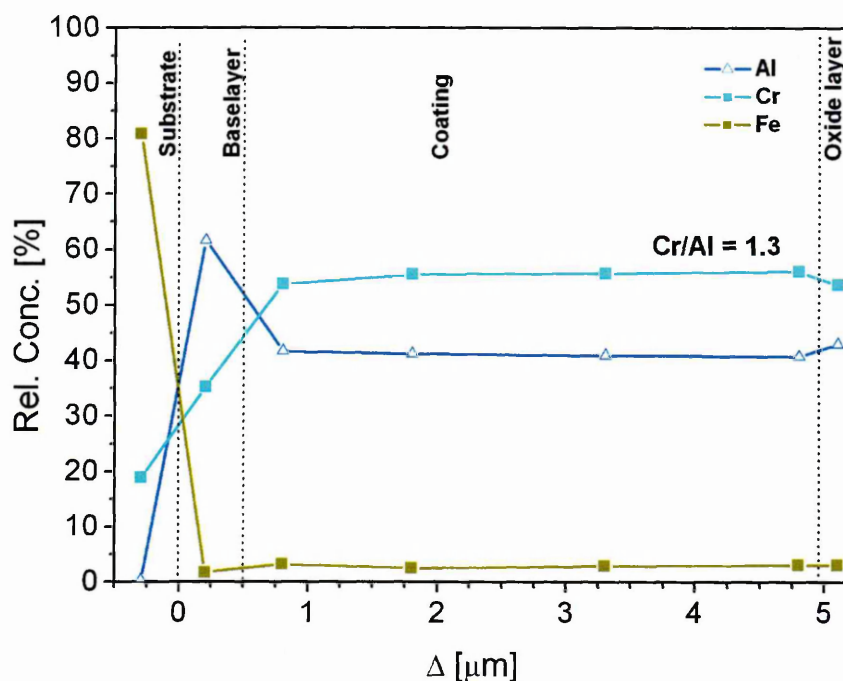


Fig. 6.26: TEM-EDS spot analysis profile over total coating cross-section after 50 h heat-treatment in laboratory air at  $850^{\circ}\text{C}$ : The Fe content is  $\sim 2.5\text{at}\%$  and the Cr/Al ratio is  $\sim 1.3$  in the coating

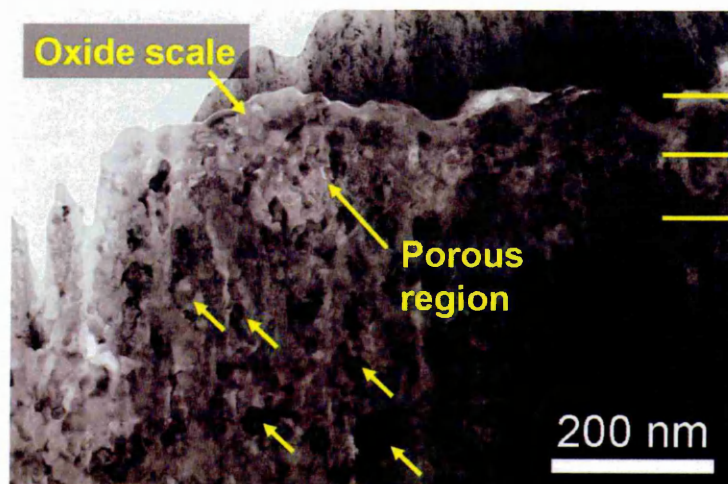


Fig. 6.27: BF-TEM micrograph of the top region of CrAlYN/CrN after 50 h heat-treatment in laboratory air at 850°C: A polycrystalline globular morphology of the bulk, a wavy oxide scale and a porous zone at the coating/scale interface are present (Arrows indicate large globular crystals)

after 50 h heat-treatment. An SAD pattern taken from the bulk (see insert in Fig. 6.18(d)) shows a variety of discrete diffraction spots. From this, the phases CrAlYN/CrN (represented by CrN), Cr<sub>2</sub>N and AlN can be identified. The previously described SAD pattern from coatings heat-treated for shorter times (see insert in Fig. 6.18(c)) reveal distinct diffraction arcs of the CrAlYN/CrN phase. These arcs are only very faint in the present pattern but are they are largely replaced by discrete diffraction spots. This implies the loss of the preferred crystallographic orientation in the coating and is a signal of the phase decomposition of CrAlYN/CrN.

At the coating top, a  $110 \pm 14$  nm thick oxide scale and a  $184 \pm 16$  nm thick, strongly voided region underneath this scale are observed (see Fig. 6.27). The oxide scale appears to be less dense and well-defined than in those films heat-treated for shorter exposure times (see Fig. 6.24). It is obvious that the scale has a wavy surface and the scale thickness changes over the length of the surface. The pores in the voided zone take a relatively large reaction volume and extend in irregular distances deep into the bulk material. Advanced outward diffusion of Cr and/or Al, the trapping of released N<sub>2</sub> and the accumulation of point defects are possi-

ble reaction mechanisms for the void formation at the interface. These reactions are suggested to be similar to those taking place after short-term oxidation of CrAlYN/CrN for 1 h exposure temperature at high temperatures of 1000°C (see Fig. 6.14(a), Sec. 6.2). TEM-EDS investigations identify elements in the oxide scale as Cr, Al and O with incorporations of Fe and Mn. The element analysis in individual grains shows the co-existence of Cr and Al with varying ratios in these crystals ( $\sim 1.8$ - $2.7$ ). This rather high ratio implies that the oxide scale is Cr-rich in comparison to the bulk coating (Cr/Al ratio  $\sim 1.32$ ) also suggest the formation of a crystal mixture from  $(\text{Cr,Al})_2\text{O}_3$  with various compositions. The GA-XRD diffractogram (see Fig. 6.17) clearly exhibits the presence of  $\text{Cr}_2\text{O}_3$ . Taking into account that the oxide is highly Al-containing, it is implied that the oxide crystals form an Al-rich  $\text{Cr}_2\text{O}_3$  phase.

In short, after heat-treatment for 50 h at 850°C, the CrAlYN/CrN film undergoes a nearly complete phase transformation into  $\text{Cr}_2\text{N}$  and AlN and forms an oxide scale consisting of  $(\text{Cr,Al})_2\text{O}_3$ . Substrate oxidation takes place at an accelerated rate, especially in regions in which the steel substrate is exposed through cracks in the protective coating, leading to the growth of  $\text{FeCr}_2\text{O}_3$  oxides.

### 6.3.5 Reactions after 100 h

SEM surface observations show the growth of large oxide crystals both on the coating surface and inside cracks after 100 h heat-treatment in laboratory air (see Fig. 6.16(e)). Facet-shaped crystals on the coating (see Fig. 6.28) can grow to sizes exceeding 500 nm with a density of  $0.35 \mu\text{m}^{-2}$ . The cracks in the coating are largely filled with crystals protruding above the specimen surface. Two different types of crystals can be identified by their shape. The majority of these crystals has a “facet-shaped” appearance (see Fig. 6.29(a)) while others are more “sausage-shaped” (see Fig. 6.29(b)). Both types of oxide consist of a mixture of Cr, Fe, Mn and O (analysed by EDS). The facet-shaped oxides are highly Mn-containing and form  $(\text{Cr,Fe,Mn})$ -oxides whereas the “sausage-shaped oxides” with their lower Mn-content can be classified as  $(\text{Cr,Fe})$ -oxides.

Fig. 6.30 shows a SEM micrograph of a cross-section of the heat-treated film. There, a crack propagates through the coating thickness. This crack is filled with a large number of crystals which can be identified as (Cr,Mn,Fe)-oxides by EDS. Large voids are present at the substrate/base layer interface and extend over a length of  $\geq 6 \mu\text{m}$ . Material which was initially present at the interface can either diffuse along the interface to fill the crack or, at the same time, migrate through the base layer into the coating. The extent of void formation on large lengths signifies that the element diffusion is in an advanced stage.

Analysis of the GA-XRD diffractogram (see Fig. 6.17) shows a similar pattern to that obtained after 50 h. Peaks appear at similar  $2\theta$  positions and can be accomplished to identify  $\text{Cr}_2\text{N}$ ,  $\text{AlN}$ ,  $\text{Cr}_2\text{O}_3$  as well as  $\text{FeCr}_2\text{O}_4$ .

Post-treatment TEM investigations can reveal microstructural changes caused by the thermal treatment (see Fig. 6.18(e)). The initially columnar structure is completely replaced by globular grains. The original column boundaries can only be identified in the lower part of the coatings. A large interaction zone which

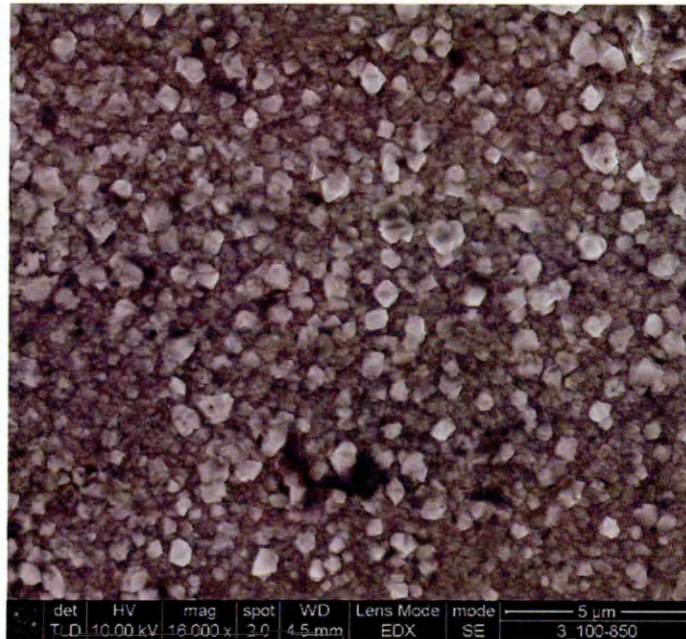
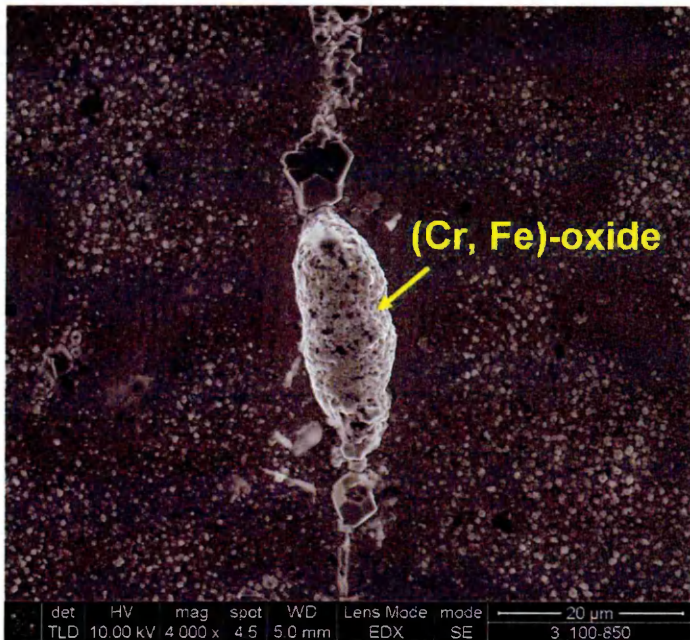


Fig. 6.28: High resolution SEM micrograph of the CrAlYN/CrN surface after 100h heat-treatment in laboratory air at 850°C: Facet-shaped oxide crystals have a density of  $0.35 \mu\text{m}^{-2}$  for crystal sizes above 500 nm



(a) Facet-shaped oxides



(b) Sausage-shaped oxides

Fig. 6.29: SEM micrographs from surface oxides after 100h heat-treatment in laboratory air at 850°C: (a) “Facet-shaped” (Cr,Fe,Mn)-oxides and (b) “sausage”-shaped (Cr,Fe)-oxides (Note differences in magnification)

arises from surface oxidation can be observed at the coating top.

TEM-EDS profiling was conducted to examine the diffusion of substrate elements into the coating (see Fig. 6.31). The plot demonstrates Fe in the base layer ( $\sim 4\text{at}\%$  metal content) and the bulk coating ( $\sim 4.75\text{at}\%$ ). Within the layered region at the top (see Fig. 6.18(e)), Fe significantly enriches to  $\sim 19\%$ . Cr (stable at  $\sim 57\text{at}\%$  in the bulk material) is also found in higher concentration in the oxidised zone ( $\sim 71\text{at}\%$ ). Al (represented with  $\sim 38\%$  in the bulk material), in contrast, is strongly depleted in this top layer ( $\sim 10\%$ ). The Cr/Al ratio in the bulk is consequently calculated to be  $\sim 1.50$  in the bulk and to be  $\sim 7.10$  in the top. Other substrate elements, e.g. Mn and Ni, are also present in the measured spectra; their relative content, however, is below the quantification limit of  $1\text{at}\%$ .

Comparing the chemical composition before and after heat-treatment, an increase in Cr/Al ratio after 100 h ( $\sim 1.50$ ) in the bulk structure becomes apparent compared to the as-deposited state ( $\sim 1.04$ ), after 5 h ( $\sim 1.15$  (see Fig. 6.19)) and

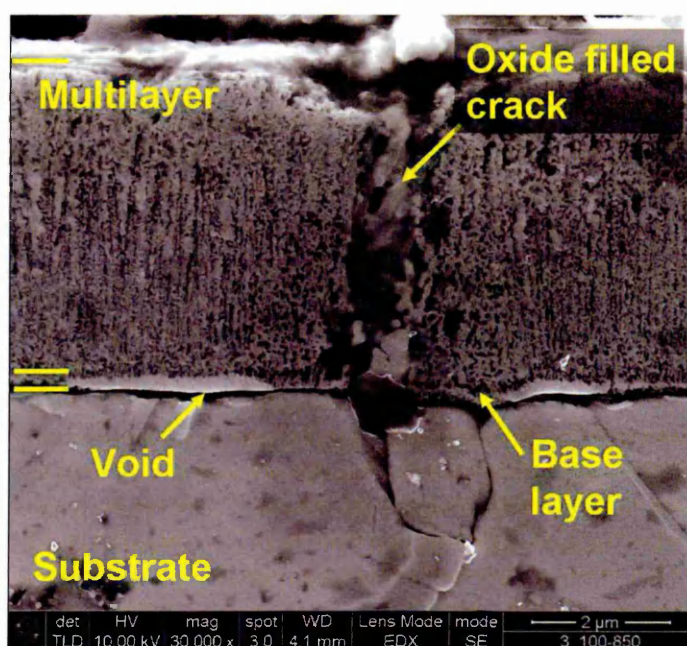


Fig. 6.30: SEM micrograph of CrAlYN/CrN coating cross-section after 100 h heat-treatment in laboratory air at  $850^{\circ}\text{C}$ : Oxides grow through a crack in the coating; voids form at the substrate/base layer interface

also 50 h ( $\sim 1.32$  (see Fig. 6.26)). This steady increase in the Cr atomic fraction most probably results from diffusion of Cr from the substrate into the coating.

TEM examination of the bulk coating shows the previously mentioned polycrystalline globular structure (see Fig. 6.32) in which individual grains are rich in either Cr or Al and Y ( $\sim 1.5\text{at}\%$ ). Analysis of an SAD pattern taken from this structure (see insert in Fig. 6.18(e)) allows the identification of CrN, Cr<sub>2</sub>N and AlN. In the previous analysis of the SAD pattern, the CrN phase was associated with the nanolayered CrAlYN/CrN structure. In the present case, however, this structure is completely replaced by the new recrystallised structure. It is therefore rather suggested that grains of a fcc-CrAlN or possibly fcc-CrAlYN are present inside a matrix of Cr<sub>2</sub>N and AlN.

TEM examination of the coating top was performed to investigate the oxidation reaction caused by the heat-treatment (see Fig. 6.32). A  $152 \pm 21\text{nm}$  thick

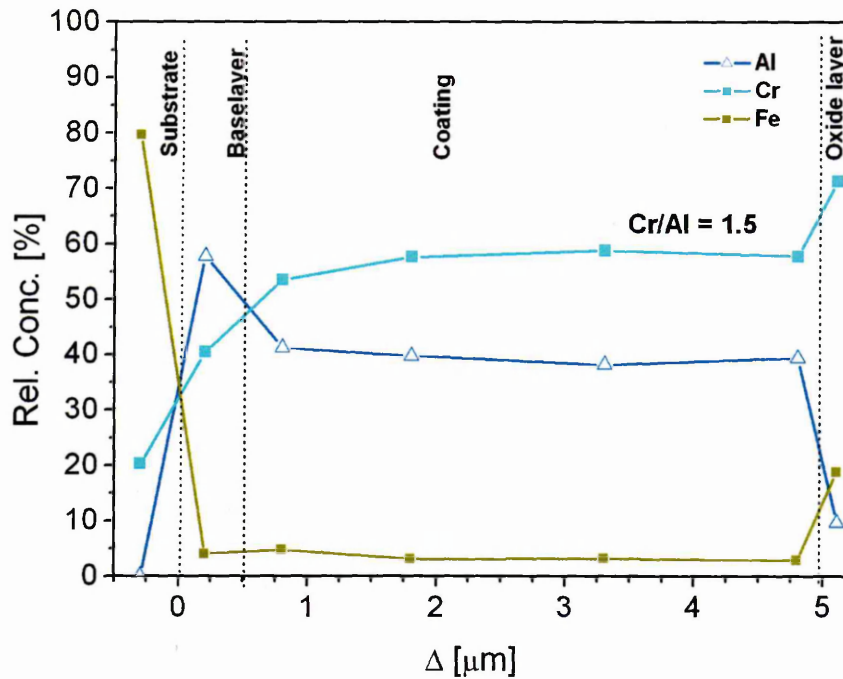


Fig. 6.31: EDS spot analysis profile over total coating cross-section after 100 h heat-treatment in laboratory air at 850°C: The Fe content is  $\sim 4.7\text{at}\%$  and the Cr/Al ratio is  $\sim 1.5$  in the bulk coating

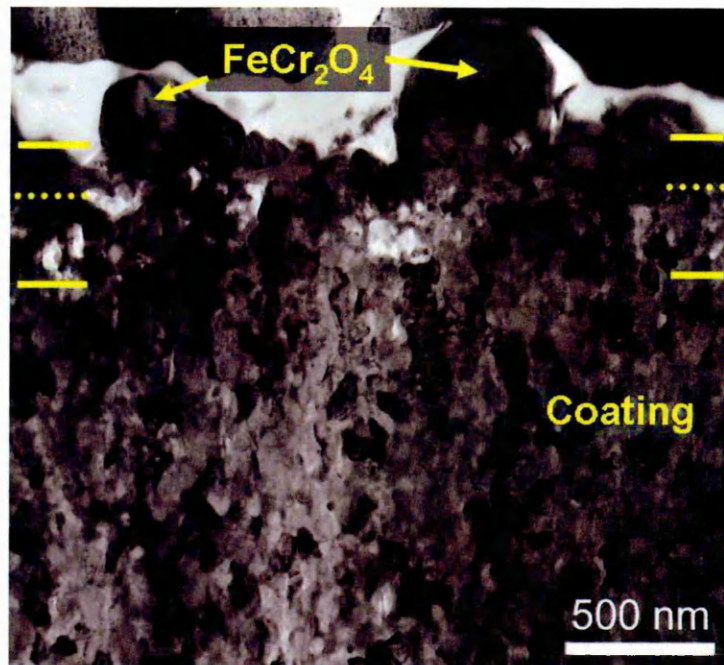


Fig. 6.32: BF-TEM micrograph of the oxide scale on CrAlYN/CrN after 100 h heat-treatment in laboratory air at 850°C: Large FeCr<sub>2</sub>O<sub>4</sub> crystals protrude from a porous (Cr,Al)<sub>2</sub>O<sub>3</sub> oxide scale

oxide scale forms. A large porous region is situated underneath the top oxide and has a thickness of  $231 \pm 16$  nm. Furthermore, large crystals protrude from the porous scale and consist of a mixture of Cr ( $\sim 53.2\text{at}\%$  metal content), Fe ( $\sim 20.6\text{at}\%$ ), Al ( $\sim 11.9\text{at}\%$ ), Mn ( $\sim 10.0\text{at}\%$ ) and Ni ( $\sim 4.2\text{at}\%$ ) in combination with O (analysed by TEM-EDS). The elemental composition of the crystals in the porous oxide is mainly governed by a mixture of Cr ( $\sim 71.4\text{at}\%$ ), Al ( $\sim 9.7\text{at}\%$ ) and O. This oxide also contains Fe ( $\sim 18\text{at}\%$ ) and Mn ( $< 1\text{at}\%$ ).

The phase composition of the crystals growing above the scale may be estimated from the combined results of TEM-EDS and GA-XRD. The elemental composition of the crystals growing above the scale gives roughly a Cr/Fe ratio of  $\sim 2.6$ . In the GA-XRD diffractogram (see Fig. 6.17), FeCr<sub>2</sub>O<sub>4</sub> is the only detected phase that contains Fe. The Cr/Fe ratio in this phase is 2 and reasonably close to the Fe/Cr ratio measured in the crystals. It is therefore suggested that the oxides protruding from the scale, are FeCr<sub>2</sub>O<sub>3</sub> crystals with partial replacement

of Fe and Cr by Al, Ni and Mn. Fe-containing oxides are also found in the cracks that form upon heating to elevated temperatures (see Fig. 6.29). These oxides may also form a  $\text{FeCr}_2\text{O}_3$  phase which then contributes to the detection of this phase in the GA-XRD diffractogram (see Fig. 6.17).

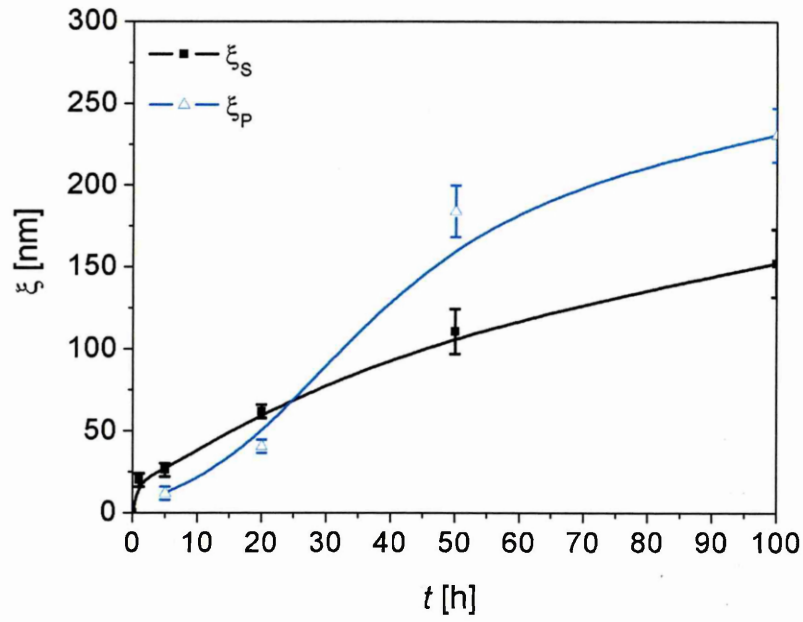
To conclude, the phase transformation is nearly complete after heat-treatment for 100 h. Phases that form during this process are fcc-CrAlN or fcc CrAlYN as well as  $\text{Cr}_2\text{N}$  and AlN. Additionally, porous, highly Fe- and Mn-containing  $(\text{Cr,Al})_2\text{O}_3$  forms on top of the coating. Furthermore,  $\text{FeCr}_2\text{O}_3$  crystals are situated on top of these oxides.

### 6.3.6 Determination of the Scale Growth Rate

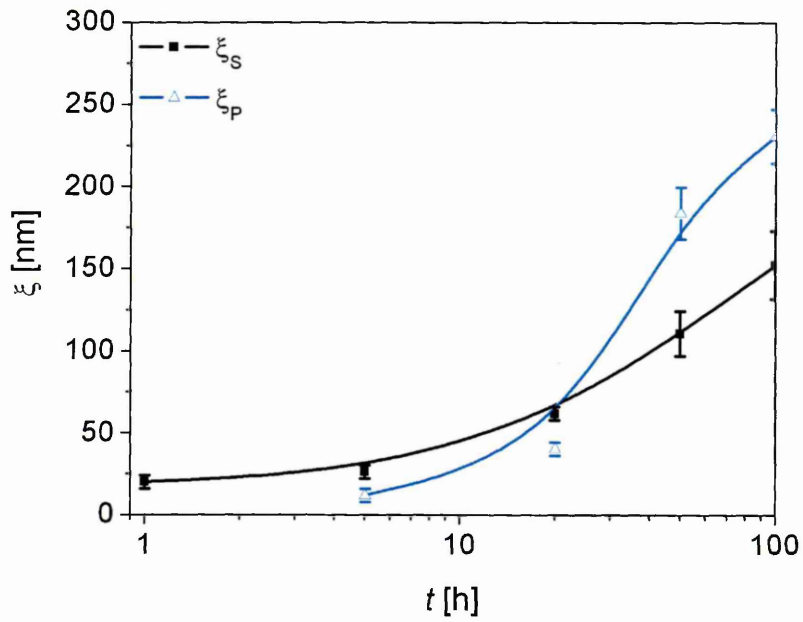
The above discussion of microstructural changes and oxidation processes occurring in CrAlYN/CrN upon heating allows an insight into the oxidation kinetics of this system. One way to access the progressive oxidation of CrAlYN/CrN is by means of oxide scale thickness  $\xi$  measurements (carried out by TEM). In the present analysis, the thickness  $\xi_S$  of the oxide scale and the thickness  $\xi_P$  of the porous layer at the coating/scale interface are presented as linear, a half-logarithmic and a half-parabolic plots (see Fig. 6.33). A linear slope in these plots signifies growth according to the corresponding rate law.

The best fit of the  $\xi_S$  is achieved when using the parabolic law (see Eq. 2.2, Sec. 2.1). The scale growth after the parabolic law is often correlated to diffusion controlled processes as rate determining factor [25, 135]. In CrAlYN/CrN, the outward diffusion of Cr and possibly Al were identified as possible oxidation mechanism. Simultaneously, inward diffusion of O is expected. The oxide growth after a parabolic law implies that these diffusion processes dominate the growth rate of the oxides on CrAlYN/CrN coatings.

The growth of the porous layer, in contrast to the scale growth, cannot be fitted clearly by one of the suggested reaction laws. The thickness of the voided zone  $\xi_p$  is found to be 10-20 nm thinner than the oxide scale when heat-treatment is carried out for <50 h. After longer heat-treatment ( $\geq 50$  h), the voided zone is

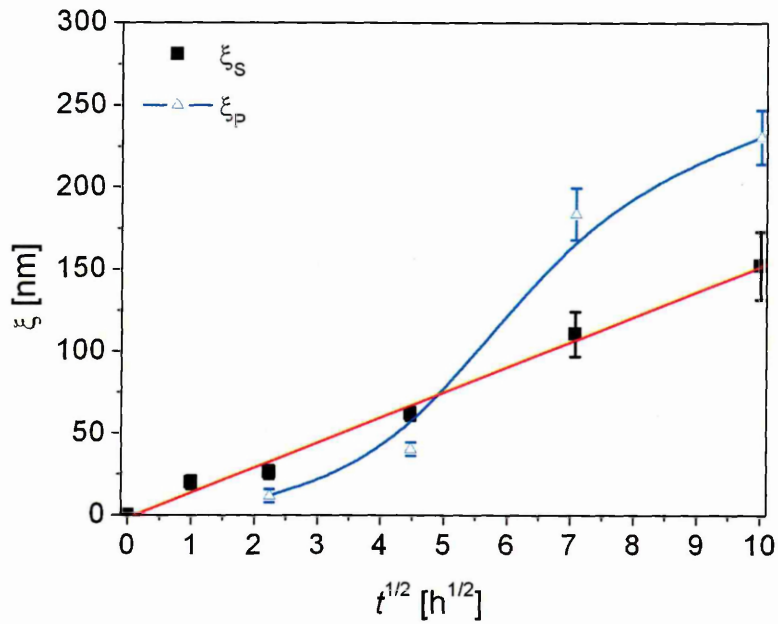


(a) Linear fit



(b) Logarithmic fit

Fig. 6.33: (a) Linear, (b) half-logarithmic and (c) half-parabolic plot of the oxide layer thickness  $\xi_S$  and the thickness  $\xi_P$  of the porous zone after isothermal heat-treatment at 850°C, determined by TEM imaging



(c) Parabolic fit

Fig. 6.33: Continued

found to be 70-80 nm thicker than the scale. The question arises which processes cause this strong rise in porous layer thickness. Outward migration of coating elements was already identified as one of the factors contributing to the formation of an porous region under the scale. Other void forming mechanisms are the precipitation of point defects, e.g. vacancies or trapped Ar [92] and the trapping of N<sub>2</sub> [30]. In CrAlYN/CrN, it is likely that N<sub>2</sub> is released during (i) the oxidation and (ii) the phase transformation. The strong increase in the thickness  $\xi_P$  of the porous layer for exposure times  $\geq 50$  h cannot be explained solely by these mechanism. The disproportionally large change in thickness coincides with the phase transformation which is in a very advanced stage after 50 h of heat-treatment. This phase transformation may be an additional source for N<sub>2</sub>. This additional N<sub>2</sub> can then accumulate under the oxide scale and may cause the observed strong rise in porous layer thickness  $\xi_p$  after 50 h heat-treatment.

## 6.4 Influence of the Energetic Particle Bombardment on the Oxidation Performance

It is well known that factors such as microstructure or chemical composition have significant influence on the oxidation performance of thin films. As the effect of the bias voltage  $U_b$  during the deposition step on the microstructure as well as mechanical properties were already investigated in detail in Sec. 5.1; the next step is to analyse the effect of a variation in  $U_b$  on the oxidation performance.

### 6.4.1 Thermogravimetric Analysis

Continuous thermogravimetric analysis (see Sec. 3.4.1) was performed as a quick test to compare the oxidation performance of CrAlYN/CrN grown at various  $U_b$ .

Fig. 6.34 compares the weigh gain  $\rho$  of various CrAlYN/CrN films as a function

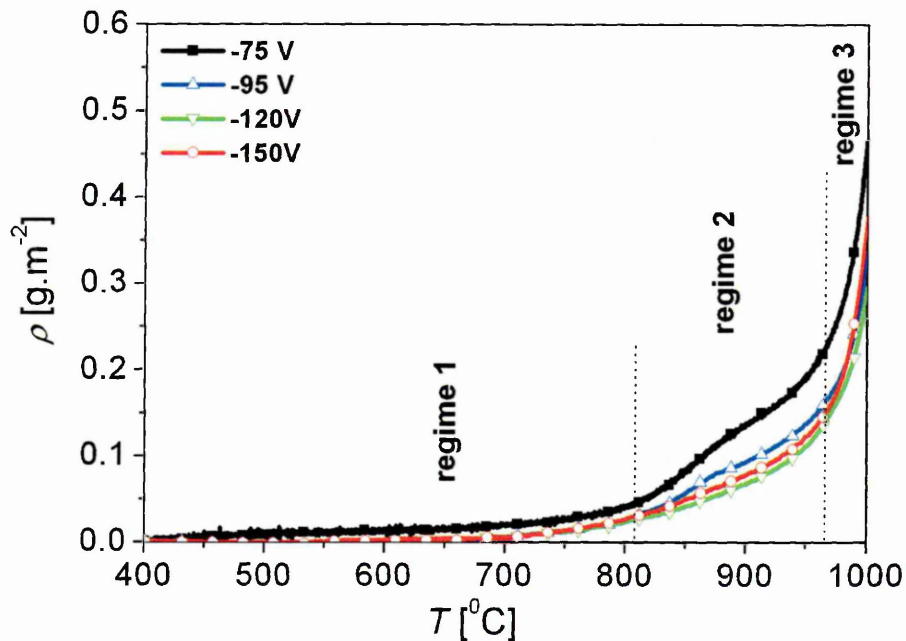


Fig. 6.34: Dynamic thermogravimetric data of CrAlYN/CrN deposited at varying  $U_b$  on 304 stainless steel substrates for thermal ramping at  $5^\circ\text{C min}^{-1}$  in dry air: CrAlYN/CrN grown at  $U_b = -120$  V has the lowest total weight gain

of temperature. The weight gain of all specimens is extremely low (weight gain rate  $<0.6 \times 10^{-5} \text{ g.m}^{-1}\text{K}^{-1}$ ) below temperatures of  $\sim 800^\circ\text{C}$  (regime 1). From  $800^\circ\text{C}$  to  $970^\circ\text{C}$  (regime 2), the weight gain of the low  $U_b$  coating ( $U_b = -75 \text{ V}$ ) progresses with a linear slope ( $1.1 \times 10^{-3} \text{ g.m}^{-1}\text{K}^{-1}$ ) whereas the  $U_b = -95 \text{ V}$  CrAlYN/CrN increases weight at a reduced rate ( $7.4 \times 10^{-4} \text{ g.m}^{-1}\text{K}^{-1}$ ). The high  $U_b$  films ( $U_b = -120 \text{ V}$  and  $-150 \text{ V}$ ), in contrast, show a steady increase in weight gain in regime 1 and 2 which cannot be fitted linearly. All coatings start to gain weight at an increased rate above temperatures of  $970^\circ\text{C} \pm 5^\circ\text{C}$  (regime 3). The weight gain in regime 3 is one order of magnitude higher compared to regime 2. Here, the high  $U_b$  coatings again oxidise at a lower rate than the low  $U_b$  coatings. The lowest rate of  $4.4 \times 10^{-3} \text{ g.m}^{-1}\text{K}^{-1}$  is observed in CrAlYN/CrN grown at  $U_b = -120 \text{ V}$ . This suggests that a high  $U_b$  during deposition generates CrAlYN/CrN coatings with improved oxidation resistance. A more comprehensive discussion of this behaviour will be given at a later stage (see Sec. 6.4.3).

## 6.4.2 Isothermal Heat-Treatment for 100 h at $850^\circ\text{C}$

Isothermal heating was performed for 100 h at  $850^\circ\text{C}$  to determine the oxidation performance of CrAlYN/CrN grown under various  $U_b$  conditions in a long-term experiment.

### 6.4.2.1 SEM Analysis

Fig. 6.35 shows the surface of the individual coatings after 100 h exposure to laboratory air at  $850^\circ\text{C}$ . Cracks are observed in the films deposited at  $U_b = -75 \text{ V}$  (see Fig. 6.35(a)). The extent of cracking notably declines when  $U_b$  is increased to  $-95 \text{ V}$  (see Fig. 6.35(b)). In contrast, cracking does not take place at all when the coating is grown at higher  $U_b \geq -120 \text{ V}$  (see Fig. 6.35(c) and 6.35(d)).

Crack networks appear in many coatings upon heating and are correlated with the residual compressive stresses in the coating and the thermal stresses induced by the heating [19, 206]. Cracking occurs when the tensile stresses induced by a difference in thermal expansion coefficient between substrate and coating exceed

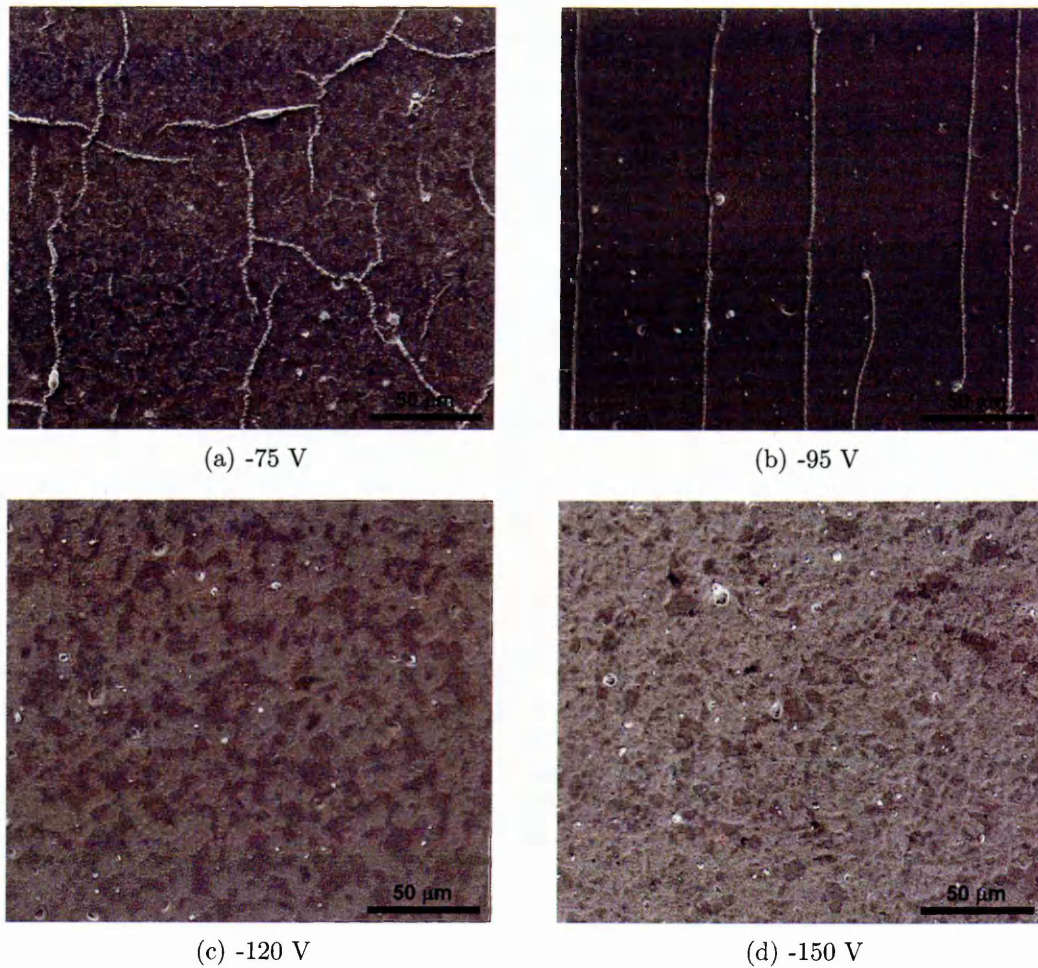


Fig. 6.35: SEM micrographs from the surface of CrAlYN/CrN deposited at different  $U_b$  after 100 h heat-treatment at 850°C: Cracks appear in the low  $U_b$  coatings ( $U_b \leq -95$  V) whereas the high  $U_b$  coatings ( $U_b \geq -120$  V) are crack-free

the residual compressive stresses in the coating. In the current investigation, the residual stresses increase from -3.3 GPa at  $U_b = -75$  V to -9.5 GPa at  $U_b = -150$  V (see Fig. 5.23(b), Sec. 5.1). The temperature at which cracking can theoretically occur first may be calculated from Eq. 6.1 (see Sec. 6.2). For purely theoretical considerations, i.e. disregarding stress relief, cracking would occur at 830°C in the film grown at  $U_b = -75$  V, at 1020°C for deposition at  $U_b = -95$  V and in the highest  $U_b$  specimen at 1465°C. Thus cracking is more likely to occur when the coating is deposited at high  $U_b$ .

#### 6.4.2.2 XRD Analysis

GA-XRD diffractograms of CrAlYN/CrN were taken to determine the phase structure after the isothermal heat-treatment (see Fig. 6.36). In all coatings, reflections are found at similar  $2\theta$  positions and allow the determination of the phases  $\text{Cr}_2\text{N}$ , AlN as well as  $\text{Cr}_2\text{O}_3$ .  $\text{FeCr}_2\text{O}_4$  is also detected. It is therefore shown that these phases form in all investigated coatings after heat-treatment and that the formation of these phases is independent of  $U_b$  applied during deposition.

#### 6.4.2.3 TEM Analysis

It was shown earlier on (see Sec.5.1.5) that microstructure of CrAlYN/CrN is strongly dependent on the  $U_b$  during deposition. The coatings deposited at  $U_b \leq -120$  V are mainly grown in a columnar structure, whereas higher  $U_b \geq -120$  V leads to a structure with single crystalline domains which are limited to the base layer at  $U_b = -120$  V but extend into the nanolayers at  $U_b = -150$  V. The latter specimen is exemplarily investigated after heating to examine the oxidation resistance of a coating with partially non-columnar microstructure.

In the coating cross-section after heat-treatment for 100 h (see Fig. 6.37), distinct areas of polycrystalline and single crystalline regions are observed next to each other. The single crystals are solely located in the lower part of the coating and do not extend to the coating tops. The nanolayer structure in the single crystalline domains can be clearly observed in these domains (see Fig. 6.38). An SAD pattern from this region (see insert 1 in Fig. 6.37) shows clearly the distinct diffraction spot of a single crystal CrAlYN/CrN (see insert in Fig. 5.8(e), Sec. 5.1.5). The boundary between the single crystalline and the polycrystalline regions is characterised by a sharp transition (see Fig. 6.39). In the polycrystalline regions, the initial nanoscale multilayer is completely replaced by globular grains. Analysis of the corresponding SAD pattern from this region (see insert 2 in Fig. 6.37) clearly shows the presence of CrN,  $\text{Cr}_2\text{N}$  and AlN. A similar phase transformation was discovered in earlier investigations in polycrystalline columnar CrAlYN/CrN after heating (see Sec. 6.3). It is therefore suggested that the

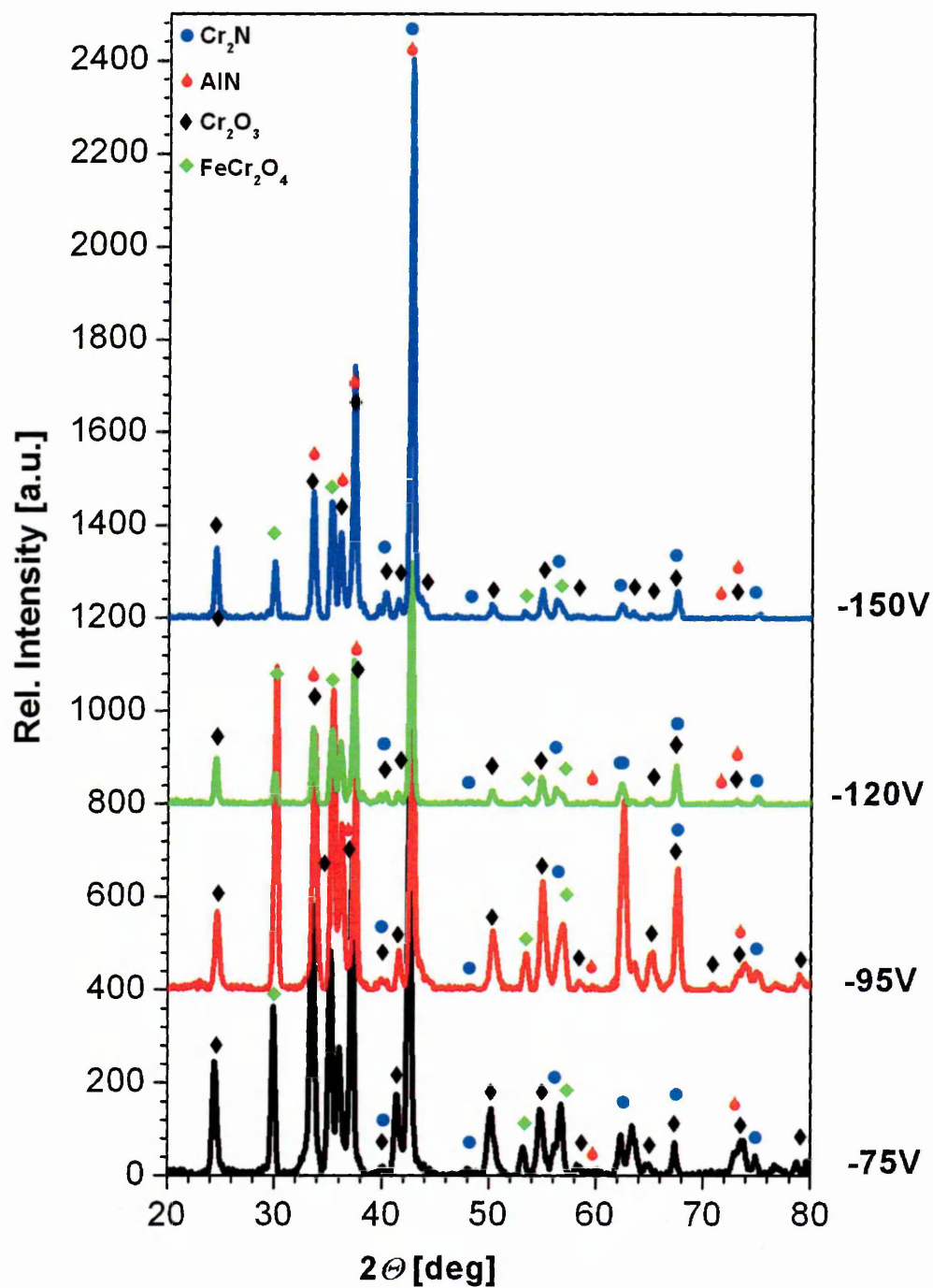


Fig. 6.36: GA-XRD pattern (incident angle  $\gamma = 2^\circ$ ) obtained from CrAlYN/CrN after heat-treatment in laboratory air for 100 h at  $850^\circ\text{C}$

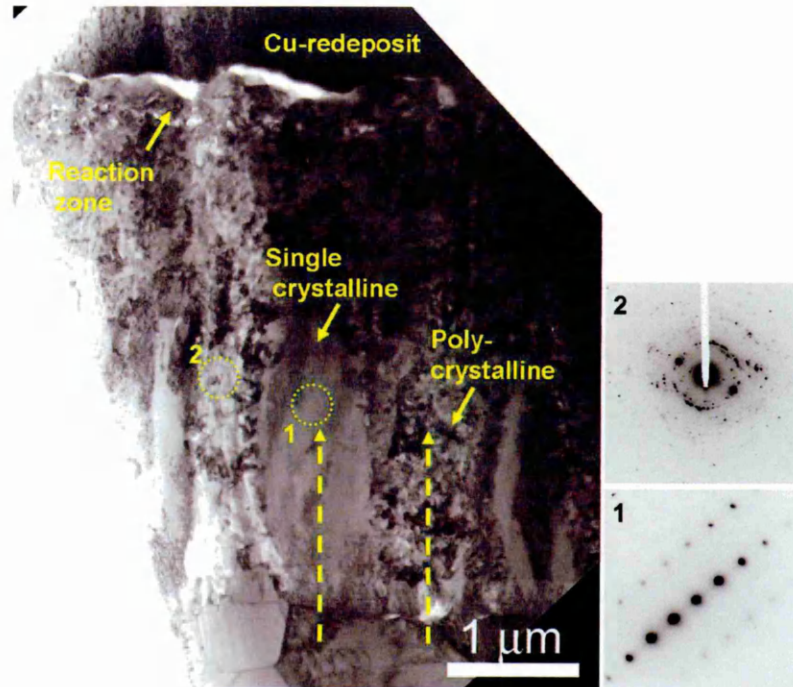


Fig. 6.37: BF-TEM micrograph of the coating cross-section and corresponding SAD pattern of CrAlYN/CrN deposited at  $U_b = -150$  V after 100 h heat-treatment at  $850^\circ\text{C}$ : A distinct morphology with a polycrystalline domain with small globular grains and a large single crystalline domain is present

phase transformation in this examined specimen is limited to regions with initially columnar structure.

The metal distribution in the single and polycrystalline regions in the lower part of the coating was analysed by TEM-EDS analysis (see dotted lines in Fig. 6.37). Fe is found in both regions (see Fig. 6.40(a)) with lower contents in the singlecrystalline regions ( $\sim 2.4\text{at}\%$  in the base layer and  $1.0\text{at}\%$  in the coating at a distance of  $0.8 \mu\text{m}$  to the substrate/base layer interface) compared to the polycrystalline domains ( $\sim 3.5\text{at}\%$  in the base layer and  $\sim 2.8\text{at}\%$  in the coating). The Cr/Al ratio in the single crystal is moreover consistently lower (1.29 compared to 1.43). The TEM-EDS analysis implies that Fe and Cr diffuse from the 304 stainless steel substrate into the coating. This diffusion processes are more pronounced in the polycrystalline regions.

It is known that the coating in as-deposited state (see Fig. 5.8(d), Sec. 5.1) has

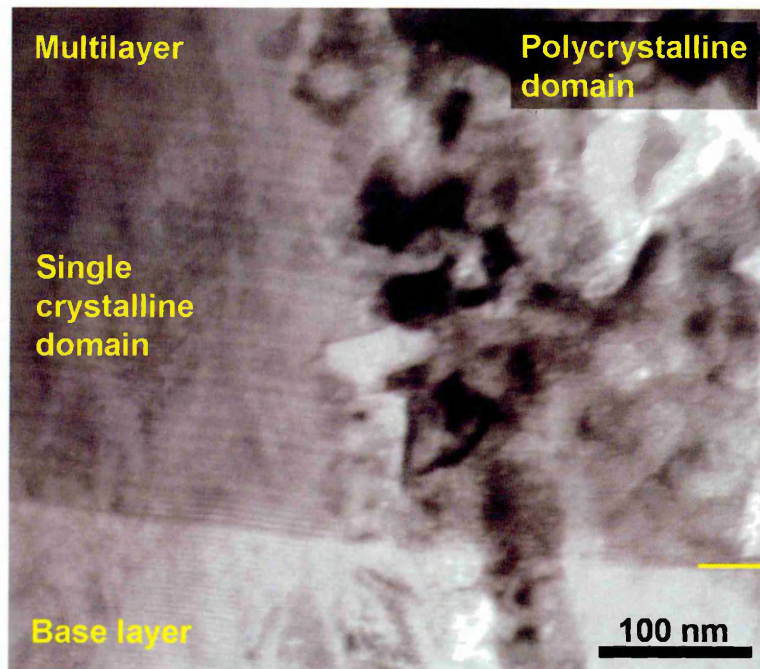


Fig. 6.38: BF-TEM micrographs of CrAlYN/CrN deposited at  $U_b = -150$  V after 100 h heat-treatment at 850°C: Nanolayers are present in the single crystal domain whereas globular crystals dominate the polycrystalline domain

domains with a columnar structure and, consequently, column boundaries. Upon heating, Cr and Fe can diffuse along these boundaries and modify the chemical composition of the coating (see Sec. 6.3). It is assumed that this compositional modification may initiate the phase transformation from a CrAlYN/CrN nanoscale multilayer into CrAlN, Cr<sub>2</sub>N and AlN. In the as-deposited single crystal domains (see Fig. 5.8(e)), these fast diffusion paths are absent and, hence, boundary diffusion is suppressed. The migration of substrate elements into the coating can therefore only take place via volume diffusion. In CrAlYN/CrN, however, the nanolayers are still present after heat-treatment for 100 h and imply that the volume diffusion in these zones is relatively low. Therefore, boundary diffusion is suggested as main diffusion mechanism in CrAlYN/CrN. As boundaries are not present inside these single crystal domains, less substrate elements can migrate into the coating and the nanolayers are preserved in these regions.

At the specimen surface, a continuous, but very inhomogeneous crystalline

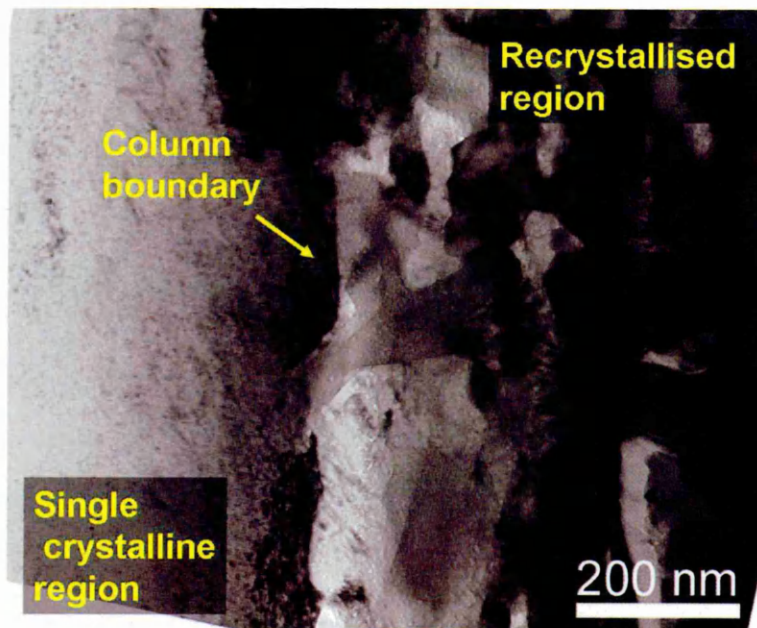
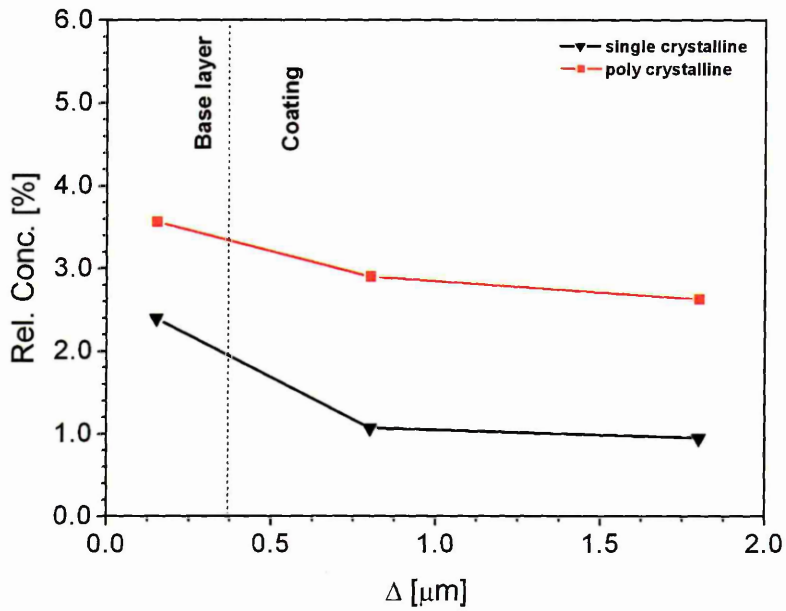


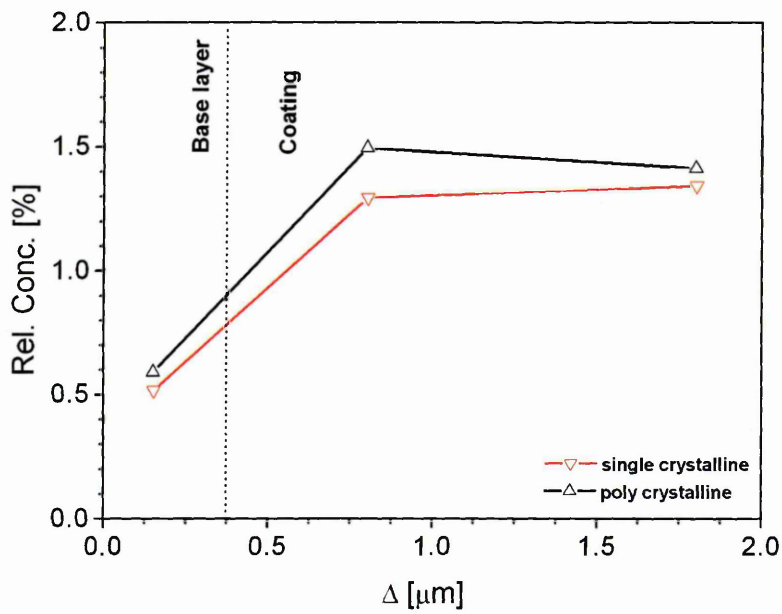
Fig. 6.39: BF-TEM micrograph of the bulk CrAlYN/CrN deposited at  $U_b = -150$  V after 100 h heat-treatment at  $850^\circ\text{C}$ : A sharp boundary is found between single crystalline and polycrystalline domains

oxide scale is found on top of the thin film (see Fig. 6.41) with a  $164\text{nm} \pm 35\text{nm}$  thick oxide scale and a  $223 \pm 40$  nm thick porous layer. The appearance of the oxide scale is identical in the regions on top of the polycrystalline and partially single crystalline regions (see Fig. 6.42). TEM-EDS identifies a mixture of Cr ( $\sim 81.3\text{at}\%$ ), Al ( $\sim 14.9\text{at}\%$ ), Fe ( $\sim 7.2\text{at}\%$ ), Ni and Mn (both  $< 1\text{at}\%$ ) and O in the scale. The GA-XRD diffractogram (see Fig. 6.36) can identify the phase structure of this oxide scale GA-XRD diffractogram. The analysis gives evidence of a  $\text{Cr}_2\text{O}_3$  phase. The TEM-EDS analysis, in contrast, presents other elements, especially Al, in the scale. Hence, it is concluded that a mixed  $(\text{Cr,Al})_2\text{O}_3$  phase with incorporations of substrate elements forms.

A comparison of the scale structure after heating between CrAlYN/CrN grown at  $U_b = -75$  V (see Fig. 6.18(e), Sec. 6.3) and  $-150$  V reveals strong differences. At  $U_b = -75$  V, the coating contains a high atomic fraction of Fe ( $\sim 18\text{at}\%$ ). Additionally, highly Mn-containing  $\text{FeCr}_2\text{O}_4$  oxides protrude from the porous scale (see Fig. 6.32, Sec. 6.3). CrAlYN/CrN grown at  $U_b = -150$  V, in contrast, contains



(a)



(b)

Fig. 6.40: Profile of the Fe content and Cr/Al ratio in the single crystalline and polycrystalline domains of CrAlYN/CrN grown at  $U_b = -150$  V after heat-treatment for 100 h in laboratory air, measured by TEM-EDS: (a) Fe atomic fraction and (b) the Cr/Al ratio are lower in the single crystal domains

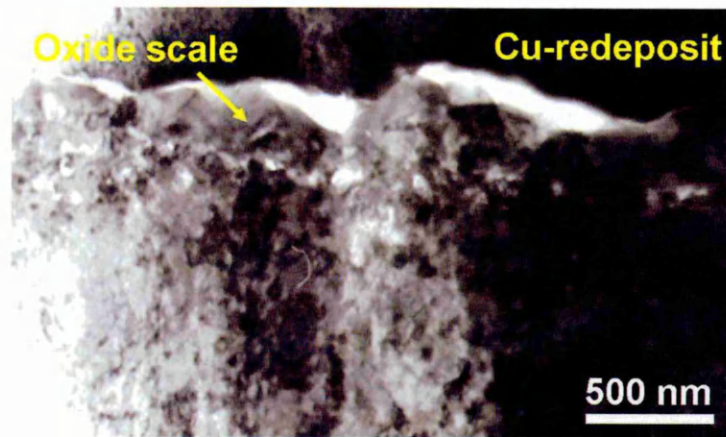


Fig. 6.41: BF-TEM micrograph of a dense oxide on CrAlYN/CrN deposited at  $U_b = -150$  V after 100 h heat-treatment at 850°C

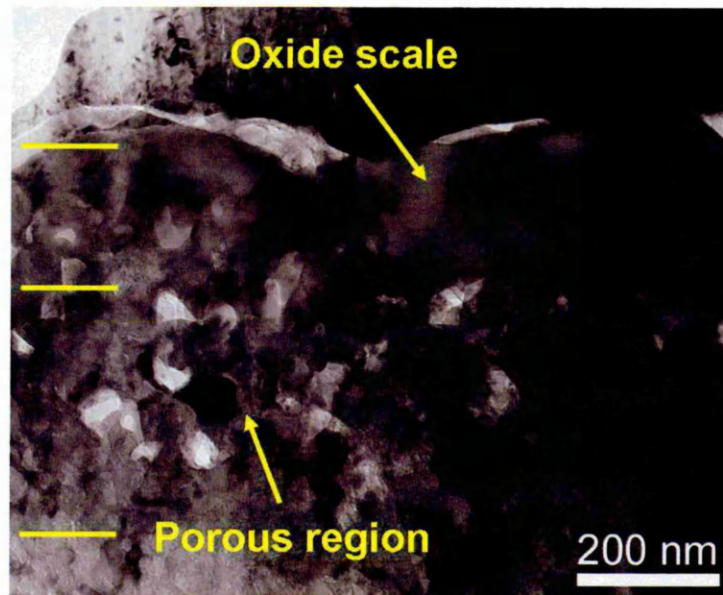


Fig. 6.42: BF-TEM micrograph of the oxide scale on CrAlYN/CrN deposited at  $U_b = -150$  V after 100 h heat-treatment at 850°C: Large crystals form a dense oxide scale. A porous zone is situated at the coating/scale interface

less Fe ( $\sim 7.2\text{at}\%$ ) and, additionally,  $\text{FeCr}_2\text{O}_4$  crystals on top of the more dense scale are completely absent. This suggests that less substrate elements migrate to the coating top and, hence, oxidation of these elements is reduced when single crystalline zones are present in the initial coating structure and the coating is free of cracks. Due to this reduced diffusion in single crystalline regions (see Fig. 6.38),

the growth of large  $\text{FeCr}_2\text{O}_4$  crystals at the outermost scale surface is inhibited.

In summary, it can be stated that the oxidation performance of CrAlYN/CrN can be engineered by a variation in  $U_b$  during thin film growth. In CrAlYN/CrN grown at  $U_b = -150$  V, a partially single crystalline coating structure is found which reduces the diffusion of substrate elements into the coating, enhances the stability of the bulk material and reduced the growth of dense, Fe-containing oxides. The main factor improving the oxidation performance of CrAlYN/CrN grown at different  $U_b$  is the removal of cracks in the coating when a high  $U_b \geq -120$  V is applied.

### 6.4.3 Thermogravimetric Analysis vs. Isothermal Heat-Treatment

In Sec. 6.4.1, a thermogravimetric analysis of the CrAlYN/CrN coating on 304 stainless steel substrates was performed which revealed that coatings grown at high  $U_b$  have a lower weight gain and, hence, a better oxidation resistance than their low  $U_b$  opponent (see Fig. 6.34).

Isothermal testing of the coatings (see Sec. 6.4.2) show that cracks are present in CrAlYN/CrN grown at low  $U_b$  (see Fig. 6.35). These cracks act as fast access routes for the oxidising medium and permit oxidation of the substrate. A weight gain in the TG test is therefore governed by the combined weight gain due to surface oxidation of the coating and oxidation of the substrate. The high  $U_b$  coatings, in contrast, are free of these cracks and the weight gain of these specimens is therefore solely governed by the coating oxidation.

The weight gain of CrAlYN/CrN grown at  $U_b = -120$  V showed the lowest weight gain of the analysed specimen (see Fig. 6.34). CrAlYN/CrN deposited at  $U_b = -150$  V has an only slightly higher weight gain. Both specimens have single crystal domains which are known to reduce the diffusion of Fe and Cr from the substrate into the coating. This reduced diffusion should, in turn, improve the oxidation resistance as the formed oxide scales are denser and protect the underlying coating better from further access of the oxidising medium. An important factor

to consider in this special case is the coating thickness (see Fig. 5.20, Sec. 5.1.5). CrAlYN/CrN grown at  $U_b = -120$  V is slightly thicker ( $4.7 \mu\text{m}$ ) than its high  $U_b = -150$  V opponent ( $4.2 \mu\text{m}$ ). It is speculated that Fe, Mn and Cr therefore require longer time to diffuse through the thicker coating and therefore reduce the oxidation rate. This in turn, could result in lower weight gain rates in the TG analysis.

## 6.5 Influence of the Chemical Composition on the Oxidation Performance of CrAlYN/CrN Coatings

In Sec. 5.3, it was investigated in detail how a variation in the power  $P_{Cr}$  on the Cr target during the deposition of the nanolayer structure affects the microstructure and the mechanical properties of CrAlYN/CrN. In the following, it will be examined how this change in  $P_{Cr}$  influenced the oxidation performance of these coatings.

### 6.5.1 Thermogravimetric Analysis

Thermogravimetric analysis (TG) (see Sec. 3.4.1) was performed to investigate the weight gain of CrAlYN/CrN on 304 stainless steel substrates as a function of

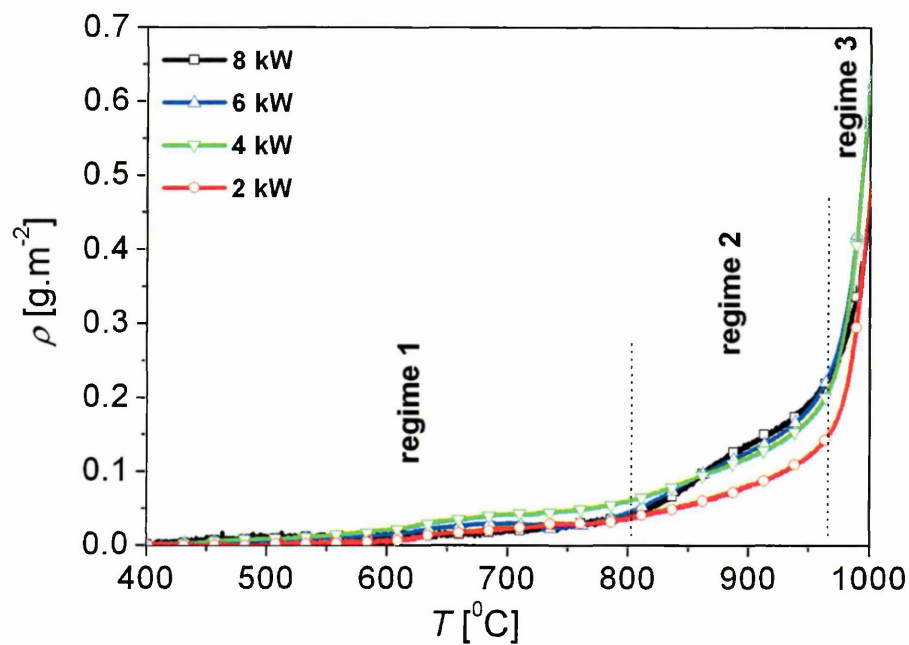


Fig. 6.43: Dynamic thermogravimetric data of CrAlYN/CrN deposited at varying  $P_{Cr}$  on 304 stainless steel substrates for thermal ramping at  $5 \text{ K}\cdot\text{min}^{-1}$  in dry air

temperature  $T$  (see Fig. 6.43). All coatings reveal a low weight gain  $\rho$  ( $<0.5 \text{ g.m}^2$ ) up to  $\sim 800^\circ\text{C}$  (regime 1). Above  $\sim 800^\circ\text{C}$ , all coatings gain weight at a higher rate. This rate is highest ( $1.1 \text{ g.m}^{-3}\text{K}^{-1}$ ) in CrAlYN/CrN deposited at  $P_{Cr}=8 \text{ kW}$ . Lower rates are determined for coatings grown at lower  $P_{Cr}$ . CrAlYN/CrN grown at the lowest  $P_{Cr}=2 \text{ kW}$  has the lowest rate ( $5.2 \text{ g.m}^{-4}\text{K}^{-1}$ ) and the lowest weight gain between  $800^\circ\text{C}$  and  $970^\circ\text{C}$  (regime 2). Above  $970^\circ\text{C}$ , a strong increase in weight gain is observed in all specimen. This onset temperature at  $970\pm 5^\circ\text{C}$  of rapid oxidation is identical in all coatings. In summary, the TG investigation implies that CrAlYN/CrN grown at  $P_{Cr}=2 \text{ kW}$  with the highest Al-content has the by far lowest weight gain.

TG analysis alone cannot provide information on the oxidation mechanism. Isothermal heat-treatment is therefore carried out to examine the oxidation performance of these coatings in more detail. The results of this examination are then compared to the results obtained from the TG test (see Sec. 6.5.3).

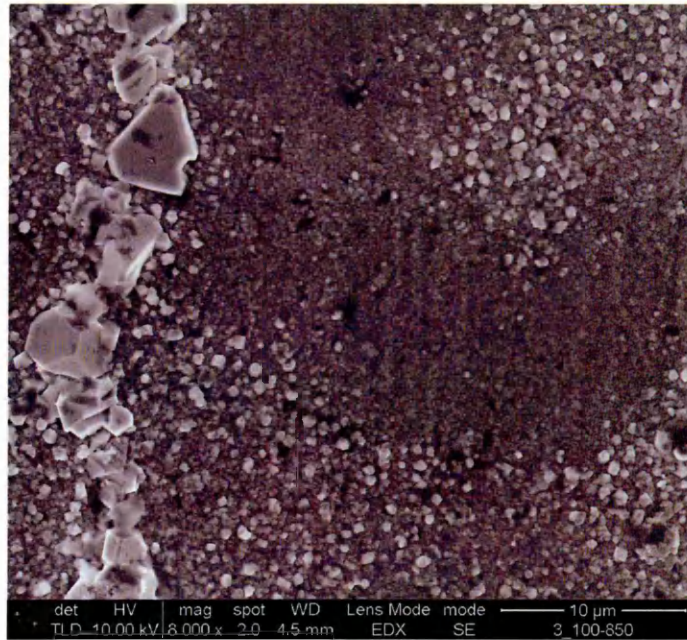
## 6.5.2 Isothermal Oxidation

To investigate the effect of  $P_{Cr}$ , and hence, the chemical composition on the long term oxidation, isothermal heat-treatment was carried out for 100 h at  $850^\circ\text{C}$  in laboratory air (see Sec. 3.4.2).

### 6.5.2.1 SEM Analysis

SEM observations of the coating surface after heating (see Fig. 6.44) shows extensive cracking of the coating with a significant amount of oxide crystals growing out of these cracks. These observations are similar in all investigated coatings.

The coating surface of CrAlYN/CrN grown at  $P_{Cr}=8 \text{ kW}$  exhibits large oxide crystals (see Fig. 6.44(a)). Crystals with a size  $>500 \text{ nm}$  have a density of  $0.35 \mu\text{m}^{-2}$  (see Fig. 6.28). As  $P_{Cr}$  is reduced, the heat-treated surfaces become smoother and fewer large crystals are visible. This is especially obvious in CrAlYN/CrN grown at  $P_{Cr}=2 \text{ kW}$ . On this specimen, the density of large crystals with a size  $>500 \text{ nm}$  is reduced by a factor of  $\sim 3$  to  $0.12 \mu\text{m}^{-2}$ . It is

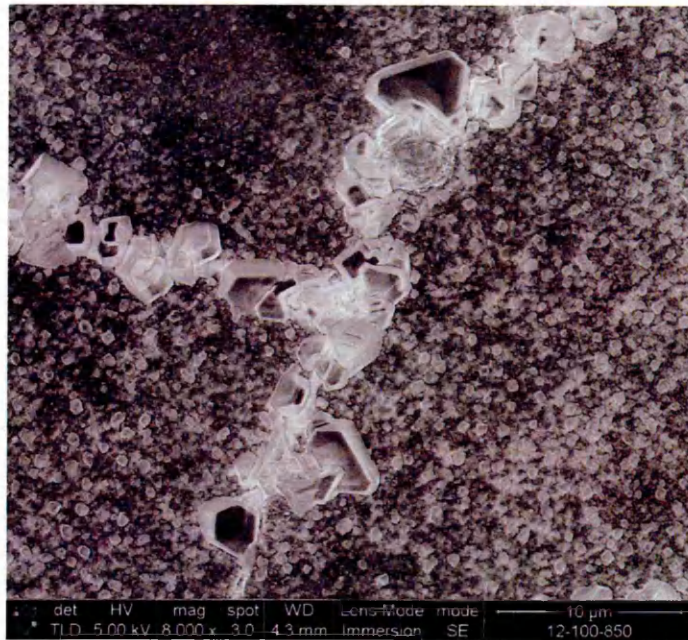


(a) 8 kW

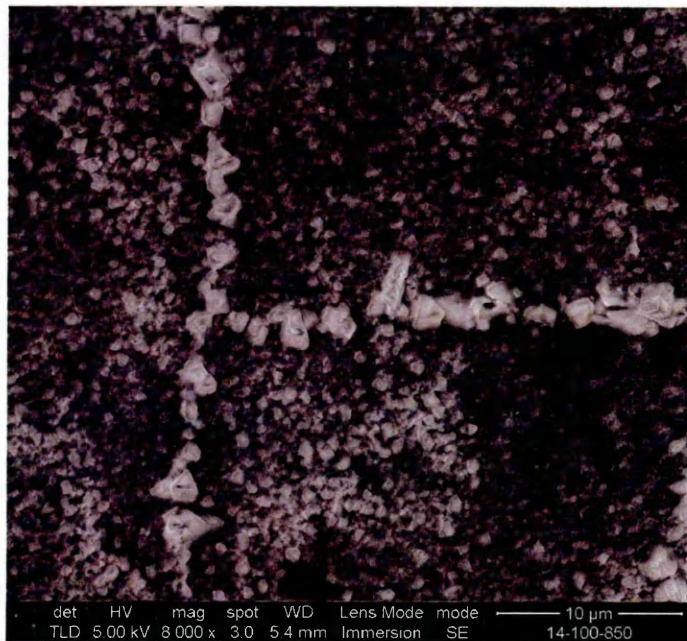


(b) 6 kW

Fig. 6.44: SEM micrographs of the surface of CrAlYN/CrN deposited at different  $P_{Cr}$  after 100 h heat-treatment at 850°C: The growth of oxide crystals is observed on the coating surface and inside cracks in all coatings



(c) 4 kW



(d) 2 kW

Fig. 6.44: Continued

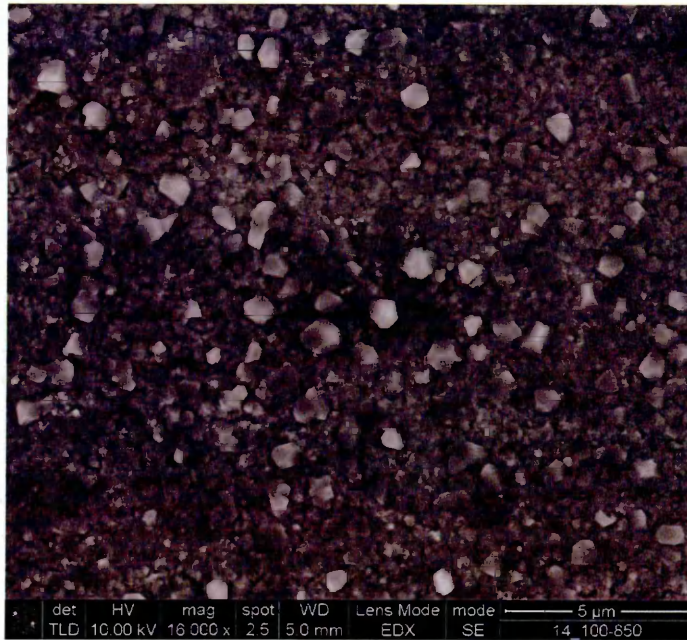


Fig. 6.45: SEM micrograph from the surface of CrAlYN/CrN deposited at  $P_{Cr} = 2$  kW after 100 h heat-treatment at  $850^{\circ}\text{C}$ : Oxide crystals with a size  $>500$  nm have a density of  $0.12\mu\text{m}^{-2}$

therefore concluded that smaller oxides form on top of CrAlYN/CrN when  $P_{Cr}$  during deposition is reduced.

### 6.5.2.2 XRD Analysis

The GA-XRD diffractograms of CrAlYN/CrN taken after 100 h isothermal heat-treatment in laboratory air at  $850^{\circ}$  are shown in Fig. 6.46. All diffractograms show a variety of reflections which can be attributed to  $\text{Cr}_2\text{N}$ , AlN,  $\text{Cr}_2\text{O}_3$  and  $\text{FeCr}_2\text{O}_4$ . In CrAlYN/CrN grown at  $P_{Cr} = 2$  kW, reflections of an additional phase can be identified (see insert in Fig. 6.46) with corundum-type  $\text{Al}_2\text{O}_3$  phase (reflections e.g. at  $2\theta = 25.23^{\circ}$  and  $51.82^{\circ}$ , JCPCD 71-1684) (see Tab. 6.6). The existence of this phase signifies that the Al atomic fraction ( $\sim 23\text{at}\%$ , Cr/Al ratio 0.56 (see Fig. 5.45, Sec. 5.3.2) in CrAlYN/CrN grown at  $P_{Cr} = 2$  kW is sufficiently high to form an  $\text{Al}_2\text{O}_3$  phase next to the previously observed  $\text{Cr}_2\text{O}_3$ . The  $\text{Cr}_2\text{O}_3$  phase diagram [203–205] predicts the formation of two corundum-type oxides at  $850^{\circ}\text{C}$  for a Cr/Al ratio of 0.5. In this experiment, theory and experiment agree with

Tab. 6.6: Selected reflections from the GA-XRD diffractogram (see Fig.6.4 identifying a corundum-type  $\text{Al}_2\text{O}_3$  phase in CrAlYN/CrN grown at  $P_{Cr}=2$  kW heat-treated for 100 h at  $850^\circ\text{C}$ )

No.	$2\theta$ [ $^\circ$ ]	d [nm]	$\text{Al}_2\text{O}_3$ (JCPCD 35-0803) $d_{\{hkl\}}$ [nm] (hkl)	Possible overlap with Phase
3	25.23	0.353	0.355 (012)	
13	37.23	2.413	0.242 (110)	$\text{AlN}$ , $\text{Cr}_2\text{O}_3$ , $\text{FeCr}_2\text{O}_4$
19	42.54	2.123	0.323 (113)	$\text{Cr}_2\text{N}$ , $\text{FeCr}_2\text{O}_4$
23	44.72	2.025	0.200 (202)	$\text{Cr}_2\text{N}$ , $\text{Cr}_2\text{O}_3$ , $\text{FeCr}_2\text{O}_4$
28	51.82	1.763	0.177 (024)	
34	56.38	1.631	0.163 (116)	$\text{Cr}_2\text{N}$ , $\text{Cr}_2\text{O}_3$ , $\text{FeCr}_2\text{O}_4$
38	59.90	1.543	0.154 (018)	
46	65.42	1.425	0.143 (214)	
52	72.93	1.296	0.127 (1010)	$\text{AlN}$ , $\text{Cr}_2\text{O}_3$

each other.

### 6.5.2.3 TEM Analysis

The TG analysis (see Fig.6.43) reveals that CrAlYN/CrN deposited at  $P_{Cr}=2$  kW has the lowest weight gain when compared to other CrAlYN/CrN grown at higher  $P_{Cr}$  in a temperature range from  $800^\circ\text{C}$  to  $970^\circ\text{C}$ .

This coating with an Al atomic fraction of  $\sim 23\text{at}\%$ , a Cr/Al ratio of  $\sim 0.56$  (see Fig. 5.45) and a near-monolithic structure (see Fig, 5.54, Sec. 5.3.4) is therefore exemplarily studied by TEM to examine the effect of  $P_{Cr}$  and hence, the chemical composition on the oxidation performance.

Cross-sectional TEM studies (see Fig. 6.47) reveal a polycrystalline coating structure with elongated grains in the bulk and a clearly defined oxide layer at the outer surface after heat-treatment at  $850^\circ\text{C}$  for 100 h. The initial columnar morphology structure (see Fig. 5.48(d), Sec. 5.3.4) is replaced by this structure of elongated crystals which occupy the places of the former columns. A large reaction zone, resulting from oxidation processes, is situated at the coating top.

TEM-EDS depth profiling across the coating cross-section (see Fig. 6.48) reveals the substrate element Fe in the coating ( $\sim 4.3\text{at}\%$  of total metal content).

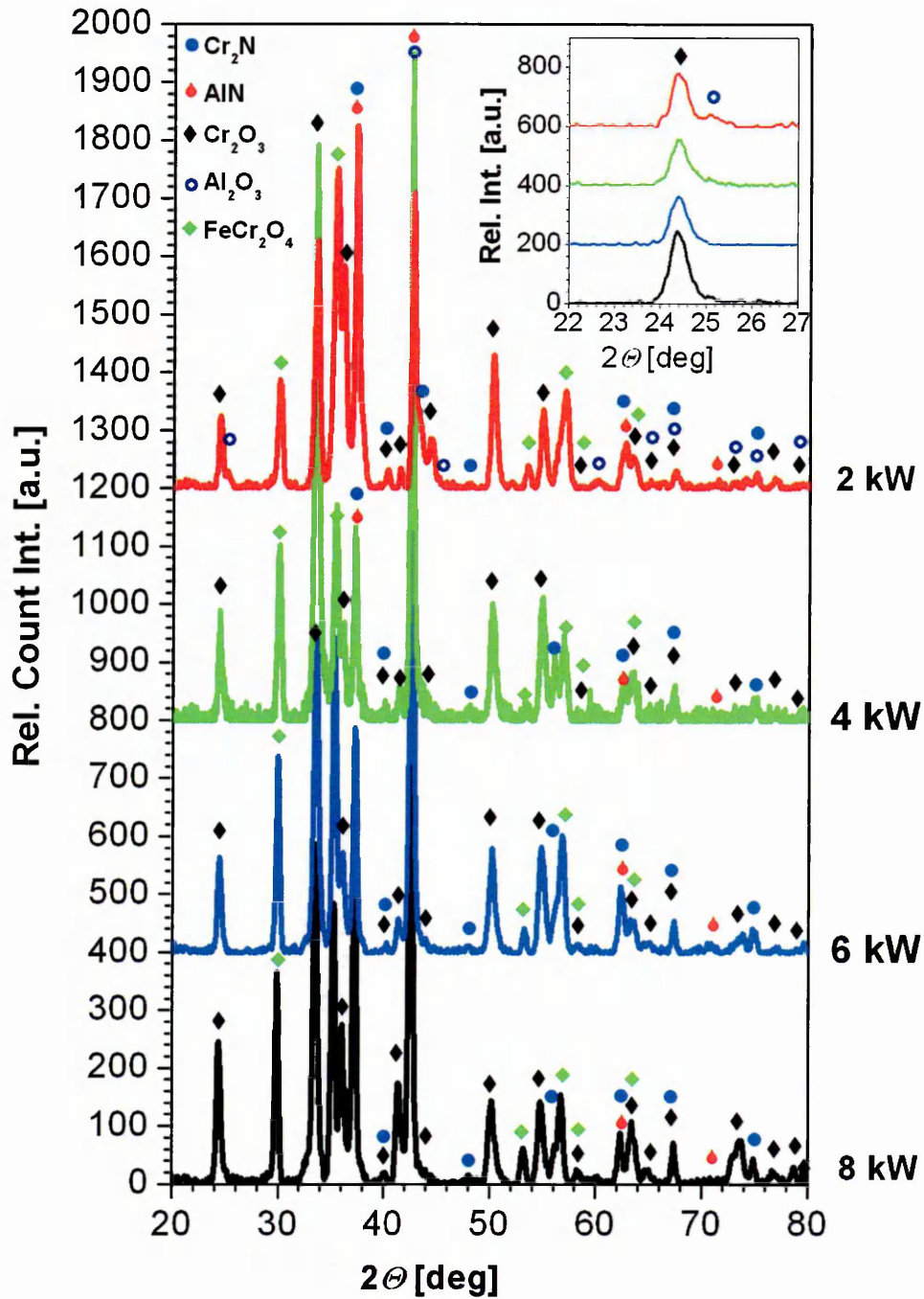


Fig. 6.46: GA-XRD pattern (incident angle  $\gamma = 2^\circ$ ) obtained from CrAlYN/CrN after heat-treatment in ambient air for 100 h at  $850^\circ\text{C}$ : An additional corundum-type  $\text{Al}_2\text{O}_3$  phase is identified in the low  $P_{Cr}$  = 2 kW coating

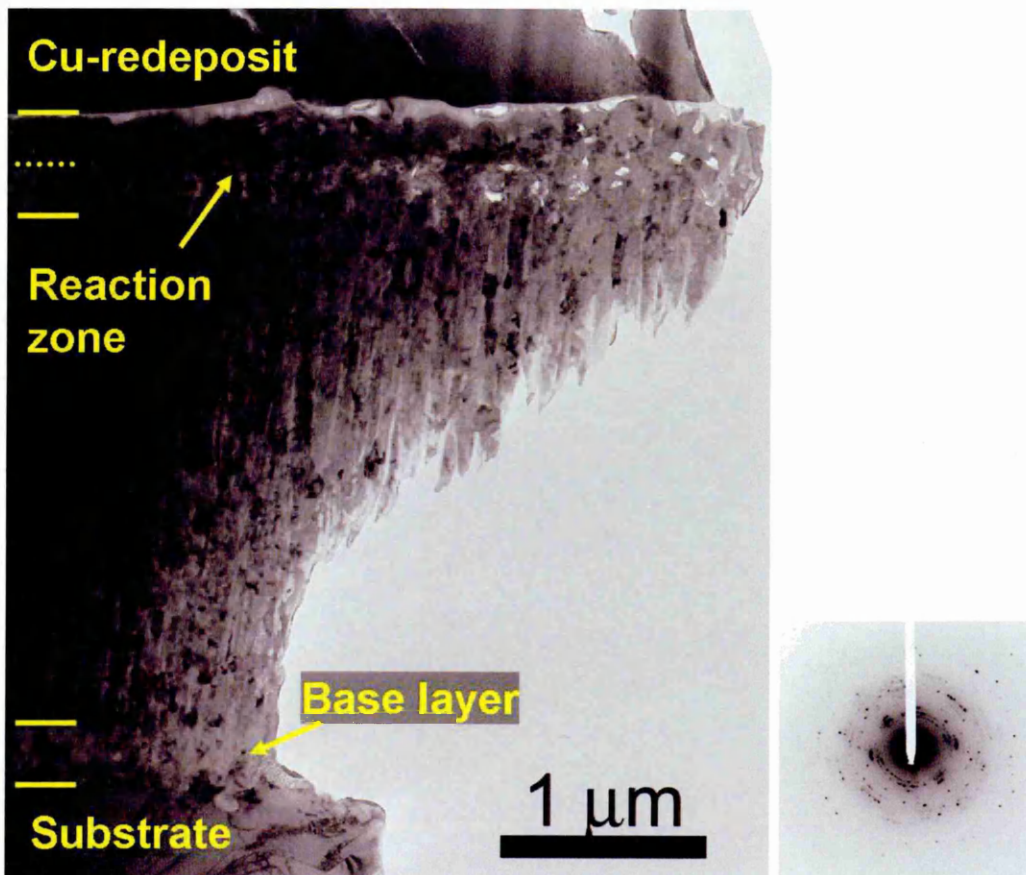


Fig. 6.47: BF-TEM micrograph and the corresponding SAD pattern from the middle of the bulk coating of CrAlYN/CrN deposited at  $P_{Cr}=2$  kW after 100 h heat-treatment at  $850^{\circ}\text{C}$

The Cr/Al ratio in the the bulk coating decreases significantly from  $\sim 1.03$  close to the base layer to  $\sim 0.68$  at the coating top just below the oxide scale. This ratio even decreases more in the scale ( $\sim 0.31$ ). The observed high Fe content in the coating implies diffusion of Fe into the coating. The change in Cr/Al ratio in the low  $P_{Cr}=2$  kW CrAlYN/CrN implies a concentration gradient across the coating which is higher Al containing towards the coating top. This gradient suggests that Al diffuses towards the coating top. The very low Cr/Al ratio ( $\sim 0.31$ ) in the oxide scale signifies the formation of an Al-rich oxide scale.

This is in clear contrast to the results obtained from CrAlYN/CrN deposited at  $P_{Cr}=8$  kW (see Fig. 6.31, Sec. 6.3). Here, diffusion of Fe was also observed. The Cr/Al ratio, however, remains constant ( $\sim 1.50$ ) across the coating thickness

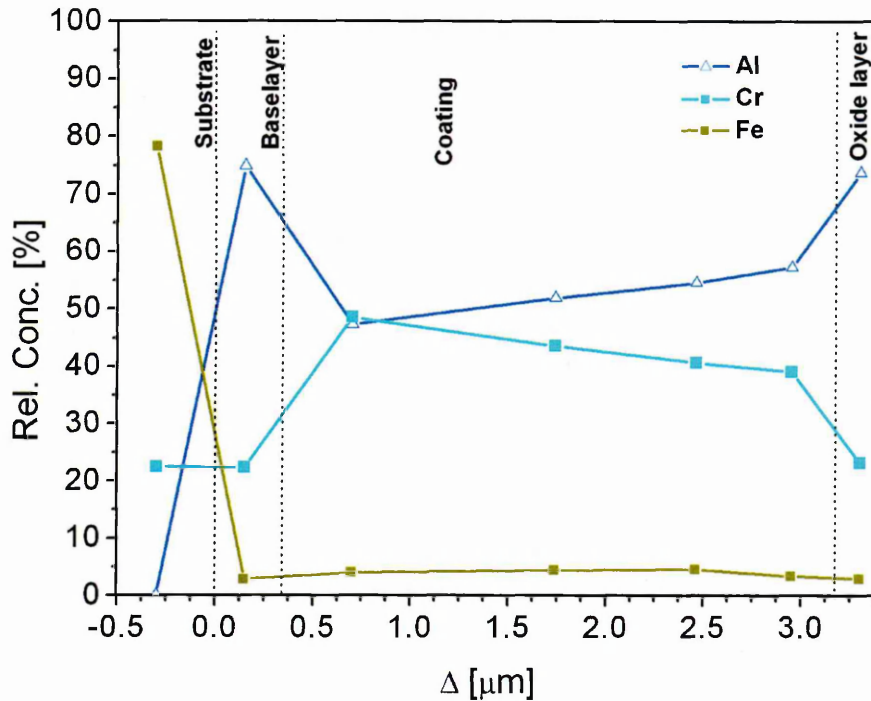


Fig. 6.48: TEM-EDX profile measured over the cross-section of CrAlYN deposited at  $P_{Cr} = 2$  kW after 100 h heat-treatment at  $850^{\circ}\text{C}$ : A concentration gradient forms in the coating region

and even increases in the oxide ( $\sim 7.10$ ). In this coating, outward diffusion is identified as main oxidation mechanism. This outward Cr diffusion to form a  $\text{Cr}_2\text{O}_3$  oxide may be balanced by steady Cr diffusion from the substrate into the coating. In CrAlYN/CrN grown at  $P_{Cr} = 2$  kW, in contrast, Al as the main oxide former migrates to the coating top. Al, however, cannot be provided from the substrate. It is therefore speculated that the outward diffusion of Al may result in a concentration gradient across the coating.

TEM analysis of the bulk material reveals that previously mentioned elongated crystals are arranged in a columnar manner and are separated from the grains in neighbouring columns by an inter-connected line of voids (see Fig. 6.49). These voids extend all the way from the coating top to the substrate. Analysis of a SAD pattern from this region (see insert in Fig. 6.47) identifies three different phases, namely CrN,  $\text{Cr}_2\text{N}$  and hcp-AlN, in the bulk material. It is suggested that the

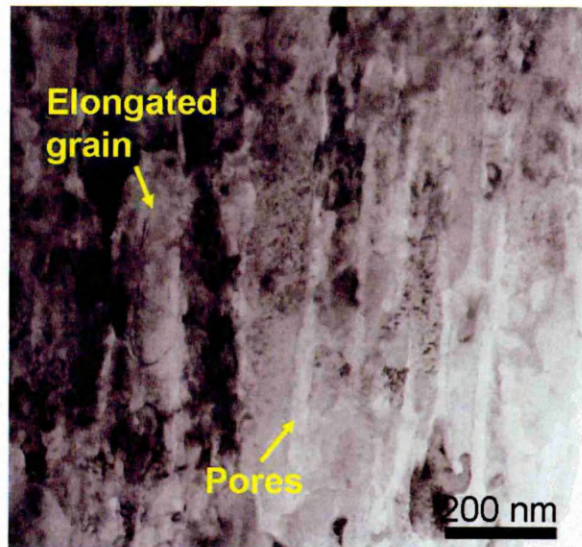


Fig. 6.49: BF-TEM micrograph of the bulk CrAlYN deposited at  $P_{Cr}= 2$  kW after 100 h heat-treatment at  $850^{\circ}\text{C}$ : Elongated crystals and large pores at the former column boundaries are present

CrN phase represents a CrAlN phase (see Sec. 6.3.5). The TEM investigation implies that a phase transformation from CrAlYN/CrN into CrAlN,  $\text{Cr}_2\text{N}$  and AlN takes place. As this phase transformation is observed in the low  $P_{Cr}$  as well as in the high  $P_{Cr}$  CrAlYN/CrN (see Sec. 6.3.5), this process depends on  $P_{Cr}$  and, hence, the chemical composition in the investigated Cr/Al range from 0.56 to 0.90.

A very dense oxide scale can be observed at the coating top (see Fig. 6.50). This scale has a very homogeneous appearance across the whole length of the analysed specimen. The scale thickness is measured to  $245\pm 9$  nm. Voids are located underneath the scale and extend into the bulk with a thickness of  $228\pm 18$  nm. TEM-EDS analysis of individual grains of the oxide scale reveal that crystals at the outer rim are rich in Al (min. Cr/Al ratio  $\sim 0.07$ ) whereas crystals close to the coating/oxide interface have a higher Cr content (max. Cr/Al ratio  $\sim 1.93$ ). The substrate elements Fe and Mn are found in all oxide crystals.

The findings of an Al-enrichment in the outer regions of the scale implies that the high Al content in the outer regions of the coating may lead to the formation

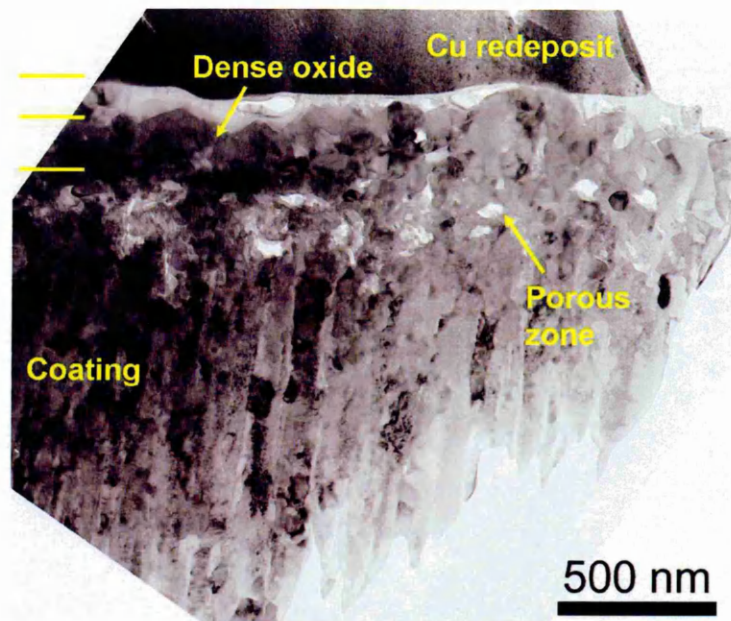


Fig. 6.50: BF-TEM micrograph of the oxide scale on CrAlYN deposited at  $P_{Cr}=2$  kW after 100 h heat-treatment at 850°C: A dense oxide scale forms

of an individual phase. The existence of an  $\text{Al}_2\text{O}_3$  phase additional to  $\text{Cr}_2\text{O}_3$  was earlier shown by GA-XRD (see Fig. 6.46). It is therefore assumed that the Al content in the oxide is so high that not only a  $\text{Cr}_2\text{O}_3$  but also a corundum  $\text{Al}_2\text{O}_3$  forms. These phases are expected to contain a substantial amount of the Al and Cr, respectively. Both phases additionally incorporate Fe, Cr and Mn.

### 6.5.3 Thermogravimetric Analysis vs. Isothermal Heat-Treatment

As seen previously, the TG analysis of CrAlYN/CrN deposited at different  $P_{Cr}$  (see Fig. 6.43) reveals that CrAlYN/CrN grown at high  $P_{Cr}=2$  kW shows a significantly lower weight gain in a temperature range from 800°C to 970°C compared to coatings grown at high  $P_{Cr}=4$  kW to 8 kW.

Microstructural analysis of this high Al-containing coating (Cr/Al ratio 0.56) after isothermal heat-treatment for 100 h reveals that the coating forms a dense oxide scale consisting of co-existing corundum-type  $\text{Cr}_2\text{O}_3$  and  $\text{Al}_2\text{O}_3$ . The exis-

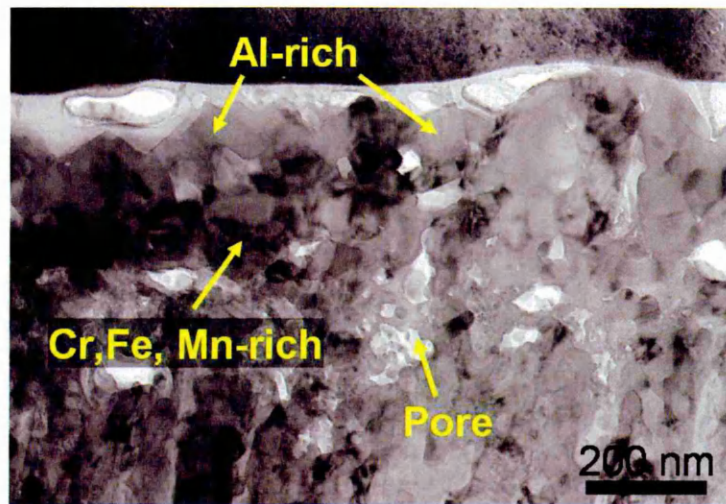


Fig. 6.51: BF-TEM micrograph of the oxide scale on CrAlYN deposited at  $P_{Cr} = 2$  kW after 100 h heat-treatment at 850°C: The outer scale is rich in Al whereas the inner scale is dominated by Cr, Fe and Mn

tence of the  $\text{Al}_2\text{O}_3$  in this system is desirable as  $\text{Al}_2\text{O}_3$  is known to form dense oxides which are able to suppress diffusion of O into the coating and, in turn, protect the underlying coating (and substrate) against further oxidation. These results imply that the low weight of the Al-rich CrAlYN/CrN grown at  $P_{Cr} = 2$  kW gain in regime 2 of the TG curve (see Fig. 6.43) may be related the formation of a dense, protective oxide scale.

This argumentation does not consider the effect of oxide formation inside through-thickness cracks in the coating. These cracks are present in all investigated coatings. The measured weight gain in the TG experiment at high temperatures therefore has to be seen as a combination of weight gain due to coating surface oxidation and substrate oxidation through cracks in the coating.

## 6.6 Chapter Summary

The oxidation behaviour of CrAlYN/CrN thin films was investigated changing the parameters oxidation temperature and time. The influence of the deposition parameters on the oxidation behaviour were investigated by altering ion bombardment and the chemical composition.

A comparison of the novel CrAlYN/CrN coating to the recently developed Ti-containing TiAlCrN/CrN coating (see Sec. 6.1) shows an improvement in oxidation performance with the removal of Ti from the coating. This enhanced oxidation performance of CrAlYN/CrN is particularly obvious from the reduction of weight gain by a factor of 5 in continuous thermogravimetric testing.

Isothermal short term oxidation tests were performed for 1 h at temperatures up to 1000°C. The as-deposited CrAlYN/CrN coating structure remains unchanged after isothermal heat-treatment at 900°C. This nanoscale multilayer structure starts to decompose into Cr<sub>2</sub>N and AlN at temperatures above 900°C. The nanolayers are thereby preserved up to 950°C. This layer structure, in contrast, is completely replaced by globular grains CrAlN, Cr<sub>2</sub>N and AlN at 1000°C. The phase transformation is completed after 1 h at 1000°C. The oxidation of the coating surface takes place with the outward diffusion of the coating elements Cr and/or Al and the subsequent formation of dense (Cr,Al)<sub>2</sub>O<sub>3</sub> scales at temperatures up to 950°C. At elevated temperatures of 1000°C, CrAlYN/CrN oxidises with the formation of a 90 nm thick, dense duplex oxide scale. This scale has an

Tab. 6.7: Observed phases before and after isothermal heat-treatment of CrAlYN/CrN for 1 h at different temperatures up to 1000°C

Temperature T [°C]	CrAlYN/CrN fcc	CrAlN fcc	Cr <sub>2</sub> N hcp	AlN hcp	(Cr,Al) <sub>2</sub> O <sub>3</sub> romb
as deposited	x				
850	x				x
900	x				x
950	x		x	x	x
1000		x	x	x	x

Al-rich outer layer and a Cr-rich inner layer and grows in a  $(\text{Cr,Al})_2\text{O}_3$  structure.

Tab. 6.8 summarises the formed phases as a function of exposure time.

Furthermore, a heat-treatment at longer exposure times up to 100 h and a medium temperature of 850°C (see Sec. 6.3) was conducted. Oxidation at 850°C results in the diffusion of substrate elements, especially Fe and Cr, from the 304 stainless steel substrate into the coating. These diffusion processes cause a change in the chemical coating composition and the resulting Cr-enrichment is suspected to promote a phase transformation from a CrAlYN/CrN nanoscale multilayer into globular CrAlN, Cr<sub>2</sub>N and Y-containing AlN. The heat-treatment additionally causes oxidation of the coating surface with the formation a porous  $(\text{Cr,Al})_2\text{O}_3$  phase oxide scale. Outward diffusion of the coating elements Cr and/or Al is speculated to be the main oxidation mechanism. This, in turn, leads to the formation of an under-dense porous layer situated at the coating/oxide scale interface. The observed oxides contain, next to Cr and Al, also substantial amounts of the substrate elements Fe and Mn which can migrate to this position via surface diffusion through cracks in the coating or by boundary diffusion through the coating itself. The atomic fraction of Fe after 100 h exposure is sufficiently high to form a separate FeCr<sub>2</sub>O<sub>4</sub> phase which is mainly located at the top of a porous scale. Furthermore, oxidation of the substrate takes place with the growth of large (Fe,Cr)-oxides in through-thickness cracks in the coating. These cracks arise from thermal stresses in the coating during heating and provide fast pathways of

Tab. 6.8: Observed phases before and after isothermal heat-treatment of CrAlYN/CrN for up to 100 h at 850°C

Time t [h]	CrAlYN/CrN fcc	CrAlN fcc	Cr <sub>2</sub> N hcp	AlN hcp	$(\text{Cr,Al})_2\text{O}_3$ romb	FeCr <sub>2</sub> O <sub>4</sub> mon
as deposited	x					
1	x				x	
5	x		x	x	x	
20	x		x	x	x	
50	x		x	x	x	x
100		x	x	x	x	x

the oxidising medium to the substrate. Tab. 6.8 summarises the presence of the individual phases as a function of time.

In order to optimise the oxidation performance of CrAlYN/CrN coatings, different process parameters were varied during the coating deposition. In the present investigation, these parameters were (i) the ion bombardment via changing the substrate bias voltage  $U_b$  in a range of -75 V to -150 V and (ii) a variation in chemical composition via controlling the power  $P_{Cr}$  on the Cr target in a range from 2 kW to 8 kW.

Controlling  $U_b$  produces CrAlYN/CrN coatings with a structure which changes from polycrystalline columnar at low  $U_b \leq -90$  V to polycrystalline columnar with large single crystalline domains at  $U_b \geq -120$  V (see Sec. 5.1). These structural changes coincide with a strong increase in residual compressive stresses  $\sigma$ . When heat-treating these specimens, thermal tensile stresses  $\sigma_{th}$  arise and cause cracking in CrAlYN/CrN with low residual stresses ( $U_b \leq -90$  V) whereas the highly stressed CrAlYN/CrN ( $U_b \geq -120$  V) remains crack free. As fast pathways for the oxidising media to the substrate are effectively closed and substrate oxidation prevented, these crack-free coatings, in consequence, reveal enhanced oxidation resistance. The diffusion of substrate elements, especially Cr, is speculated to be the main factor limiting the thermal stability of columnar CrAlYN/CrN ( $U_b = -120$  V) leading to a phase transformation from CrAlYN/CrN into CrAlN, Cr<sub>2</sub>N and AlN (see Sec. 6.3). These diffusion processes are significantly reduced in CrAlYN/CrN grown with a single crystal structure ( $U_b \geq -150$  V) and the nanoscale multilayer is therefore retained in these regions after heat-treatment for 100 h. This lower diffusivity additionally reduced the atomic fraction of substrate elements in the oxide scale and prevents the formation of the FeCr<sub>2</sub>O<sub>4</sub>. The oxidation of the high  $U_b$  CrAlYN/CrN is therefore improved by their partial single crystal structure.

A variation in  $P_{Cr}$  provides CrAlYN/CrN coatings which have equal atomic fractions of Cr and Al (Cr/Al ratio  $\sim 0.89$ ) at  $P_{Cr} = 8$  kW and are rich in Al (Cr/Al ratio  $\sim 0.56$ ) at  $P_{Cr} = 2$  kW (see Sec. 5.3). After heat-treatment for 100 h at 850°C (see Sec. 6.5), the previously reported phase transformation from CrAlYN/CrN

into CrAlN, Cr<sub>2</sub>N and AlN takes place in all investigated specimens. This phase transformation is therefore not affected by the change in chemical composition in the examined Cr/Al ratio range. CrAlYN/CrN grown at high  $P_{Cr}$ = 4 kW to 8 kW form the previously reported Cr<sub>2</sub>O<sub>3</sub> oxides which form predominantly by outward Cr diffusion (see Sec. 6.3). In the Al-rich CrAlYN/CrN deposited at  $P_{Cr}$ = 2 kW, in contrast, outward diffusion of Al is suggested as main oxidation mechanism, resulting in the formation of a highly dense oxide scale. This scale has a Al-rich outer oxide and an Cr-rich inner oxide. These oxides consist of the two corundum-type phases Cr<sub>2</sub>O<sub>3</sub> and Al<sub>2</sub>O<sub>3</sub>. Al<sub>2</sub>O<sub>3</sub>, in turn, is known for its formation of dense oxides which can reduce the diffusion of O into the underlying material and therefore effectively protect this material against further oxidation. The high Al atomic fraction in CrAlYN/CrN grown at low  $P_{Cr}$  can therefore enhanced the oxidation performance of CrAlYN/CrN.

# CHAPTER 7

---

---

## Conclusion and Further Work

---

---

In the previous chapters, a detailed description of the results obtained during this study, was given. This chapter will summarise the main results. It will furthermore give an indication for further work.

### 7.1 Summary of the results

In this study, the novel nanoscale multilayer CrAlYN/CrN coating was investigated in detail. Here, a short overview of the obtained results will be given.

#### 7.1.1 Implementation of High Power Impulse Magnetron Sputtering as Etching Pre-Treatment Technique

One of the aims of these studies was the implementation of the novel high power impulse magnetron sputtering (HIPIMS) technique as substrate surface etching pre-treatment.

During the HIPIMS pre-treatment step, 304 stainless steel substrates are subjected to ion bombardment in a Cr/Ar plasma (see Sec. 5.1). It was shown that these impinging ions effectively remove contaminations and produce atomically

clean surfaces. These surfaces then provide a base for the growth of well adherent coatings. Two different types of growth relationships between these polycrystalline substrates and a CrAlN baselayer have been identified in this study. CrAlN nucleates in either local epitaxy or axiotaxy directly on large areas of the atomically clean substrate surfaces. This epitaxial growth relationship of substrate and coating, in turn, provides excellent adhesion. It was furthermore observed that coatings grown after a HIPIMS pre-treatment are nearly free of macro-particle induced growth defects and have smooth surfaces.

Another aspect of this work is a comparison of the HIPIMS pre-treatment with other pre-treatment techniques. One of these is the cathodic arc (CA) metal ion etching. It is well established that surfaces pre-treated by this technique reveal clean interfaces. Subsequently deposited coatings grow in local epitaxial structures which enhance the substrate/coating adhesion compared to other techniques [72, 74, 168]. However, a drawback of the CA pre-treatment is the generation of macro-particles which are ejected from the target [166, 207]. The research within this PhD project has shown that these defects can be avoided by the implementation of HIPIMS as an etching pre-treatment technique. The removal of these defects was found to significantly improve the performance of subsequently grown coatings, e.g. the tribological performance. Coatings with HIPIMS pre-treatment therefore outperform conventionally etched coatings.

### **7.1.2 Design and Development of the Novel Nanoscale Multilayered CrAlYN/CrN Coatings**

Within the scope of this thesis, a new type of nanoscale multilayer coating was developed using CrAlYN/CrN. As a variety of possible process parameters can be tuned in PVD deposition, two conditions were specifically investigated: (i) the effect of energy of ion bombardment during coating growth and (ii) the chemical composition.

The energy of ion bombardment was controlled by a variation of the substrate bias voltage  $U_B$  in a range of -75 V to -150 V (see Sec. 5.1). The coating mor-

phology is modified from polycrystalline columnar with inter-columnar voids at low  $U_b$  to a mixed structure of polycrystalline columnar domains and large single crystalline domains at high  $U_b$ . These structures can be explained according to Messier's structure zone model (see Sec. 2.3 or [66]). The mechanical properties of these new CrAlYN/CrN coatings are therefore strongly dependent on  $U_b$ . The deposition at higher  $U_b$  gives rise to increased compressive stress levels, higher hardness and an enhanced wear resistance with low wear rates in a range of  $10^{-16} \text{ m}^3\text{N}^{-1}\text{m}^{-1}$  to  $10^{-17} \text{ m}^3\text{N}^{-1}\text{m}^{-1}$ . A drawback of the high stresses, however, is the limitation in substrate/coating adhesion.

The chemical composition in CrAlYN/CrN was steered by a modification in the power  $P_{Cr}$  on the Cr target between 2 kW and 8 kW (see Sec. 5.3). The high  $P_{Cr}$  CrAlYN/CrN has equal atomic fractions of Cr and Al (Cr/Al ratio  $\sim 0.90$ ) whereas the low  $P_{Cr}$  coating is rich in Al (Cr/Al ratio  $\sim 0.56$ ). This lower Cr content coincides with a reduction in the CrN layer thickness on the nanometer scale. In case of deposition at  $P_{Cr} = 2 \text{ kW}$ , this CrN layer thickness is reduced to the point in which a "near-monolithic" structure forms. Most mechanical properties are only marginally affected by this variation in  $P_{Cr}$  and, hence, in chemical composition. Only the wear resistance of CrAlYN/CrN strongly deteriorates as  $P_{Cr}$  is lowered.

### 7.1.3 Oxidation Performance

CrAlYN/CrN was developed as an oxidation resistant coating with the aim to compete with conventional Ti-containing coatings.

The novel CrAlYN/CrN was therefore compared to a TiAlYN/CrN coating in thermogravimetric testing. It was shown that the onset temperature of rapid oxidation can be increased from  $950^\circ\text{C}$  in TiAlYN/CrN to  $970^\circ\text{C}$  in the Ti-free CrAlYN/CrN. The oxidation rate is furthermore up to 5 times slower in CrAlYN/CrN. The newly developed CrAlYN/CrN has therefore an outstanding oxidation performance which is superior to Ti-containing coatings.

To study the oxidation mechanisms, CrAlYN/CrN coatings on 304 stainless steel substrates were investigated under different oxidation conditions: (i) short

term oxidation for 1 h up to 1000°C and (ii) long term oxidation for up to 100 h at 850°C. Additionally, it was examined how the structural changes obtained by a variation in  $U_b$  and the changes in chemical composition obtained by controlling  $P_{Cr}$  impact on the oxidation performance of these nanoscale multilayers.

In short term heating experiments for 1 h (see Sec. 6.2), two competing processes are identified to take place in CrAlYN/CrN: (i) phase decomposition and (ii) coating oxidation. The as-deposited coating structure with its nanoscale multilayer retains unchanged up to 900°C. At 950°C, in contrast, the meta-stable compound starts to decompose into the stable phases  $Cr_2N$  and hcp-AlN. At the same time, surface oxidation takes place with the formation of a  $(Cr,Al)_2O_3$  phase. Isothermal treatment at elevated temperatures of 1000°C result in growth of a 90 nm thick, dense duplex-oxide with an Al-rich outer layer and a Cr-rich inner layer.

In long term heating at 850°C (see Sec. 6.3), thin film degradation was controlled by the following processes (i) phase decomposition, (ii) coating oxidation and (iii) oxidation of the substrate. Similar to the short term experiments, the CrAlYN/CrN coating decomposition into  $Cr_2N$  and hcp-AlN was observed. This process starts already after 5 h of heat-treatment and is largely completed after 100 h. The diffusion of the substrate element Cr is suggested as one of the driving forces for this phase transformation. Oxidation of the coating takes place with the formation of a  $(Cr,Al)_2O_3$  oxide scale. This scale contains a substantial atomic fraction of substrate elements, such as Fe and Mn which can reach the coating surface by (i) surface diffusion through the cracks in the coating and (i) boundary diffusion through the bulk coating.

Further analysis was performed to evaluate the effect of (i) the ion bombardment during deposition, changed by a variation in the substrate bias voltage  $U_b$  and (ii) the chemical composition, controlled by the power  $P_{Cr}$  on the Cr target, on the oxidation resistance of CrAlYN/CrN nanoscale multilayer coatings.

Two main factors were found to affect the oxidation resistance of CrAlYN/CrN grown at different  $U_b$  (see Sec. 6.4.2): (i) cracking and (ii) the diffusion of substrate

elements through the coating. Upon heating, cracks appear in the coating due to a mismatch in thermal expansion between CrAlYN/CrN and 304 stainless steel. These cracks then permit fast pathways for the oxidising medium to the substrate and cause substrate oxidation. Cracking is prevented by growing the coating at high  $U_b$  and the underlying substrate is therefore effectively protected against the oxidising environment. As previously described (see Sec. 6.3), the diffusion of substrate elements, especially Cr and Fe, along the column boundaries in columnar CrAlYN/CrN is suggested to cause a phase transformation in the bulk and increase the surface oxidation. This diffusion processes can be reduced when CrAlYN/CrN is grown in a partially single crystalline structure, as obtained from deposition at high  $U_b$ . These dense structures limit the diffusion of substrate elements to the coating top and therefore reduce the oxidation.

The crucial factor to impact on the oxidation performance of CrAlYN/CrN grown at various  $P_{Cr}$  (see Sec. 6.5), is the chemical composition. CrAlYN/CrN grown at high  $P_{Cr}$  has a high Cr atomic fraction and therefore forms  $(CrAl)_2O_3$  oxides which provide protection of the underlying material. CrAlYN/CrN grown at low  $P_{Cr}$ , in contrast, is rich in Al and, as a consequence, forms highly dense scales consisting of  $Cr_2O_3$  and  $Al_2O_3$ . These dense scales are more efficient than the  $(Cr,Al)_2O_3$  oxides to limit diffusion processes through the coating and therefore protect the underlying material more effectively from further oxidative attack.

## 7.2 Conclusion

In Sec. 1.1 of Chapter 1, the aims and objectives of this thesis were described. Here, a conclusion will be given, in how far these aims have been accomplished.

- The substrate/coating interface was successfully engineered by ion bombardment from a HIPIMS generated plasma. The implementation of this novel substrate pre-treatment technique can significantly improve the coating density and thin film adhesion compared to conventional substrate pre-treatment techniques and therefore offers an excellent alternative for the

substrate cleaning step.

- A novel generation of CrAlYN/CrN nanoscale multilayer coatings was developed. These coatings reveal good mechanical properties and excellent wear behaviour.
- A comprehensive understanding of the oxidation performance of CrAlYN/CrN nanoscale multilayer coatings was obtained. It was not possible to identify the role of Y in these processes.
- The novel Ti-free CrAlYN/CrN are able to effectively protect steel substrates against attack in an oxidising atmosphere. During these studies, only this type of substrate material was investigated. Further work is ongoing on  $\gamma$ -TiAl substrates [208].
- It was possible to establish a correlation between the coating microstructure, the chemical composition and the oxidation resistance of the new CrAlYN/CrN.

### 7.3 Future Work

Various aspects regarding the development and optimisation of CrAlYN/CrN nanoscale multilayer films could not be addressed within the frame work of this thesis. Some suggestions for further work could be:

#### Further Work in View of the Pre – Treatment

- to investigate the effect of different pre-treatment conditions, e.g. pressure, target power, pulse frequency on the interface chemistry and growth properties of subsequently grown coatings.
- to expand the range of HIPIMS from a pure substrate pre-treatment technique to coating deposition by HIPIMS.

### **Future Work in View of the Coating Development**

- to study the effect of other deposition parameters, e.g. pressure, temperature, target composition on the microstructure, the mechanical, tribological and oxidation performance of CrAlYN/CrN coatings.
- to change the chemical composition by introducing higher Y contents in a range of a few at%.

### **Future Work in View of the Coating Oxidation**

- to carry out diffusion experiments, e.g. with marker elements, to determine the diffusion rates of Fe and, especially, Cr in the coating.
- to investigate the effect of further substrate materials on the thermal stability of CrAlYN/CrN.
- to engineer the residual stress levels, e.g. by bias gradients during growth to control coating cracking.

---

---

# Bibliography

---

---

- [1] D. S. Rickerby and A. Matthews. *Advanced Surface Coatings: A Handbook of Surface Engineering*. Blackie and Son Ltd., Glasgow, 1991.
- [2] J. A. Ghani, I. A. Choudhury, and H. H. Masjuki. Performance of P10 TiN Coated Carbide Tools when End Milling AISI H13 Tool Steel at High Cutting Speed. *J. Mat. Proc. Technol.*, 153-154:1062, 2004.
- [3] M. Sokovic, J. Kopac, L. A. Dobrzanski, and M. Adamiak. Wear of PVD-Coated Solid Carbide End Mills in Dry High-Speed Cutting. *J. Mat. Proc. Technol.*, 157-158:422, 2004.
- [4] C. Leyens, R. Braun, M. Fröhlich, and P. Eh. Hovsepian. Recent Progress in the Coating Protection of Gamma Titanium Aluminides. *JOM*, 58(1):17, 2006.
- [5] C. Leyens, R. Braun, P. Eh. Hovsepian, and W.-D. Münz. Environmental Protection of  $\gamma$  Titanium Aluminides. In *Gamma Titanium Aluminides*, p. 551. TMS, Warrendale, US, 2003.
- [6] M. Fröhlich, R. Braun, and C. Leyens. Oxidation Resistant Coatings in Combination with Thermal Barrier Coatings on  $\gamma$ -TiAl Alloys for High Temperature Applications. *Surf. Coat. Technol.*, 201(7):3911, 2006.
- [7] C. Brecher, T. Schroder, H. Schlattmeier, and C. Bugiel. Load Carrying Capacity of PVD-Coated Automotive Gears. *VDI Berichte*, 1904:1107, 2005.
- [8] L. Guzman, G. K. Wolf, and G. M. Davies. PVD-IBAD Zinc Coating Development for Automotive Application. *Surf. Coat. Technol.*, 174-175:665, 2003.
- [9] J. Lin, B. Mishra, J. J. Moore, and W. D. Sproul. Microstructure, Mechanical and Tribological Properties of  $\text{Cr}_{1-x}\text{Al}_x\text{N}$  Films Deposited by Pulsed-Closed Field Unbalanced Magnetron Sputtering (P-CFUBMS). *Surf. Coat. Technol.*, 201(7): 4329, 2006.
- [10] P. Eh. Hovsepian, D. B. Lewis, Q. Luo, W.-D. Münz, P. H. Mayrhofer, C. Mitterer, Z. Zhou, and W. M. Rainforth. TiAlN Based Nanoscale Multilayer Coatings Designed to Adapt their Tribological Properties at Elevated Temperatures. *Thin Solid Films*, 485(1-2):160, 2005.
- [11] V. Kouznetsov, K. Macak, J. M. Schneider, U. Helmersson, and I. Petrov. A Novel Pulsed Magnetron Sputter Technique Utilizing Very High Target Power Densities. *Surf. Coat. Technol.*, 122(2-3):290, 1999.

- [12] K. Macak, V. Kouznetsov, J. Schneider, U. Helmersson, and I. Petrov. Ionized Sputter Deposition Using an Extremely High Plasma Density Pulsed Magnetron Discharge. *J. Vac. Sci. Technol. A*, 18(4 II):1533, 2000.
- [13] A. P. Ehiasarian, R. New, W.-D. Münz, L. Hultman, U. Helmersson, and V. Kouznetsov. Influence of High Power Densities on the Composition of Pulsed Magnetron Plasmas. *Vacuum*, 65(2):147, 2002.
- [14] S. A. Barnett. Mechanic and Dielectric Properties. In M. H. Francombe and J. L. Vossen (Eds.), *Physics of Thin Films*, p. 2. Academic Press, Boston, 1993.
- [15] S. PalDey and S. C. Deevi. Single Layer and Multilayer Wear Resistant Coatings of (Ti,Al)N: A Review. *Mater. Sci. Eng. A*, 342(1-2):58, 2003.
- [16] Q. Luo, P. Eh. Hovsepian, D. B. Lewis, W.-D. Münz, Y. N. Kok, J. Cockrem, M. Bolton, and A. Farinotti. Tribological Properties of Unbalanced Magnetron Sputtered Nano-Scale Multilayer Coatings TiAlN/VN and TiAlCrYN Deposited on Plasma Nitrided Steels. *Surf. Coat. Technol.*, 193(1-3):39, 2005.
- [17] F.-R. Weber, F. Fontaine, M. Scheib, and W. Bock. Cathodic Arc Evaporation of (Ti,Al)N Coatings and (Ti,Al)N/TiN Multilayer-Coatings - Correlation between Lifetime of Coated Cutting Tools, Structural and Mechanical Film Properties. *Surf. Coat. Technol.*, 177-178:227, 2004.
- [18] N. J. M. Carvalho, E. Zoestbergen, B. J. Kooi, and J. Th M. De Hosson. Stress Analysis and Microstructure of PVD Monolayer TiN and Multilayer TiN/(Ti,Al)N Coatings. *Thin Solid Films*, 429(1-2):179, 2003.
- [19] D. McIntyre, J. E. Greene, G. Hakansson, J.-E. Sundgren, and W.-D. Münz. Oxidation of Metastable Single-Phase Polycrystalline  $Ti_{0.5}Al_{0.5}N$  Films: Kinetics and Mechanisms. *J. Appl. Phys.*, 67(3):1542, 1990.
- [20] M. I. Lembke. *Oxidation Behaviour of TiAlN Based Nanolayered Hard Coatings*. PhD thesis, Sheffield Hallam University, 2003.
- [21] M. I. Lembke, D. B. Lewis, W.-D. Münz, and J. M. Titchmarsh. Significance of Y and Cr in TiAlN Hard Coatings for Dry High Speed Cutting. *Surf. Eng.*, 17(2):153, 2001.
- [22] R. Prescott and M. J. Graham. The Formation of Aluminum Oxide Scales on High-Temperature Alloys. *Oxidation Metals*, 38(3):233, 1992.
- [23] P. Panjan, B. Navinsek, A. Cvelbar, I. Milosev, and A. Zalar. Oxidation of TiN, ZrN, TiZrN, CrN, TiCrN and TiN/CrN Multilayer Hard Coatings Reactively Sputtered at Low Temperature. *Thin Solid Films*, 281-282(1-2):298, 1996.
- [24] O. Kubaschewski and B. E. Hopkins. *Oxidation of Metals and Alloys*. Butterworth & Co. Ltd., London, UK, 1962.
- [25] P. Kofstad. *High Temperature Corrosion*. Elsevier Applied Science Publishers, London, UK, 1988.
- [26] D. Gupta and P. S. Ho. Diffusion Processes in Thin Films. *Thin Solid Films*, 72(3):399, 1980.

- [27] S. Hofmann and H. A. Jehn. Oxidation Behavior of  $\text{CrN}_x$  and  $(\text{Cr,Al})\text{N}_x$  Hard Coatings. *Mat. Corr.*, 41(12):756, 1990.
- [28] NIST Chemistry WebBook. NIST National Institute of Standards and Technology. <http://webbook.nist.gov/chemistry/>, No.69, Release June 2005.
- [29] A. Kostov and B. Friedrich. Selection of Crucible Oxides in Molten Titanium and Titanium Alloys by Thermo-Chemistry Calculations. *J. Min. Met.*, 41 B:113, 2004.
- [30] P. H. Mayrhofer, H. Willmann, and C. Mitterer. Oxidation Kinetics of Sputtered Cr-N Hard Coatings. *Surf. Coat. Technol.*, 146-147:222, 2001.
- [31] M. I. Lembke, D. B. Lewis, and W. D Münz. Localized Oxidation Defects in TiAlN/CrN Superlattice Structured Hard Coatings Grown by Cathodic Arc/Unbalanced Magnetron Deposition on Various Substrate Materials. *Surf. Coat. Technol.*, 125(1):263, 2000.
- [32] L. Rebouta, F. Vaz, M. Andritschky, and M. F. Da Silva. Oxidation Resistance of (Ti, Al, Zr, Si)N Coatings in Air. *Surf. Coat. Technol.*, 76-77(Part 1):70, 1995.
- [33] R. F. Bunshah. Deposition Technologies: An Overview. In R. F. Bunshah (Ed.), *Handbook of Deposition Technologies for Films and Coatings*. Noyes Publications, Westwood, US, 1994.
- [34] D. M. Mattox. *Handbook of Physical Vapour Deposition (PVD) Processing - Film Formation, Adhesion, Surface, Preparation and Contamination Control*. Noyes Publications, Westwood, US, 1998.
- [35] M. A. Lieberman and A. J. Lichtenberg. *Principles of Plasma Discharges and Materials Processing*. Wiley & Sons, Inc., New York, US, 1994.
- [36] M. Nastasi, W. Müller, and W. Ensinger. Ion Implantation and Thin-Film Deposition. In A. Anders (Ed.), *Handbook of Plasma Immersion Ion Implantation and Deposition*, p. 125–242. Wiley Interscience Publications, New York, US, 2000.
- [37] P. Sigmund. Sputtering by Ion Bombardment: Theoretical Concepts. In R. Berisch (Ed.), *Sputtering by Particle Bombardment*, Vol. 1, p. 9–72. Springer Verlag, Berlin, D, 1981.
- [38] P. Sigmund. Theory of Sputtering. I. Sputtering Yield of Amorphous and Polycrystalline Targets. *Phys. Rev.*, 184(2):383, 1969.
- [39] S. L. Rohde. Sputter Deposition. In *ASM Handbook Vol. 5: Surface Engineering*, p. 573–581. ASM International, 1994.
- [40] J. A. Thornton and J. E. Greene. Sputter Deposition Processes. In R. F. Bunshah (Ed.), *Handbook of Deposition Technologies for Films and Coatings*, p. 249–319. Noyes Publications, Westwood, US, 1994.
- [41] I. Safi. Recent Aspects Concerning DC Reactive Magnetron Sputtering of Thin Films: A Review. *Surf. Coat. Technol.*, 127(2-3):203, 2000.
- [42] G. Falcone. Theory of Collisional Sputtering. *Surf. Sci.*, 187(1):212, 1987.

- [43] K. M. Wasa, M. Kitabatake, and H. Adachi. *Thin Film Materials Technology: Sputtering of Compound Materials*. Noyes Publications, Westwood, US, 2004.
- [44] A. Matthews, K. S. Fancey, A. S. James, and A. Leyland. Ionization in Plasma-Assisted Physical Vapour Deposition Systems. *Surf. Coat. Technol.*, 61(1-3):121, 1993.
- [45] R. J. Goldston and P. H. Rutherford. *Introduction to Plasma Physics*. IOP Publ., Bristol, UK, 1995.
- [46] S. M. Rossnagel and K. L. Saenger. Optical Emission in Magnetrons: Nonlinear Aspects. *J. Vac. Sci. Technol. A*, 7(3):968, 1989.
- [47] I. V. Svadkovski, D. A. Golosov, and S. M. Zavatskiy. Characterisation Parameters for Unbalanced Magnetron Sputtering Systems. *Vacuum*, 68(4):283, 2002.
- [48] N. Savvides and B. Window. Unbalanced Magnetron Ion-Assisted Deposition and Property Modification of Thin Films. *J. Vac. Sci. Technol. A*, 4(3):504, 1986.
- [49] P. J. Kelly and R. D. Arnell. Magnetron Sputtering: A Review of Recent Developments and Applications. *Vacuum*, 56(3):159, 2000.
- [50] U. Helmersson, M. Lattemann, J. Alami, J. Böhlmark, A. P. Ehiasarian, and J. T. Gudmundsson. High Power Impulse Magnetron Sputtering Discharges and Thin Film Growth: A Brief Review. In *48th Annual Technical Conference Proceedings of the Society of Vacuum Coaters*, p. 458. SVC Publishing, San Diego, US, 2005.
- [51] A. P. Ehiasarian, W.-D. Münz, L. Hultman, U. Helmersson, and I. Petrov. High Power Pulsed Magnetron Sputtered CrN<sub>x</sub> Films. *Surf. Coat. Technol.*, 163-164: 267, 2003.
- [52] J. Böhlmark, J. Alami, C. Christou, A. P. Ehiasarian, and U. Helmersson. Ionization of Sputtered Metals in High Power Pulsed Magnetron Sputtering. *J. Vac. Sci. Technol. A*, 23(1):18, 2005.
- [53] U. Helmersson, M. Lattemann, J. Böhlmark, A. P. Ehiasarian, and J. T. Gudmundsson. Ionized Physical Vapor Deposition (IPVD): A Review of Technology and Applications. *Thin Solid Films*, 513(1-2):1, 2006.
- [54] J. Alami, K. Sarakinos, G. Mark, and M. Wuttig. On the Deposition Rate in a High Power Pulsed Magnetron Sputtering Discharge. *Appl. Phys. Lett.*, 89(15): 154104, 2006.
- [55] R. F. Bunshah. Evaporation: Processes, Bulk Microstructures and Mechanical Properties. In R. F. Bunshah (Ed.), *Handbook of Deposition Technologies for Films and Coatings*, p. 131–248. Noyes Publications, Westwood, US, 1994.
- [56] B. Juttner. Cathode Spots of Electric Arcs. *J. Phys. D*, 34(17):103, 2001.
- [57] I. Petrov, P. Losbichler, D. Bergstrom, J. E. Greene, W.-D. Münz, T. Hurkmans, and T. Trinh. Ion-Assisted Growth of Ti<sub>1-x</sub>Al<sub>x</sub>N/Ti<sub>1-y</sub>Nb<sub>y</sub>N Multilayers by Combined Cathodic-Arc/Magnetron-Sputter Deposition. *Thin Solid Films*, 302 (1-2):179, 1997.

- [58] W.-D. Münz, D. B. Lewis, S. Creasey, T. Hurkmans, T. Trinh, and W. Ijzendor. Defects in TiN and TiAlN Coatings Grown by Combined Cathodic Arc/Unbalanced Magnetron Technology. *Vacuum*, 46(4):323, 1995.
- [59] S. M. Rossnagel. Thin Film Deposition with Physical Vapor Deposition and Related Technologies. *J. Vac. Sci. Technol. A*, 21(5):S74, 2003.
- [60] W.-D. Münz, I. J. Smith, D. B. Lewis, and S. Creasey. Droplet Formation on Steel Substrates during Cathodic Steered Arc Metal Ion Etching. *Vacuum*, 48(5):473, 1997.
- [61] H. W. Wang, M. M. Stack, S. B. Lyon, P. Eh. Hovsepian, and W.-D. Münz. Wear Associated with Growth Defects in Combined Cathodic Arc/Unbalanced Magnetron Sputtered CrN/NbN Superlattice Coatings during Erosion in Alkaline Slurry. *Surf. Coat. Technol.*, 135(1):82, 2000.
- [62] H. W. Wang, M. M. Stack, S. B. Lyon, P. Eh. Hovsepian, and W.-D. Münz. Corrosion Behaviour of Macroparticle Defects in Arc Bond-Sputtered CrN/NbN Superlattice Coatings. *Surf. Coat. Technol.*, 126(2-3):279, 2000.
- [63] J. A. Thornton. The Microstructure of Sputter-Deposited Coatings. *J. Vac. Sci. Technol. A*, 4(6):3059, 1986.
- [64] J. E. Greene. Nucleation, Film Growth, and Microstructural Evolution. In R. F. Bunshah (Ed.), *Handbook of Deposition Technologies for Films and Coatings*, p. 681–762. Noyes Publications, Westwood, US, 1994.
- [65] B. A. Movchan and V. A. Demchishin. Study of the Structure and Properties of Thick Vacuum Condensates of Nickel, Titanium, Tungsten, Aluminum Oxide and Zirconium Dioxide. *Phys. Metals Metallogr.*, 28(4):83, 1969.
- [66] R. Messier, A. P. Giri, and R. A. Roy. Revised Structure Zone Model for Thin Film Physical Structure. *J. Vac. Sci. Technol. A*, 2(2):500, 1984.
- [67] D. M. Mattox. Surface Effects on the Growth, Adhesion and Properties of Reactively Deposited Hard Coatings. *Surf. Coat. Technol.*, 81(1):8, 1996.
- [68] H. Oettel and R. Wiedemann. Residual Stresses in PVD Hard Coatings. *Surf. Coat. Technol.*, 76-77:265, 1995.
- [69] P. J. Kelly and R. D. Arnell. Development of a Novel Structure Zone Model Relating to the Closed-Field Unbalanced Magnetron Sputtering System. *J. Vac. Sci. Technol. A*, 16(5):2858, 1998.
- [70] K. Koski, J. Holsa, J. Ernoult, and A. Rouzaud. The Connection between Sputter Cleaning and Adhesion of Thin Solid Films. *Surf. Coat. Technol.*, 80(1):195, 1996.
- [71] A. P. Ehiasarian, J. G. Wen, and I. Petrov. Interface Microstructure Engineering by High Power Impulse Magnetron Sputtering for the Enhancement of Adhesion. *J. Appl. Phys.*, 101(5):054301, 2007.

- [72] C. Schönjahn, L. A. Donohue, D. B. Lewis, W.-D. Münz, R. D. Twesten, and I. Petrov. Enhanced Adhesion through Local Epitaxy of Transition-Metal Nitride Coatings on Ferritic Steel Promoted by Metal Ion Etching in a Combined Cathodic arc/unbalanced Magnetron Deposition System. *J. Vac. Sci. Technol. A*, 18(4 II): 1718, 2000.
- [73] C. Schönjahn, H. Paritong, W.-D. Münz, R. D. Twesten, and I. Petrov. Influence of the Interface Composition on the Corrosion Behavior of Unbalanced Magnetron Grown Niobium Coatings on Steel. *J. Vac. Sci. Technol. A*, 19(4):1392, 2001.
- [74] C. Schönjahn, M. Bamford, L. A. Donohue, D. B. Lewis, S. Forder, and W.-D. Münz. Interface between TiAlN Hard Coatings and Steel Substrates Generated by High Energetic Cr<sup>+</sup> Bombardment. *Surf. Coat. Technol.*, 125(1):66, 2000.
- [75] C. Schönjahn. *Surface Treatment in a Cathodic Arc Plasma: Key Step for Interface Engineering*. PhD thesis, Sheffield Hallam University, 2001.
- [76] C. Schönjahn, A. P. Ehasarian, D. B. Lewis, R. New, W.-D. Münz, R. D. Twesten, and I. Petrov. Optimization of in Situ Substrate Surface Treatment in a Cathodic Arc Plasma: A Study by TEM and Plasma Diagnostics. *J. Vac. Sci. Technol. A*, 19(4):1415, 2001.
- [77] M. Lattemann, A. P. Ehasarian, J. Böhlmark, P. A. O. Persson, and U. Helmersson. Investigation of High Power Impulse Magnetron Sputtering Pretreated Interfaces for Adhesion Enhancement of Hard Coatings on Steel. *Surf. Coat. Technol.*, 200(22-23):6495, 2006.
- [78] A. P. Ehasarian, P. Eh. Hovsepian, M. Lattemann, J. Böhlmark, and U. Helmersson. High Power Impulse Magnetron Sputtering (HIPIMS) Pre-Treatment for the Deposition of Hard Coatings. In *48th Annual Technical Conference Proceedings of the Society of Vacuum Coaters*, p. 480. SVC Publishing, Denver, US, 2005.
- [79] J.-H. Huang, C.-H. Ma, and H. Chen. Effect of Ti Interlayer on the Residual Stress and Texture Development of TiN Thin Films Deposited by Unbalanced Magnetron Sputtering. *Surf. Coat. Technol.*, 201(6):3199, 2006.
- [80] J.-H. Huang, F.-Y. Ouyang, and G.-P. Yu. Effect of Film Thickness and Ti Interlayer on the Structure and Properties of Nanocrystalline TiN Thin Films on AISI D2 Steel. *Surf. Coat. Technol.*, 201(16-17):7043, 2007.
- [81] D.-F. Lii, H. Jowlay, and L. Minghung. The Effects of TiAl Interlayer on PVD TiAlN Films. *Surf. Coat. Technol.*, 99(1):196, 1998.
- [82] P. Eh. Hovsepian, D. B. Lewis, W.-D. Münz, S. B. Lyon, and M. Tomlinson. Combined Cathodic Arc/Unbalanced Magnetron Grown CrN/NbN Superlattice Coatings for Corrosion Resistant Applications. *Surf. Coat. Technol.*, 120-121:535, 1999.
- [83] P. Eh. Hovsepian, D. B. Lewis, and W.-D. Münz. Recent Progress in Large Scale Manufacturing of Multilayer/Superlattice Hard Coatings. *Surf. Coat. Technol.*, 133-134:166, 2000.

- [84] Q. Luo, G. Robinson, M. Pittman, M. Howarth, W.-M. Sim, M. R. Stalley, H. Leitner, R. Ebner, D. Caliskanoglu, and P. Eh. Hovsepian. Performance of Nano-Structured Multilayer PVD Coating TiAlN/VN in Dry High Speed Milling of Aerospace Aluminium 7010-T7651. *Surf. Coat. Technol.*, 200(1-4):123, 2005.
- [85] S.-K. Tien and J.-G. Duh. Effect of Heat Treatment on Mechanical Properties and Microstructure of CrN/AlN Multilayer Coatings. *Thin Solid Films*, 494(1-2): 173, 2006.
- [86] J.-K. Park and Y.-J. Baik. The Crystalline Structure, Hardness and Thermal Stability of AlN/CrN Superlattice Coating Prepared by D.C. Magnetron Sputtering. *Surf. Coat. Technol.*, 200(5-6):1519, 2005.
- [87] S. A. Barnett and A. Mandan. Superhard Superlattices. *Phys. World*, 45:48, Jan 1998.
- [88] W.-D. Münz, D. B. Lewis, P. Eh. Hovsepian, C. Schönjahn, A. P. Ehasarian, and I. J. Smith. Industrial Scale Manufactured Superlattice Hard PVD Coatings. *Surf. Eng.*, 17(1):15, 2001.
- [89] Q. Luo, W. M. Rainforth, L. A. Donohue, I. Wadsworth, and W.-D. Münz. Tribological Investigation of TiAlCrN and TiAlN/CrN Coatings Grown by Combined Steered Arc/Unbalanced Magnetron Deposition. *Vacuum*, 53(1-2):123, 1999.
- [90] P. Panjan, B. Navinsek, A. Cvelbar, A. Zalar, and J. Vlcek. High-Temperature Oxidation of TiN/CrN Multilayers Reactively Sputtered at Low Temperatures. *Surf. Coat. Technol.*, 98(1-3):1497, 1998.
- [91] S.-K. Tien, J.-G. Duh, and J.-W. Lee. Oxidation Behavior of Sputtered CrN/AlN Multilayer Coatings during Heat Treatment. *Surf. Coat. Technol.*, 201(9-11):5138, 2007.
- [92] L. Hultman. Thermal Stability of Nitride Thin Films. *Vacuum*, 57(1):1, 2000.
- [93] A. C. Vlasveld, S. G. Harris, E. D. Doyle, D. B. Lewis, and W.-D. Münz. Characterisation and Performance of Partially Filtered Arc TiAlN Coatings. *Surf. Coat. Technol.*, 149(2-3):217, 2002.
- [94] I. J. Smith, W.-D. Münz, L. A. Donohue, I. Petrov, and J. E. Greene. Improved  $Ti_{1-x}Al_xN$  PVD Coatings for Dry High Speed Cutting Operations. *Surf. Eng.*, 14(1):37, 1998.
- [95] W.-D. Münz, L. A. Donohue, and P. Eh. Hovsepian. Properties of Various Large-Scale Fabricated TiAlN- and CrN-Based Superlattice Coatings Grown by Combined Cathodic Arc/Unbalanced Magnetron Sputter Deposition. *Surf. Coat. Technol.*, 125(1):269, 2000.
- [96] L. A. Donohue, D. B. Lewis, W.-D. Münz, M. M. Stack, S. B. Lyon, H.-W. Wang, and D. Rafaja. Influence of Low Concentrations of Chromium and Yttrium on the Oxidation Behaviour, Residual Stress and Corrosion Performance of TiAlN Hard Coatings on Steel Substrates. *Vacuum*, 55(2):109, 1999.

- [97] E. Pflügener, A. Schröer, P. Voumard, L. A. Donohue, and W.-D. Münz. Influence of Incorporation of Cr and Y on the Wear Performance of TiAlN Coatings at Elevated Temperatures. *Surf. Coat. Technol.*, 115(1):17, 1999.
- [98] C. Leyens. Oxiadationsverhalten und Oxidationsschutz von Titanlegierungen und Titanaluminiden (in German). In M. Peters and C. Leyens (Eds.), *Titan und Titanlegierungen*, p. 197–244. Wiley VCH Verlag, Weinheim, Germany, 2002.
- [99] T. Hurkmans. *The Microstructure and Properties of Unbalanced Magnetron Sputtered CrN<sub>x</sub> Coatings*. PhD thesis, Sheffield Hallam University, 2002.
- [100] T. Hurkmans, D. B. Lewis, H. Paritong, J. S. Brooks, and W.-D. Münz. Influence of Ion Bombardment on Structure and Properties of Unbalanced Magnetron Grown CrN<sub>x</sub> Coatings. *Surf. Coat. Technol.*, 114(1):52, 1999.
- [101] J. P. De Luca and J. M. Leitnaker. Review of Thermodynamic Properties of the Cr-N System. *J. Am. Ceram. Soc.*, 56(3):126, 1973.
- [102] F.-H. Lu and H.-Y. Chen. Phase Changes of CrN Films Annealed at High Temperature Under Controlled Atmosphere. *Thin Solid Films*, 398-399:368, 2001.
- [103] F.-H. Lu, H.-Y. Chen, and C.-H. Hung. Degradation of CrN Films at High Temperature Under Controlled Atmosphere. *J. Vac. Sci. Technol. A*, 21(3):671, 2003.
- [104] H.-Y. Chen and F.-H. Lu. Phase Transformation in Chromium Nitride Films. *J. Vac. Sci. Technol. A*, 21(3):695, 2003.
- [105] J.-N. Tu, J.-G. Duh, and S.-Y. Tsai. Morphology, Mechanical Properties, and Oxidation Behavior of Reactively Sputtered Cr-N Films. *Surf. Coat. Technol.*, 133-134:181, 2000.
- [106] I. Milosev, J. M. Abels, H.-H. Strehblow, B. Navinsek, and M. Metikos-Hukovic. High Temperature Oxidation of Thin CrN Coatings Deposited on Steel. *J. Vac. Sci. Technol. A*, 14(4):2527, 1996.
- [107] T. Kacsich, K.-P. Lieb, A. Schaper, and O. Schulte. Oxidation of Thin Chromium Nitride Films: Kinetics and Morphology. *J. Phys.: Condens. Matter*, 8(49):10703, 1996.
- [108] T. Kacsich and K.-P. Lieb. Oxidation of Thin CrN and Cr<sub>2</sub>N Films Analyzed Via Nuclear Reaction Analysis and Rutherford Backscattering Spectrometry. *Thin Solid Films*, 245(1-2):4, 1994.
- [109] I. Milosev, H.-H. Strehblow, and B. Navinsek. Comparison of TiN, ZrN and CrN Hard Nitride Coatings: Electrochemical and Thermal Oxidation. *Thin Solid Films*, 303(1-2):246, 1997.
- [110] D. B. Lee, Y. C. Lee, and S. C. Kwon. High Temperature Oxidation of a CrN Coating Deposited on a Steel Substrate by Ion Plating. *Surf. Coat. Technol.*, 141(2-3):227, 2001.
- [111] D. B. Lee, Y. D. Jang, H. S. Myung, and J. G. Han. High-Temperature Oxidation of Magnetron-Sputtered Cr-N-Coated Steels. *Thin Solid Films*, 506-507:369, 2006.

- [112] H. C. Barshilia, N. Selvakumar, B. Deepthi, and K. S. Rajam. A Comparative Study of Reactive Direct Current Magnetron Sputtered CrAlN and CrN Coatings. *Surf. Coat. Technol.*, 201:2193, 2006.
- [113] J. C. Sanchez-Lopez, D. Martinez-Martinez, C. Lopez-Cartes, A. Fernandez, M. Brizuela, A. Garcia-Luis, and J. I. Onate. Mechanical Behavior and Oxidation Resistance of Cr(Al)N Coatings. *J. Vac. Sci. Technol. A*, 23(4):681, 2005.
- [114] A. E. Reiter, V. H. Derflinger, B. Hanselmann, T. Bachmann, and B. Sartory. Investigation of the Properties of  $Al_{1-x}Cr_xN$  Coatings Prepared by Cathodic Arc Evaporation. *Surf. Coat. Technol.*, 200(7):2114, 2005.
- [115] A. Sugishima, H. Kajioka, and Y. Makino. Phase Transition of Pseudobinary Cr-Al-N Films Deposited by Magnetron Sputtering Method. *Surf. Coat. Technol.*, 97(1-3):590, 1997.
- [116] A. Kimura, M. Kawate, H. Hasegawa, and T. Suzuki. Anisotropic Lattice Expansion and Shrinkage of Hexagonal TiAlN and CrAlN Films. *Surf. Coat. Technol.*, 169-170(1):367, 2003.
- [117] Y. Makino and K. Nogi. Synthesis of Pseudobinary Cr-Al-N Films with B1 Structure by RF-Assisted Magnetron Sputtering Method. *Surf. Coat. Technol.*, 98(1-3):1008, 1998.
- [118] T. Hurkmans, D. B. Lewis, J. S. Brooks, and W.-D. Münz. Chromium Nitride Coatings Grown by Unbalanced Magnetron (UBM) and Combined arc/unbalanced Magnetron (ABS) Deposition Techniques. *Surf. Coat. Technol.*, 86-87(Part 1):192, 1996.
- [119] X.-Z. Ding and X. T. Zeng. Structural, Mechanical and Tribological Properties of CrAlN Coatings Deposited by Reactive Unbalanced Magnetron Sputtering. *Surf. Coat. Technol.*, 200(5-6):1372, 2005.
- [120] J. L. Endrino, G. S. Fox-Rabinovich, and C. Gey. Hard AlTiN, AlCrN PVD Coatings for Machining of Austenitic Stainless Steel. *Surf. Coat. Technol.*, 200(24):6840, 2006.
- [121] H. Hasegawa, M. Kawate, and T. Suzuki. Effects of Al Contents on Microstructures of  $Cr_{1-x}Al_xN$  and  $Zr_{1-x}Al_xN$  Films Synthesized by Cathodic Arc Method. *Surf. Coat. Technol.*, 200(7):2409, 2005.
- [122] M. Brizuela, A. Garcia-Luis, I. Braceras, J. I. Onate, J. C. Sanchez-Lopez, D. Martinez-Martinez, C. Lopez-Cartes, and A. Fernandez. Magnetron Sputtering of Cr(Al)N Coatings: Mechanical and Tribological Study. *Surf. Coat. Technol.*, 200(1-4):192, 2005.
- [123] O. Banakh, P. E. Schmid, R. Sanjines, and F. Levy. High-Temperature Oxidation Resistance of  $Cr_{1-x}Al_xN$  Thin Films Deposited by Reactive Magnetron Sputtering. *Surf. Coat. Technol.*, 163-164:57, 2003.
- [124] U. Bardi, S. P. Chenakin, F. Ghezzi, C. Giolli, A. Goruppa, A. Lavacchi, E. Miorin, C. Pagura, and A. Tolstogousov. High-Temperature Oxidation of CrN/AlN Multi-layer Coatings. *Appl. Surf. Sci.*, 252(5):1339, 2005.

- [125] E. Huber and S. Hofmann. Oxidation Behaviour of Chromium-Based Nitride Coatings. *Surf. Coat. Technol.*, 68-69:64, 1994.
- [126] M. Hirai, H. Saito, T. Suzuki, H. Suematu, W. Jiang, and K. Yatsui. Characteristics of Cr-Al-N-O thin films Prepared by Pulsed Laser deposition. In *Surface Engineering 2001 - Fundamentals and Applications*, p. 255. Mat. Res. Soc., Nagoya, Japan, 2002.
- [127] D. B. Lewis, L. A. Donohue, M. Lembke, W.-D. Münz, R. Jr. Kuzel, V. Valvoda, and C. J. Blomfield. Influence of the Yttrium Content on the Structure and Properties of  $Ti_{1-x-y-z}Al_xCr_yY_zN$  PVD Hard Coatings. *Surf. Coat. Technol.*, 114(2):187, 1999.
- [128] J. L. Endrino and V. Derflinger. The Influence of Alloying Elements on the Phase Stability and Mechanical Properties of AlCrN Coatings. *Surf. Coat. Technol.*, 200(1-4):988, 2005.
- [129] J. Zhujing, L. Changqing, Y. Li, and W. Weitao. Corrosion Performance of Ion-Plated Titanium and Yttrium-Modified TiN Coatings. *Surf. Coat. Technol.*, 46(3):307, 1991.
- [130] L. A. Donohue, I. J. Smith, W.-D. Münz, I. Petrov, and J. E. Greene. Microstructure and Oxidation-Resistance of  $Ti_{1-x-y-z}Al_xCr_yY_zN$  Layers Grown by Combined Steered-arc/Unbalanced-Magnetron-Sputter Deposition. *Surf. Coat. Technol.*, 94-95(1-3):226, 1997.
- [131] M. I. Lembke, J. M. Titchmarsh, D. B. Lewis, and W.-D. Münz. Investigation of the Oxidation Behaviour of a TiAlCrYN PVD Hard Coating. In *Growth, Evolution and Properties of Surfaces, Thin Films and Self-Organized Structures*, p. 6571. Mat. Res. Soc., Warrendale, US, 2001.
- [132] X. Peng and F. Wang. Morphologic Investigation and Growth of the Alumina Scale on Magnetron-Sputtered CoCrAl NCs with and without Yttrium. *Corros. Sci.*, 45(10):2293, 2003.
- [133] V. Provenzano, K. Sadananda, N. P. Louat, and J. R. Reed. Void Formation and Suppression during High Temperature Oxidation of MCrAlY-Type Coatings. *Surf. Coat. Technol.*, 36(1-2):61, 1988.
- [134] Q. G. Zhou, X. D. Bai, X. Y. Xue, Y. H. Ling, X. W. Chen, J. Xu, and D. R. Wang. The Influence of Y Ion Implantation on the Oxidation Behaviour of ZrN Coating. *Vacuum*, 76(4):517, 2004.
- [135] P. Kofstad. Fundamental Aspects of Corrosion by Hot Gases. *Mater. Sci. Eng. A*, A120-1(1-2):25, 1989.
- [136] W.-D. Münz, D. Schulze, and F. J. M. Hauzer. New Method for Hard Coatings: ABS (Arc Bond Sputtering). *Surf. Coat. Technol.*, 50(2):169, 1992.
- [137] A. P. Ehasarian. Unpublished Results.
- [138] H. Jenett. Electron-Impact Secondary Neutral Mass Spectrometry (SNMS). In H. Bubert and H. Jenett (Eds.), *Surface and Thin Film Analysis*, p. 122-140. Wiley-VCH, Weinheim, 2003.

- [139] J. S. Colligon, H. Kheyrandish, J. M. Walls, and J. Wolstenholme. Quantitative Secondary Neutral Mass Spectroscopy of Thin Films. *Thin Solid Films*, 200(2): 293, 1991.
- [140] B. C. Cullity and S. R. Stock. *Elements of X-ray Diffraction*. Prentice Hall, Indianapolis, US, 2003.
- [141] International Centre for Diffraction Data. ICPP-JCPDS Database of Crystallographic Data, Release 2000.
- [142] D. N. Lee. A Model for Development of Orientation of Vapour Deposits. *J. Mater. Sci.*, 24(12):4375, 1989.
- [143] T. Li, M. Li, and Y. Zhou. Phase Segregation and its Effect on the Adhesion of Cr-Al-N Coatings on K38G Alloy Prepared by Magnetron Sputtering Method. *Surf. Coat. Technol.*, 201(18):7692, 2007.
- [144] D. B. Lewis, Q. Luo, P. Eh. Hovsepian, and W.-D. Münz. Interrelationship between Atomic Species, Bias Voltage, Texture and Microstructure of Nano-Scale Multilayers. *Surf. Coat. Technol.*, 184(2-3):225, 2004.
- [145] S. Logothetidis, N. Kalfagiannis, K. Sarakinos, and P. Patsalas. Investigation of Bilayer Period and Individual Layer Thickness of CrN/TiN Superlattices by Ellipsometry and X-Ray Techniques. *Surf. Coat. Technol.*, 200(22-23):6176, 2006.
- [146] V. Valvoda, R. J. Kuzel, R. Cerny, D. Rafaja, J. Musil, S. Kadlec, and A. J. Perry. Structural Analysis of TiN Films by Seemann-Bohlin X-Ray Diffraction. *Thin Solid Films*, 193-194(1):401, 1990.
- [147] A. J. Perry, V. Valvoda, and D. Rafaja. X-Ray Residual Stress Measurement in TiN, ZrN and HfN Films Using the Seemann-Bohlin Method. *Thin Solid Films*, 214(2):169, 1992.
- [148] L. Reimer. *Scanning Electron Microscopy. Physics of Image Formation and Microanalysis*. Springer, Berlin, D, 1998.
- [149] D. B. Williams and C. B. Carter. *Transmission Electron Microscopy: A Textbook for Materials Science*. Springer, Berlin, D, 1996.
- [150] B. Fultz und J. M. Howe. *Transmission Electron Microscopy and Diffractometry of Materials*. Springer, Berlin, D, 2005.
- [151] C. C. Ahn (Ed.). *Transmission Electron Energy Loss Spectrometry in Materials and the EELS ATLAS*. Wiley-VCH, Weinheim, D, 2006.
- [152] Q. Luo, Z. Zhou, W. M. Rainforth, and P. Eh. Hovsepian. TEM-EELS Study of Low-Friction Superlattice TiAlN/VN Coating: The Wear Mechanisms. *Tribol. Lett.*, 24(2):171, 2006.
- [153] J. Sekler, P. A. Steinmann, and H. E. Hintermann. Scratch Test: Different Critical Load Determination Techniques. *Surf. Coat. Technol.*, 36(1-2):519, 1988.
- [154] S. J. Bull and E. G. Berasetegui. An Overview of the Potential of Quantitative Coating Adhesion Measurement by Scratch Testing. *Tribol. Int.*, 39(2):99, 2006.

- [155] P. A. Steinmann, Y. Tardy, and H. E. Hintermann. Adhesion Testing by the Scratch Test Method: The Influence of Intrinsic and Extrinsic Parameters on the Critical Load. *Thin Solid Films*, 154(1-2):333, 1987.
- [156] Verein Deutscher Ingenieure. PVD and CVD hard coatings - Quality assurance - Characteristic profiles and fields of application of hard coatings. *VDI-Technical Norm, volume=VDI 3824*, 2001.
- [157] N. Vidakis, A. Antoniadis, and N. Bilalis. The VDI 3198 Indentation Test Evaluation of a Reliable Qualitative Control for Layered Compounds. *J. Mat. Proc. Technol.*, 143-144:481, 2003.
- [158] E. J. Bienk, H. Reitz, and N. J. Mikkelsen. Wear and Friction Properties of Hard PVD Coatings. *Surf. Coat. Technol.*, 76-77(Part 2):475, 1995.
- [159] H. Ahmadi and D. Y. Li. Mechanical and Tribological Properties of Aluminide Coating Modified with Yttrium. *Surf. Coat. Technol.*, 161(2-3):210, 2002.
- [160] L. Riestler, P. J. Blau, E. Lara-Curzio, and K. Breder. Nanoindentation with a Knoop indenter. *Thin Solid Films*, 377-378:635, 2000.
- [161] W. C. Oliver and G. M. Pharr. Improved Technique for Determining Hardness and Elastic Modulus using Load and Displacement Sensing Indentation Experiments. *J. Mater. Res.*, 7(6):1564, 1992.
- [162] W. C. Oliver and G. M. Pharr. Measurement of Hardness and Elastic Modulus by Instrumented Indentation: Advances in Understanding and Refinements to Methodology. *J. Mater. Res.*, 19(1):3, 2004.
- [163] A. Anders. Physics of Arcing, and Implications to Sputter Deposition. *Thin Solid Films*, 502(1-2):22, 2006.
- [164] A. P. Ehasarian, P. Eh. Hovsepian, L. Hultman, and U. Helmersson. Comparison of Microstructure and Mechanical Properties of Chromium Nitride-Based Coatings Deposited by High Power Impulse Magnetron Sputtering and by the Combined Steered Cathodic arc/unbalanced Magnetron Technique. *Thin Solid Films*, 457(2):270, 2004.
- [165] R. R. Aharonov, M. Chhowalla, S. Dhar, and R. P. Fontana. Factors Affecting Growth Defect Formation in Cathodic Arc Evaporated Coatings. *Surf. Coat. Technol. Tec*, 82(3):334, 1996.
- [166] S. Creasey, D. B. Lewis, I. J. Smith, and W.-D. Münz. SEM Image Analysis of Droplet Formation during Metal Ion Etching by a Steered Arc Discharge. *Surf. Coat. Technol.*, 97(1-3):163, 1997.
- [167] C. Detavernier, A. S. Ozcan, J. Jordan-Sweet, E. A. Stach, J. Tersoff, F. M. Ross, and C. Lavoie. An Off-Normal Fibre-Like Texture in Thin Films on Single-Crystal Substrates. *Nature*, 426(696):641, 2003.
- [168] C. Schönjahn, D. B. Lewis, W.-D. Münz, and I. Petrov. Substrate Ion Etching in Combined Steered Cathodic Arc-UBM Deposition System: Effects on Interface Architecture, Adhesion, and Tool Performance. *Surf. Eng.*, 16:176, 2000.

- [169] C. Reinhard, A. P. Ehiasarian, and P. Eh. Hovsepian. CrN/NbN Superlattice Structured Coatings with Enhanced Corrosion Resistance Achieved by High Power Impulse Magnetron Sputtering Interface Pre-Treatment. *Thin Solid Films*, 515 (7-8):3685, 2007.
- [170] J. Takadom and H. H. Bennani. Influence of Substrate Roughness and Coating Thickness on Adhesion, Friction and Wear of TiN Films. *Surf. Coat. Technol.*, 96 (2-3):272, 1997.
- [171] F. Svahn, A. Kassman-Rudolphi, and E. Wallen. The Influence of Surface Roughness on Friction and Wear of Machine Element Coatings. *Wear*, 254(11):1092, 2003.
- [172] X. Chu, S. A. Barnett, M. S. Wong, and W. D. Sproul. Reactive Unbalanced Magnetron Sputter Deposition of Polycrystalline TiN/NbN Superlattice Coatings. *Surf. Coat. Technol.*, 57(1):13, 1993.
- [173] A. R. Denton and N. W. Ashcroft. Vegard's Law. *Phys. Rev. A*, 43(6):3161, 1991.
- [174] D. N. Lee. Textures and Structures of Vapor Deposits. *J. Mater. Sci.*, 34(11):2575, 1999.
- [175] J. Pelleg, L. Z. Zevin, S. Lungo, and N. Croitoru. Reactive-Sputter-Deposited TiN Films on Glass Substrates. *Thin Solid Films*, 197(1-2):117, 1991.
- [176] A. J. Perry, V. Valvoda, and D. Rafaja. On the Residual Stress and Picostructure of Titanium Nitride Films. II. A Picostructural Model. *Vacuum*, 45(1):11, 1994.
- [177] Q. Luo, D. B. Lewis, P. Eh. Hovsepian, and W.-D. Münz. Transmission Electron Microscopy and X-Ray Diffraction Investigation of the Microstructure of Nanoscale Multilayer TiAlN/VN Grown by Unbalanced Magnetron Deposition. *J. Mater. Res.*, 19(4):1093, 2004.
- [178] U. C. Oh and J. H. Je. Effects of Strain Energy on the Preferred Orientation of TiN Thin Films. *J. Appl. Phys.*, 74(3):1692, 1993.
- [179] J.-L. Ruan, J.-L. Huang, J. S. Chen, and D.-F. Lii. Effects of Substrate Bias on the Reactive Sputtered Zr-Al-N Diffusion Barrier Films. *Surf. Coat. Technol.*, 200 (5-6):1652, 2005.
- [180] K. Chu, P. W. Shum, and Y. G. Shen. Substrate Bias Effects on Mechanical and Tribological Properties of Substitutional Solid Solution (Ti, Al)N Films Prepared by Reactive Magnetron Sputtering. *Mater. Sci. Eng. A*, 131(1-3):62, 2006.
- [181] D. B. Lewis, S. Creasey, Z. Zhou, J. J. Forsyth, A. P. Ehiasarian, P. Eh. Hovsepian, Q. Luo, W. M. Rainforth, and W.-D. Münz. The Effect of (Ti+Al):V Ratio on the Structure and Oxidation Behaviour of TiAlN/VN Nano-Scale Multilayer Coatings. *Surf. Coat. Technol.*, 177-178:252, 2004.
- [182] P. H. Mayrhofer, C. Mitterer, L. Hultman, and H. Clemens. Microstructural Design of Hard Coatings. *Prog. Mater. Sci.*, 51(8):1032, 2006.

- [183] C. Mendibide, J. Fontaine, P. Steyer, and C. Esnouf. Dry Sliding Wear Model of Nanometer Scale Multilayered TiN/CrN PVD Hard Coatings. *Tribol. Lett.*, 17(4):779, 2004.
- [184] C. P. Constable, D. B. Lewis, J. Yarwood, and W.-D. Münz. Raman Microscopic Studies of Residual and Applied Stress in PVD Hard Ceramic Coatings and Correlation with X-Ray Diffraction (XRD) Measurements. *Surf. Coat. Technol.*, 184(2-3):291, 2004.
- [185] Q. Luo, W. M. Rainforth, and W.-D. Münz. TEM Observations of Wear Mechanisms of TiAlCrN and TiAlN/CrN Coatings Grown by Combined Steered-arc/Unbalanced Magnetron Deposition. *Wear*, 225-229(I):74, 1999.
- [186] G. Hakansson. *Growth of Compound and Superlattice Thin Films: Effects of Energetic Particle Bombardment*. PhD thesis, Linköping University, 1991.
- [187] Z. Czigany and G. Radnoczi. Columnar Growth Structure and Evolution of Wavy Interface Morphology in Amorphous and Polycrystalline Multilayered Thin Films. *Thin Solid Films*, 347(1-2):133, 1999.
- [188] D. B. Lewis, I. Wadsworth, W.-D. Münz, R. Kuzel, and V. Valvoda. Structure and Stress of TiAlN/CrN Superlattice Coatings as a Function of CrN Layer Thickness. *Surf. Coat. Technol.*, 116-119:284, 1999.
- [189] H. Scheerer, H. Hoche, E. Broszeit, B. Schramm, E. Abele, and C. Berger. Effects of the Chromium to Aluminum Content on the Tribology in Dry Machining using (Cr,Al)N Coated Tools. *Surf. Coat. Technol.*, 200(1-4):203, 2005.
- [190] S. J. Bull, D. S. Rickerby, and A. Jain. The Sliding Wear of Titanium Nitride Coatings. *Surf. Coat. Technol.*, 41(3):269, 1990.
- [191] C. P. Constable, J. Yarwood, G. Robinson, Q. Luo, D. B. Lewis, and W.-D. Münz. Investigation of Wear Processes on Worn Tools Using Raman Microscopy. *Surf. Eng.*, 18(2):127, 2002.
- [192] S.-K. Tien and J.-G. Duh. Comparison of Microstructure and Phase Transformation for Nanolayered CrN/AlN and TiN/AlN Coatings at Elevated Temperatures in Air Environment. *Thin Solid Films*, 515(3):1097, 2006.
- [193] G. E. D'Errico, E. Guglielmi, and G. Rutelli. A Study of Coatings for End Mills in High Speed Metal Cutting. *J. Mat. Proc. Technol.*, 92-93:251, 1999.
- [194] J. F. Shackelford and W. Alexander. *CRC Materials Science and Engineering Handbook*. CRC Press, Boca Raton, US, 2001.
- [195] MatWeb Materials Property Data. AISI Type 304 Stainless Steel. <http://www.matweb.com>, accessed in 02/2007.
- [196] F. D. Lai and J. K. Wu. High Temperature and Corrosion Properties of Cathodic-Arc-Plasma-Deposited CrN Coatings. *Surf. Coat. Technol.*, 64(1):53, 1994.
- [197] H. Willmann, P. H. Mayrhofer, P. O. A. Persson, A. E. Reiter, L. Hultman, and C. Mitterer. Thermal Stability of Al-Cr-N Hard Coatings. *Scripta Mater.*, 54(11):1847, 2006.

- [198] J. E. Schilbe. Substrate Alloy Element Diffusion in Thermal Barrier Coatings. *Surf. Coat. Technol.*, 133-134:35, 2000.
- [199] P. Y. Hou, Y. Niu, and C. Van Lienden. Analysis of Pore Formation at Oxide-Alloy Interfaces - I: Experimental Results on FeAl. *Oxidation Metals*, 59(1):41, 2003.
- [200] M. Yamashita, Y. Sasaki, H. Ito, H. Ohsato, and N. Shibata. Fabrication of Aluminum Nitride Thin Film and its Oxidation Behavior. *Zairyo*, 55(8):785, 2006.
- [201] D. Suryanarayana. Oxidation Kinetics of Aluminum Nitride. *J. Am. Ceram. Soc.*, 73(4):1108, 1990.
- [202] F. Gesmundo and P. Y. Hou. Analysis of Pore Formation at Oxide-Alloy Interfaces. II. Theoretical Treatment of Vacancy Condensation for Immobile Interfaces. *Oxidation Metals*, 59(1):63, 2003.
- [203] D. M. Roy and R. E. Barks. Subsolidus Phase Equilibria in  $\text{Al}_2\text{O}_3\text{-Cr}_2\text{O}_3$ . *Nature Phys. Sci.*, 2:118, 1972.
- [204] S. S. Kim and T. H. Sanders Jr. Thermodynamic Modeling of the Isomorphous Phase Diagrams in the  $\text{Al}_2\text{O}_3\text{-Cr}_2\text{O}_3$  and  $\text{V}_2\text{O}_3\text{-Cr}_2\text{O}_3$  Systems. *J. Am. Ceram. Soc.*, 84(8):1881, 2001.
- [205] T. M. Besmann, N. S. Kulkarni, and K. E. Spear. Thermochemical Analysis and Modeling of the  $\text{Al}_2\text{O}_3\text{-Cr}_2\text{O}_3$ ,  $\text{Cr}_2\text{O}_3\text{-SiO}_2$ , and  $\text{Al}_2\text{O}_3\text{-Cr}_2\text{O}_3\text{-SiO}_2$  Systems Relevant to Refractories. *J. Am. Ceram. Soc.*, 89(2):638, 2006.
- [206] G. Kleer, R. Kassner, E.-M. Meyer, M. G. Schinker, and W. Doell. Effect of Process Parameters on the Residual Stresses and the Wear Behavior of Aluminum Nitride Physical Vapor Deposition Coatings. *Surf. Coat. Technol.*, 54-55:167, 1992.
- [207] I. Petrov, L. Hultman, U. Helmersson, J.-E. Sundgren, and J. E. Greene. Microstructure Modification of TiN by Ion Bombardment during Reactive Sputter Deposition. *Thin Solid Films*, 169(2):299, 1989.
- [208] I. M. Ross, W. M. Rainforth, Z. Zhou, J. C. Walker, C. Reinhard, A. P. Ehiasarian, P. E. Hovsepian, and R. Braun. Oxidation performance of Nano-scale Multilayer Coatings on  $\gamma\text{-TiAl}$ . In *Electron Microscopy and Analysis Group Conference 2007 (EMAG 2007)*. accepted for publication, Glasgow, UK, 2007.